Chemomechanics of Calcium Leaching of Cement-Based Materials at Different Scales: The Role of CH-Dissolution and C-S-H-Degradation on Strength and Durability Performance of Materials and Structures.

by

Franz H. Heukamp

Diplom-Ingenieur, Technische Universität München (1999)
Ingénieur Civil des Ponts et Chaussées, Ecole Nationale des Ponts et Chaussées (1999)
Diplôme des Etudes Aprofondies Structures, Solides et Systèmes Mécaniques (1999)

Submitted to the Department of Civil and Environmental Engineering
in partial fulfillment of the requirements for the degree of

Doctor of Philosophy

at the

MASSACHUSETTS INSTITUTE OF TECHNOLOGY

February 2003

BARKER

MASSACHUSETTS INSTITUTE OF TECHNOLOGY
FEB 2 4 2003
LIBRARIES

© Massachusetts Institute of Technology

The author hereby grants to Massachusetts Institute of Technology permission to reproduce and
to distribute copies of this thesis document in whole or in part.

Signature of Author .....
Department of Civil and Environmental Engineering
30 September 2002

Certified by .....
Franz-Josef Ulm
Esther and Harold E. Edgerton Associate Professor of Engineering Mechanics
Thesis Supervisor

Accepted by .....
Oral Buyukozturk
Chairperson, Department Committee on Graduate Students

Chemomechanics of Calcium Leaching of Cement-Based Materials at Different Scales: The Role of CH-Dissolution and C-S-H-Degradation on Strength and Durability Performance of Materials and Structures.

by

Franz H. Heukamp

Submitted to the Department of Civil and Environmental Engineering
on 30 September 2002, in partial fulfillment of the
requirements for the degree of
Doctor of Philosophy

Abstract

Calcium leaching is a durability threat for cement-based materials employed in critical infrastructures, such as Nuclear Waste Storage Systems. This thesis presents a comprehensive study of the material and structural consequences of calcium leaching on the strength and deformation behavior of cementitious materials. Starting from a three-level microstructural division of the heterogeneous microstructure of cement-based materials, a series of experimental and theoretical investigations is conducted leading to the development of a novel constitutive model and model-based simulations of the long-term mechanical performance of concrete structures subjected to calcium leaching.

A chemically accelerated leaching device is developed using an ammonium nitrate solution to obtain asymptotically leached specimens in short times. An acceleration rate of 300 compared to natural leaching is obtained. The strength domain of leached cement pastes and mortars is evaluated through triaxial compression tests and uniaxial tension tests, revealing an important strength loss and an increased pressure sensitivity of the materials at failure, associated with leaching.

A micromechanical approach for the homogenization of the elastic properties and the strength properties based on the three microstructural levels is developed. These developments allow estimating the relations between the microstructural changes and poroelastic properties including Biot-coefficient and Biot-modulus. In addition, upscaling schemes for the cohesion and friction properties on different levels of cement-based materials are developed. Through this the influence of the Interfacial Transition Zone on the strength of intact and leached materials is evaluated. The micromechanical elements of the analysis are combined in a chemoporoplastic constitutive model. The porosity created by calcium dissolution (chemical porosity) is identified as a state variable, relating dissolution process and mechanical properties.

The model is implemented in a commercial finite-element program, and model-based simulations show the predictive capability of the developed approach to improve the durability design of concrete structures subjected to calcium leaching.

Thesis Supervisor: Franz-Josef Ulm
Title: Esther and Harold E. Edgerton Associate Professor of Engineering Mechanics

Contents

List of Figures

List of Tables

Acknowledgments

I want to express my gratitude to the three members of my thesis comittee for their support. In particular to Franz-Josef Ulm for the enthusiasm and interest with which he followed my work, as well as for the financial support which he provided and which allowed full-time work on this study. Jack Germaine shared his great expertise on experimental research with me and was available around the clock - I am very grateful for this. Olivier Coussy added at regular intervals his outside-MIT-view on my research which helped me a lot, both through the technical advice and his personal remarks.

In addition to the members of the committee, many people helped in different ways to make this work possible. Among them are Stephen Rudolph who provided excellent machining work at very short notices; Mike Frongillo who patiently taught me how to use the FEGSEM microscope; the support staff in the CEE depertment, particularly Alice and Cynthia.

I have to thank the other members of the Ulm-research group from whom I learned a lot during my time at MIT: Marc Mainguy, Emilio Silva, Georgios Constantinides, Eric Lemarchand, Eugene Chuang and Hesson Park. A special thanks goes to Dirk Mohr who was an excellent listener and critic concerning all my ideas and findings and who helped to clarify them. Last, I want to thank all my friends from my student residence "Elmbrook" and MIT for their support: Paul, Dwight, Peter, Benoît, Gaetano, Davide and Andrea - many thanks.

Part I

General Presentation

Chapter 1

Introduction

1.1 Industrial Context

Today, the durability of infrastructure elements is one of the major challenges in Civil Engineering. The maintenance of existing concrete structures has become a heavy financial burden for infrastructure owners. In 1998, the Federal Highway Administration (FHA) invested more than $30 billion in the maintenance of different elements of the highway infrastructure [110] alone. In the near future, the design of future infrastructure elements will take into account life cycle cost analysis that include later rehabilitation projects. The classical features of durability problems include freeze-thaw damage, chloride induced damage and more recently, calcium leaching. Besides the classical infrastructure elements such as roads and bridges, the question of concrete durability was raised in the past years in the context of nuclear waste storage. In several countries (U.S., France, etc.), concrete structures will be used in the storage of weak and medium radioactive nuclear waste [151]. The applications range from structures at the storage site through the outside layer of waste containers to usage as containers in which vitrified waste will be stored. Other areas where the durability with respect to calcium leaching is of concern are dams, water storage tanks, water/sewage pipes and tunnels. Figure 1-1 displays some characteristic examples.

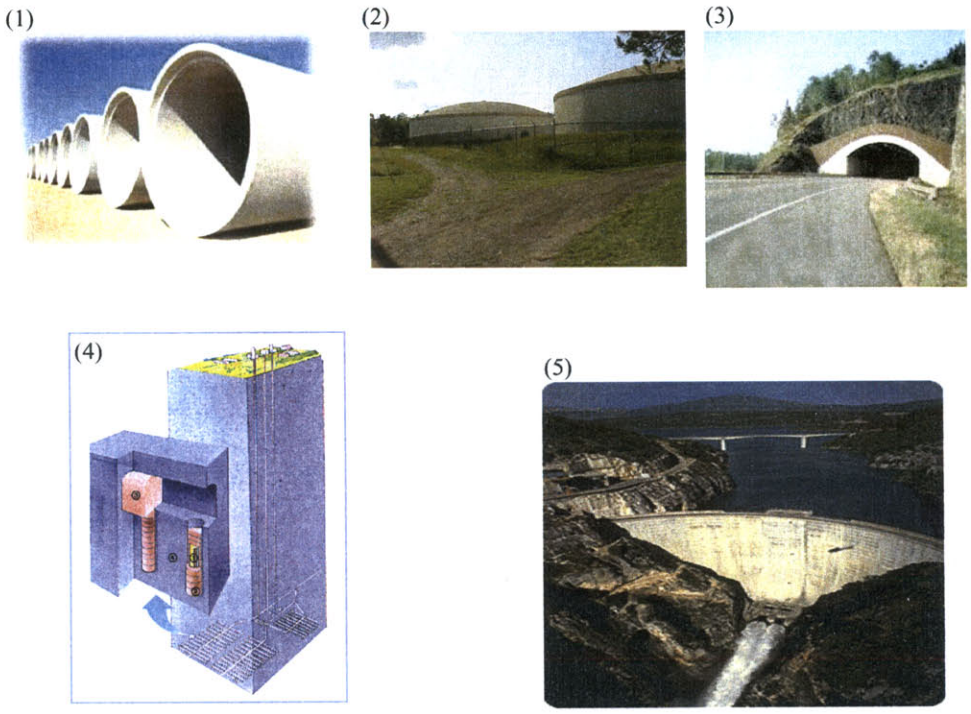

Figure 1-1: Examples of structures that can be affected by calcium leaching: Pipes, water storage tanks, tunnels, nuclear waste storage elements (site structure and containments) and dams. Pictures 1-3 from web catalogues. Pictures 4-5 from EDF.

1.2 Characteristics of Calcium Leaching of Cementitious Materials

Calcium leaching is an ubiquitous process wherever concrete is in contact with water. In a typical cement paste, calcium makes up for roughly 30% of the solid mass. It is by far the most abundant element in cementitious materials. The pH value that typically can be measured in the pore solution of cementitious materials is higher than 12.5, creating a very basic environment. As a consequence, water that has pH values below this level is "aggressive" to concrete, that is it leads to the dissolution of minerals, mainly containing calcium. This process of dissolution, together with the transport of the dissolved calcium in the pore solution, a process that usually takes place by diffusion, is called calcium leaching. Although the leaching phenomenon is obvious for cement chemists [141], the systematic study of the involved chemical and transport processes is relatively recent. In 1992, Adenot [3] showed that the leaching process is governed in its time scale by the diffusion process, as the dissolution is much faster. The primacy of the diffusion process of the leaching time scale was further experimentally confirmed by observation of sharp leaching fronts. These fronts separate zones where one mineral is still present from a zone where it has been dissolved. Figure 1-2 shows an image of a leached paste with sharp fronts.

1.3 Research Motivation

The usage of concrete in all kinds of construction projects has not been reduced although many more "high-tech materials" have been developed in the past years. Concrete is comparatively cheap, easy to work with and provides good mechanical performance and shielding capacities. The durability performance of concrete will be the key to its future utilization in longterm structural applications. These applications bring about new challenges:

- Material properties of concretes have to be predicted over time periods up to several hundred years, which is for example the life time of medium radioactive waste storage sites.
- Critical material properties like strength, deformation behavior and transport proper-

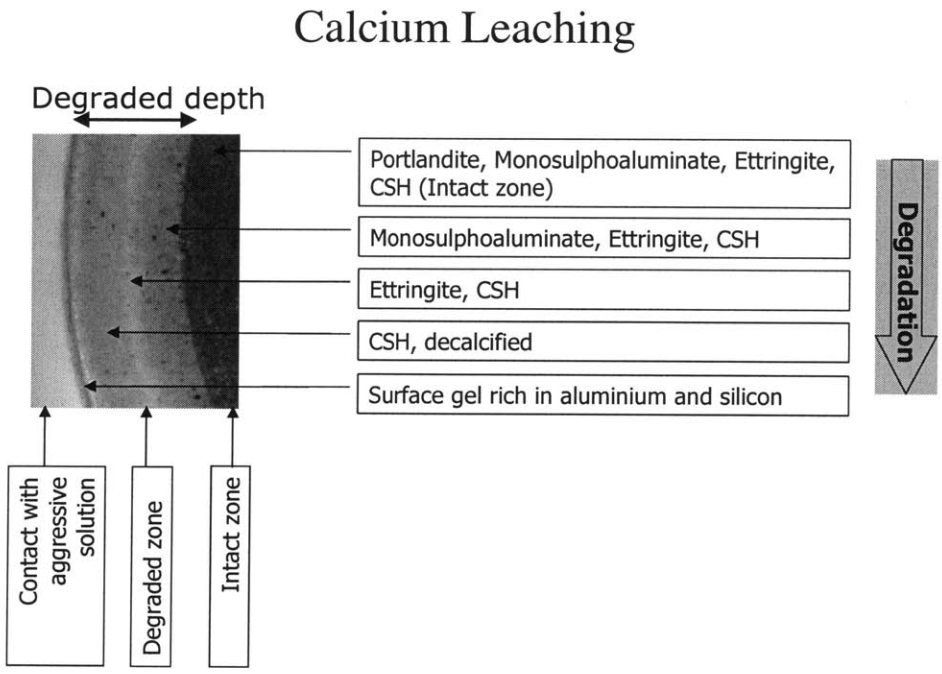

Figure 1-2: Observed sharp dissolution fronts in a cement paste. Adapted from [3]

ties involve complex interactions between different chemical processes that affect the microstructure of the material and the mechanical performance at multiple scales.

- Monitoring of existing structures becomes now possible through sophisticated measurement devices that can be installed permanently in a given structure. Knowledge based monitoring programs are required that process the data and suggest maintenance steps.

In this context, several research projects have been conducted on the topic of calcium leaching. They can be roughly classified in studies that focused primarily on the understanding of the chemical processes linked to calcium leaching ([3], [49], [115]), the development of artificial leaching techniques ([56], [128]) and the degradation of stiffness and uniaxial compressive strength ([30], [80], [37]).

This research aims to answer the *why* and *how* of the material degradation. *Why does the material degrade in calcium leaching?* and *how can the residual strength capacity be used?* These questions are addressed in a holistic way, ranging from microstructural investigation over material testing and structural analysis.

1.3.1 Research Objectives

A comprehensive approach is presented to address the scientific challenge. It is composed of experimental investigation, theory and modeling, experimental validation and computer simulations. It studies the effects of leaching at different length scales ranging from the material microstructure to the material level and the structural level, following the four research objectives:

Objective 1: *Determine the multiaxial strength and deformation behavior of cementitious materials subjected to calcium leaching.* The knowledge about the strength evolution in calcium leaching is reviewed at the three levels of microstructure that characterize cementitious materials. The residual multiaxial strength and the deformation behavior are assessed in triaxial compression and tension tests. As a prerequisite to the experimental investigation, an accelerated leaching device is developed.

Objective 2: *Develop micromechanical estimates for the multiaxial strength properties of partially leached cementitious materials.* The experimental approach to strength is limited to

homogeneous material states. Only the intact and asymptotically leached materials can be tested. For the strength properties of partially leached cementitious materials a micromechanical estimate is developed. This approach is based on continuum micromechanics.

Objective 3: *Develop a material model for cementitious materials that undergo calcium leaching.* A constitutive model for cementitous materials subjected to calcium leaching is presented. It is a chemoplastic model composed of a diffusion dissolution part considering the leaching of the two main minerals and a poromechanical description of strength and deformation. Albeit a macroscopic model, it contains the micromechanical analysis of strength and deformation behavior.

Objective 4: *Assess the residual load bearing capacity at the structural level during calcium leaching.* The final objective is to study the durability performance of cementitious materials at a structural level. To this end, the model is implemented in a commercial finite element program. Running model-based simulations offers the possibility to investigate the structural performance of partially or completely leached materials.

These four objectives make up a comprehensive approach to the performance of cementitious materials subjected to leaching. Figure 1-3 summarizes the approach.

1.3.2 Industrial and Scientific Benefits

Associated to the research objectives are some industrial and scientific benefits. They include:

- Additional knowledge about the properties of cementitious materials when subjected to leaching, based on the experimental work.
- An expansion of micromechanical techniques into the area of strength homogenization.
- The constitutive model, which links chemical degradation and mechanical performance.
- A finite element based computational tool to investigate the durability performance of concrete structures in the course of calcium leaching.

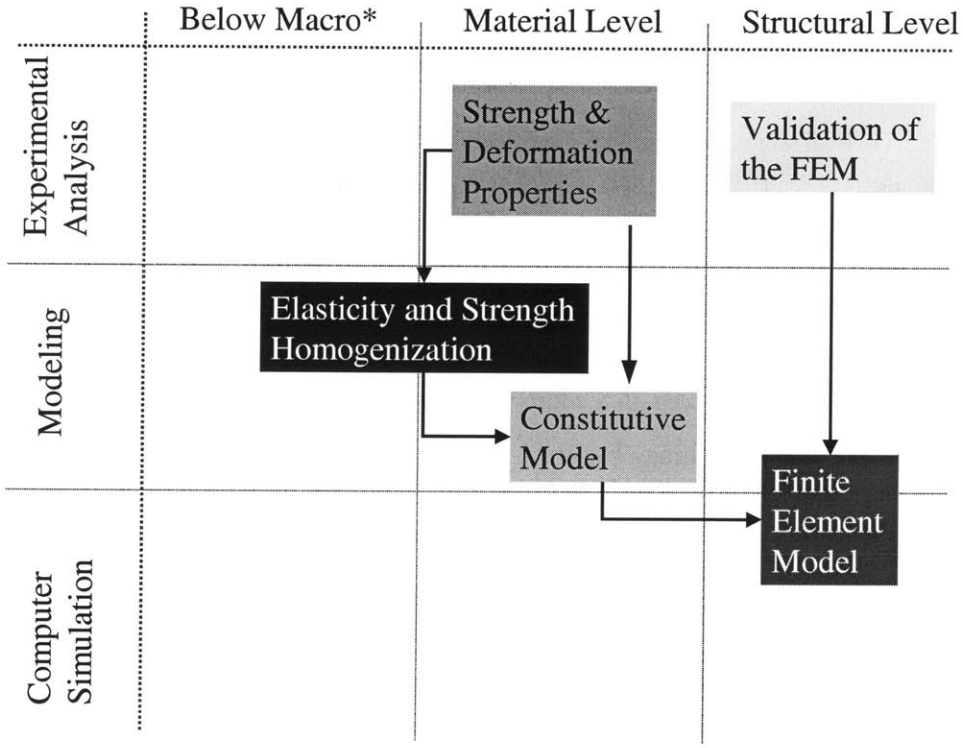

Figure 1-3: Overview of the comprehensive approach followed in this study. * The category "Below Macro" is inspired by the special issue of the Journal of Engineering Mechanics [Vol. 128, N° 8]. It designates summarily the length scales involved in the micromechanical analysis.

1.4 Outline of Thesis

This thesis is divided into four major parts. The first part deals with the presentation of the topic and comprises two chapters. Following this introduction, Chapter 2 discusses the existing knowledge about the effects of calcium leaching on cementitious materials. This discussion is guided by a proposed three-level microstructure.

The second part focuses on the experimental aspects of this study. Chapter 3 presents the design and operation of an accelerated leaching device involving ammonium nitrate. This design is based on a 1-D think model of the leaching process, focusing on two leaching fronts. Chapter 4 describes the composition of the tested materials, a cement paste and a mortar. In addition, some microstructural analysis results from Scanning Electron Microscopy are presented showing the consequences of calcium leaching. Chapters 5 and 6 form a close unit as both report results from triaxial compression and tension tests on leached cementitious materials. The focus of Chapter 5 is on the residual strength domain of these materials, while Chapter 6 describes the deformation behavior. Together, they establish the validity of the effective stress concept at failure for leached materials and educe the failure criteria for leached cement paste and mortar.

Part three of this study focuses on the modeling aspects. Chapter 7 presents the micromechanical analysis of the elastic and poroelastic properties for cementitious materials and their evolution with leaching. Estimates for Young's modulus, Biot coefficient and Biot modulus are developed. Chapter 8 contains the extension of the micromechanical estimates to strength properties. Structured into high and low confinement stress states, homogenization methods for the frictional coefficient and the cohesion are put forward. Chapter 9 presents the complete constitutive model for cementitious materials subjected to calcium leaching. It includes a dissolution-diffusion part, which describes the degradation state through a new state variable, the chemical porosity. The mechanical performance is modeled with a chemoporoplastic approach that includes a micromechanical identification of the sources of dissipation as well as the experimental and micromechanical developments.

The fourth part presents the model-based simulations. Chapter 10 describes the validation of the finite element model through comparison with three different experimental investigations. These are the compression of partially leached cylinders, three-point bending of a partially leached notched beam and the evolution of the four-point bending strength with leaching time.

Chapter 11 demonstrates the capacity of the model-based simulations in durability design. Using an Ultra High Performance Concrete in four-point bending, its durability performance is analyzed. Based on these results, some recommendations for the design of durable cementitious materials are drawn. Chapter 12 summarizes the results of this study and gives suggestions for further research.

In the appendix, additional information is provided. This includes the test evaluation formulae, some aspects of the micromechanical calculations and the implementation of the constitutive model into the finite element program.

Chapter 2

Microstructure of Cementitious Materials: General Properties and the Effect of Leaching

This chapter gives an overview of the multiscale microstructure of cementitious materials and how calcium leaching manifests itself at the different scales both chemically and mechanically. First, a three-level microstructure is proposed for cementitious materials, based on the mechanical length scales. These levels will serve throughout this study as a guide-post for the experimental and analytical investigations. With the three levels at hand, the characteristics of the microstructure at each level are discussed. In addition, chemical and mechanical effects of calcium leaching are described. From this discussion, the blanks in the knowledge about the effects of calcium leaching on cementitious materials are identified and an outline of the work in this study follows.

Notations

A notation specific to cement chemistry will be used throughout this Chapter and the other parts of this study. Table 2.1 shows the abbreviations used in cement chemistry. In addition, C-S-H is used as an abreviation for Calcium Silicate Hydrates at an unspecified mass ratio. w/c designates the water - cement mass ratio of a cementitious material.

Cement Chemistry Notation	
C	CaO
S	SiO_2
A	Al_2O_3
F	Fe_2O_3
$\underline{S}$	SO_3
H	H_2O

Table 2.1: Cement chemistry convention

2.1 Three-Level Microstructure

2.1.1 Introduction

This section introduces a division of the microstructure of cementitious materials in three levels. The division is based on mechanical considerations and serves as a blueprint for the further analysis of the leaching effects on cementitious materials in this chapter and throughout this study.

2.1.2 Mechanical Length Scales

For the mechanical investigation of materials, in general different length scales can be distinguished with respect to the microstructural features and the analysis techniques that are used. The relevant length scales for current investigation techniques span from tens of nanometers to the centimeter scale. The length scale at which an investigation is performed is chosen considering the type of information that is sought, how it manifests itself at a higher scale and how it is treated analytically. Depending on the studied material, one length scale corresponds to the desired scale of operation of the material. This scale determines at which other scales below, information will be gathered. Depending on the analytical treatment, a separation of the scales at which information is extracted might be necessary. In this way a heterogeneous microstructure can be broken down into elementary levels of governing heterogeneity of the matrial.

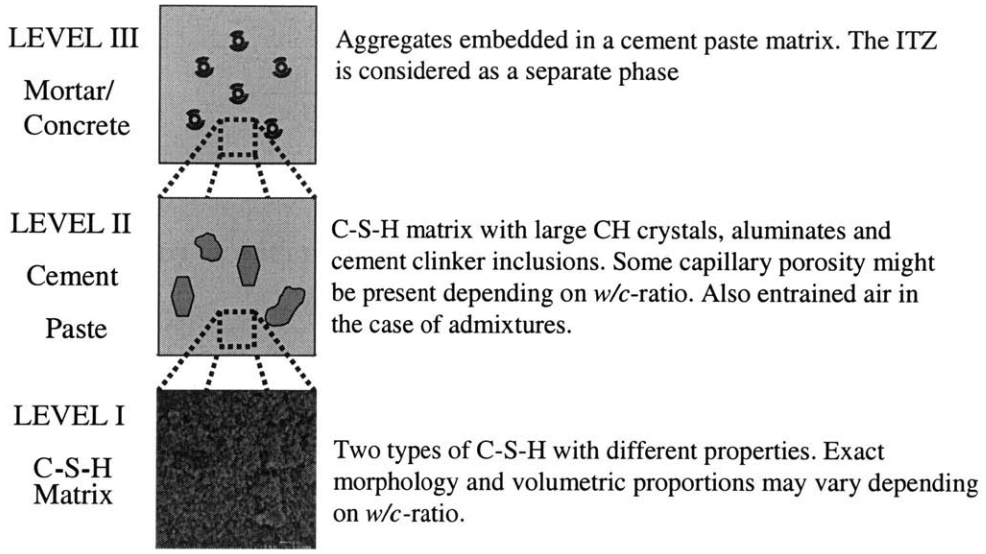

Figure 2-1: The three-level material structure of cementitious materials. Adapted from [37].

2.1.3 Proposed Three-Level Microstructure

For cementitious materials we propose a division of the nanometer to meter range in three levels, as sketched in Figure 2-1. The first level covers the length domain from 10^{-8} m to 10^{-6} m and corresponds to the C-S-H matrix. The second level covers the domain from 10^{-6} m to 10^{-4} m which corresponds to cement paste; the third domain of a characteristic length scale 10^{-4} m to 10^{-1} m correspond to mortar and concrete. This break-down of the heterogeneous microstructure leads to a separation of the considered scales by one or several orders of magnitude. A similar division has been used successfully by Constantinides [37].

Mineralogical Phase	mass %
C_3S	50-70
C_2S	15-30
C_3A	5-10
C_4AF	5-15

Table 2.2: Typical mineralogical composition of a Portland cement

2.2 Chemical and Physical Characteristics of the Microstructural Levels

2.2.1 Hydration of Cement

The hydration process of cement lays the foundation for the discussion of the chemical and physical characteristics of cementitious materials. The cement particles have a diameter in the micrometer range corresponding thus to the length scale of Level II. The hydration of the cement leads to different microstructural products that manifest themselves at different length scales discussed in the sequel. The cement consists of four clinker phases, which react with the water in a process that is called hydration. In an ordinary Portland cement, the clinker phases are tricalcium silicates, C_3S, dicalcium silicates, C_2S, tricalcium aluminates, C_3A, and tetracalcium aluminum ferrites, C_4AF. A standard mineralogical composition of Portland cements is presented in Table 2.2. Among the four clinker phases, we describe the hydration of aluminates and silicates briefly. They form the most important part of the microstructure of a cement paste.

Aluminate hydration

The hydration of the tricalcium aluminates is a rapid process that leads to calcium aluminates which are called AFm phases. A set[1] of hydration reactions is [141]:

$$\begin{aligned} 2C_3A + 27H &\longrightarrow C_4AH_{19} + C_2AH_8 \\ 2C_3A + 21H &\longrightarrow C_4AH_{13} + C_2AH_8 \\ C_3A + CH + 12H &\longrightarrow C_4AH_{13} \end{aligned} \tag{2.1}$$

In addition to this phase, Ettringite (AFt in the notation of Taylor [141]) forms in the presence of sulfates (SO_4^{2-}) and water:

$$C_3A + 3C\underline{S}H_2 + 26H \longrightarrow C_6A\underline{S}_3H_{32} \tag{2.2}$$

Once the sulfate ions are consumed, the Ettringite becomes an AFm phase according to the following reaction:

$$2C_3A + C_6A\underline{S}_3H_{32} + 4H \longrightarrow 3C_4A\underline{S}_3H_{12} \tag{2.3}$$

The hydration of the C_4AF is very similar to the hydration of the C_3A except for the slower kinetics. The reactions (2.1) can be written analogously with the aluminum being replaced by iron. The size of the end products of the aluminate hydration is in the 10^{-6} m range, located on Level II.

Silicate Hydration

The hydration of silicates leads to the main products of the cement hydration. The hydration of the two silicate phases is very similar and can be divided in three stages [141]:

1. Dissolution of the clinker grains (C_3S and C_2S);
2. Diffusion of the ions that are formed in the interstitial solution;
3. Precipitation as the saturation point for the different hydrates is attained.

[1] The expression "set" indicates that the reactions are consistent among themselves. Depending on the source slightly different writings can be found.

As the precipitation takes place, the ion concentration in the solution is lowered and more clinker is dissolved. The hydration reaction of the silicate can be written according to [142]:

$$\begin{aligned} 2C_3S + 10.6H &\longrightarrow C_{3.4}S_2H_8 + 2.6CH \\ 2C_2S + 8.6H &\longrightarrow C_{3.4}S_2H_8 + 0.6CH \end{aligned} \tag{2.4}$$

The calcium hydroxide (CH) which is also called Portlandite constitutes approximately 20 to 25vol-% of the hydration product. The characteristic size of Portlandite is in the hundreds of micrometers and is located on Level II of the microstructure. The calcium silicate hydrates (C-S-H) which constitute 50 to 70vol-% of the hydration product have a much smaller characteristic size and form Level I of the microstructure.

2.2.2 Level I: C-S-H Matrix

Level I of a cementitious material refers to the C-S-H matrix. The C-S-H is the smallest microstructural phase (characteristic length scale 10^{-9} to 10^{-7} m) and the most important hydration product (50-70% of the hydration product by volume). The composition of the C-S-H is variable, which is the reason for its hyphenated notation [141]. It depends primarily on the composition of the cement. A common way of characterizing the compositional differences in C-S-H is the C/S (mass)-ratio. This ratio can vary in general between 0.7 and 2.3. For Ordinary Portland Cement (OPC) this ratio varies between 1.2 and 2.3 with a mean value of 1.75. The C-S-H are poorly crystalline although an organized microstructure exists at the *nanometer scale* [141]. The density of C-S-H varies between $2,300$ and $2,600\,\mathrm{kg/m^3}$ depending on their exact composition . The appearance of C-S-H under the microscope varies considerably, depending on the observation time during the hydration reaction and the cement composition. Different types of C-S-H were identified (I through IV) [141] with respect to their morphology, as Environmental Scanning Electron Microscopy (ESEM) micrographs of some typical C-S-H phases show (Figures 2-2 and 2-3). Some natural minerals such as Tobermorite [61] and Jennite [101] were suggested as natural analogs to the C-S-H structure although it has become clear in more recent works ([124], [51], and [74]) that these analogs are incomplete and perhaps misleading. Among the C-S-H, different ways of distinguishing the products according to their

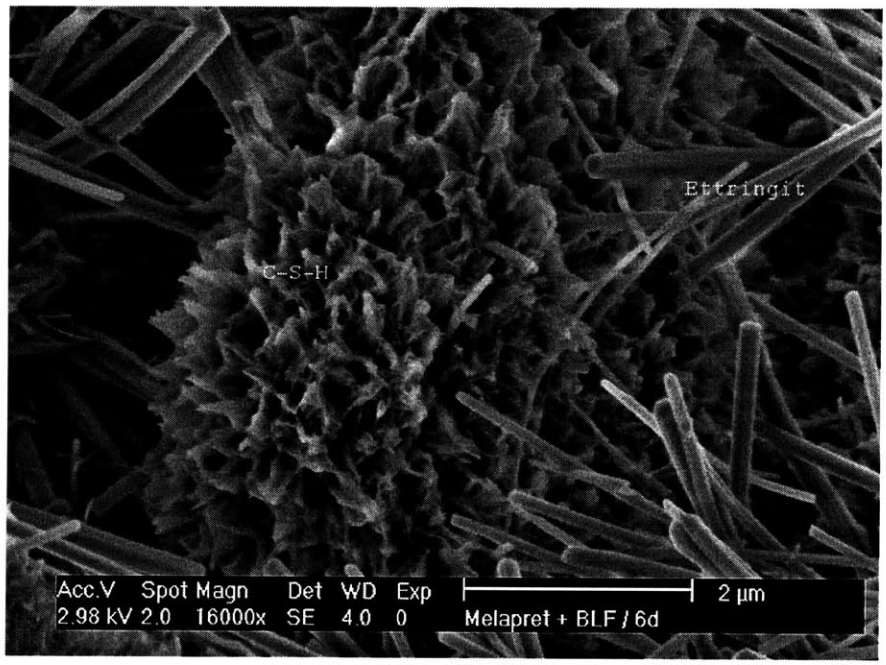

Figure 2-2: ESEM micrograph of an OPC paste, showing $C-S-H$ clusters and Ettringite fibers. From [126]. Reprinted with Permission.

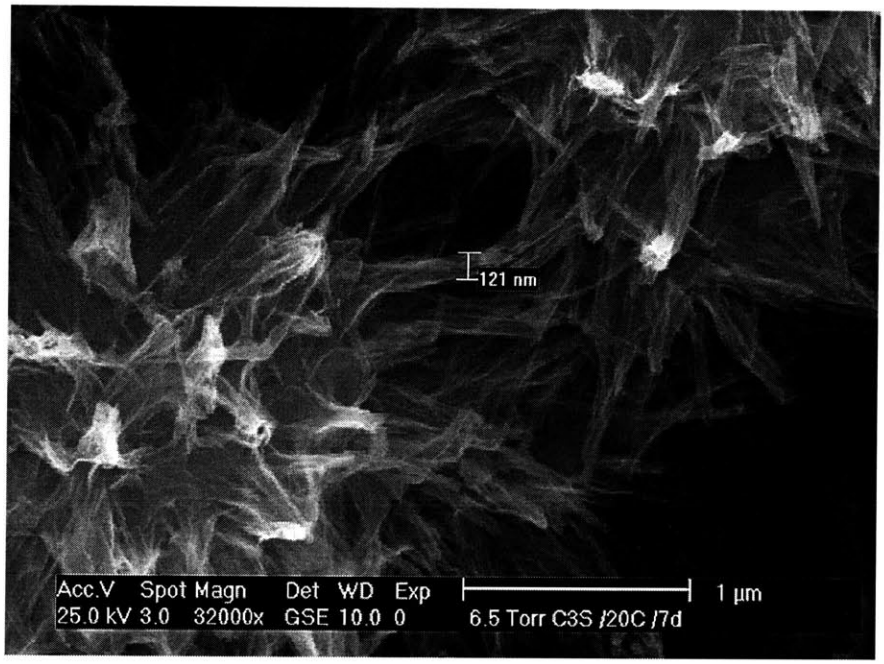

Figure 2-3: ESEM micrograph focusing on the $C-S-H$ microstructure. From [126]. Reprinted with permission.

Elastic Modulus (GPa)	Intact	Degraded	Residual Value (%)
C-S-H_α	21.7 ± 2.2	3.0 ± 0.8	14
C-S-H_β	29.4 ± 2.4	12.0 ± 1.2	41

Table 2.3: Elastic Modulus of the C-S-H obtained by nanoindentation (Mean/St. Dev.). From [37]

hydration location or density have been proposed ([142], [37]):

- Outer products or low-density C-S-H, which are the first hydration products as they form on the outside of a clinker grain.
- Inner products or high-density C-S-H, which form within the clinker phases as the hydration progresses.

From a mechanical point of view two types of C-S-H are considered. Following Constantinides [37] these are labeled C-S-H_α and C-S-H_β. They have different physical properties [142]. The density of C-S-H_α is roughly $1,910\,\mathrm{kg/m^3}$ while for the C-S-H_β it is $2,100\,\mathrm{kg/m^3}$. Moreover, the elastic properties of the C-S-H were measured with nanoindentation by Acker [2] and Constantinides [37]. This testing method allows for the measurement of elastic properties at a length scale of $10^{-7}\,\mathrm{m}$ and can therefore be used to determine properties at Level I. Figure 2-4 shows a schematic picture of a nanoindentation experimental setup. During the test, an indenter with a diamond tip is pushed into the specimen. Both the force, P, and the penetration depth, h, are recorded. From a $P-h$ curve (Figure 2-5 shows a typical example), the Young's modulus can be extracted based on the unloading curve. This is done by considering a somewhat modified Hertz-Boussinesq problem (contact of a tip with an infinite elastic half-space) in a linear elastic medium ([111], [44], [57] and [153]). Table 2.3 gives the mean values for the Young's modulus of the two C-S-H phases: C-S-H_α and C-S-H_β. The results show a considerable difference in the elastic modulus: The low-density C-S-H is the softer material. Parallel tests by Acker [2] on a different cementitious materials gave similar results and suggest that the obtained Young's modulus is intrinsic for C-S-H. The volume distribution between the two types of C-S-H depends on the mix design. The C-S-H_α phase forms first, as the water gets in contact with the clinker. Only after the water diffuses into the clinker grains does the formation of the C-S-H_β phase starts. In other words, the high-density C-S-H forms later and if the

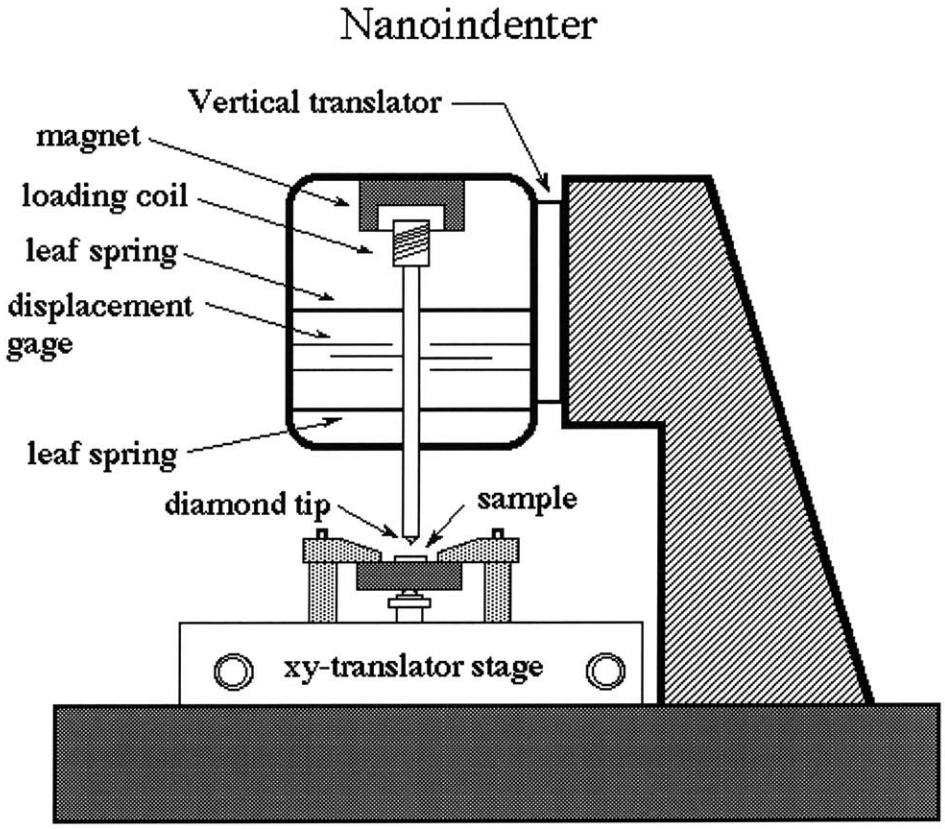

Figure 2-4: Schematic representation of a nanoindentation device. From [44].

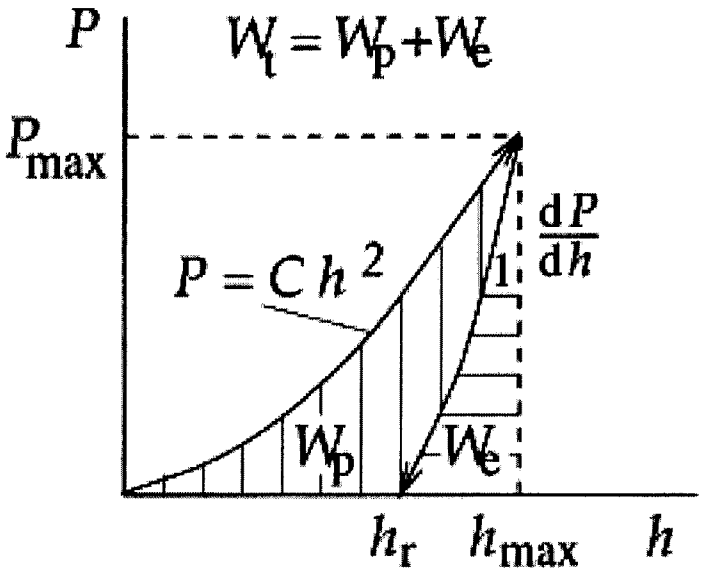

Figure 2-5: Typical loading-unloading P-h curve.

water supply for the hydration is exhausted too quickly (for low w/c-cement based materials) it is likely that no or little C-S-H_β might form at all. The composition can be predicted based on the cement water mixture with hydration models (see for example [17]). The microhardness of C-S-H has also been measured, but a correlation with strength has not been presented yet. Currently, the nanoindentation tests can only be evaluated for elastic properties.

Additional information about the elementary C-S-H structure, which would correspond to a Level "0", can be obtained through Nuclear Magnetic Resonance (NMR). NMR measurements revealed the presence of silicate chains of varying length in C-S-H ([49], [26], [115], [117]). The chain length, or polymerization, has been suggested to be related to the mechanical properties of C-S-H such as the cohesion [113]. The chain length depends on the degree of hydration and the C/S ratio. The chain length can alternatively be illustrated by the connectivity of the $Si\,O_4$ tetrahedrons as displayed in Figure 2-6. Q_0 is the denomination of an isolated tetrahedron while Q_1 designates a tetrahedron that is connected to only one other tetrahedron. Q_2 through Q_4 describe connections of two through four tetrahedrons. A special case is the Q_{2p} tetrahedron which is part of a repeated Dreierkette but shares only one of its oxygen atoms. The different

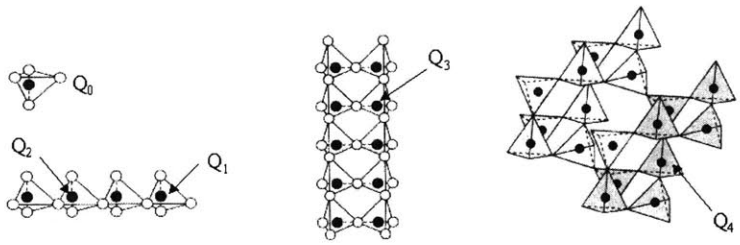

Figure 2-6: Schematic representation of the different connectivities of $Si\,O_4$ tetrahedrons. From [115].

connectivities are. With the aid of NMR, it is possible to distinguish very precisely between the different degrees of connectivity, characterized by Q_x. This is true both in a qualitative and quantitative manner. Figure 2-7 shows the results from a ^{29}Si NMR experiment on an OPC paste [115]. The spectra are decomposed according to the different degrees of connectivity. With this type of information at hand, it is possible to compare the average chain length of different C-S-H specimen and particularly at different C/S ratios. A standard way of comparing chain lengths is the calculation of the ratio $(Q_2 + Q_{2p})/Q_1$ which basically looks at the number of middle elements of a chain (the Q_2) relative to end members of a chain (the Q_1). A ratio of 1.5, which is a standard value for C-S-H, corresponds to an average chain of five $Si\,O_4$ tetrahedrons. Figure 2-8 gives a schematic representation of the C-S-H structure, including the characteristic distance between the Si-chains.

An important property of C-S-H is the capacity to substitute some of its Si and Ca atoms with other atoms such as Al, Fe and S, that is the C-S-H formed in this way have different degrees of impurity but this configuration can be chemically more stable than the original configuration. This is of great relevance for calcium leaching [49]: Calcium leaching of cement-based materials leads to a chemical equilibrium at which some calcium remains.

2.2.3 Level II: Cement Paste

In addition to the homogeneous C-S-H matrix, the phases that are present on Level II are Portlandite (CH), Aluminates and unhydrated clinker.

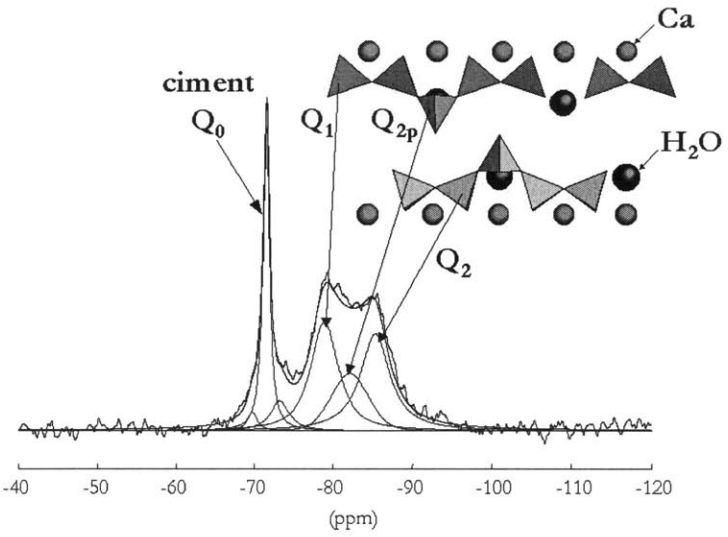

Figure 2-7: Decomposition of the ^{29}Si NMR spectra of an OPC paste. From [115].

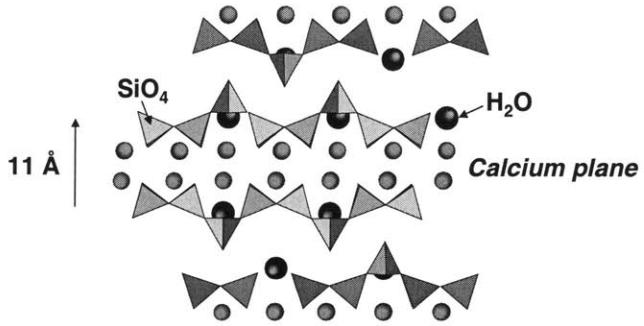

Figure 2-8: Schematic structure of the C – S – H. From [115].

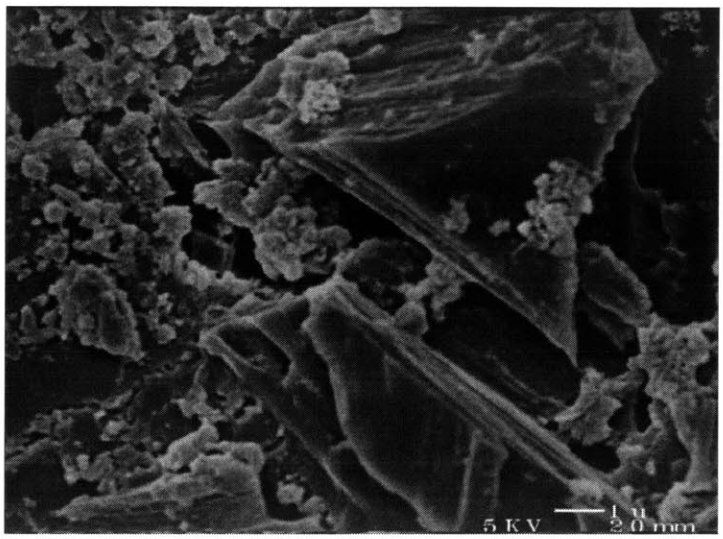

Figure 2-9: Scanning Electron Microscopy graph showing Portlandite crystals in an OPC paste.

Calcium Hydroxide (CH)

Calcium hydroxides generally make up for about 20 to 25% of the hydration products by volume. The stoichiometry of Portlandite is well defined and it generally forms hexagonal crystals. The size of these crystals is usually several hundred micrometers when the crystals can grow into open space. This is the usual case, and Portlandite that is trapped in C-S-H (Level I and below) with smaller sizes, are the exception. The density of Portlandite is $2,240\,\mathrm{kg/m^3}$. Figure 2-9 displays some larger clusters of Portlandite crystals as they were observed in Scanning Electron Microscopy during the experimental part of this study.

The Young's modulus of Portlandite is relatively easy to measure as crystals can be grown. The values given in the open literature vary between 35 and 40 GPa [2, 14, 37, 155]. The influence of Portlandite on the strength of cementitious materials is generally believed to be more detrimental than beneficial due to the inhomogeneity created in the C-S-H matrix and the fracture mechanical down sides such as stress concentrations [40]. In addition, the hexagonal crystal tends to cleavage failure. For this reason, in cases where strength optimization is of importance, concrete mix designers have aimed at obtaining Portlandite free hydration products [122]. This can be achieved by admixtures such as silica fume which in the so called Pozzolanic

reaction consumes the Portlandite. This reaction reads:

$$\mathrm{CH} + \mathrm{S} \rightarrow \text{C-S-H} \tag{2.5}$$

Modern High Performance Concretes (HPC) make use of this technique. For the elastic properties, the presence of Portlandite crystals is beneficial due to its high Young's modulus ([37], [141]).

Aluminates

Aluminates form during the hydration of cement (Eqs. (2.1) and (2.3)) very quickly. They are responsible for the first stiffening of a cement paste which makes them important for the workability of the paste. Ettringite forms needle shaped crystals with a length on the order of a micrometer and a density of $1,750\,\mathrm{kg/m^3}$. Calcium aluminates form well crystallized hexagonal plates in the micrometer range and have densities ranging from $1,950$ to $2,020\,\mathrm{kg/m^3}$ depending on the stoichiometry of the formed product. For the aluminate phases very little information on elasticity and strength properties are available, mostly because their quantity is relatively small. In general for the final strength of a paste they are considered to be less important [136].

Unhydrated Clinker

Depending on the quantity of water available for the hydration reaction, some of the clinker grains in the cement might remain unhydrated. This is the case when the w/c-ratio is below 0.38. Modern high performance and ultra-high performance concretes have water-cement ratios that are as low as 0.2 or 0.25; and a considerable amount of unhydrated clinker can be found at Level II of the microstructure. The clinker grains have a diameter in the micrometer range and extremely high Young's moduli. Acker [2] and Velez et al. [152] report values from indentation measurements varying between 125 and 160 GPa, depending on the type of clinker. Table 2.4 summarizes the data and the corresponding reference.

	E [GPa]	ν [1]	References
C_3S-Clinker	135±7	0.3	Acker [2]
	147±5	0.3	Velez et al. [152]
C_2S-Clinker	140±10	0.3	Acker [2]
	130±20	0.3	Velez et al. [152]
C_3A-Clinker	160±10		Acker [2]
	145±10		Velez et al. [152]
C_4AF-Clinker	125±25		Velez et al. [152]
CH	35.24		Beaudoin [14]
	48		Wittmann [155]
	39.77÷44.22	0.305÷0.325	Monteiro & Chang [106]
	36±3		Acker [2]
	38±5		Constantinides [37]

Table 2.4: Measurements of elastic properties of cement clinker and Portlandite.

Mechanical Properties of Cement Paste as a Composite Material

The different elements of the microstructure that were described, plus pores which will be discussed below, form a cement paste. The mechanical performance of such a composite material is well known because it can be tested on larger specimens. The properties of a cement paste depend strongly on the amount of each constituents. The most important parameter here is the w/c-ratio. We focus here on standard cementitious materials that have w/c-ratios above 0.38 so that all clinker phases are consummed in the hydration reaction. For a $w/c = 0.5$ cement paste, Constantinides [37] determined the elastic properties with different methods (see Table 2.5). A typical value for the Young's modulus of a cement paste is around 20 GPa. The strength of cement pastes is commonly tested by uniaxial compression tests. The compressive strength of a standard paste (w/c=0.5) is 50 MPa [109]. The tensile strength of cement pastes is lower. Generally as a rule of thumb, 10% of the compressive strength is reached in tension. The frictional behavior of cement pastes, that is the capacity to carry higher loads through increased mean stress, has rarely been determined experimentally.

2.2.4 Level III: Mortar/Concrete

From a compositional point of view, the difference between a cement paste (Level II) and a mortar or concrete (Level III) is in the addition of aggregates. The aggregates are graded in their size to improve the packing. Depending on the mix design and application, they range from

Modulus [GPa]	Lev. II Int.	Lev. II Deg.	Lev. III Int.	Lev. III Deg.
UPV-Pulse Modulus	22.8 ± 0.5	3.6 ± 0.2	26.5 ± 1.8	5.3 ± 0.1
RF-Dynamic Modulus	21.7 ± 0.1	3.2 ± 0.1	25.2 ± 0.1	4.9 ± 0.1
UC-Static Modulus	18.6 ± 0.6	0.7 ± 0.2	21.6 ± 0.4	0.5 ± 0.1

Table 2.5: Summary of elastic moduli for a cement paste (Level II) and mortar (Level III) at w/c =0.5 obtained by different methods: UPV,RF and UC. Results from [37]

diameters of approximately 0.1 mm to 10 cm. However, besides the aggregates, an additional feature is newly created: The interface between aggregates and the cement pastes. Adding aggregates to a cement paste generally increases the stiffness of the material because of the high Young's modulus of the aggregates. Table 2.5 summarizes the Young's modulus measurements for a mortar with a water-cement ratio of 0.5 by Constantinides [37]. The strength however does not necessarily increase. This is due to the interface between the aggregates and the paste which influences the overall behavior of mortars and concrete. The interface is also called the Interfacial Transition Zone (ITZ) as it is characterized by a gradually changing composition from the aggregate away. Generally the ITZ contains a higher porosity than the cement paste (in fact that is its very definition) and higher concentrations of Portlandite and Ettringite. [136]. Several explanations for this were put forward:

- An increased w/c-ratio close to the aggregates leads to increased Portlandite and Ettringite presence [102].
- The so called "Wall effect" leads to a zone of increased porosity and favors the presence of the rather large Portlandite and Ettringite crystals [96].
- Syneresis, the property of a gel to contract, leads to expulsing the liquid while the total volume of the system remains constant [127].

A thin layer immediately adjacent to the aggregates was identified by some authors as a duplex layer of Portlandite and C-S-H [10], however its existence remains debated as other authors could not verify it [132].

It is generally agreed upon that the ITZ reduces the strength of cementitious composite materials. However, no concise model exists that can quantify this reduction. This is mainly due to the absence of good measurements of the mechanical properties of the ITZ itself. Attempts

have been made to characterize the strength of the ITZ by microhardness measurements [103], [159]. The relative hardness compared with bulk paste is consistently found to be between 25 and 40% but the absolute values vary significantly (ranging between 10 MPa and 100 MPa). In addition, the relation between hardness and strength of the ITZ is unclear due to the inhomogeneous microstructure [96]. Modern HPC that are Portlandite free due to the Pozzolanic reaction (Eq. (2.5)) do not suffer from the detrimental effects of the ITZ. The absence of Portlandite leads to a homogeneous paste around the aggregates, and the strength is much higher than the strength of ordinary concretes. Generally, failure of HPC occurs by the breaking of the aggregates [11]. The uniaxial compressive strength of a low quality mortar is around 35 MPa, that is considerably lower than the one of the paste, which highlights the role of the ITZ on the strength of a cementitious material. The frictional behavior of concrete and mortars is well documented (see for example [47] and the references therein). For example, the deviatoric compressive strength of a mortar or concrete can be expressed through:

$$\sqrt{J_2} = \delta \Sigma_M - c \tag{2.6}$$

where $J_2 = \sqrt{1/2\mathbf{S} : \mathbf{S}}$ is the second invariant of the stress deviator $\mathbf{S} = \boldsymbol{\Sigma} - \Sigma_M \mathbf{1}$. $\Sigma_M = 1/3\mathrm{tr}\boldsymbol{\Sigma}$ is the mean stress, δ the friction coefficient and c the cohesion. Values for the friction coefficients for mortars and concretes vary between 1 and 1.4 depending on the mix design [47, 109].

2.2.5 Porosity

The porosity of cementitious materials is scaled in a similar way as the hydration products. Figure 2-10 gives an overview of the different pore sizes [117] which will be discussed next and the standard measurement techniques, which are presented in Tables 2.6 through 2.10.

Porosity on Level I

At the level of the C-S-H matrix, most of the total porosity of cementitious materials is present. A class of pores with diameters below 2nm (also called micropores or gelporosity) are associated with the layer structure of the C-S-H (see Figure 2-8). While this length scale is not accessible to direct visual observation, different models were proposed to explain indirect experimental

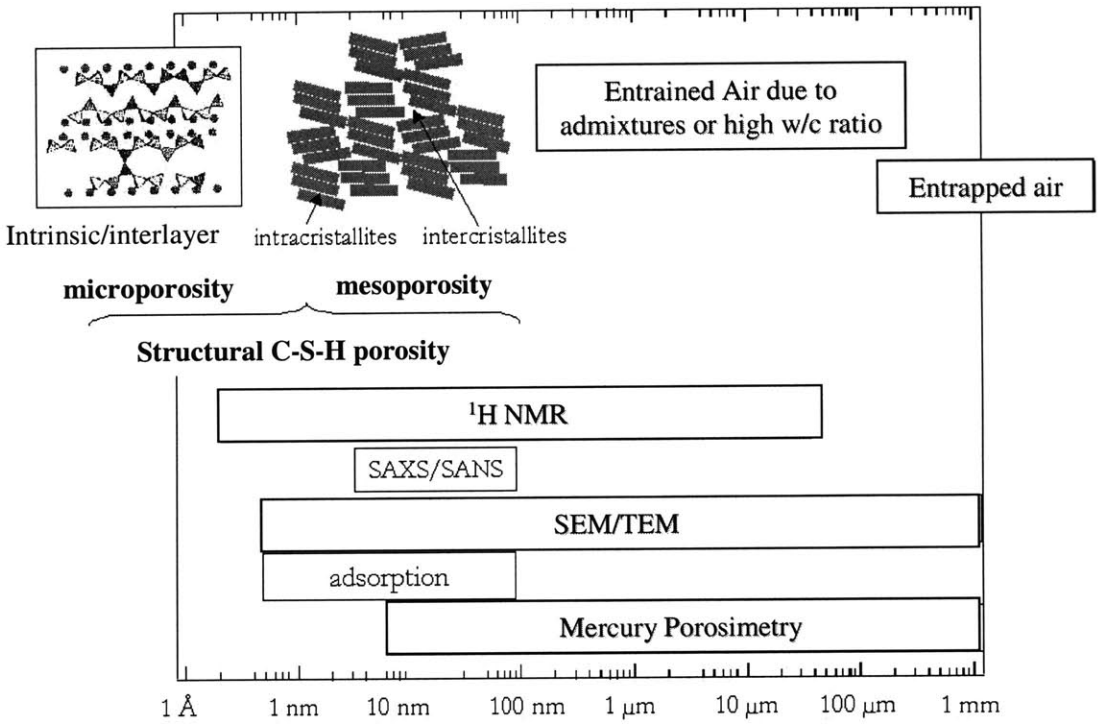

Figure 2-10: Length scales of the different porosity types in pastes and the working range of the measurement techniques. Figure adapted from [115].

observation such as nitrogen adsorption measurements. The model by Powers and Brownyard [118] predicts 28% porosity and an interlayer space of the C-S-H of 1.8 nm.[2] Other models, for example the one by Feldman and Sereda [52], assume interlayer spaces between 0.5 and 2.5 nm. Models that distinguish between two types of C-S-H predict different individual porosities but the same average porosity [142]. These small pores have been suggested to form a zone of hindered adsorption and are important for creep and shrinkage of the C-S-H matrix [2], [146]. The water in the micropores is chemically bound to the surface [156, 157, 158] so that for the transport properties, micropores are despite their large total volume not particularly detrimental. For the strength and stiffness of a C-S-H matrix, the influence of the micropores has never been clearly evaluated given that their volume is intrinsic to the hydration process and therefore cannot be changed by mix design.

Porosity on Level II

On level II, a second class of pores is generally present. These pores are often referred to as capillary pores and have a characteristic size in the micrometer range. The capillary pores are created in two different ways [136]: The first source is the shrinkage of the hydration products as the water is chemically incorporated into the hydration products. The water that is chemically bound has a density of up to $1,250\,\mathrm{kg/m^3}$. The space that is liberated in the course of hydration gradually densifies, a process also called chemical shrinkage, becomes porespace of micrometer size. The second source of capillary pores is superfluous water for the hydration process (i.e. for a w/c-ratio > 0.38). For a $w/c = 0.5$ paste the capillary porosity is on the order of 3-5%. This class of pores is certainly detrimental to both stiffness and strength of cement pastes. The water-cement ratio dependent strength of pastes has its origin in the corresponding difference in capillary porosity. Furthermore, the transport properties of pastes are largely affected by the presence of capillary pores.

Porosity on Level III

Pores on level III are called macropores. They have sizes in the millimeter range and are usually involuntarily created through poor vibration during the placement. Some intentionally created

[2] Pores of this size remain accessible to water molecules, which have a size of approximately 2.4Å (=0.24nm).

ADSORPTION TECHNIQUES
Water adsorption-desorption and nitrogen adsorption-desorption are standard techniques for the porosity measurement in the nanometer range [11]. This technique uses the change in density of a gas in the proximity of a surface. Using the so called BET (Brunauer-Emmett-Teller) equations, the variation in the adsorbed gas as the pressure changes is related to the specific surface of the material. From the Kelvin-Laplace equations, the pore size distribution can be deduced. Different gases can be used in this technique. The downside of the method is the necessity to dry the material [11, 141]. This automatically entrains a modification in the microstructure of the material. In addition, a geometrical representation of the pores has to be assumed in the calculations which can falsify the results considerably [124].

Table 2.6: Adsorption techniques for porosity measurements

pores by air entrainment agents, which enhance the freeze-thaw resistance might be of that size. The macropores are detrimental to the mechanical properties of mortars and concretes. They are preferential paths for all transport phenomena. In the the Three-Level microstructure, no pores are considered at Level III.

2.3 Calcium Leaching Effects on the Microstructure Levels

This section gathers the information available on the consequences of calcium leaching on cementitious materials. Based on the Berner leaching curve a general overview of the leaching phenomenon is given. Subsequently, the chemical and mechanical effects on the different levels of the microstructure are discussed.

2.3.1 Berner Leaching Curve

Calcium leaching of cementitious materials is controlled by the chemical equilibrium of the calcium - silicate - water system. Berner [18] compiled a large number of solubility test data from the open literature in forming the diagram shown in Figure 2-11. The diagram plots the equilibrium C/S-ratio of the hydration products as a function of the free calcium concentration in the pore solution. The different tests line up on a curve characterized by three almost linear pieces, characterizing different zones with distinct properties. The zone for calcium concentrations higher than $20\,\mathrm{mol/m^3}$ is the equilibrium zone of Portlandite. Portlandite is

MERCURY POROSIMETRY (MIP)
Mercury porosimetry is one of the most popular techniques for the pore size analysis in ceramic materials. During the measurement, mercury is pushed into the open porosity and the pore size distribution can be obtained from the pressure and the volume measurements, using the Washburn equation [11]. Again, this method requires drying of the specimen which changes the pore structure of cementitious materials. In addition, a geometrical representation of the porosity is necessary (cylindrical) which can particularly falsify the result if in a connected pore space the diameter increases. Diamond [43] showed that in this case, all the porosity will be associated with the smaller pore size of the beginning of the pore channel because once the mercury passed through the smaller section, it penetrates into the larger one without increase in the pressure. Diamond concluded therefore that mercury porosimetry gives a reasonable measurement of the total porosity (perhaps modified through prior drying) while the pore size distribution tends to be shifted towards the smaller pore sizes

Table 2.7: Mercury porosimetry for porosity measurements.

SEM/TEM
SEM/TEM micrographs are direct ways to visualize the porosity [154]. The resolution of these images depends very much on the specimen preparation and is limited currently to the nanometer scale. The risk of a specimen modification during the preparation process has been discussed in [124]. An additional difficulty is the 2D nature of the images although they can be overcome with stereometric techniques [154]. SEM/TEM give good qualitative information and some quantitative information. However, the deduction of a complete pore size distribution is difficult.

Table 2.8: SEM/TEM porosity measurements.

SMALL ANGLE SCATTERING
Small angle X-ray or neutron scattering are sophisticated and powerful techniques that give access to the roughness and the fractality of the solid surface [3]. From these data, conclusions on the total porosity and the pore shape can be drawn [89]. The advantage of these methods is that no prior drying is necessary. The difficulty lies in the interpretation of data coming from inhomogeneous materials. which limits the application.

Table 2.9: Small angle scattering porosity measurements.

WATER-BASED WEIGHT MEASUREMENTS
The simplest technique to measure the porosity is to compare the weight of saturated and dried specimens. Knowing the density of water, the pore space can be determined from the weight difference. The drawback is in the drying temperature of 105 °C which leads to the evaporation of some chemically bound water and hence to an overestimation of the porosity.

Table 2.10: Water-based porosity measurements.

stable in the cement paste (Level II) only for calcium concentrations higher than 20 mol/m^3. The C-S-H equilibrium is characterized by the second straight line, between calcium concentrations of 2 mol/m^3 and 20 mol/m^3. In this domain, the equilibrium depends primarily on the C/S-ratio. The C/S-ratio in C-S-H varies naturally between C/S=1.2 and C/S=2.3; and in a C-S-H matrix, different ratios are present at a time. In consequence, the C-S-H with the higher C/S-ratio dissolve first. The third part in this curve for calcium concentrations below 2 mol/m^3 corresponds to silicon rich gels which are the end product of calcium leaching. These gels do not naturally exist in a cement paste [3].

2.3.2 Leaching Effects on Level I: C-S-H Matrix

The chemical equilibrium of C-S-H depends heavily on the C/S-ratio. As leaching proceeds and the calcium concentration in the pore fluid is lowered, the equilibrium between fluid phase and C-S-H leads to a progressive C-S-H dissolution, depending on the C/S-ratio. This is an incongruent type of dissolution. In this dissolution process, the C-S-H that dissolve do not undergo a solid transformation after some calcium has been dissolved from their structure but, as Faucon showed [49], they dissolve entirely and reprecipitate at a lower C/S-ratio. Therefore, in a global sense, the calcium leaching leads to a transformation of the C-S-H matrix in terms of its C/S-ratio: As leaching goes on, the average C/S-ratio in the C-S-H matrix is reduced. This effect that follows from equilibrium considerations was also observed through NMR analysis: Porteneuve [115] showed that the leaching process leads to a decrease in C/S-ratio. This decrease in C/S-ratio is accompanied by an increase in the average chain length as expressed by the connectivity - a polymerization of the C-S-H takes place.

To investigate the effect of leaching on the elasticity modulus of the two C-S-H types,

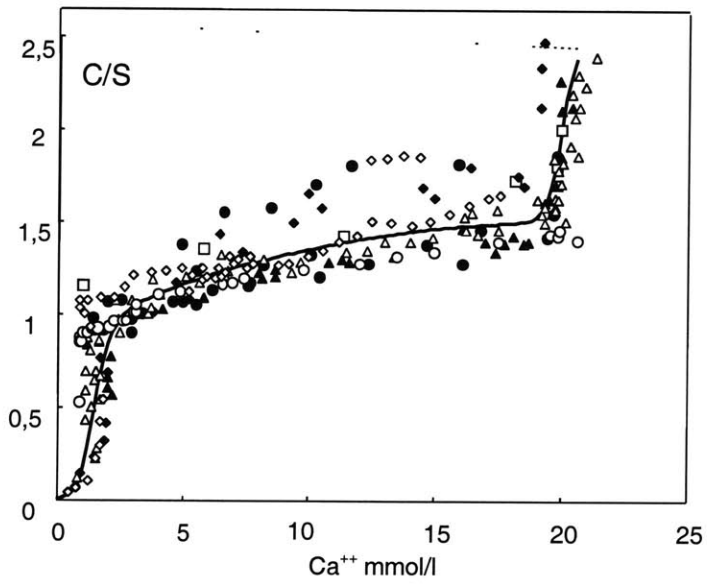

Figure 2-11: Compilation of solubility tests of different cement pastes. Depending on the calcium concentration in the solution in contact (x-Axis), the equilibrium for hydration products with different C/S ratios is displayed. From [18].

Constantinides [37] used instrumented nanoindentation to measure the Young's modulus of C-S-H leached to C/S=0.8. Table 2.3 shows the obtained results. Figure 2-12 shows the histogram of the test series. The distinction in two families of C-S-H from the mechanical tests coincides with the chemical model calculations [142]. The degradation of the elastic modulus is much more pronounced for C-S-H_α than for C-S-H_β phase. From the nanoindentation measurements, Constantinides [37] also deduced microhardness values for the degraded C-S-H matrix[3]. The distribution of the results is shown in Figure 2-13. A separation in two families is obtained for the hardness values (C-S-H_α and C-S-H_β) in the same way as for the Young's modulus.

The stability of the C-S-H matrix at a C/S value of approximately 0.8 has been reported by several researchers ([3], [31], [144]), which suggests that no complete dissolution of the C-S-H takes place. This is counterintuitive to Berner's result (Fig. 2-11) that indicate that if the calcium concentration in the pore solution tends to zero, the existence of any C-S-H becomes chemically impossible. Faucon [50], however showed that this unexpected stability of the C-S-H is due to the capacity of the C-S-H to incorporate Fe-ions into their structure. Figure 2-14 shows schematically how the Fe ions are incorporated into the C-S-H structure, filling the Ca^{2+} spaces which were shown in Figure 2-8. From this consideration it follows that C-S-H matrices derived from cements with low iron content are less stable in the final degradation state than if an OPC is used which contains 3 to 5(mass)% of Fe [49]. In such a case the stability of the C-S-H increases and the Berner-curve loses its validity.

The microporosity of the C-S-H does not change as long as the C/S-ratio remains greater than 1. This was shown by Adenot[3] who through Small Angle Neutron Scattering (SANS) determined that the fractal dimension of C-S-H is 2.7 and does not change for C/S>1. The fractality is directly related to the porosity. However, if the C/S ratio is below 1, which is the case for the asymptotically leached C-S-H, the fractal dimension is 2.0. Although the difference in fractality is small, the textural difference in course of the leaching process indicates that some change in the microporosity of the C-S-H takes place. Such a change in microporosity is expected to affect both the stiffness and the strength of the C-S-H phases. Direct measurements of this gel porosity are out of reach, though.

[3]For intact C-S-H, Constantinidis determined a value of 0.8 GPa for C-S-H_α and 0.9 GPa for C-S-H_β.

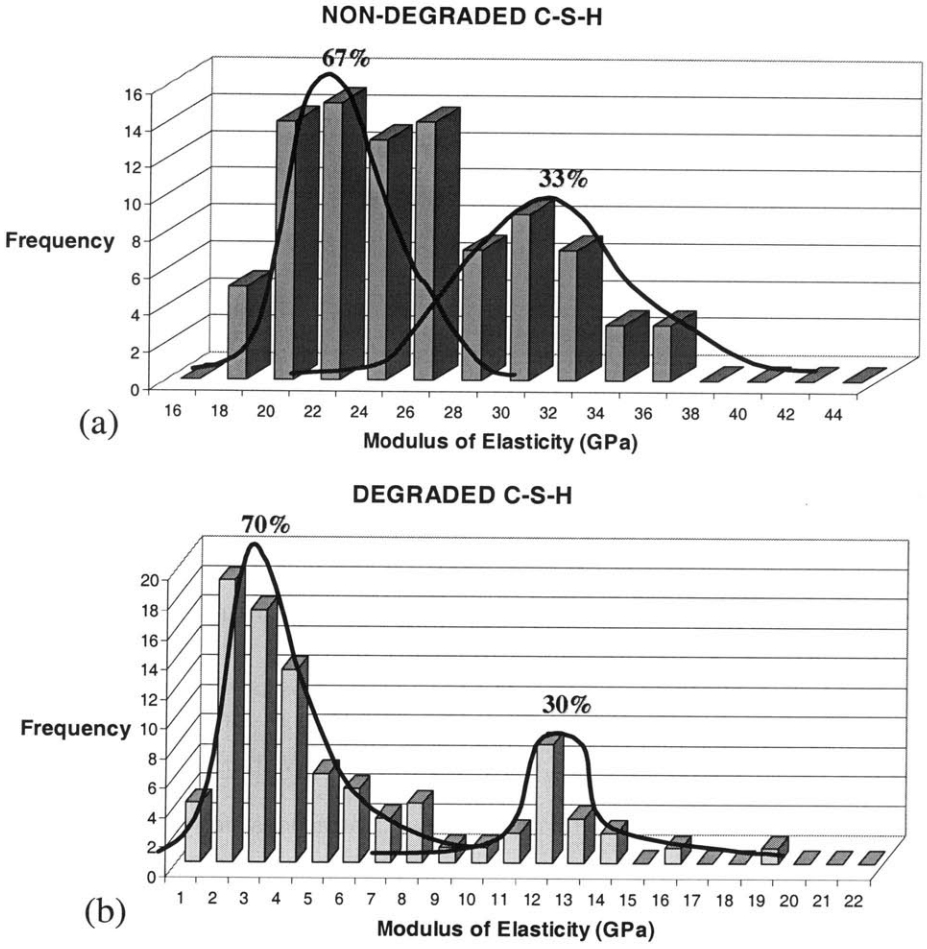

Figure 2-12: Nanoindentation histogram for intact and degraded C-S-H. From [37].

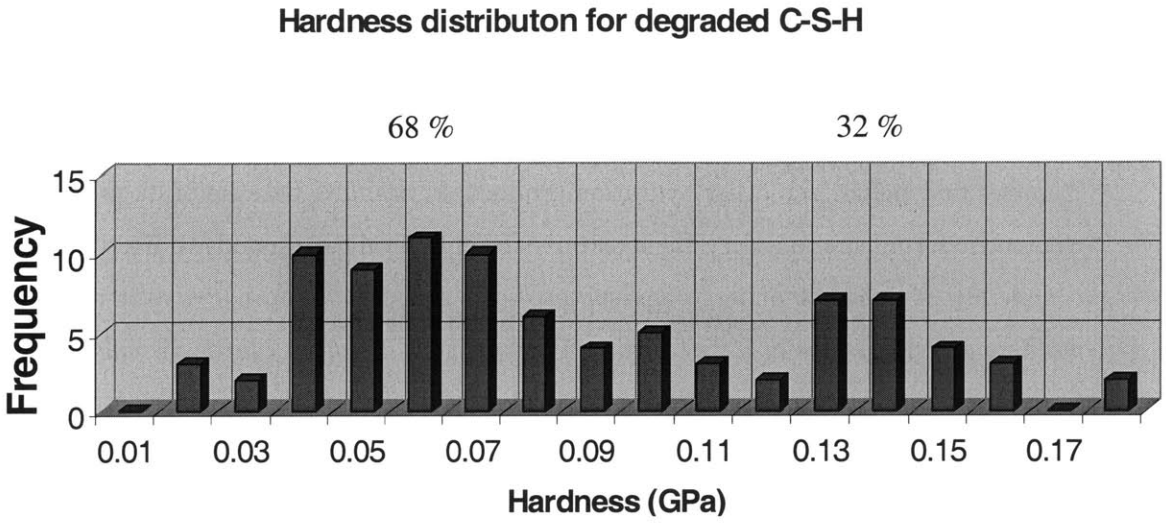

Figure 2-13: Hardness measurements on degraded C-S-H. Courtesy of Constantinides.

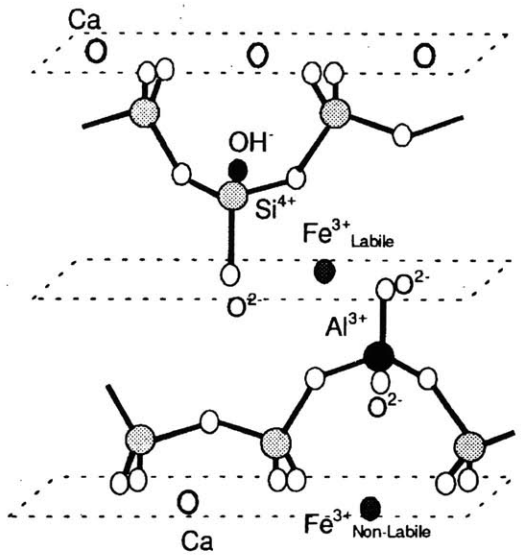

Figure 2-14: Schematical illustration of the Fe incorporation into $C-S-H$ in the Ca planes. From [49].

2.3.3 Leaching Effects on Level II: Cement Paste

Portlandite

The Berner-curve shows that Portlandite minerals in a cement paste have the highest solubility of all calcium containing hydration products. As calcium leaching takes place, Portlandite dissolves first before any other hydration product. Portlandite because of its well defined stoichiometric form (due to its crystal structure, the only form corresponds to Eq. (2.4)), dissolves completely; it does not undergo any solid-to-solid transformation, nor does it reprecipitate in a different form. Zones in a paste where Portlandite is dissolved can be visually distinguished from intact paste material, which makes it easy to determine the progression of the leaching process. The space occupied by Portlandite prior to dissolution becomes part of the porosity. The size of these new pores are at the micrometer level and they join with the naturally existing capillary pores. In a paste with $w/c = 0.5$, the additional porosity created through Portlandite dissolution is on the order of 10 to 15%.

Aluminates

The aluminates constitute a relatively small part of an OPC paste. Ettringite ($C_3A3C\underline{S}H_{32}$) and Monosulfoaluminates ($C_3AC\underline{S}H_{12}$) have high C/S ratios and in accord with the Berner-curve they are dissolved in the beginning of the leaching process. Adenot [3] showed that aluminates do not undergo any transformation, which is due to their tendency to form well developed crystals. The dissolution of aluminates creates an additional pore space in the micrometer range, however the quantity of this porosity is relatively small, within 1 to 3% of the total volume of a paste.

Unhydrated Clinker

Unhydrated clinker phases that exist in pastes with low w/c-ratios undergo a series of transformations. Porteneuve [117] showed that the remaining clinker grains start to hydrate in the presence of deionized water, forming the standard hydration products according to Eqs. (2.4) and (2.1). Eventually, these late hydration products dissolve at a later stage. The beneficial

aspect of the presence of unhydrated clinker with respect to leaching is that the late hydration gives an additional life time to low w/c-ratio pastes.

Porosity on Level II

Calcium leaching has an important effect on the porosity at Level II. In addition to porosity increase through the dissolution of Portlandite and aluminates, the C-S-H decalcification creates new pores at Level II. Carde [30] identified the porosity due to C-S-H decalcification by leaching cement pastes without Portlandite (consumed in the Pozzolanic reaction, Eq. (2.5)). The porosity created through leaching of C-S-H for a standard OPC paste (w/c =0.5) is around 7%, that is roughly half of the porosity created by the dissolution of Portlandite. This additional porosity is also in the micrometer range, which can be concluded from the fact that the microporosity (gelporosity) of C-S-H does not change to this extend [3]. Galle [54] connfirmed by Mercury Intrusion Porosimetry (see Figure 2-15) that the newly created porosity is not part of the microporosity. Porteneuve [115], [116] and Philippot [114], provided further evidence by means of an NMR investigation, that the microporosity of the C-S-H is not affected by leaching[4].

Effect on the Mechanical Performance of a Paste

The effect of leaching on the elastic properties of an OPC cement paste has been investigated by Constantinides [37] and is reported in Table 2.5. The residual value for the Young's modulus for the $w/c = 0.5$ cement paste is 16%. This is a dramatic change in material properties, that is more important than the degradation of the Young's modulus at Level I (see Figure 2-12). This underlines the particularly detrimental effect of the additional porosity created by leaching at Level II. The reduction in compressive strength was determined by a number of researchers [31], [80]. For a paste that is leached to its asymptotic calcium concentration, the residual strength is roughly 10% of the initial value. The effect of leaching on the tensile strength has not been investigated for cement pastes, nor the evolution of the frictional capacity of cement

[4]This result needs to be taken with care: The effect of the paramagnetic elements (Iron etc.) in the cement is very strong compared to the water movements in an ^{1}H NMR experiment. Porteneuve & Philoppot need to make strong hypothesis for the exchange conditions of the water layer attached to the solid, which can be questioned [39].

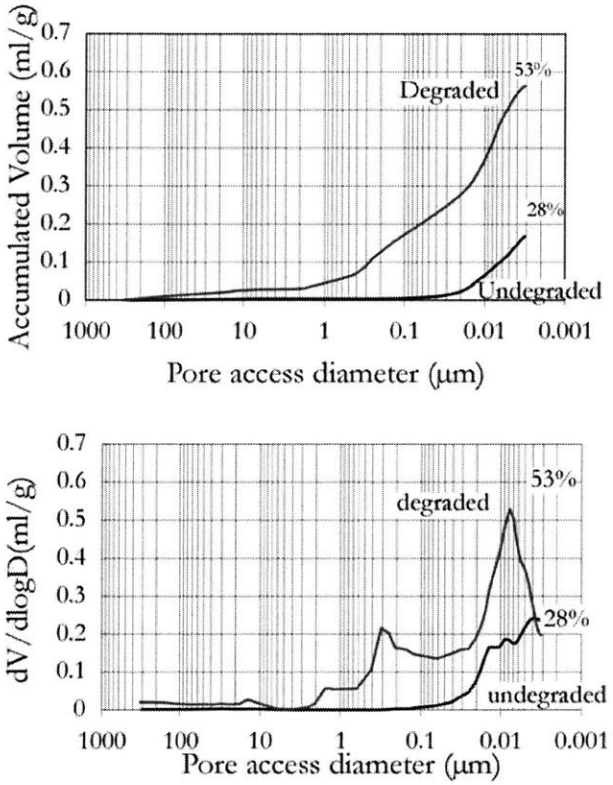

Figure 2-15: MIP measurements on an asymptotically leached cement paste ($w/c = 0.4$). Adapted from [54].

pastes subjected to calcium leaching.

2.3.4 Leaching Effects on Level III: Mortar/Concrete

The effect of leaching on Level III concerns primarily the ITZ. The aggregates are inert to calcium leaching unless they contain Ca-phases which is not further pursued in this study. The ITZ in an undegraded mortar/concrete is characterized by high Portlandite and aluminates concentrations and a high porosity. The effect of the Portlandite and aluminates dissolution is of the same nature as for the paste but magnified through their higher concentrations. Note that for a HPC which has no ITZ, no particular effects are to be expected. For an OPC based mortar Table 2.5 shows the results of elasticity measurements by Constantinides [37] on asymptotically leached specimens. Similar to the results for a leached paste, the Young's modulus is reduced to 16% of the initial value. The degradation of the uniaxial compressive strength was measured by Carde [31] and Le Bellego [80] to be 10% of the initial value. The tensile strength of leached mortars was tested by Le Bellego [80] only on partially leached specimens. The reported residual strength of 70% is likely to decrease with further leaching. Similar to pastes, the evolution of the frictional behavior of leached mortars has not been investigated.

2.4 Concluding Remarks

This Chapter presented a non-exhaustive review of the existing information in the open literature on both the chemical and mechanical effects of calcium leaching on cementitious materials. The Three-Level microstructure which we introduced based on mechanical length scales finds its expression in the morphological aspects of the microstructure. It will continue to serve in the remainder of this investigation as a structure to the analysis. From the discussion of the existing knowledge about the effects of leaching on cementitious materials the following open questions arise:

- On Level I, the strength of C-S-H remains unknown, both in the intact and the leached state. Particularly, no direct experimental access seems possible at this time.
- On Level II, the evolution of the uniaxial compressive strength with leaching has been investigated. However, both the uniaxial tensile strength and the frictional behavior have

not been covered with respect to changes provoked by leaching. In addition, the role of the C-S-H matrix as an element of the composite material paste and its evolution with leaching is unsolved. Moreover, the large additional porosity created by calcium leaching on Level II suggests that:

1. The deformational behavior of leached pastes is considerably different from intact pastes. This has been observed in uniaxial compression tests but is unresolved for multiaxial stress states.
2. The role of the pore fluid can become more important through leaching. Together with the reduction in solid stiffness measured for the C-S-H matrix, the large porosity may lead to a material which is sensitive to the pressure of the pore fluid.

- On Level III, the evolution of the uniaxial compressive strength is known. Much like for pastes, the effect of leaching on the frictional behavior and the tensile strength is unresolved. The role of the ITZ in leached mortars and concrete is also of concern. In addition, similar effects of the pore fluid pressure on the material behavior as discussed for pastes are to be expected for mortars.

These open questions are the blueprint of the investigations presented in the following chapters. On Levels II and III we examine the multiaxial strength properties and the deformation behavior of leached materials in triaxial tests (Chapters 5 and 6). In addition, the role of the pore fluid pressure is investigated. As the strength of the C-S-H matrix cannot be measured experimentally at this point, we propose an analytical technique to obtain its value based on the composite strength of the paste (Chapter 8). Also with an analytical approach we aim at clarifying the role of the ITZ on the mortar/concrete strength and how it is affected by leaching (Chapter 8). Table 2.11 summarizes the existing and missing knowledge about leached materials and the proposed approaches in this investigation.

M. Level	Exist. Inform	Missing Inform.	Prop. Approach	Chapter
I	C-S-H Elasticity	C-S-H strength	Analyt.: Mech. Model	7, 8
	[37]			
II	Elasticity	Frictional behavior	Exp.: Triax Testing	5, 6
	[28], [80]			
	Uniax. Comp. Strength	Tensile Strength	Exp.: Tensile tests	5, 6
	[28], [80]	Pore Pressure Infl.	Exp.: Triax Testing	5, 6
III	Elasticity	Frictional behavior	Exp.: Triax Testing	5, 6
	Uniax. Comp. Strength	Tensile Strength	Exp.: Tensile tests	5, 6
	[28], [80]	Pore Pressure Infl.	Exp.: Triax Testing	5, 6
		ITZ role	Analyt.: Mech. Model	7, 8

Table 2.11: Overview of the existing and missing knowledge about leached cementitious materials.

Part II

Experimental Chemo-Mechanics

Chapter 3

Design and Operation of an Accelerated Leaching Procedure

The goal of the experimental campaign is to determine the strength and deformation properties of asymptotically leached cement pastes and mortars (Levels II and III of the proposed microstructural division). The rationale of working with asymptotic leaching states is the homogeneous leaching state, which allows one to experimentally assess the mechanical behavior. In turn, once the asymptotic states are known, the properties of intermediate states can be obtained by chemomechanical modeling. This is the focus of Chapters 7 to 9 in this report.

A prerequisite for the experimental assessment of the material properties in the asymptotically leached state is a leaching method, that is operational for these materials in a reasonable time. This chapter presents design considerations for an accelerated calcium leaching device and its practical application and results. Starting point for the design is a novel one-dimensional diffusion-dissolution model, which considers two dissolution fronts, one corresponding to the dissolution of Portlandite, the other to the dissolution of C-S-H with C/S-ratio equal to one. Although the two fronts do not represent all of the leached minerals, by pertaining to two different levels in the microstructure (I and II) they preserve the main characteristics of the leaching process of cement-based materials. Based on the analysis of the invariants of the model equations, the leaching device is developed. For an appropriate practical design of the actual leaching device, the leaching times are predicted for cylindrical specimens with both the ana-

lytical solution of the 1-D think model and a more sophisticated finite-element based solution. It is shown that the 1-D think model agrees well with actually observed leaching times, which justifies the approach. In Chapter 9, the same model will be further developed in 3D, for the implementation of model-based simulations of concrete structures subjected to leaching.

3.1 Design Considerations

3.1.1 Introduction

One problem when evaluating the impact of calcium leaching on the mechanical performance of cementitious materials is the time necessary to obtain uniformly leached specimens. In industrial applications of concrete, deionized water is the most aggressive solution to be present. As a consequence, in many applications such as nuclear waste storage, deionized water has become the design scenario for calcium leaching of concrete structures. It has been found that calcium leaching in this reference scenario is diffusion governed [3]. Locally, the chemical equilibrium is always fulfilled, compared to the diffusion time scale. The leaching rates are very low: Deionized water leaches a 1 cm thick piece of concrete in roughly 300 years [3]. For laboratory experiments, using deionized water is not an optimum choice and a means of accelerating the leaching process is necessary in order to leach the specimens in a reasonable time. This need was recognized early on in the research on calcium leaching. Two ways of accelerating calcium leaching of cementitious materials were put forward. The first approach, pioneered by Saito et al. [128] and Gérard [56], uses an electrochemical means of acceleration: An electrical field is applied to the concrete specimen and the migration of the calcium ions is accelerated due to the strong electrical field. The ion migration in the presence of an electrical field is not a diffusion driven process so that the nature of the accelerated leaching procedure is different from the reference scenario. In practice, the ion migration leads to a zone of high calcium concentration close to the cathode and an almost calcium depleted zone close to the anode, which does not correspond to the calcium concentration gradients characteristic of a diffusion driven process. In addition, the acceleration factor is limited by the field strength and reaches in practice values of about 100, meaning that a given thickness of concrete is leached in 1 hundredth of the time necessary for leaching with deionized water.

The second approach is based on a replacement of deionized water by a different solution agent, ammonium nitrate (NH_4NO_3). In the calcium-leaching research community, this technique was first employed by Carde [31] although the aggressiveness of ammonium nitrate solutions on cementitious materials had been known for a long time [105], [81]. The accelerating effect of this second approach is based on the increase of the concentration gradient in the pore solution as more calcium can be dissolved in the presence of ammonium nitrate. This technique preserves the character of the diffusion driven process. In order to understand how an ammonium nitrate accelerated test actually works and to design an optimum accelerated leaching device, we introduce a simple dissolution-diffusion model.

3.1.2 1-D Two-Front Leaching Model

Calcium leaching is characterized by many sharp dissolution fronts that propagate through a cementitious material driven by the calcium diffusion in the pore solution (see Section 1.2). Figure 1-2 displays the multiple fronts corresponding to the dissolution of different minerals at different chemical equilibrium conditions.

Two different approaches to the modeling of the leaching process can be found in the literature:

1. The discrete mineral model, in which all different types of hydration products with distinct chemical equilibria are considered. This approach was put into practice by Adenot[3], who considered 12 mineral phases and their corresponding fronts in a 1-D diffusion setting. Being anchored in the physical chemistry of cement-based materials, tracing the mechanical consequences of the leaching of all individual minerals would be a difficult task.

2. The smeared dissolution model in which the equilibrium formulation is continuous and based on the Berner-curve. Gérard [56], Ulm et al. [150], Mainguy [92, 93] and Le Bellego [80] used this approach which leads to very good leaching predictions. This approach has been coupled with macroscopic phenomenological chemomechanical models with fitted material functions for the stiffness and strength evolution, namely in the context of damage theory [56], [80] and chemoplasticity [150].

A suitable compromise between these two approaches is a model that focuses on the con-

sequences of calcium leaching on the mechanical material properties, by considering the two dissolution processes that affect most the mechanical behavior; that is the Portlandite dissolution and the C-S-H dissolution at well defined equilibrium states. This is the approach we pursue in this study to cover the essential aspects of calcium leaching. Through the Portlandite dissolution, evolutions on Level II of the microstructure are incorporated. Consideration of the C-S-H front assures that changes on Level I are taken into account. The main advantage of this approach is that the focus on two fronts limits the number of modeled material states to three: The intact state and the asymptotically leached state, which are both accessible to experimental investigation and an intermediate state in which only Portlandite has been leached. This intermediate state can be assessed through model-based interpolation of the material properties. The two-front approach is retained for the design of the accelerated leching device, considering:

- The Portlandite dissolution front, which marks the beginning of the leaching process (see Berner-curve, Fig. 2-11). This dissolution front describes well the changes on Level II that is the Portlandite dissolution but also the aluminates at calcium concentrations close to the one of the Portlandite dissolution. This front is associated with a strong increase in porosity which affects greatly the material performance.

- The C-S-H front at C/S=1, which corresponds to the asymptotic leaching state, thus separating a material that is being leached from a material that undergoes no further changes. In addition, the C-S-H being part of Level I, this front takes into account material transformations at this scale.

The proposed approach can be seen as an extension of the 1D-one-front dissolution model of Mainguy and Coussy [93] to which a second dissolution front is added that imparts the mechanical performance of calcium leached cement-based materials.

3.1.3 Model Equations

In the two-front model developed below, we consider the material as a porous medium, composed of two superposed continua, the fluid phase and the solid. In terms of the microstructural levels, this corresponds to either Level II or III, depending on whether a paste or a mortar/concrete is being leached. The different solid phases at either level are lumped into a general "solid"

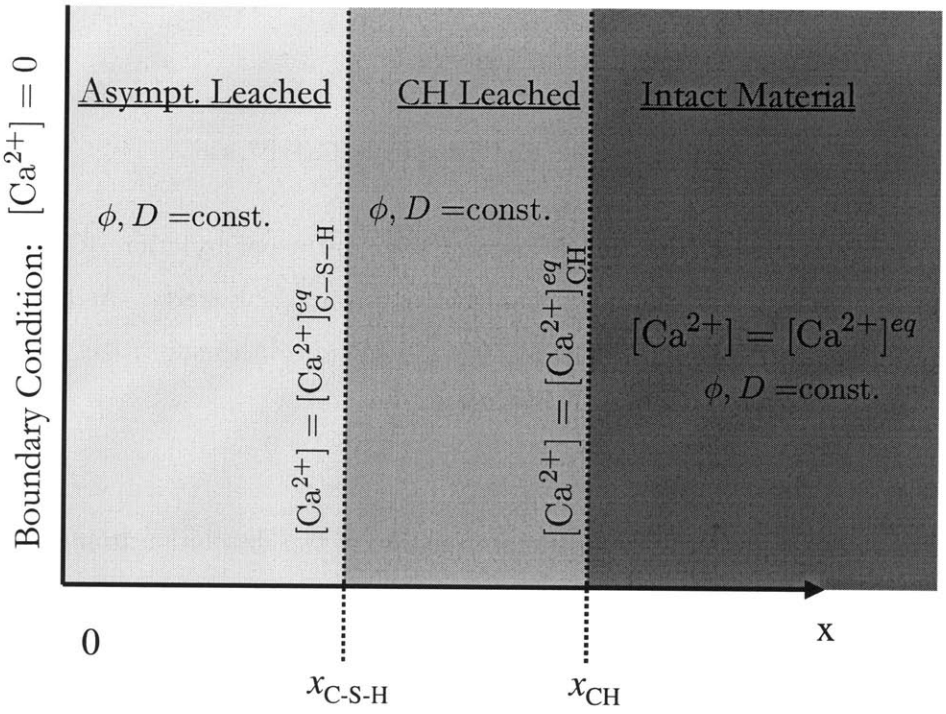

Figure 3-1: Schematic overview of the 1D - model geometry.

phase while the voids are considered to be saturated with a fluid, which itself is a mixture composed of water and dissolved calcium ions and ammonium nitrate). We consider a simplified one-dimensional setting, an infinite half space with spacial variable $x > 0$. Figure 3-1 shows schematically the model geometry and assumptions. Three zones are distinguished: x_{CH} and $x_{\mathrm{C-S-H}}$ denote the location of the CH and the C-S-H dissolution fronts, respectively. The first zone, $x_{\mathrm{CH}} < x$, corresponds to the intact material. No leaching has occurred here and the calcium concentration in the pore solution is equal to the initial equilibrium concentration. In the second zone, $x_{\mathrm{C-S-H}} < x < x_{\mathrm{CH}}$, the Portlandite and the aluminates are dissolved. In the third zone, $0 \leq x < x_{\mathrm{C-S-H}}$, also the C-S-H are decalcified to C/S=1.0, which we consider as the asymptotically leached material state. For simplicity, we assume in the three zones that:

- $\mathcal{H}1$: The porosity is constant.
- $\mathcal{H}2$: The diffusivity is constant.

The initial conditions for the three zones read:

$$t < 0 : [\mathrm{Ca}^{2+}](t < 0) = [\mathrm{Ca}^{2+}]^{eq}, \forall x \tag{3.1}$$

where $[\mathrm{Ca}^{2+}]$ represents the calcium concentration in the pore solution. $[\mathrm{Ca}^{2+}]^{eq}$ is the initial calcium concentration in the fluid phase before any leaching starts. At time $t = 0$, a zero calcium concentration is imposed at $x = 0$, and maintained thereafter:

$$t \geq 0;\ x = 0 : [\mathrm{Ca}^{2+}] = 0 \tag{3.2}$$

This boundary condition leads to the propagation of two dissolution fronts into the material bulk that separate three zones. The mass conservation of the calcium in the fluid phase reads for the three zones:

$$0 \leq x < x_{\mathrm{C-S-H}} : \frac{\partial(\phi[\mathrm{Ca}^{2+}])}{\partial t} - \frac{\partial}{\partial x}\left[D\frac{\partial(\phi[\mathrm{Ca}^{2+}])}{\partial x}\right] = 0 \tag{3.3}$$

$$x_{\mathrm{C-S-H}} < x < x_{\mathrm{CH}} : \frac{\partial(\phi[\mathrm{Ca}^{2+}])}{\partial t} - \frac{\partial}{\partial x}\left[D\frac{\partial(\phi[\mathrm{Ca}^{2+}])}{\partial x}\right] = 0 \tag{3.4}$$

$$x_{\mathrm{CH}} < x : [\mathrm{Ca}^{2+}] = [\mathrm{Ca}^{2+}]^{eq} \tag{3.5}$$

and the continuity of the $[\mathrm{Ca}^{2+}]$-concentration of the fronts requires that:

$$x = x_{\mathrm{C-S-H}} : [\mathrm{Ca}^{2+}] = [\mathrm{Ca}^{2+}]^{eq}_{\mathrm{C-S-H}} \tag{3.6}$$

$$x = x_{\mathrm{CH}} : [\mathrm{Ca}^{2+}] = [\mathrm{Ca}^{2+}]^{eq}_{\mathrm{CH}} \tag{3.7}$$

where $[\mathrm{Ca}^{2+}]^{eq}_{\mathrm{C-S-H}}$ and $[\mathrm{Ca}^{2+}]^{eq}_{\mathrm{CH}}$ are the equilibrium concentrations for calcium corresponding to the C-S-H and CH fronts, respectively. Furthermore, the mass conservation at the two

dissolution fronts is expressed by the following Rankine-Hugoniot jump conditions ([70], [120]):

$$x = x_{\text{C-S-H}} \quad : \quad D\mathcal{M}_{\text{Ca}^{2+}} \left[\left(\phi \frac{\partial([\text{Ca}^{2+}])}{\partial x} \right)_{x^{-}_{\text{C-S-H}}} - \left(\phi \frac{\partial([\text{Ca}^{2+}])}{\partial x} \right)_{x^{+}_{\text{C-S-H}}} \right] - [[\rho_s(1-\phi)]] \frac{dx_{\text{C-S-H}}}{dt} = 0 \tag{3.8}$$

$$x = x_{\text{CH}} : \phi D\mathcal{M}_{\text{Ca}^{2+}} \left(\frac{\partial([\text{Ca}^{2+}])}{\partial x} \right)_{x_{\text{CH}}} - \rho_{\text{CH}} \phi^c \frac{dx_{\text{CH}}}{dt} = 0 \tag{3.9}$$

where superscripts + and - denote upstream and downstream at the dissolution front; $\mathcal{M}_{\text{Ca}^{2+}}$ denotes the molar mass of calcium ($40\,\text{g}\,/\,\text{mol}$), $[[\rho_s(1-\phi)]] = \Delta m_s$ is the jump in solid mass density due to calcium leaching from the C-S-H structure; $m_{\text{CH}} = \rho_{\text{CH}}\phi^c$ is the change in calcium mass due to Portlandite dissolution so that $\phi^c = \phi - \phi_0$ denotes the chemical porosity, that is the porosity created through the Portlandite dissolution process in excess of the initial porosity ϕ_0. Equations (3.1) through (3.9) form a closed set of equations that allow solving the boundary value problem analytically.

C-S-H Zone

To solve the equations for the C-S-H zone ($0 \leq x < x_{\text{C-S-H}}$), we introduce the following linear transform of the variables:

$$\begin{aligned} x &= Xx'; t = Tt'; [\text{Ca}^{2+}] = C[\text{Ca}^{2+}]'; \phi = F\phi'; \\ [\text{Ca}^{2+}]^{eq}_{\text{C-S-H}} &= C^{eq}_{\text{C-S-H}} [\text{Ca}^{2+}]^{eq\prime}_{\text{C-S-H}}; [[\rho_s(1-\phi)]] = \Delta m_s = M m'_s \\ D &= \Delta D'; \mathcal{M}_{\text{Ca}^{2+}} = \overline{\mathcal{M}}\mathcal{M}'; [\text{Ca}^{2+}]^{eq} = C^{eq}[\text{Ca}^{2+}]^{eq\prime} \end{aligned} \tag{3.10}$$

where $(...)'$-quantities are the dimensionless counterparts of the variable (...). Use of (3.10) in (3.3) and (3.8) yields the dimensionless conservation laws in the C-S-H zone and at the C-S-H dissolution front:

$$0 \leq x' < x'_{\text{C-S-H}} : \left[\frac{X^2}{\Delta T} \right] \frac{\partial(\phi'[\text{Ca}^{2+}]')}{\partial t'} - \frac{\partial}{\partial x'} \left[D' \frac{\partial(\phi'[\text{Ca}^{2+}]')}{\partial x'} \right] = 0 \tag{3.11}$$

$$x' = x'_{\mathrm{C-S-H}}:$$
$$\left[\frac{\Delta\overline{\mathcal{M}}FCT}{X^2M}\right] D'\mathcal{M}' \left[\left(\phi'\frac{\partial([\mathrm{Ca}^{2+}]')}{\partial x'}\right)_{x'^{-}_{\mathrm{C-S-H}}} - \left(\phi'\frac{\partial([\mathrm{Ca}^{2+}]')}{\partial x'}\right)_{x'^{+}_{\mathrm{C-S-H}}}\right] \tag{3.12}$$
$$- \quad m'_s\frac{dx'_{\mathrm{C-S-H}}}{dt'} = 0;$$

Analogously, the transformed initial condition (3.1), boundary conditions (3.2) and the continuity condition (3.6) read:

$$t' \leq 0 : \frac{C}{C^{eq}}[\mathrm{Ca}^{2+}]' = [\mathrm{Ca}^{2+}]^{eq\prime} \forall x' \tag{3.13}$$
$$x' = 0 : [\mathrm{Ca}^{2+}]' = 0 \tag{3.14}$$
$$x' = x'_{\mathrm{C-S-H}} : \frac{C}{C^{eq}_{\mathrm{C-S-H}}}[\mathrm{Ca}^{2+}]' = [\mathrm{Ca}^{2+}]^{eq\prime}_{\mathrm{C-S-H}} \tag{3.15}$$

The transformed set of equations (3.11) through (3.14) will satisfy the same equations as the initial set provided that:

$$\frac{C}{C^{eq}_{\mathrm{C-S-H}}} = \frac{C}{C^{eq}} = \frac{X^2}{\Delta T} = \frac{\overline{\mathcal{M}}FC}{M} = 1 \tag{3.16}$$

Finally, combining (3.10) and (3.16) leads to identifying the following invariants:

$$\overline{[\mathrm{Ca}^{2+}]} = \frac{[\mathrm{Ca}^{2+}]}{[\mathrm{Ca}^{2+}]^{eq}_{\mathrm{C-S-H}}}; \xi = \frac{x}{2\sqrt{Dt}}; \varepsilon_{\mathrm{C-S-H}} = \frac{\phi[\mathrm{Ca}^{2+}]^{eq}_{\mathrm{C-S-H}}\mathcal{M}_{\mathrm{Ca}^{2+}}}{\Delta m_s} \tag{3.17}$$

$\overline{[\mathrm{Ca}^{2+}]}$ is the normalized calcium concentration and ξ is the classical Boltzmann variable for one-dimensional diffusion problems. In turn $\varepsilon_{\mathrm{C-S-H}}$ appears as a macroscopic solubility parameter which describes the solubility of $\mathrm{C-S-H}$ in the porous medium. As we will see below, the solubility parameter is one key to the acceleration of the leaching process.

The solution of the differential equation (3.11) yields:

$$0 \leq \xi < \xi_d^{\mathrm{C-S-H}} : \overline{[\mathrm{Ca}^{2+}]} = \frac{\mathrm{erf}(\xi)}{\mathrm{erf}(\xi_d^{\mathrm{C-S-H}})} \tag{3.18}$$
$$\xi = \xi_d^{\mathrm{C-S-H}} : \overline{[\mathrm{Ca}^{2+}]} = 1 \tag{3.19}$$

where $\mathrm{erf}(\xi)$ is the error function, $\mathrm{erf}(\xi) = \frac{2}{\pi^2}\int_0^{\xi}\exp\left(-t^2\right)dt$; $\xi_d^{\mathrm{C-S-H}} = \frac{x_{\mathrm{C-S-H}}}{2\sqrt{Dt}}$ denotes the location of the C-S-H front in dimensionless coordinates. Determination of this parameter requires the solution of the second diffusion equations in the "CH zone"($x_{\mathrm{C-S-H}} < x < x_{\mathrm{CH}}$) which is shown next.

Portlandite (CH) Zone

We introduce the following set of linear transforms:

$$\begin{aligned} x &= Xx'; t = Tt'; [\mathrm{Ca}^{2+}] = C[\mathrm{Ca}^{2+}]'; \phi = F\phi'; [\mathrm{Ca}^{2+}]_{\mathrm{CH}}^{eq} = C_{\mathrm{CH}}^{eq}[\mathrm{Ca}^{2+}]_{\mathrm{CH}}^{eq\prime} \\ [\mathrm{Ca}^{2+}]_{\mathrm{C-S-H}}^{eq} &= C_{\mathrm{C-S-H}}^{eq}[\mathrm{Ca}^{2+}]_{\mathrm{C-S-H}}^{eq\prime}; m_{\mathrm{CH}} = M_{\mathrm{CH}}m'_{\mathrm{CH}}; D = \Delta D'; \\ \mathcal{M}_{\mathrm{Ca}^{2+}} &= \overline{\mathcal{M}}\mathcal{M}'; [\mathrm{Ca}^{2+}]^{eq} = C^{eq}[\mathrm{Ca}^{2+}]^{eq\prime} \end{aligned} \tag{3.20}$$

Inserting (3.20) in (3.4) and (3.9) yields:

$$x'_{\mathrm{C-S-H}} < x' < x'_{\mathrm{CH}} : \left[\frac{X^2}{\Delta T}\right]\frac{\partial(\phi'[\mathrm{Ca}^{2+}]')}{\partial t'} - \frac{\partial}{\partial x'}\left[D'\frac{\partial(\phi'[\mathrm{Ca}^{2+}]')}{\partial x'}\right] = 0 \tag{3.21}$$

$$x' = x'_{\mathrm{CH}} : \left[\frac{\Delta\overline{\mathcal{M}}FCT}{X^2M_{\mathrm{CH}}}\right]D'\mathcal{M}'\phi'\left[\frac{\partial([\mathrm{Ca}^{2+}]')}{\partial x'}\right]_{x'^{-}_{\mathrm{CH}}} - m'_{\mathrm{CH}}\frac{dx'_{\mathrm{CH}}}{dt'} = 0 \tag{3.22}$$

The transformed initial condition (3.1) and the continuity conditions (3.6), (3.7) read:

$$x' = x'_{\mathrm{C-S-H}} : \frac{C}{C_{\mathrm{C-S-H}}^{eq}}[\mathrm{Ca}^{2+}]' = [\mathrm{Ca}^{2+}]_{\mathrm{C-S-H}}^{eq\prime} \tag{3.23}$$

$$x' \geq x'_{\mathrm{CH}} : \frac{C}{C_{\mathrm{CH}}^{eq}}[\mathrm{Ca}^{2+}]' = [\mathrm{Ca}^{2+}]_{\mathrm{CH}}^{eq\prime} \tag{3.24}$$

$$t' \leq 0 : \frac{C}{C^{eq}}[\mathrm{Ca}^{2+}]' = [\mathrm{Ca}^{2+}]^{eq\prime}\forall x' \tag{3.25}$$

The transformed set of equation will satisfy the same equations as the initial one provided that:

$$\frac{C}{C_{\mathrm{CH}}^{eq}} = \frac{C}{C^{eq}} = \frac{C}{C_{\mathrm{C-S-H}}^{eq}} = \frac{X^2}{\Delta T} = \frac{\overline{\mathcal{M}}FC}{M_{\mathrm{CH}}} = 1 \tag{3.26}$$

The invariants then are:

$$\overline{[\mathrm{Ca}^{2+}]} = \frac{[\mathrm{Ca}^{2+}]}{[\mathrm{Ca}^{2+}]^{eq}_{\mathrm{C-S-H}}}; \xi = \frac{x}{2\sqrt{Dt}}; \varepsilon_{\mathrm{CH}} = \frac{\phi[\mathrm{Ca}^{2+}]^{eq}_{\mathrm{C-S-H}}\mathcal{M}_{\mathrm{Ca}^{2+}}}{m_{\mathrm{CH}}} \tag{3.27}$$

To facilitate the compatibility between the two zones we choose the same dimensionless calcium concentration as in the C-S-H zone. Similarly to the C-S-H zone, the invariant of interest for an acceleration is $\varepsilon_{\mathrm{CH}}$ which includes also the C-S-H equilibrium condition.

Substituting (3.27) into (3.4) yields an ordinary differential equation with respect to ξ:

$$\xi_{\mathrm{C-S-H}} < \xi < \xi_{\mathrm{CH}} : \frac{\partial^2\overline{[\mathrm{Ca}^{2+}]}}{\partial\xi^2} + 2\xi\frac{\partial\overline{[\mathrm{Ca}^{2+}]}}{\partial\xi} = 0 \tag{3.28}$$

together with the continuity conditions:

$$\xi = \xi_{\mathrm{C-S-H}} : \overline{[\mathrm{Ca}^{2+}]} = \frac{[\mathrm{Ca}^{2+}]^{eq}_{\mathrm{C-S-H}}}{[\mathrm{Ca}^{2+}]^{eq}_{\mathrm{C-S-H}}} = 1 \tag{3.29}$$

$$\xi = \xi_{\mathrm{CH}} : \overline{[\mathrm{Ca}^{2+}]} = \frac{[\mathrm{Ca}^{2+}]^{eq}_{\mathrm{CH}}}{[\mathrm{Ca}^{2+}]^{eq}_{\mathrm{C-S-H}}} = c > 1 \tag{3.30}$$

The general solution of (3.28) is:

$$\overline{[\mathrm{Ca}^{2+}]} = C_1 + C_2\,\mathrm{erf}(\xi) \tag{3.31}$$

where C_1 and C_2 are constants to be determined from the continuity conditions (3.23), (3.24):

$$\overline{[\mathrm{Ca}^{2+}]} = \frac{\mathrm{erf}(\xi_{\mathrm{CH}}) - c\,\mathrm{erf}(\xi_{\mathrm{C-S-H}}) + (c-1)\,\mathrm{erf}(\xi)}{\mathrm{erf}(\xi_{\mathrm{CH}}) - \mathrm{erf}(\xi_{\mathrm{C-S-H}})} \tag{3.32}$$

Furthermore, substituting (3.27) into (3.9) yields for the first term of the Portlandite dissolution front in (3.9):

$$\phi D\mathcal{M}_{\mathrm{Ca}^{2+}}\left(\frac{\partial([\mathrm{Ca}^{2+}])}{\partial x}\right)_{x_{\mathrm{CH}}} = \frac{\phi\sqrt{\frac{D}{\pi t}}\mathcal{M}_{\mathrm{Ca}^{2+}}[\mathrm{Ca}^{2+}]^{eq}_{\mathrm{C-S-H}}(c-1)\exp(-\xi^2_{\mathrm{CH}})}{\mathrm{erf}(\xi_{\mathrm{CH}}) - \mathrm{erf}(\xi_{\mathrm{C-S-H}})} \tag{3.33}$$

and the second term is:

$$m_{\mathrm{CH}}\frac{dx_{\mathrm{CH}}}{dt} = m_{\mathrm{CH}}\xi_{\mathrm{CH}}\sqrt{\frac{D}{t}} \tag{3.34}$$

Equation (3.9) describing the Portlandite dissolution front can then be rewritten as:

$$\varepsilon_{\mathrm{CH}}(c-1)\exp(-\xi_{\mathrm{CH}}^2) - \sqrt{\pi}\xi_{\mathrm{CH}}(\mathrm{erf}(\xi_{\mathrm{CH}}) - \mathrm{erf}(\xi_{\mathrm{C-S-H}})) = 0 \tag{3.35}$$

This expression involves not only the dimensionless location of the CH-front, ξ_{CH}, but also the location of the C-S-H front, $\xi_{\mathrm{C-S-H}}$, so that information from the C-S-H zone is required to solve for the location of the Portlandite front. More precicesly, using (3.17) and (3.32), the different terms of (3.8) can be rewritten as:

$$\left[\frac{\partial\overline{[\mathrm{Ca}^{2+}]}}{\partial\xi}\right]_{\xi^+_{\mathrm{C-S-H}}} = \frac{2}{\sqrt{\pi}}\frac{\exp(-\xi^2_{\mathrm{C-S-H}})(1-c)}{\mathrm{erf}(\xi_{\mathrm{CH}}) - \mathrm{erf}(\xi_{\mathrm{C-S-H}})} \tag{3.36}$$

$$\left[\frac{\partial\overline{[\mathrm{Ca}^{2+}]}}{\partial\xi}\right]_{\xi^-_{\mathrm{C-S-H}}} = \frac{2}{\sqrt{\pi}}\frac{\exp(-\xi^2_{\mathrm{C-S-H}})}{\mathrm{erf}(\xi_{\mathrm{C-S-H}})} \tag{3.37}$$

$$\Delta m_s \frac{dx_{\mathrm{C-S-H}}}{dt} = \Delta m_s \xi_{\mathrm{C-S-H}}\sqrt{\frac{D}{t}} \tag{3.38}$$

Use of (3.36) through (3.38) in (3.8) delivers the following dimensionless expression of the mass conservation at the C-S-H front:

$$\varepsilon_{\mathrm{C-S-H}}\left(\frac{\exp(-\xi^2_{\mathrm{C-S-H}})}{\mathrm{erf}(\xi_{\mathrm{C-S-H}})} - \frac{\exp(-\xi^2_{\mathrm{C-S-H}})(1-c)}{\mathrm{erf}(\xi_{\mathrm{CH}}) - \mathrm{erf}(\xi_{\mathrm{C-S-H}})}\right) - \sqrt{\pi}\xi_{\mathrm{C-S-H}} = 0 \tag{3.39}$$

Equations (3.35) and (3.39) form a set of two nonlinear equations for the unknown front locations $\xi_{\mathrm{C-S-H}}$ and ξ_{CH}. They have to be solved simultaneously to find the respective locations, which can be performed with standard numerical techniques [97]. The required input data for the solution are the chemical equilibrium concentrations $[\mathrm{Ca}^{2+}]^{eq}_{\mathrm{CH}}$ and $[\mathrm{Ca}^{2+}]^{eq}_{\mathrm{C-S-H}}$ in addition to porosity, diffusivity and the changes in mass.

3.2 Chemical Analysis of the Leaching Process

This section is devoted to the determination of the equilibrium concentrations $[\mathrm{Ca}^{2+}]^{eq}_{\mathrm{CH}}$ and $[\mathrm{Ca}^{2+}]^{eq}_{\mathrm{C-S-H}}$, required for the solution of the two-front model. The chemical equilibrium problem of Portlandite and C-S-H in an ammonium nitrate solution is considered.

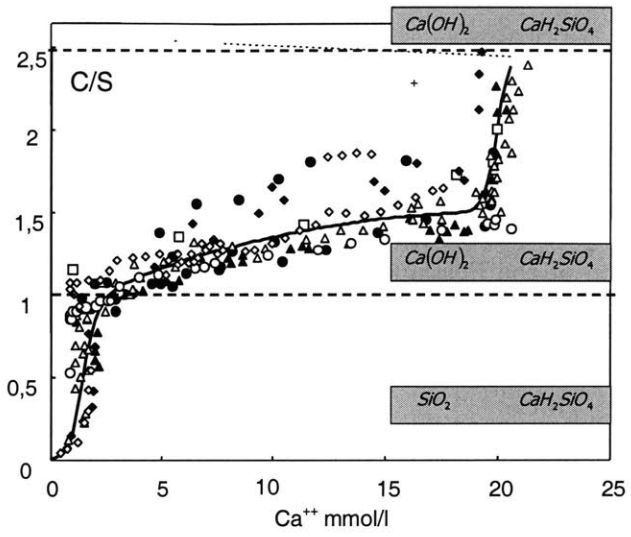

Figure 3-2: Three regions (according to their C/S ratio) and the corresponding components propsed by Berner [18].

3.2.1 Chemical Equilibrium Calculation with Ammonium Nitrate

Berner [18] suggested that the chemical system cement-water which contains many different phases can be simplified for solubility calculations. Figure 3-2 shows the Berner-curve and the three regions suggested by Berner together with the main components that are considered in each one of them. In fact, to simplify the chemical equilibrium calculations, only two components are taken into account plus the leaching agent. The existing experimental observations for the solubility of cement hydrates in water which are shown in the Berner-curve are well reproduced by the simplified analysis that Berner suggests. Berner provides the equilibrium concentrations for water as leaching agent (see Figure 3-2). For our purpose, the equilibrium concentrations need to be calculated for the case of the ammonium nitrate solution. The solubility constants used in the calculations are given in Table 3.1. The solubility constants describe the equilibrium of a reaction of the type:

$$A_x B_{y(s)} \longrightarrow xA + yB \tag{3.40}$$

Component	$\log K_{so}$
$Ca(OH)_2$	-5.20
CaH_2SiO_4 at C/S = 1	-8.16
SiO_2 at C/S = 1	-6.00

Table 3.1: Solubility constants used in the calculations

where the equilibrium constant is defined as:

$$K = \{A\}^x \{B\}^y \tag{3.41}$$

Brackets {...} denote the activity of a component. As concentrations are easier to measure than activities, they are the preferred variables to work with. The relation between the two is given by

$$\{A\} = \gamma_A [A] \tag{3.42}$$

where γ_A is the activity coefficient. For dilute solutions, the activity coefficients can be considered equal to one. There exist different approaches to account for the fact that at higher concentrations, the activities and concentrations of the species do not coincide (for an overview see e.g. [137]). In the case of cementitious materials, the concentrations of the species in the pore solution are very high (total dissolved species $> 10^{-3}$ mol / l) so that the classical approaches of taking into account the ion interactions (Davis, Debye-Hueckel etc.) do not suffice. In addition, spacial interactions need to be taken into account for which the so called Pitzer equations are generally employed [59]. In the calculations, the equilibrium concentrations of Portlandite and CaH_2SiO_4 are determined in the presence of a 6M ammonium nitrate solution. This is the typical concentration used by other researchers in the field [28]. The equilibrium calculations were performed with the geochemical code PHREEQC [112] that is publicly available. The results for the free calcium concentration in the pore solution are:

$$[Ca^{2+}]^{eq}_{CH} = 2.7\,\text{mol}/\text{l} \tag{3.43}$$

$$[Ca^{2+}]^{eq}_{C-S-H} = 0.5\,\text{mol}/\text{l} \tag{3.44}$$

These values need to be compared to $20\times10^{-3}\,\mathrm{mol/l}$ and $2\times10^{-3}\,\mathrm{mol/l}$ respectively, which are the equilibrium concentrations in deionized water [18]. The chemical calculation shows therefore that the value of the invariant $\varepsilon_{\mathrm{C-S-H}}$ (Eq. (3.17)) increases by approximately a factor 250.

Moreover, in the case of the Portlandite dissolution, that is $\mathrm{CaOH_2} \rightarrow \mathrm{Ca^{2+}} + 2\mathrm{OH^-}$, the mechanisms of the dissolution reaction can be illustrated as well. Ammonium Nitrate dissociates according to:

$$\mathrm{NH_4NO_3} \rightleftharpoons \mathrm{NH_4^+} + \mathrm{NO_3^-} \tag{3.45}$$

A redox reaction takes place that consumes the ammonia ($\mathrm{NH_4^+}$) and part of the nitrate ($\mathrm{NO_3^-}$) and that produces nitrogen and $\mathrm{H^+}$. The two half reactions read:

$$\frac{1}{5}\mathrm{NO_3^-} + \frac{6}{5}\mathrm{H^+} + e^- \rightleftharpoons \frac{1}{10}\mathrm{N_2} + \frac{3}{5}\mathrm{H_2O}; pe^0 = 21.05 \tag{3.46}$$

$$\frac{1}{8}\mathrm{NO_3^-} + \frac{5}{4}\mathrm{H^+} + e^- \rightleftharpoons \frac{1}{8}\mathrm{NH_4^+} + \frac{3}{8}\mathrm{H_2O}; pe^0 = 14.09 \tag{3.47}$$

where the pe^0 are equilibrium constants of the half reactions. The proton production in this reaction favors the dissolution of Portlandite as the $\mathrm{OH^-}$ ions of the Portlandite are immediately compensating for them. Moreover, the $\mathrm{H^+}$ production of ammonium nitrate is not automatic but depends very much on the availability of $\mathrm{OH^-}$ to compensate. In other words, in contrast to strong acids, which would lower the pH values of the solution much more, ammonium nitrate, an oxidizer, develops its capacity to compensate the $\mathrm{OH^-}$ as they become available. This is one of the reasons why the ammonium nitrate solution is similar in its effects of calcium leaching to deionized water. At the same time, other phases that form in the solution and that could limit the free calcium concentration through their low solubility do not exist. For instance, calcium nitrate has a very high solubility so that no limitation to the process from that side occurs.

Finally, one question that is of importance for the experimental realization of the leaching process is the renewal cycle of the ammonium nitrate solution, which needs to guarantee that there is always enough ammonia to sustain the reaction. The equilibrium between ammonium

Case	$D[m^2 s^{-1}]$	ϕ	$[Ca^{2+}]^{eq}_{CH}$	$[Ca^{2+}]^{eq}_{C-S-H}$	m_{CH}	Δm_s
Deionized Water	5×10^{-11}	0.6	22mmol/l	2mmol/l	$182\,kg\,/\,m^3$	$338\,kg\,/\,m^3$
Ammonium Nitrate [6M]	5×10^{-11}	0.6	$2.7\,mol\,/\,l$	$0.5\,mol\,/\,l$	$182\,kg\,/\,m^3$	$338\,kg\,/\,m^3$

Table 3.2: Physical Parameters for leaching

(NH_4^+) and aqueous ammonia (NH_{3aq}) is given by:

$$NH_4^+ \rightleftharpoons NH_{3aq} + H^+ \tag{3.48}$$

$$\frac{\{NH_{3aq}\}\{H^+\}}{\{NH_4^+\}} = 10^{-9.25} \tag{3.49}$$

The equilibrium constant of 9.25 signifies that as long as the pH is below 9.25, enough ammonia is present for the leaching reaction to proceed. In other words, a simple pH measurement will indicate when the solution needs to be replaced.

3.2.2 Comparison with Multiple Front Approach

Use of the equilibrium concentrations (3.43), (3.44) in $(3.17)_3$ and $(3.27)_3$ allows the determination of the macroscopic solubility parameters, ε_{C-S-H} and ε_{CH}, which are the input for the solution of the two-front problem (3.35) and (3.39). The results will first be compared to the multiple front formulations by Adenot [3]. This is the focus of this section, in which the leaching times of a cylinder are estimated, and which is the basis for the experimental leaching device developed and presented in Section 3.4.

Table 3.2 gives the values for the different physical parameters involved in the model formulation. The m_{CH} values were determined under the assumption that the chemical porosity created through Portlandite dissolution is 15%, which is an average value for a $w/c = 0.5$ cement paste [29]. The change in calcium mass is 54% of the total mass change involved in the Portlandite dissolution (calcium accounts for 54% of the Portlandite mass, the Portlandite density being $2,240\,kg\,/\,m^3$). To calculate Δm_s we use XRF[1] data on unleached and leached cement

[1]XRF stands for X-ray fluorescence anlysis. X-ray fluorescence and location of absorption edges can be used to identify quantitatively the elements present in a sample. The core-electron energy levels are not strongly perturbed by the chemical environment of the atom since the electric fields acting on these electrons are completely dominated by the nuclear charge. Their atomic energy level fingerprint is not perturbed by the more complex environment. The elemental abundance of a particular element can be determined by measuring the difference in X-ray absorption just above and just below an absorption edge of that element [1].

#		Calc. Step	Add. Info
A	Portlandite Volume	15%	[29]
B	Calcium in A	$0.54 \times 0.15 = 0.08$	
C	m_{CH} [=B$\times\rho_{CH}$]	$m_{CH} = 182\,kg\,/\,m^3$	ρ_{CH} =2.24g /cm^3
D	Tot. Ca^{2+} in unleached paste	$0.35 \times 1.92\,g\,/cm^3$	XRF
E	Tot. Ca^{2+} in leached paste	$0.1 \times 1.52\,g\,/cm^3$	XRF
F	Tot dissolved Ca^{2+} [D-E]	$520\,kg\,/\,m^3$	
G	Diss. Ca^{2+} from C-S-H [F-C]	$\Delta m_s = 338\,kg\,/\,m^3$	

Table 3.3: Calculation steps for the model paramters

paste specimens together with the density information. In the unleached state, about 35% of the mass is calcium, the density is about $1,920\,kg\,/\,m^3$(mass of solid per total volume). After leaching, about 10% of the solid is calcium and the density is reduced to $1,520\,kg\,/\,m^3$. This yields a total mass of dissolved calcium of $520\,kg\,/\,m^3$. The part attributed to the C-S-H decalcification is the difference between the total change and the dissolution of the calcium bound in the Portlandite that is $\Delta m_s = 338\,kg\,/\,m^3$. Table 3.3 gives an overview of the calculation steps. The dimensionless parameters of the model take the following values:

$$\varepsilon_{CH} = \frac{\phi[Ca^{2+}]^{eq}_{C-S-H}\mathcal{M}_{Ca^{2+}}}{m_{CH}} = 6.59 \times 10^{-2} \tag{3.50}$$

$$\varepsilon_{C-S-H} = \frac{\phi[Ca^{2+}]^{eq}_{C-S-H}\mathcal{M}_{Ca^{2+}}}{\Delta m_s} = 3.55 \times 10^{-2} \tag{3.51}$$

$$c = \frac{[Ca^{2+}]^{eq}_{CH}}{[Ca^{2+}]^{eq}_{C-S-H}} = 11;\ \text{deionized water} \tag{3.52}$$

$$c = \frac{[Ca^{2+}]^{eq}_{CH}}{[Ca^{2+}]^{eq}_{C-S-H}} = 5.4;\ 6M - NH_4NO_3 \tag{3.53}$$

Solving the equations (3.35) and (3.39) for the case of deionized water yields $\xi_{CH} = 0.027$ and $\xi_{C-S-H} = 0.0021$. This result can be compared with the model calculations by Adenot [3], in which the diffusion problem with 12 fronts is solved numerically, and in which both porosity and the diffusivity varies from one zone to the other. Table 3.4 shows the comparison between the Portlandite front and the C-S-H front for C/S=1.0 from Adenot's numerical solution and the analytical solution of the two-front model. Despite the rough assumptions of constant porosity and diffusivity, the analytical solution of the two-front approach gives the same order

	Adenot [3]	2-front model
$\xi_{CH}[-]$	1.1×10^{-2}	2.7×10^{-2}
$\xi_{C-S-H}[-]$	2.2×10^{-3}	2.1×10^{-3}

Table 3.4: Comparison of model results with the simplified analytical solution.

of magnitude results as the much more sophisticated numerical model by Adenot.

3.3 Application: Prediction of Leaching Duration

3.3.1 Steady State Diffusion in a Cylinder

Of interest is the one dimensional solution for the leaching of a cylinder which we want to design for the leaching of the test specimens. In a cylinder with Radius R, the diffusion equation is given by:

$$\frac{\partial(\phi[Ca^{2+}])}{\partial t} - \frac{1}{r}\frac{\partial}{\partial r}\left[D\frac{\partial(\phi[Ca^{2+}])}{\partial r}\right] = 0 \tag{3.54}$$

To simplify the problem we assume that the diffusion is in a steady state, which means that the diffusion between the contour and the leaching fronts is instantaneous.[2] Problem equations (3.1) to (3.9) can then be rewritten in cylindrical coordinates:

$$t < 0 : [Ca^{2+}] = [Ca^{2+}]^{eq}, r \in [0, R] \tag{3.55}$$

$$r = R, t > 0; [Ca^{2+}] = 0; \tag{3.56}$$

$$t > 0; r_{C-S-H} < r < R : \frac{1}{r}\frac{\partial}{\partial r}\left[\frac{\partial(\phi[Ca^{2+}])}{\partial r}\right] = 0 \tag{3.57}$$

$$t > 0; r_{CH} < r < r_{C-S-H} : \frac{1}{r}\frac{\partial}{\partial r}\left[\frac{\partial(\phi[Ca^{2+}])}{\partial r}\right] = 0 \tag{3.58}$$

[2]This hypothesis is often made in radial diffusion problems to obtain an analytical solution. It is valid if the mass to dissolve is large compared to the equilibrium concentration, i.e. for ε_{CH} and $\varepsilon_{C-S-H} \ll 1$.

$$
\begin{aligned}
r &= r_{\text{C-S-H}}, t > 0; [\text{Ca}^{2+}] = [\text{Ca}^{2+}]^{eq}_{\text{C-S-H}} \\
r &= r_{\text{CH}}, t > 0; [\text{Ca}^{2+}] = [\text{Ca}^{2+}]^{eq}_{\text{CH}}
\end{aligned} \tag{3.59}
$$

$$
\begin{aligned}
t > 0; r = r_{\text{C-S-H}} \quad : \quad & D\mathcal{M}_{\text{Ca}^{2+}} \left[\left(\phi \frac{\partial([\text{Ca}^{2+}])}{\partial r} \right)_{r^{-}_{\text{C-S-H}}} - \left(\phi \frac{\partial([\text{Ca}^{2+}])}{\partial r} \right)_{r^{+}_{\text{C-S-H}}} \right] \\
- \quad & [[\rho_s(1-\phi)]] \frac{dr_{\text{C-S-H}}}{dt} = 0
\end{aligned} \tag{3.60}
$$

$$
t > 0; r = r_{\text{CH}} : \phi D\mathcal{M}_{\text{Ca}^{2+}} \left(\frac{\partial([\text{Ca}^{2+}])}{\partial r} \right)_{r_{\text{CH}}} - \rho_{\text{CH}} \phi_c \frac{dr_{\text{CH}}}{dt} = 0 \tag{3.61}
$$

The general solution of (3.56) or (3.57) is given by:

$$
[\text{Ca}^{2+}] = C_1 + C_2 \ln r \tag{3.62}
$$

where C_1 and C_2 are integration constants to be determined by the boundary and continuity conditions.

Portlandite Zone

For the Portlandite zone the solution together with the boundary conditions reads for the dimensionless calcium concentration:

$$
R'_{\text{CH}} < R' < R'_{\text{C-S-H}} : \overline{[\text{Ca}^{2+}]} = \left(\ln \left(\frac{R'_{\text{CH}}}{R'_{\text{C-S-H}}} \right) + (c-1) \ln \left(\frac{R'}{R'_{\text{C-S-H}}} \right) \right) \times \ln \left(\frac{R'_{\text{C-S-H}}}{R'_{\text{CH}}} \right) \tag{3.63}
$$

where we introduced the adimensional radii $R' = \frac{r}{R}$, $R'_{\text{CH}} = \frac{r_{\text{CH}}}{R}$ and $R'_{\text{C-S-H}} = \frac{r_{\text{C-S-H}}}{R}$.

The front equation for the Portlandite dissolution (3.61) reads here:

$$
D\varepsilon_{\text{CH}} \frac{c-1}{R_{\text{CH}} \ln \frac{R'_{\text{CH}}}{R'_{\text{C-S-H}}}} - \frac{dR'_{\text{CH}}}{R^2 dt} = 0 \tag{3.64}
$$

where $\varepsilon_{CH} = \frac{\phi[Ca^{2+}]^{eq}_{C-S-H}\mathcal{M}_{Ca^{2+}}}{m_{CH}}$ is still given by $(3.27)_3$.

Integration of (3.64) between time 0 and time t yields:

$$\frac{4D\varepsilon_{CH}(c-1)t}{R^2} = 2R'^2_{CH}\ln\frac{R'_{CH}}{R'_{C-S-H}} + 1 - R'^2_{CH} \tag{3.65}$$

C-S-H Zone

In the C-S-H zone, the solution of (3.58) reads in dimensionless form:

$$R'_{C-S-H} < R' < 1 : \overline{[Ca^{2+}]} = \frac{\ln R'}{\ln R'_{C-S-H}} \tag{3.66}$$

and the C-S-H front equation is given by

$$D\varepsilon_{C-S-H}\frac{(c-1)\ln R'_{C-S-H} - \ln\frac{r_{CH}}{r_{C-S-H}}}{R'_{C-S-H}\ln\frac{R'_{CH}}{R'_{C-S-H}}\ln R'_{C-S-H}} - \frac{dR'_{C-S-H}}{R^2dt} = 0 \tag{3.67}$$

where $\varepsilon_{C-S-H} = \frac{\phi[Ca^{2+}]^{eq}_{C-S-H}\mathcal{M}_{Ca^{2+}}}{\Delta m_s}$ is still given by $(3.17)_3$.

Equation (3.67) leads to an integral equation. Equations (3.65) and (3.67) form a set of non-linear equations for the adimensional variables of the front locations R'_{C-S-H} and R'_{CH}.

3.3.2 Time for Asymptotic Leaching of a Cylinder

The question of interest to us is the estimation of the time it takes to asymptotically leach a cylinder. This time corresponds to the time when the C-S-H front reaches the center of the cylinder. At this point the Portlandite front already reached the center and the solution (??) is not valid anymore. When the Portlandite front reaches the center, the new continuity conditions of the Portlandite zone are:

$$t > 0; [Ca^{2+}](r_{C-S-H}, t) = [Ca^{2+}]^{eq}_{C-S-H}; \tag{3.68}$$

$$t > 0; \frac{\partial[Ca^{2+}]}{\partial r}(R, t) = 0; \tag{3.69}$$

Condition (3.69) is a symmetry condition in the center. With these two conditions, the solution of Eq.(3.56) leads to a constant calcium concentration in the Portlandite zone:

$$\overline{[Ca^{2+}]} = 1; 0 < R' < R'_{C-S-H} \tag{3.70}$$

For $R' > R'_{C-S-H}$ the problem simplifies to a diffusion problem with one front, for which the solution of the front movement reads [90]:

$$\frac{-4D\varepsilon_{C-S-H}t}{R^2} = 2R'^2_{C-S-H} \ln \frac{1}{R'_{C-S-H}} + R'^2_{C-S-H} - 1 \tag{3.71}$$

The C-S-H front reaches the center when R'_{C-S-H} is equal to zero; which yields:

$$t_{C-S-H} = \frac{R^2}{4D\varepsilon_{C-S-H}} \tag{3.72}$$

This is the time it takes for the C-S-H front to reach the center after the Portlandite front has reached the center. For a cylinder with diameter 11.5 mm (a suggested size issuing from requirements on subsequent mechanical tests), $t_{C-S-H} = 13{,}473$ days for leaching with deionized water. In the case of Ammonium Nitrate accelerated leaching, it is around 54 days (where we took $[Ca^{2+}]^{eq}_{C-S-H}$ to be $0.5\,mol/l$).

The time for the Portlandite front to reach the center can be quickly deduced from the solution of (3.65). The front reaches the middle for $R'_{CH} = 0$:

$$t_{CH} = \frac{R^2}{4D\varepsilon_{CH}(c-1)} \tag{3.73}$$

With the given values for the different physical constants (Table 3.2, Eq. (3.39)), t_{CH} is about 725 days in the case of deionized water and 7 days with the 6M ammonium nitrate solution, both for a specimen with a 11.5mm diameter. The total leaching time can then be estimated by adding t_{C-S-H} and t_{CH}:

$$t_{final} = t_{C-S-H} + t_{CH} = \frac{R^2}{4D\varepsilon_{C-S-H}} + \frac{R^2}{4D\varepsilon_{CH}(c-1)} \tag{3.74}$$

In summary, it appears that in the case of ammonium nitrate based leaching, we can expect to

obtain asymptotically leached specimens (diameter 11.5 mm) in approximately 60 days, while the deionized water would need some 39 years for the same result. Obviously, the hypothesis of steady state diffusion, necessary for an analytical solution to the problem, is important. To illustrate our purpose, Figure 3-3 shows finite element simulations of the leaching of a cylinder. The two sharp fronts can be clearly distinguished. It is clear from the time it takes for the Portlandite front to reach the center that the steady state assumptions leads to a slight underestimation of the leaching times. Still, the results obtained with the steady state assumption provide the right order of magnitude, that is roughly 60 days for a complete leaching of the 11.5 mm cylinder.

3.4 Practical Realization of the Leaching Device

3.4.1 Setup

The results from the two-front model highlight the large acceleration potential of an ammonium nitrate based leaching technique. This section describes the chosen experimental realization of the device and its performance compared to the expected results from the model.

So that the device should be simple to install and require low maintenance, a set of plastic containers was mounted on an oscillating table, as shown in Figure 3-4. The containers hold each about 2 kg of the ammonium nitrate solution at 480 g / kg or 6 mol of ammonium nitrate per kilogram of total solution[3]. Inside the container, up to 28 cement paste or mortar specimens are immersed in the highly concentrated ammonium nitrate solution. The specimens have a diameter of 11.5 mm and a length of 60 mm. This corresponds in total to approximately $190 \times 10^{-6}\,\mathrm{m}^3$ of cementitious material in one container. The specimens are aligned and can move easily as the table oscillates. The oscillation provides a simple means to assure good mixing of the aggressive solution. During the leaching procedure, nitrogen gas is pushed through the containers to prevent any contact of CO_2 with the specimens which would lead to carbonation[4].

[3] This leads to a density of $1,180\,\mathrm{kg}/\mathrm{m}^3$.

[4] The emphasis on the good mixing of the solution and the carbonation prevention was also stressed from the literature review and personal communications with [80], [31] and the CEA Paris through J. Sercombe.

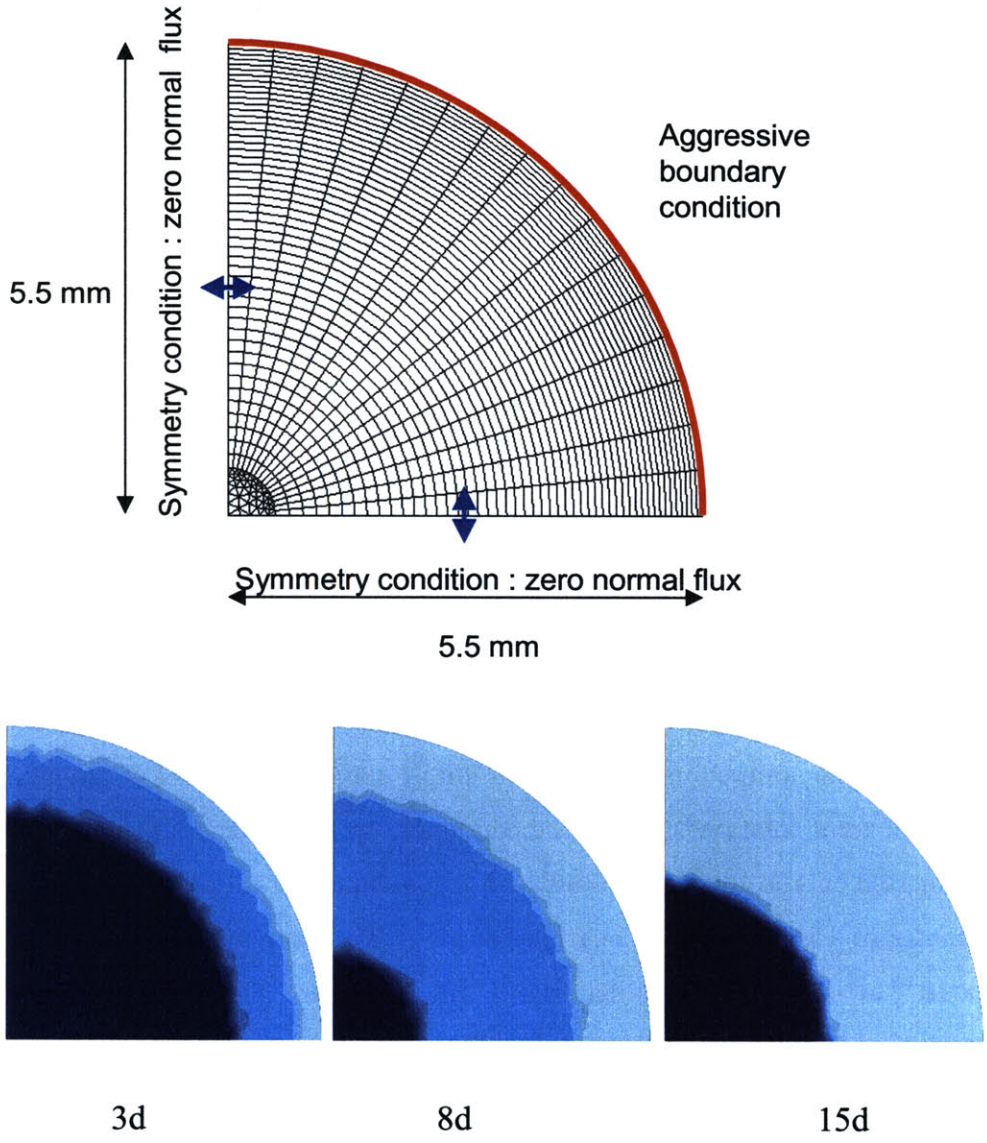

Figure 3-3: Results from finite element simulations of calcium leaching in ammonium nitrate, based on the three-dimensional extension (see Chapter 9) of the model presented in this chapter.

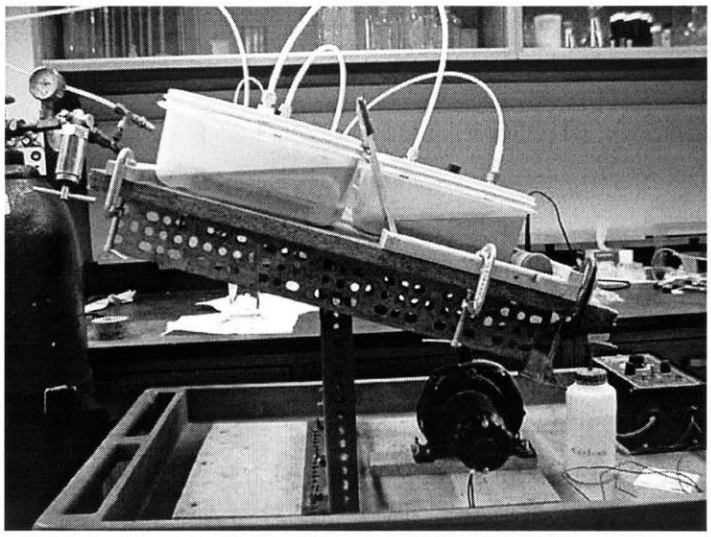

Figure 3-4: Oscialting table with several containers that each contain the ammonium nitrate solution.

3.4.2 Results

The following results were obtained with the developed leaching device:

- The pH value, measured during the leaching procedure, never exceeded 8.5, indicating according to Eq. (3.49) that the volume of the ammonium nitrate solution is sufficiently large to avoid any change in the solution during the leaching process. This meets the low maintenance requirement of the device.

- The evolution of the Portlandite front was monitored visually. After 9 days of leaching, the Portlandite front reached the center. This is on the same order as the predicted values (7 days with steady state assumption) of the two-front model and confirms the strong accelerating effect of the ammonium nitrate.

- The effective acceleration factor of the leaching procedure can be defined as:

$$a_{\mathrm{CH}} = \left(\frac{\xi^1_{\mathrm{CH}}}{\xi^0_{\mathrm{CH}}}\right)^2 \tag{3.75}$$

where $\xi^1_{CH} = x_{CH}/2\sqrt{Dt_1}$ and $\xi^0_{CH} = x_{CH}/2\sqrt{Dt_0}$ define the Portlandite front locations. t_0 is the time necessary to reach the center when leaching with deionized water is performed, t_1 is the corresponding duration in the ammonium nitrate solution. Evaluating (3.75) comes down to comparing the ratio of the leaching times. The value of a_{CH} is close to 300, assuming the same diffusion coefficent and based on the reported times in the literature for deionized water (for example $2\sqrt{D}\xi_{d0} = 0.1\,\mathrm{mm}/\sqrt{\mathrm{d}}$ [80]).

- The dissolution of calcium in the different other mineral phases particularly the C-S-H phases requires additional time and was monitored through periodic XRF measurements of the bulk calcium concentration. Figure 3-5 shows the development of the calcium content for the cylindrical cement paste specimen. The 9 days, at which the Portlandite front reached the center is marked and it is clearly observable that the calcium concentration continues to decrease as the other minerals get dissolved. In fact, looking at the measured values, it seems that it takes roughly 60 days to asymptotically leach the cement paste specimens. Again, the two-front model based on the steady state diffusion assumption predicted 60 days. The accelerating effect of the ammonium nitrate solution is confirmed. A second acceleration factor can be defined for the C-S-H front:

$$a_{C-S-H} = \left(\frac{\xi^1_{C-S-H}}{\xi^0_{C-S-H}}\right)^2 \tag{3.76}$$

  where $\xi^0_{C-S-H} = x_{C-S-H}/2\sqrt{Dt_0}$ and $\xi^1_{C-S-H} = x_{C-S-H}/2\sqrt{Dt_1}$ define the C-s-H front locations. t_0 is the time necessary to reach the center when leaching with deionized water is performed, t_1 is the corresponding duration in the ammonium nitrate solution. Based on the model results (Table 3.4), a_{C-S-H} takes the value 250.

- An obvious question concerns the limit of the acceleration: Can one actually improve the acceleration factor by increasing the concentration of ammonium nitrate? The solubility of ammonium nitrate in water is approximately 680 g / kg at 20°C [12], which needs to be compared to the 480 g / kg employed in the experimental setup. However, increasing the ammonium nitrate concentration beyond the 6M concentration did not accelerate the leaching process beyond the already obtained rates. The reason for this has its origin in

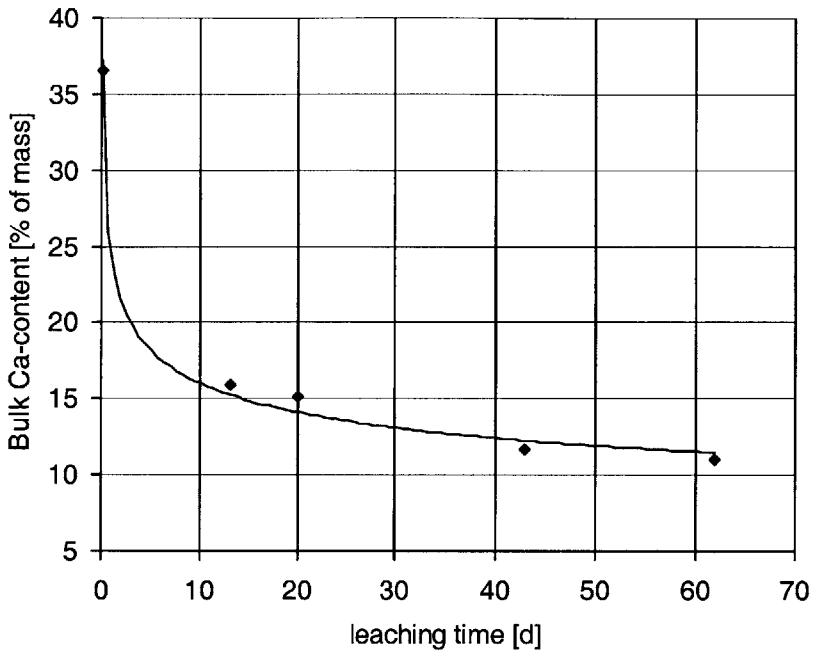

Figure 3-5: Total calcium content in a cylindrical specimen as leaching takes place. The solid curve presents a least-square fit to the measurments.

the composition of the specimens themselves: The total concentration of Portlandite is limited and increasing the ammonium nitrate concentration beyond 6 moles per kilogram of solution does not yield a higher calcium concentration in the fluid phase and hence no additional acceleration. For the C-S-H decalcification an additional acceleration could be expected because the calcium concentration to be leached is higher.

- In addition, it was tested whether the leaching process with an ammonium nitrate solution is in fact governed in its time scale by the diffusion process. In a tests series, cement pastes were ground to powder that passes through a sieve with a hole size of 5×10^{-4} m. These powders were put in contact with the ammonium nitrate solution (480 g / kg) during different time periods. After the specified duration, solution and remaining powder were separated in a centrifuge. From the obtained powder, the calcium concentration was determined via XRF. The results, summarized in Table 3.5, point out that after a very

Contact time [min]	% of Ca leached
0	0
1	69
10	86
100	86
900	86

Table 3.5: Results from leaching on cement paste powders.

short time (a couple of minutes), due to the still finite size of the powder particles which indicates some diffusion, the leaching process comes to an end. This confirms that in the same way as for leaching with deionized water [3], also for the ammonium nitrate solution the dissolution reaction is much faster than the diffusion and that a local chemical equilibrium exists compared to the diffusion time scale.

- Besides cement paste, also mortars were leached in the ammonium nitrate solution. The obtained front propagation velocities and leaching times were identical to the ones of cement paste. This confirms experimental results by Bourdette [25].

3.5 Concluding Remarks

In this Chapter a model-based design of an accelerated leaching device was presented. While the two-front leaching model will be extended to three dimensions in Chapter 9 in view of model-based simulations of entire concrete structures, the following conclusions relevant for the developed leaching device can be drawn:

- The two-front model focuses on the Portlandite leaching front and the C/S=1 C-S-H front. This assures that the main aspects of calcium leaching of cementitious materials are preserved: The two important microstructural levels I and II are involved. In addition, both the first and the last mineral to lose equilibrium and the two most abundant minerals are traced in this approach. Table 3.6 gives an overview of the main characteristics of the leaching process that has been developed in this Chapter.

- The one-dimensional model-based simulations give a correct order of magnitude of the dissolution time. The invariants of the model provide a good understanding of how an

Characteristics of calcium leaching with an ammonium nitrate solution

C-S-H Front (Level I) and Portlandite Front (Level II) cover transformations on two microstructural levels.

Local chemical equilibrium exists compared to diffusion time scale.

The acceleration is governed through the invariants $\varepsilon_{C-S-H} = \frac{\phi[Ca^{2+}]^{eq}_{C-S-H}\mathcal{M}_{Ca^{2+}}}{\Delta m_s}$ and $\varepsilon_{CH} = \frac{\phi[Ca^{2+}]^{eq}_{C-S-H}\mathcal{M}_{Ca^{2+}}}{m_{CH}}$ which are adimensional macroscopic solubility parameters.
Increasing this invariant leads to higher acceleration rates. This is limited only by the actual calcium concentration in the solid.

The leaching device delivers asymptotically leached specimens for mechanical testing.

Table 3.6: Characteristics of calcium leaching with an ammonium nitrate solution.

acceleration of calcium leaching can be chemically controlled: ε_{CH} and ε_{C-S-H} are a sort of macroscopic solubility parameters. Through a calculation of the chemical equilibrium in a $Ca - Si - H_2O$ system their values can be determined. The accelerated leaching device is an efficient easy-to-use application. It can be used to classify the natural resistance of different types of cementitious materials to calcium leaching or as a quality control instrument.

- In the context of this investigation, the leaching device will be used to leach cement pastes and mortars (Levels II and III) for further mechanical testing. In this context, the speed of leaching and the simplicity of the device are particularly important.

Chapter 4

Tested Materials and Observed Microstructural Changes through Calcium Leaching

This Chapter provides details on the materials that are used in the experimental part of this study and on the observed microstructural changes induced by calcium leaching. After describing the mix design of the cement paste (Level II) and mortar (Level III), density and porosity measurements are presented as well as Scanning Electron Microscopy (SEM) observations. The density and porosity measurements are performed on centimeter scale paste and mortar specimens. In the SEM micrographs, the characteristics of the microstructure are shown at length scales between 10^{-8} m and 10^{-4} m, that is at the characteristic scale of Levels I through III.

4.1 Materials

4.1.1 Cement Paste

The cement paste was prepared at a water to cement (mass) ratio of $w/c = 0.5$. This corresponds to a water-cement ratio typical of a standard concrete, which is used in many applications. The effect of different w/c-ratios on leaching kinetics and compressive strength evolution in leaching has been studied by other researchers [3], [28] and is not further considered in this investigation.

OPC Type I	CaO	SiO_2	Al_2O_3	MgO	SO_3	Na_2O
	62.3	20.8	4.4	3.8	2.9	0.39
	Fe_2O_3	K_2O	C_3Al	C_3S	C_2S	Ignition loss
	2.4	1.28	8	53	20	0.66

Table 4.1: Type I Portland cement constituents, in mass percent. Analysis made by producer. [100]

The used cement is a type I Portland cement which was obtained directly from the producer, Dragon Cements, Portland, Maine. The composition of the cement is given in Table 4.1[1]. The cement has a relatively high amount of tricalcium silicate (C_3S). We recall the hydration reactions (2.4) for tricalcium silicate and dicalcium silicate:

$$\begin{aligned} 2C_3S + 10.6H &\longrightarrow C_{3.4}S_2H_8 + 2.6CH \\ 2C_2S + 8.6H &\longrightarrow C_{3.4}S_2H_8 + 0.6CH \end{aligned} \tag{4.1}$$

The hydration reactions show that 2 mol of tricalcium silicate lead to 2.6 mol of Portlandite while 2 mol of dicalcium silicate only produce 0.6 mol of Portlandite. Given the relatively high C_3S content in our cement, the hydrated cement paste will have a relatively high Portlandite content.

The paste is cast after mixing of the cement and water into PVC tubes with a diameter of 11.5 mm and a length of 60 mm. After 24 hours of curing in the closed tube, the specimens are demolded and cured in saturated lime solution at 20 °C for at least 28 days before being employed further.

4.1.2 Mortars

The mortar specimens utilized in this study were produced at a water/cement/sand mass ratio of $w/c/s = 1/2/4$ so that the same w/c-ratio as in the paste is respected. The aggregates are a fine Nevada sand with a density of $2,650\,\mathrm{kg/m^3}$ and $d_{60} = 0.23\,\mathrm{mm}$ and $d_{30} = 0.17\,\mathrm{mm}$

[1] A frequently used way to calculate the cement composition from the constituents is the Bogue calculation [23]. It has been found that the results issued from this technique can be quite far away from the actual composition [141]. Indeed, for the case of the cement used in this study, the Bogue equations would lead to negative concentrations of some components. This is why we rely here on the composition provided by the producer.

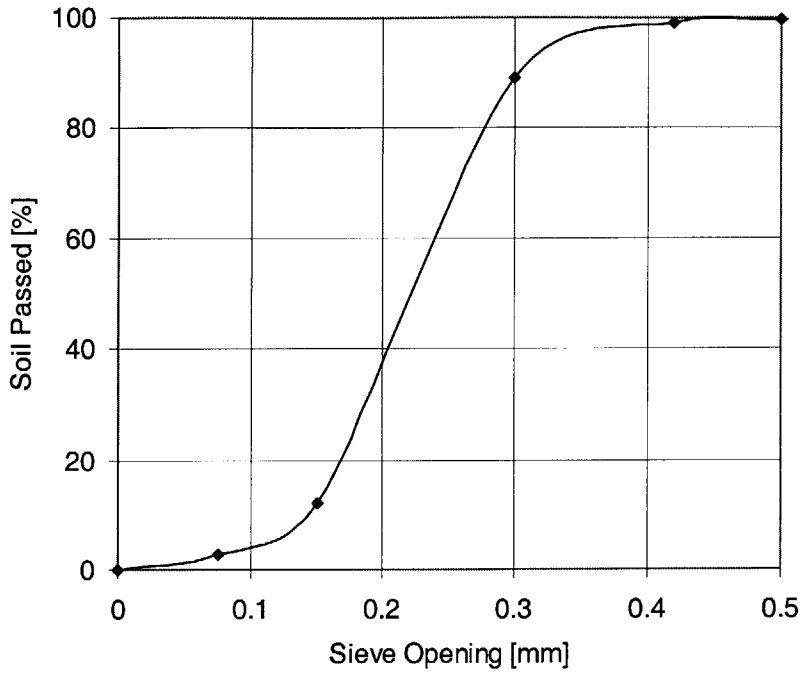

Figure 4-1: Grading of the Nevada sand used for the mortars.

where d_x signifies that x percent of the sand mass has grains of a diameter below d. Figure 4-1 shows the entire grading curve. The small grain sizes are used to obtain homogeneous mortar specimens in cylindrical specimens with diameters of roughly one centimeter. This sand is a reference material in the geotechnical group at MIT and has been tested in many laboratories throughout the U.S., particularly for the VELACS[2] project [5] so that its properties are well known. In particular, the water adsorption of the sand was tested to be negligible. In the mortar mixing procedure, first cement and sand are mixed before the water is added. The mortar were cast in the same cylindrical PVC molds as the paste. The rather small specimen size which was chosen to shorten the leaching time, still leads to an acceptable variability in material properties. Indeed, in a series of preliminary uniaxial compression tests, the variability

[2]VErification of Liquefaction Analysis using Centrifuge Studies, a collaborative research project among geotechnical laboratories around the world between 1989 and 1994.

OPC Type I	Uniaxial strength $f_{c28}[MPa]$	Number of tests	relative error [%]
Cement paste	54.1	5	5.6
Mortar	36.6	5	1.6

Table 4.2: Uniaxial compression strength of the cement paste and mortar.

of the specimens was tested. Table 4.2 shows the values for these tests and the relative error computed as the ratio of standard deviation and average value. The relative error was smaller than 6%, which is an acceptable value according to the ASTMC39 [8].

4.2 Porosity and Density Measurements

The porosity development is a key factor in the microstructure of cementitious materials that are subjected to leaching. The experimental determination of the porosity is a delicate task (see Tables 2.6 through 2.10 for an overview of the different techniques). For the measurement of the total porosity, the easiest technique, which also avoids most of the intrinsic problems of the other techniques, is the porosity measurement with water. This technique involves drying at 105 °C and leads to the evaporation of the chemically not bound water in the microstructure of a cementitious material (see Table 4.4 for an overview of the different forms of water in cementitious materials). This simple technique gives a good total porosity measurement as long as the water is accessible to the entire pore structure, which is a reasonable assumption for our high w/c-ratio cement-based materials. This method allows for a good comparison between the asymptotically leached and intact paste and mortar. In the experiments, the intact mortar and paste specimens are saturated for several weeks. The leached specimens are saturated in deionized water, after they have been asymptotically leached with the accelerated leaching device. Then the surface is dried quickly before the weight of the saturated specimen is determined. Finally, the specimen is placed in the oven and dried at 105 °C until no further change in mass is observed. From the change in mass, the change in porosity can be inferred, taking $1,000\,\mathrm{kg}\,/\,\mathrm{m}^3$ as the density of water.

The density of the specimens was determined from volume and mass measurements. The accuracy of these measurements was 10^{-5} m for the length (relative error 10^{-4}) and 10^{-6} kg for the mass (relative error 2×10^{-4}). In addition, the density was determined with the Archimedes

	Cement Paste		Mortar	
Specimen	Non-Degraded	Degraded	Non-Degraded	Degraded
Porosity [%]	39.7 ± 1.1	63.2 ± 1.6	27.5 ± 0.4	40.1 ± 2.4
Density$_{(sat.)}$[kg / m^3]	1898 ± 9	1351 ± 12	2171 ± 15	1831 ± 19

Table 4.3: Porosity and density measurements on degraded and non-degraded cement paste and mortar specimens (Mean+-St. Dev.).

Principle. The mass of the specimens was determined in air (m_{air}) and under water (m_{water}) and the density was determined from:

$$\rho_{specimen}=\rho_{water} \times \frac{m_{air}}{m_{air} - m_{water}} \tag{4.2}$$

where $\rho_{specimen}$ and ρ_{water} are the density of the specimen and the water, respectively. The two techniques gave identical results.

Table 4.3 shows the results of the porosity and the density measurements on the intact and asymptotically leached paste and mortar. The increase in porosity in the leaching process is considerable: An increase of 24 percentage points is measured for the paste. In the mortar, the increase is 12 percentage points and given that the aggregates in the mortar account for roughly 50% of the volume, the increase in the mortar porosity is also about 24 percentage points with respect to the cement paste volume. Due to the large porosity increase, the density of the paste decreases considerably. The decrease is smaller in the mortar due to the aggregates.

4.3 Microstructural Analysis through SEM Micrographs

SEM microscopy is an appropriate means for the analysis of microstructural features of cementitious materials. In this experimental study, the cement pastes and mortars were observed under the SEM in the undegraded and degraded state. The typically observed length scales go from 10^{-8} m to 10^{-4} m. This gives access to the different microstructural features on Levels I through III. In particular, the analysis focuses on the changes in morphology of the C-S-H matrix, the size and morphology of the pore space created by leaching and the size and appearance (compact, porous) of the ITZ.

Water vapor: Water vapor is found in partially filled larger voids of the macropores. It occupies the empty space, and contributes to the thermodynamic equilibrium of the water-vapor system in the capillary pores.
Capillary water: Water in the capillary and larger pores is free from the influence of the attracting surface forces. Wàter in voids larger than 50 nm is considered free and its removal does not result in any deformation.
Adsorbed water: Water under the influence of attractive surface forces, is referred to as adsorbed water. $5-6$ molecular layers form a surface layer of $1.3-1.5$ nm thickness. This water is lost after drying the sample below 30% relative humidity (RH).
Interlayer water: This water forms between two solid surfaces, is usually held in micropores by hydrogen bonding. A RH less than 11% can cause its removal, which leads to shrinkage deformation and volumetric changes.
Chemically combined water: This water is chemically combined within the different hydration products. It is not lost, except at very elevated temperatures at which chemical decomposition of the individual constituent takes place.

Table 4.4: Different forms of water present in a cementitious material adapted from [52]

4.3.1 Specimen Preparation

The SEM microscopy is performed on disks with the diameter of the originally cast specimens (11.5 mm) and a height of approximately 7 mm. After being stored in the curing bath or the leaching solution, the specimens are cut to the described length with a diamond saw and following recommendations by Stutzman [138] are immediately after immersed in an epoxy resin[3]. After one week of immersion, the resin in the specimens is cured during 24 hours at 60 °C. The specimens are polished on a semi automatic polishing table of the Center of Materials Science and Engineering (CMSE). The polishing steps consist of papers with grades 120, 320 and 600 and diamond solutions of the following sizes: 6 μm, 3 μm, 1 μm and 0.25 μm. After the last polishing step, the surface debris is removed in an ultrasonic bath. The specimens are then mounted on metal stubs and coated with a Gold-Palladium layer of 300 Å. The used microscope is a JEOL 6320FV SEM from CMSE. Generally, low acceleration voltages (between 1 and 5 kV) are used and relatively large working distances (between 10 and 20 mm), which reduces the charging of the specimen.

[3]The epoxy resin is "LR White " hard from the London Resin Company, Reading, U.K.

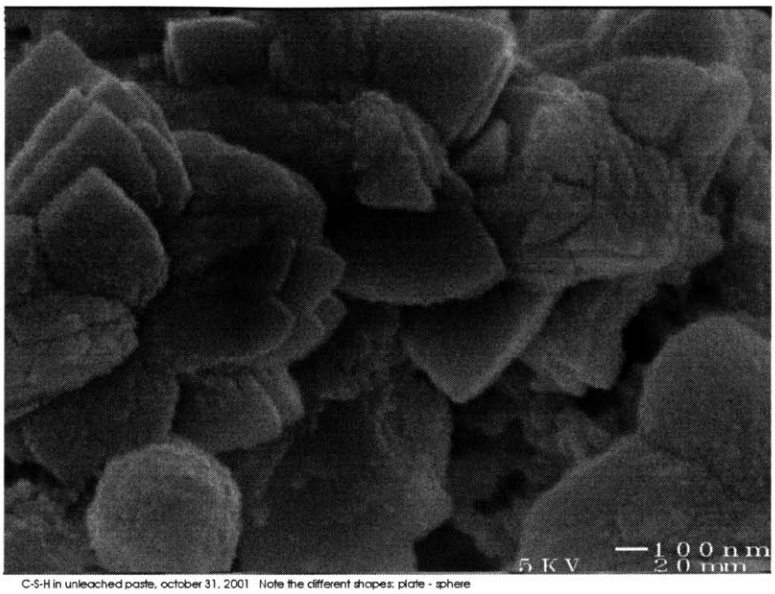

Figure 4-2: Coliflower and plate shaped C-S-H structures in an unleached paste.

4.3.2 Micrographs

Level I: C-S-H Matrix

Figure 4-2 through 4-4 show the smallest level of detail that can be attained in the experimental setting, which corresponds roughly to Level I. The C-S-H are clustered in different particles that can be distinguished. The different morphologies of unstructured C-S-H which are visible in Figure 4-2, are a cauliflower-like C-S-H and the more plate shaped forms. The unordered agglomeration of particles visible for example in Figure 4-3 shows how the outer products that form on a cement grain grow towards each other. The inner products cannot be visualized separately. The effect of leaching on the C-S-H matrix is difficult to follow in the SEM with the necessary magnification. Figure 4-5 shows a 20k magnification micrograph of the leached microstructure. The smallest visible scale is roughly 10^{-7} m. After the leaching, the C-S-H matrix appears more homogeneous and the distinctive particles disappeared; that is at Level I leaching leads to a more homogeneous material.

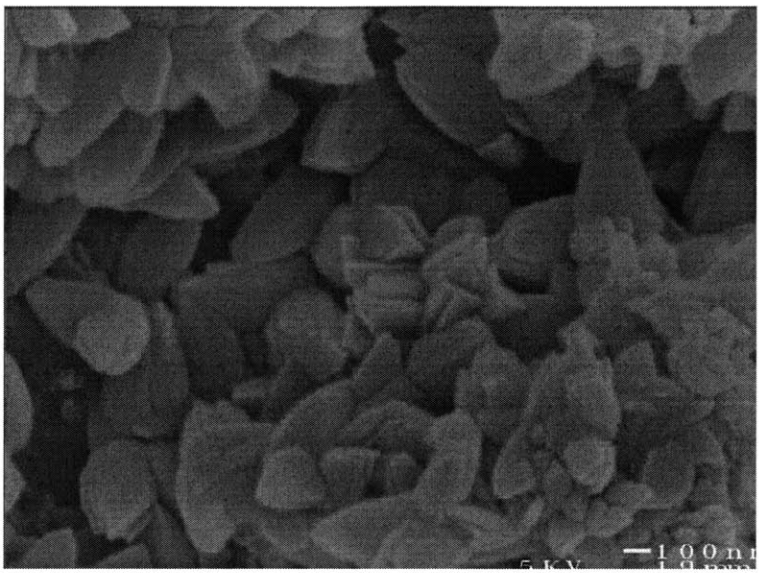

Figure 4-3: Detail of the microstructure of an unleached paste. Shows compact C-S-H clusters.

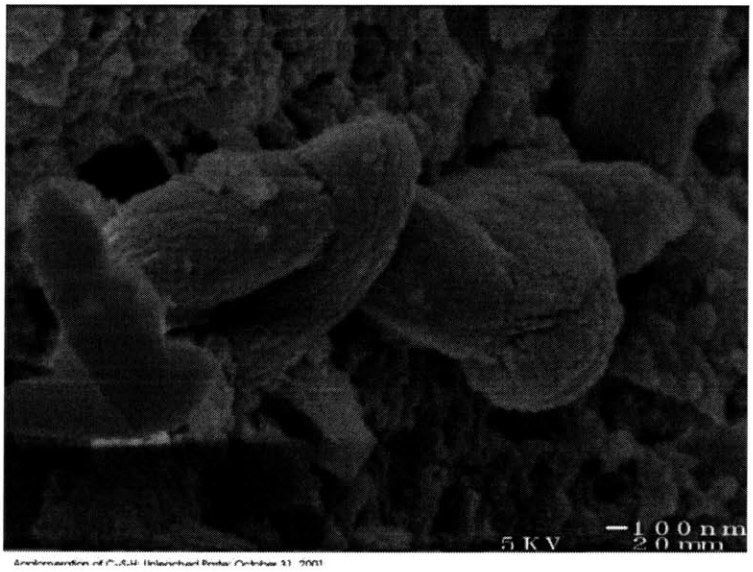

Figure 4-4: C-S-H agglomerations in an undegraded paste.

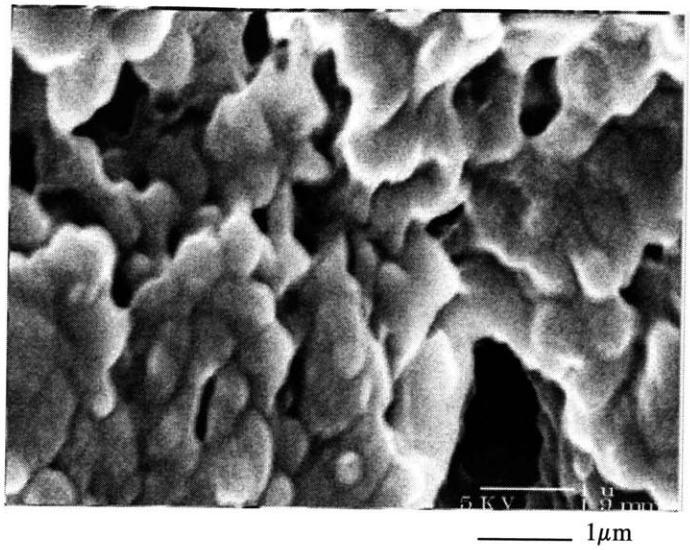

Figure 4-5: Highest possible resolution on a leached microstructure - showing homogeneous leached C-S-H structure.

Level II: Cement Paste

Figure 4-6 shows the typical appearance of a Portlandite crystal, that manifests itself at Level II. The Portlandite crystals are not always perfect as they fill existing pore spaces. A crystal size of several micrometers is typical. Figures 4-7 (a) through (d) display the typical features of the unleached microstructure at Level II. These micrographs were taken in an Environmental Scanning Electron Microscope (ESEM). Under an ESEM wet specimens can be studied which explains the different appearance of the microstructure. Figure 4-7(a) shows the homogeneous C-S-H matrix with a needle shaped appearance. Intermixed are Portlandite crystals that appear white and can be recognized by their hexagonal shape. A similar structure is visible in Figure 4-7(b) at a smaller magnification. Figures 4-7(c) and (d) show the compact structure of an unleached paste at Level II. Particularly, Figure 4-7(d) displays a large Portlandite crystal. It is characteristic for the material to have chunks of compact hydration products which also explains the pore size scale introduced in Chapter 2: The hydration products have an intrinsic (micro) porosity and the larger (macro) pores can be found between the compact assembly of hydration products, which form around a cement grain.

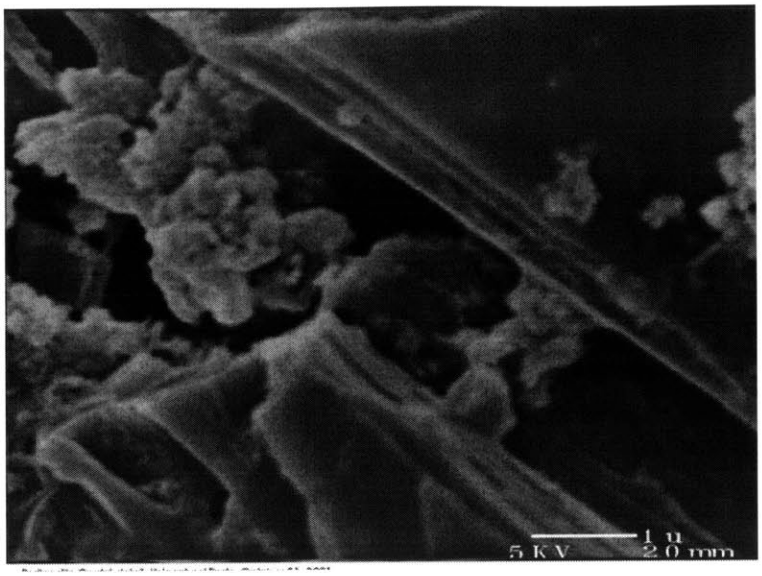

Figure 4-6: Portlandite crystals in an undegraded paste.

The microstructure at Level II when leaching occurred is very much changed. Figures 4-8 and 4-9 show the effect of the leaching process at Level II. Visibly, an additional "chemical" porosity is created as the Portlandite crystals are dissolved. A large density of new pores in the range of 100 nm is created, but also some pores in the micrometer range. Particularly the larger voids are created from the dissolution of the large Portlandite crystals such as the one shown in Figure 4-6. The characteristic texture of the unleached microstructure, i.e. the clusters of hydration products, has been largely eroded. Now, a more uniform washed-out appearance of the remaining microstructure prevails. This fits well with the known mechanisms of C-S-H decalcification presented in Chapter 2: As the C-S-H shift to lower C/S-ratios by dissolution and reprecipitation, the reprecipitation is not bound any more to the original hydration sites i.e. cement grains. The reprecipitated partially decalcified C-S-H form a more regular microstructure.

Level III

On Level III where the composite material is composed of paste, inclusions and ITZ, the main focus of our SEM analysis is the size and the structure of the ITZ. Figure 4-10 shows the

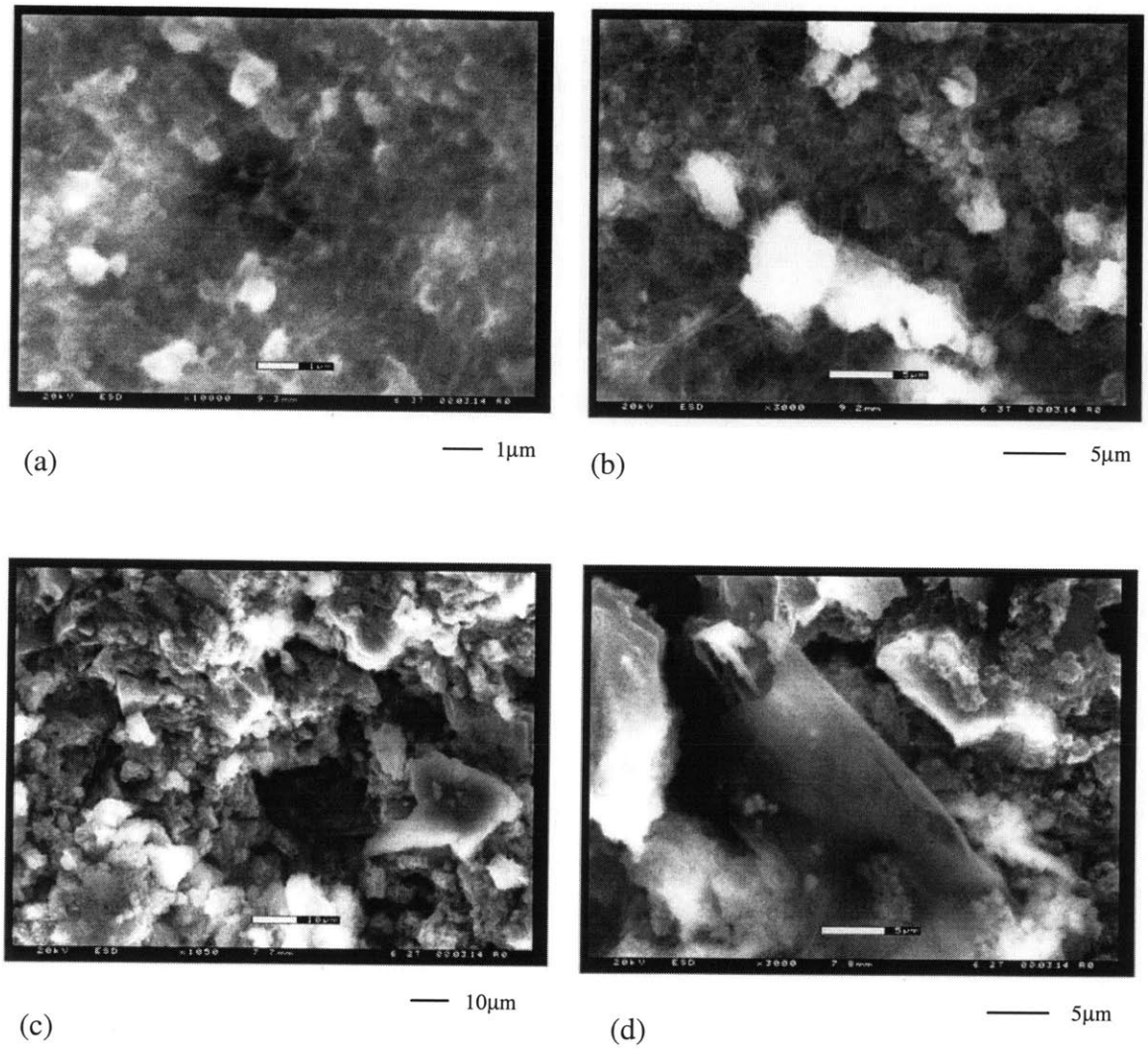

Figure 4-7: Appearance of the Level II microstructure. On (a) and (b) Portlandite crystals (white) are visible among C-S-H which is almost transparent in ESEM. On (c) at a larger scale multiple hydration product agglomerations are visible; in (d) a Portlandite crystal dominats the picture. These pictures were taken with an ESEM - for which no drying and surface treatment is necessary.

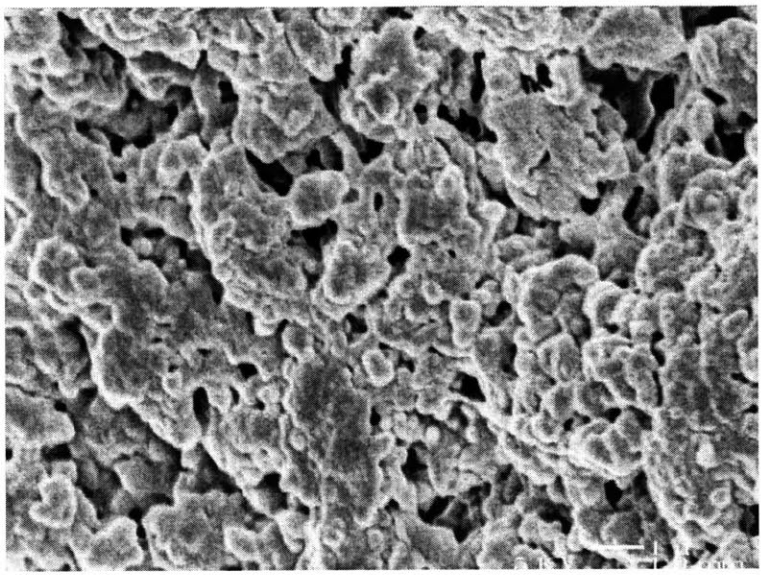

Figure 4-8: Typical microstructure of leached paste. (Level II).

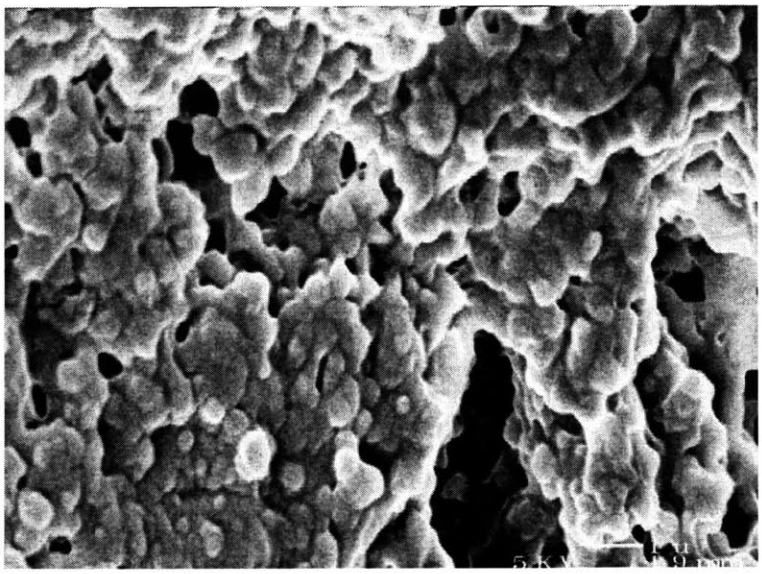

Figure 4-9: Porous microstructure of a leached paste.

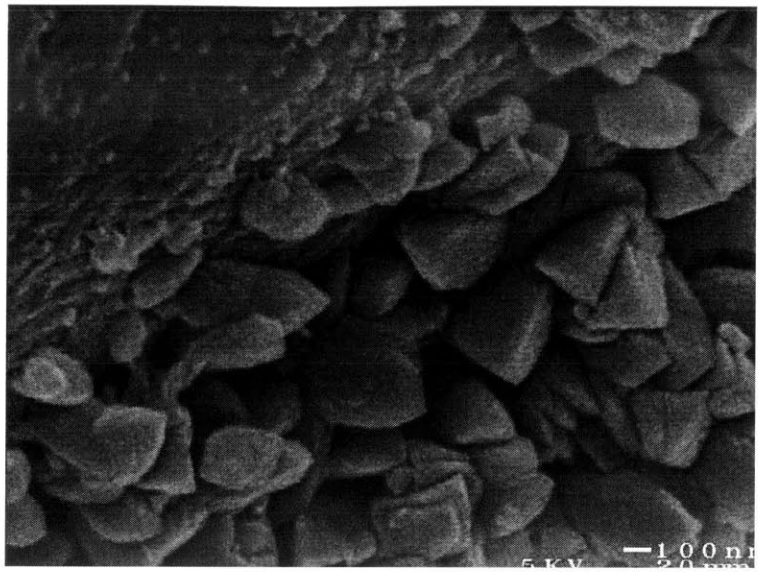

Figure 4-10: Interface between sand grain and paste in an unleached mortar.

appearance of the interface between a sand grain and the bulk paste in an unleached mortar. The increased porosity is difficult to be visualized on a plane section, but the wall effect close to the grain is visible in the packing of the hydration products close to the sand grain. The hexagonally shaped particles are Portlandite crystals. Figures 4-11 (a) through (d) show the appearance of the ITZ in a leached mortar. The four figures display, at increasing magnification, the same zone with a sand grain on the left side of the picture. Figure 4-11 (a) shows that the porosity close to the grain decreases away from the grain. The size of the ITZ can be estimated to be roughly 20 to 30 μm. The pores in the ITZ are mostly in the micrometer range (Figures 4-11 (a) through (d)). In terms of morphology, no preferential direction in pore orientation can be detected; and most of the pores can be described as spherical.

4.4 Concluding Remarks

The microstructural changes induced by leaching on the microstructure at Levels I through III relate primarily to a significant increase in porosity:

- Water-based porosity measurements show that calcium leaching creates an additional

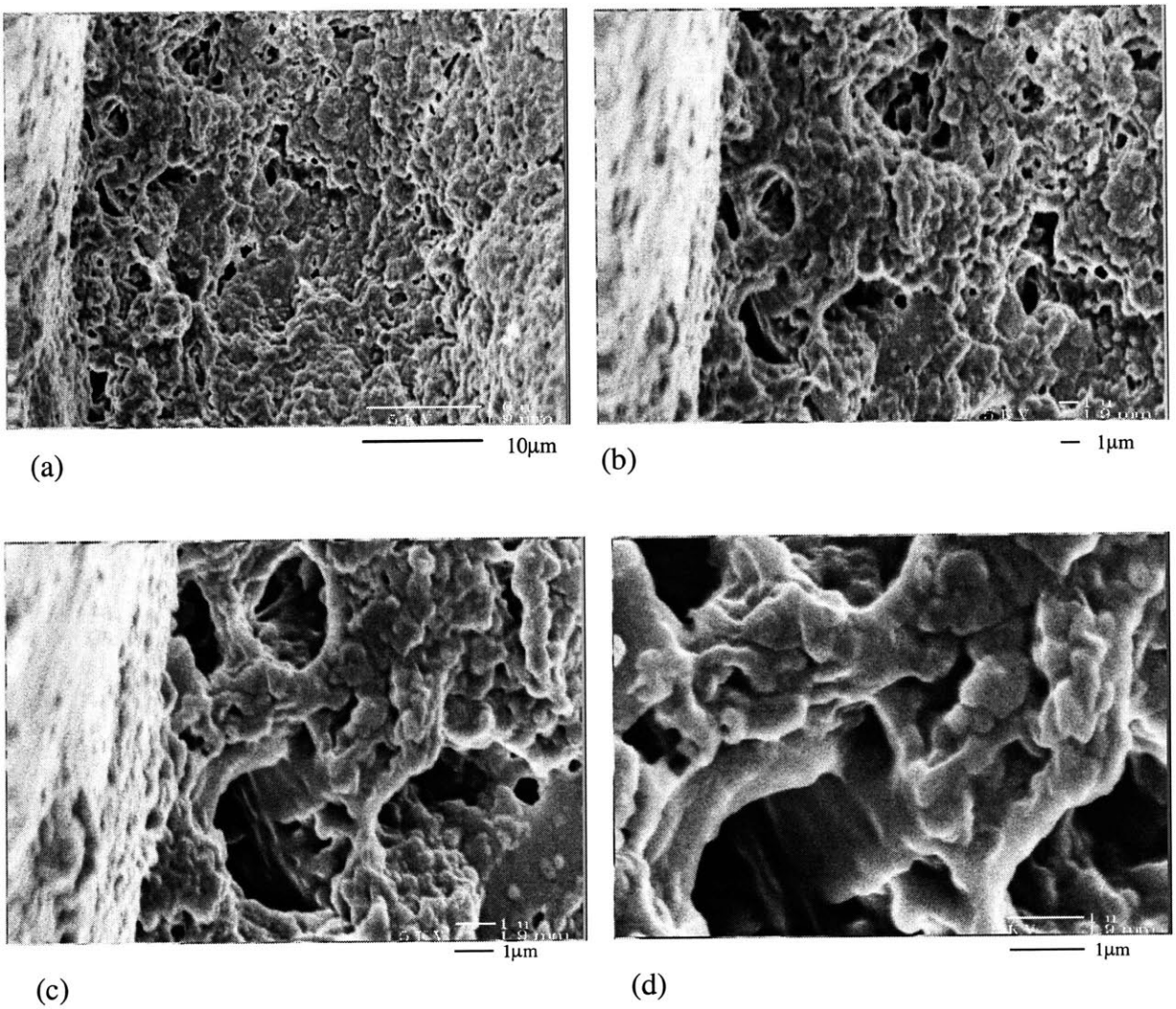

Figure 4-11: Series of micrographs at increasing magnification featuring the grain/matrix interface in the leached mortar (Level III). The sand grain is on the left in pictures (a) through (c).

chemical porosity of some 24 percentage points in a cement paste and 12 percentage points in a mortar.

- SEM micrographs provide evidence that leaching leads to a more homogeneous microstructure at Levels I and II. The initial appearance of the microstructure with distinctive particles originating from the fixation of the hydration around cement grains changes: The leached C-S-H matrix (Level I) is smoother and more compact owing to the more regular reprecipitation of the C-S-H at lower C/S-ratios. The dramatic change in porosity, however, occurs at Level II; partly due to the leaching of Portlandite, which exists as crystals in the undegraded paste, but also due to the volume loss of C-S-H. The new pores have micrometer size diameters, which are generally detrimental to the mechanical material properties.

- In leached mortars, SEM micrographs show an ITZ that has a characteristic size of 20 to 30 μm, based on the visual observation of the porosity distribution. Micrometer size spherical pores characterize the ITZ and make it, similarly to unleached cementitious materials, the weakest link in the composite material.

Chapter 5

Strength Behavior

This chapter presents the triaxial compression and uniaxial tension tests on leached cement pastes (Level II) and mortars (Level III). The goal of these tests is to construct the strength domain of leached cementitious materials[1]. First, the theoretical background and the hypothesis made during the test evaluations are presented. Then, the results from the triaxial compression tests are discussed. The chapter closes with the description of the tensile tests and a discussion of the corresponding results. Since extensive data on the strength of intact concretes under multiaxial stress states are available in the open literature (for example [47]), the strength domain of undegraded cementitious materials are not a priority in this study: Only for comparison to the leached materials, some tests are preformed.

5.1 Theoretical Background and Physical Quantities

This and the next chapter make extensive use of triaxial tests. A number of physical quantities are introduced in this section along with some elements of the mechanics of porous media [41], which we will use for the test interpretation.

5.1.1 Kinematics

For evaluation purposes of the triaxial tests, we consider the cement paste and mortar specimens as porous media composed of a solid and a saturated pore space. The initial volume of the

[1] A strength test for cementitious materials on Level I is currently not available - see Section 2.3.2.

porous medium, that is the specimen, is denoted by V_0, the solid volume by V_s and the fluid volume by V_f. The Lagrangian porosity ϕ, corresponds to the ratio of current fluid volume and the initial volume of the porous medium:

$$\phi = \frac{V_f}{V_0} = \frac{V - V_s}{V_0} \tag{5.1}$$

where V is the volume of the specimen in the deformed configuration. The mass conservation of the fluid phase leads to a relation between the change in fluid mass per unit initial volume and the change in porosity reading:

$$m_f - m_{f0} = \rho_f \phi - \rho_{f0} \phi_0 \tag{5.2}$$

where m_f and m_{f0} are the current and initial fluid mass per unit initial volume, respectively. ρ_f and ρ_{f0} denote the current and the initial fluid density. In the evaluation of the triaxial tests, relation (5.2) is used to convert the fluid mass measurements to porosity changes. The change in the solid volume can be expressed as:

$$\frac{dV_s}{dt} = \int_{V_s} \frac{d\varepsilon_v^s}{dt} dV \tag{5.3}$$

where ε_v^s denotes the volumetric strain in the solid. The change in porosity can be written taking the total time derivation of (5.1):

$$\frac{d\phi}{dt} = \frac{1}{V_0} \left(\frac{dV}{dt} - \int_{V_s} \frac{d\varepsilon_v^s}{dt} dV \right) \tag{5.4}$$

For the test evaluation we assume that the solid deformation is negligible:

$$\mathcal{H}1 : \frac{d\phi}{dt} \simeq \frac{1}{V_0} \frac{dV}{dt} \tag{5.5}$$

5.1.2 Conjugated Strain and Stress Measurements

The strains in the triaxial tests are evaluated with respect to the current configuration, leading to Euler strains, natural strains or logarithmic strains[2], identified by the superscript "ln". In particular, the volumetric strain is evaluated from:

$$E_v^{\ln} = \int_{V_0}^{V} \frac{dV}{V} = \ln \frac{V}{V_0} \tag{5.6}$$

The axial strain of a cylindrical specimen reads:

$$E_{zz}^{\ln} = \int_{L_0}^{L} \frac{dL}{L} = \ln \frac{L}{L_0} \tag{5.7}$$

The conjugated stresses to strain measurements can be determined from the external work rate which reads:

$$\frac{dW_{ext}}{dt} = \int_V \mathbf{\Sigma} : \mathbf{D} dV + p \frac{dV_f}{dt} \tag{5.8}$$

where $\mathbf{\Sigma}$ is the Cauchy stress tensor, $\mathbf{D}$ is the tensor of Euler strain rates, the integration of which leads to logarithmic strains, and p is the fluid pressure. Introducing the strain definitions (5.6) and (5.7) and assuming a cylindrical stress state characterized by a radial stress Σ_{rr} equal to the hoop stress $\Sigma_{\theta\theta}$ and an axial stress Σ_{zz}, (5.8) becomes:

$$\frac{dW_{ext}}{dt} = 2\Sigma_{rr} \frac{dE_{rr}^{\ln}}{dt} V + \Sigma_{zz} \frac{dE_{zz}^{\ln}}{dt} V + p \frac{dV_f}{dt} \tag{5.9}$$

or equivalently, dividing the work rate in a volumetric and a deviatoric part:

$$\frac{dW_{ext}}{dt} = (\Sigma_M + p) \frac{d\phi}{dt} V_0 + (\Sigma_{zz} - \Sigma_{rr}) \left(\frac{dE_{zz}^{\ln}}{dt} - \frac{1}{3} \frac{dE_v^{\ln}}{dt} \right) V \tag{5.10}$$

where we used (5.4) and (5.1).

[2] In a one-dimensional setting, natural strains are introduced via the integral of $\frac{dl}{l}$ considering the length change dl with respect to the current length l. The three-dimensional extension of this concept is due to Hencky [64].

5.1.3 Stress Evaluations

The Cauchy stress $\boldsymbol{\Sigma}$ is defined in the deformed configuration of the porous medium. To calculate the radial and axial stresses, Σ_{rr} and Σ_{zz}, during the test, the deformed section of the cylindrical specimen is determined. Two cases are distinguished:

1. Under hydrostatic loading, for which $\Sigma_{zz} = \Sigma_{rr} = \Sigma_{\theta\theta}$, the cylindrical shape of the specimen is preserved. The ratio between current and initial volume reads:

$$\frac{V}{V_0} = \frac{R^2 L}{R_0^2 L_0} \tag{5.11}$$

where R and L are the current radius and length, respectively, while R_0 and L_0 are the corresponding values in the initial configuration. Using assumption (5.5), the current radius can be determined from the porosity measurements and the length change measurement according to:

$$R = \sqrt{\frac{(1 - \phi + \phi_0)\, R_0^2 L_0}{L}} \tag{5.12}$$

where ϕ_0 is the porosity in the initial configuration. With the updated radius at hand, the vertical stress can be readily computed from the vertical force F, that is $\Sigma_{zz} = F/\pi R^2$.

2. Following hydrostatic loading, a deviatoric loading is applied. In this deviatoric loading, the cylindrical shape of the specimens is not preserved. Instead, the deformed longitudinal shape is observed to be parabolic. In this case, the radius becomes a quadratic function of the vertical coordinate. We note R_{ref}, L_{ref} and ϕ_{ref} the radius, length and porosity at the onset of the deviatoric loading. The maximum radius in the center of the specimen reads:

$$\frac{R_{\max}}{R_{top}} = \frac{1}{4}\left(\sqrt{30\frac{V}{V_{ref}} \times \frac{L_{ref}}{L} \times \left(\frac{R_{ref}}{R_{top}}\right)^2 - 5} - 1\right) \tag{5.13}$$

where R_{top} is the radius at the top of the specimen. This radius is assumed not to change during the deviatoric loading. The ratio between current and reference volume is evaluated, using (5.4) and (5.5):

$$\frac{V}{V_{ref}} = 1 + \frac{\phi - \phi_{ref}}{1 + \phi_{ref} - \phi_0};\ \frac{R_{ref}}{R_{top}} = 1 \tag{5.14}$$

Combining (5.13) and (5.14) yields:

$$\frac{R_{t,\max}}{R_{ref}} = \frac{1}{4}\left(\sqrt{30\left(\frac{1+\phi-\phi_0}{1+\phi_{ref}-\phi_0}\right)\times\frac{L_{ref}}{L}-5}-1\right) \tag{5.15}$$

The magnitude of the vertical Cauchy Stress in the specimen center is then calculated from the vertical load applied during the deviatoric loading

$$\delta F_z = \pi R_{t,\max}^2\left(\Sigma_{zz}-\Sigma_{zz,ref}\right) \tag{5.16}$$

with $\Sigma_{zz,ref} = \Sigma_{rr} = \Sigma_{\theta\theta}$ the mean stress at the end of a prior hydrostatic loading ($\Sigma_{rr} = \Sigma_{\theta\theta}$ held constant during deviator loading). "δ" indicates the change in a parameter after the hydrostatic loading phase is concluded.

5.2 Triaxial Compression Tests

The behavior of leached cementitious materials under multiaxial stress states which is of interest in many critical civil engineering applications, is largely unknown. A convenient way of assessing the strength and deformation properties in multiaxial stress states is the use of triaxial tests.

5.2.1 Test Design

The triaxial test device in this study is adapted from common configuration in the MIT Geotechnical Laboratory. In the triaxial test, cylindrical specimens are tested and a radial stress is applied by a pressurized fluid along with a vertical force. Figures 5-1 (a) through (c) display the triaxial equipment used in this test series. It consists of a steel chamber filled with silicon oil and seated on a brass base and a steel shaft with an internal load cell on its end (Figures 5-1 (a) and (b)). The movement of the base is controlled and used for displacement driven tests. The vertical shaft connects through a steel ball on the upper side to the external frame, guaranteeing a moment free connection (Figure 5-1 (a)). The interior of the steel chamber is sealed to the bottom by an o-ring which gets compressed by the four bolts that attach the steel chamber to its base. On the top, the shaft passes through an O-ring seal. The details of the specimen connection are shown in Figure 5-1 (c). On the top of the specimen a half

Device	Range	Resolution	Stability
Axial Strain LVDT	5 cm	$\pm 1 \times 10^{-4}$(0.1 mV)	$\pm 1 \times 10^{-3}$(1 mV)
Volumetric LVDT	45 cm^3	$\pm 1 \times 10^{-4}$(0.1 mV)	$\pm 1 \times 10^{-3}$(1 mV)
Cell Pressure Transducer	35 MPa	3×10^{-4} MPa(0.001 mV)	3×10^{-3} MPa(0.01 mV)
Load Cell 1	44.59 kN	0.2 N(0.001 mV)	2 N(0.01 mV)
Load Cell 2	17.27 kN	0.2 N(0.001 mV)	2 N(0.01 mV)

Table 5.1: Transducer characteristics as measured by the data acquisition system. The resolution and stability calculations for the LVDT are based on dimensions of an average specimen (Length 23 mm and diameter 11.5 mm).

sphere-shaped steel end connects to the specimen. Its curved side is received by another steel end with a hallow half sphere shape. The upper steel cap connects to the load cell through a pressure contact. On the bottom of the specimen, a porous stone made of steel is placed. It is there for draining purposes which will be detailed later. The porous stone sits on a hollow steel cylinder. Through this cylinder, an exterior water entrance is connected. The hollow steel cylinder itself is placed in a steel base (see Figure 5-1(b)). The seal is assured by an O-ring in the base. The specimen and the additional elements are placed in a latex tube[3], and the exterior stress is applied by the oil pressure. The latex material is impermeable to oil and any water in the specimen.

The change in fluid mass per unit volume, $m_f - m_{f0}$, is measured in the experimental setup at the end of the fluid mass supply tube that connects to the bottom of the specimen. The change in fluid mass is measured as a volume change via an LVDT (Linear Variable Differential Transformer) transducer with infinite resolution. Through the fluid mass supply, the pore pressure p is also measured via a pressure transducer. The oil pressure in the cell is measured with an identical pressure transducer. The imposed vertical displacement δu_z (displacement controlled test) is measured through an additional LVDT transducer at the bottom of the cell. The characteristics of these devices and of the internal load cell are summarized in Table 5.1. Figure 5-2 displays the different quantities measured during a test. The high pressure triaxial test system includes two data acquisition systems. A local system is used for test control purposes while a central system is used for the data storage. The local system makes use of an analog-to-digital conversion card, which allows the control of the testing procedure based on

[3]Latex tube purchased as gastronomic tubing through McMaster Carr, N.J.

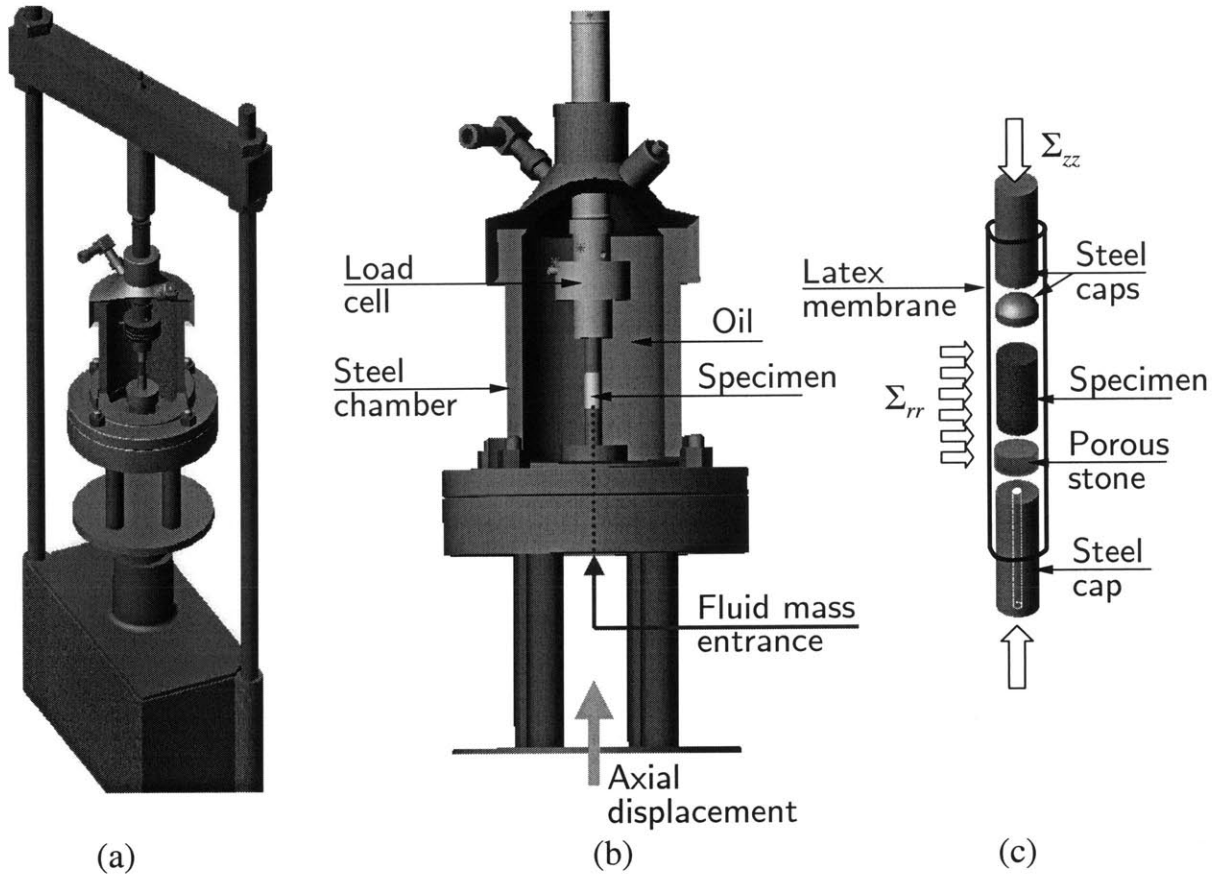

Figure 5-1: View of the triaxial cell assembly.

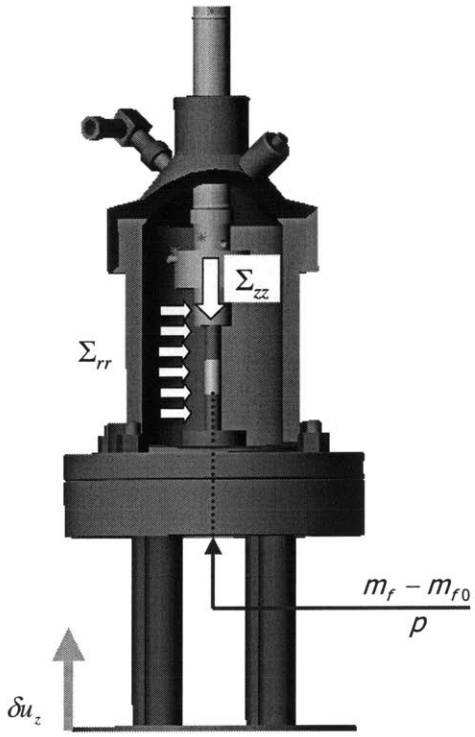

Figure 5-2: Scheme of the different measured and prescribed test characteristics.

specially in the MIT geotechnical lab written testing software [133].

The test device allows carrying out tests under different fluid pressure - fluid mass conditions:

- In a drained test, the pore pressure is kept constant at $p = p_0$, and fluid is extracted from or pushed into the specimen to keep the pressure constant. The corresponding change in fluid mass is recorded and converted into a change in porosity according to relation (5.2).
- In an undrained test, the fluid supply is closed and the change in fluid mass is zero. The pore pressure can still be measured but because of the deformability of the tubing and transducers and pressure losses at connections, the measured values always underestimate the real fluid pressure in the specimen. Since no change in fluid mass is measured, the change in porosity is not accessible in an undrained test.

5.2.2 Testing Procedure

To construct the strength domain, deviatoric loading tests at increasing confinement are performed. In these tests, the deviatoric stress (i.e. the difference between radial and vertical stress $|\Sigma_{zz} - \Sigma_{rr}|$) is increased at the same time as the confinement, expressed by the magnitude of the mean stress, $\Sigma_M = \frac{1}{3}\text{tr}\boldsymbol{\Sigma}$, is increased. Both invariants are governed by a displacement controlled increase in the vertical stress while the radial stress, which is equal to the cell pressure, is kept constant.

An important parameter in the tests is the loading velocity. In order to have a truly drained test, the fluid pressure has to remain constant throughout the specimen. This implies that a certain loading rate must not be exceeded which allows the specimen to equilibrate the pore pressure. In a preliminary test on leached and unleached pastes, the necessary total testing time was determined following the procedure suggested by Bishop and Henkel [21], which is based on the consolidation theory by Terzaghi [143]. In hydrostatic compression, a pressure p^0 was applied and the subsequent volume change was measured over time. From the recorded curve, volume change over square root of time, the time for 100% consolidation can be determined along with the consolidation coefficient c_v, which takes into account the drainage conditions (i.e. drainage on one side through the porous stone). Then following consolidation theory, a time for failure t_f is determined which needs to be respected in the tests in order to obtain drained test

Specimen	Time to failure
undegraded	10.6 days
degraded	4.2 hours

Table 5.2: Time to failure necessary according to the consolidation theory for a drained test.

results. Table 5.2 gives the t_f values for the degraded and undegraded paste specimens. From the value for the degraded specimen we deduce a loading strain rate of $\left|\dot{E}_{zz}\right| = 5\times10^{-6}\,\mathrm{s}^{-1}$ which is kept constant throughout the test series. We assume that the drainage in mortars is at least as good as in cement paste so that the same loading rate is being used. From the time to failure for undegraded materials it appears that a drained test for these materials is difficult to realize: During tests of a duration of several days or weeks, creep effects would become important, which may suggest that there is some connection between creep and drainage conditions for the undegraded saturated pastes. In this series, the tests on undegraded specimens where run at the same strain rate as the degraded ones, which means that they cannot be considered completely drained.

The loading steps in the deviatoric tests involves two loading phases:

1. A proportional pore pressure–hydrostatic stress loading is applied first. The pore pressure p is monitored through the fluid mass, and the hydrostatic stress Σ_M^{hyd} through the cell pressure device. The specimen is kept at constant consolidation pressure during 15 hours to allow secondary compression to take place. During this hydrostatic loading, the logarithmic volume strain is evaluated from (5.6) and the current specimen radius from (5.12).

2. A deviatoric loading part is then applied, during which the cell pressure is kept constant, while an additional axial load $\delta F < 0$ is applied until failure of the specimen. During this second loading phase, the confinement[4] increases. The logarithmic strains are evaluated according to (5.6) and (5.7) while the current radius is determined from (5.15). The reference radius corresponds to the radius at the end of the hydrostatic loading phase. Failure of the specimen occurs in the specimen center and the stresses are determined from (5.16).

[4]Confinement designates the magnitude of the mean stress Σ_M.

	Paste		Mortar	
	Initial	Degraded	Initial	Degraded
Friction Coefficient δ [1]	0.82	0.56	1.02	0.81
Cohesion c [MPa]	17.11	1.15	9.82	0.96
Cohesion pressure $\rho = \frac{c}{\delta}$ [MPa]	20.87	2.06	9.63	1.19

Table 5.3: Experimentally determined Drucker-Prager strength parameters of unleached and leached cement pastes and mortars [Drained test results].

5.2.3 Results

The failure points of the leached materials in drained tests are shown in Figures 5-3 (a) and (b) in a $|\Sigma_{zz} - \Sigma_{rr}| \times \Sigma_M$ plane. The deviatoric stress at failure increases with increasing confinement, showing that the leached materials are mean-stress sensitive, that is they are frictional materials. The dependence of deviatoric strength and confinement is linear. In the chosen stress space, the linear dependence between deviatoric stress and mean stress is described by a Drucker-Prager criterion which reads:

$$F(\boldsymbol{\Sigma}) = \begin{cases} \sqrt{J_2} + \delta\left(\Sigma_M - \rho\right) \leq 0 \\ \sqrt{J_2} + \delta\Sigma_M - c \leq 0 \end{cases} \tag{5.17}$$

where $\sqrt{J_2} = \sqrt{\frac{1}{2}\mathbf{S}:\mathbf{S}} = \sqrt{\frac{1}{3}} \times |\Sigma_{rr} - \Sigma_{zz}|$ is the second invariant of stress deviator $\mathbf{S} = \boldsymbol{\Sigma} - \Sigma_M\mathbf{1}$ in the triaxial test. δ is the friction coefficient while ρ is a cohesion pressure which corresponds to the mean stress for which no deviatoric stress can be supported. In turn, c which is equal to the product $\delta \times \rho$, is called the cohesion and corresponds to the deviatoric stress in a mean stress free experiment. Note that the cohesion pressure is an extrapolated value into the tensile mean stress domain. Its validity needs to be verified in subsequent tensile tests. Table 5.3 summarizes the parameters for the Drucker-Prager strength envelope resulting from the drained tests on leached pastes and mortars as well as for the unleached pastes and mortars.

In undrained tests, the strength performance of the leached materials is very different. Figure 5-3(a) shows the results for undrained tests on cement pastes: The deviatoric stress at failure is virtually constant for all mean stress levels. The frictional capacity that was present in the drained loading case vanished. It is important to note, that the stress evaluation in

undrained tests cannot be based on true Cauchy stresses because of the experimental setup described above: As the fluid mass supply to the specimen is closed for an undrained test, the volumetric deformation cannot be measured and the area correction according to (5.15) is not possible. The displayed stresses are therefore Boussinesq stresses (i.e. related to the initial configuration). In the case of a uniaxial compression test in which $\Sigma_{rr} = 0$, the drained and undrained results should actually match which gives a good idea of the difference between Cauchy and Boussinesq stresses. In the case of the leached mortar, Figure 5-3(b) shows the undrained test results. For low confinement pressures, $\Sigma_M \geq -2\,\text{MPa}$, the mortars show some frictional behavior. When the confinement increases, the deviator loading capacity remains constant. It is likely that the initial frictional behavior is an artifact due to entrapped air in the mortar. Indeed, the analysis of a saturation curve for leached mortars showed that complete saturation is reached at $\Sigma_M \simeq -1.6\,\text{MPa}$[5].

Results from drained tests at different pore pressure levels are shown in Figure 5-4. The pore pressure ranges from $p = 0$ to $p = 9\,\text{MPa}$. Figure 5-4 shows three examples of such test results for $p = 3$, 6 and 9 MPa. Correcting the mean stress Σ_M at failure by the applied pore pressure, that is $\Sigma'_M = \Sigma_M + p$, the obtained strength values in the $|\Sigma_{zz} - \Sigma_{rr}| \times \Sigma'_M$ plane, align on the same straight line of the drained test carried out at $p = 0$ (i.e. Fig. 5-3(b)). In terms of the Drucker-Prager yield surface, we have:

$$F(\boldsymbol{\Sigma}) = \sqrt{J_2} + \delta\,(\Sigma_M + \beta p - \rho) \leq 0 \tag{5.18}$$

where β is the Coussy coefficient [41]. The obtained results displayed in Figure 5-4 show that $\beta = 1$ for calcium depleted cement paste materials. This phenomenon is referred to as effective stress concept and applies here at failure.

[5]The incomplete saturation is only of concern in undrained loading situations in which no volume changes are determined. In drained loading cases, the saturation is guaranteed by the initial saturation phase.

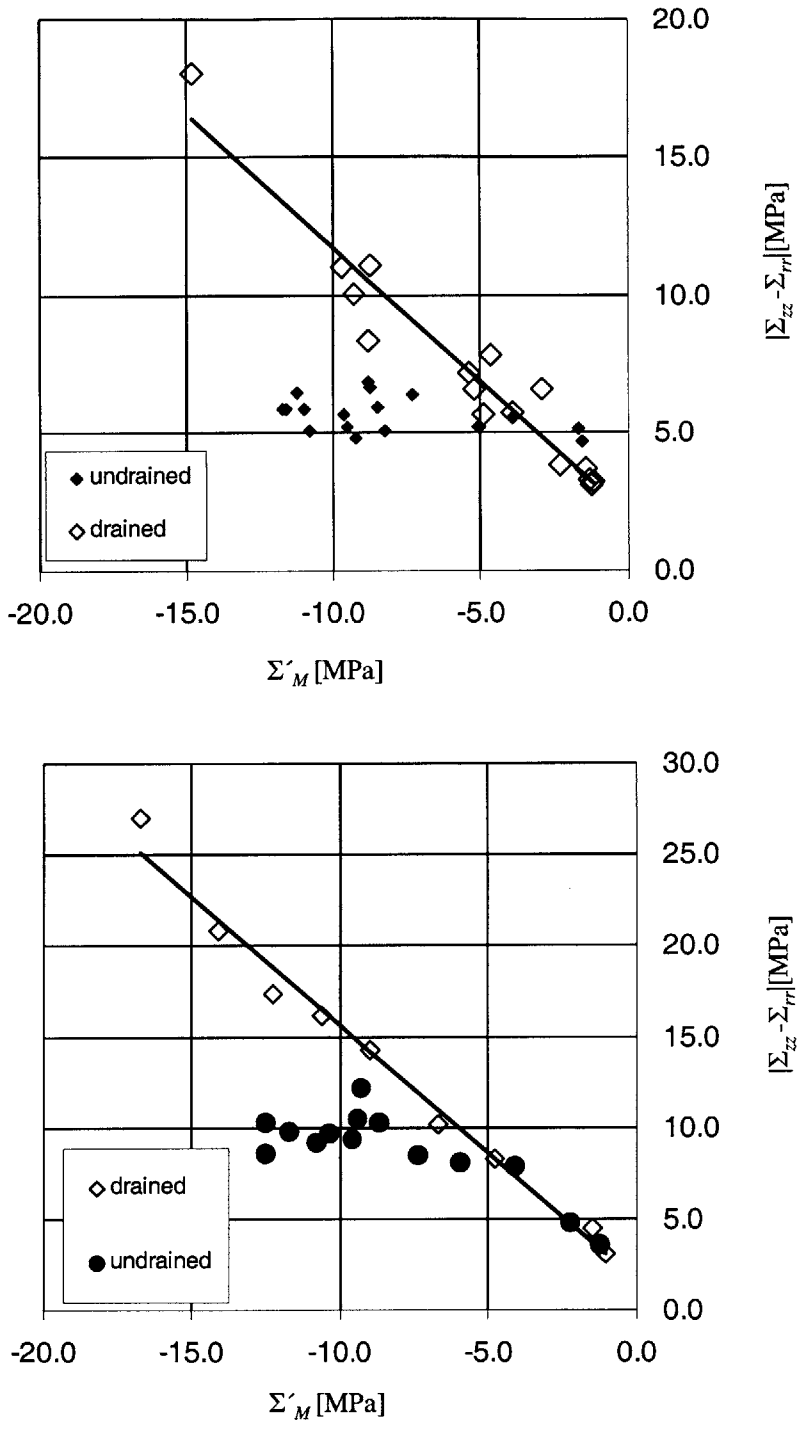

Figure 5-3: Ultimate strength for the degraded materials: (a) cement paste, (b) mortar.

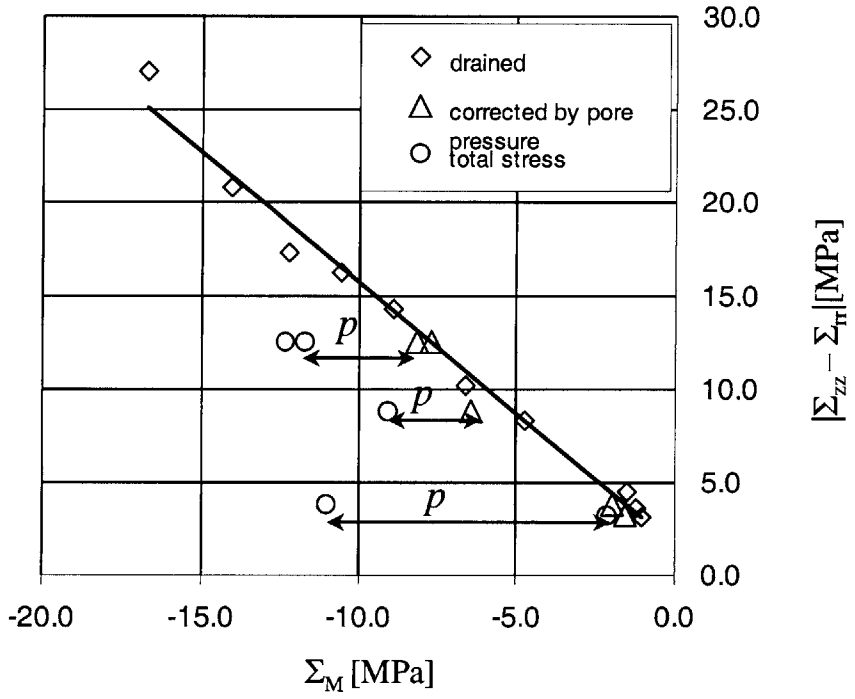

Figure 5-4: Drained triaxial strength tests on calcium depleted mortars with different constant pore pressures: measured total stresses and pore pressure corrections.

5.2.4 Discussion

Drained Strength

From the drained tests on leached pastes and mortars we note that the degradation effect is specifically strong on the cohesion pressure (Table 5.3): Both the mortar and the cement paste lose almost 90% of their initial cohesion pressure although the porosities are very different in both materials (see Table 4.3). This indicates that the changed C-S-H matrix properties (Level I) are more likely the source for this chemical decohesion rather than the change in porosity, which is to the largest part due to Portlandite dissolution. This confirms suggestions by Faucon et al. [51] and Pellenq et al. [113] based on statistical mechanics simulations of the C-S-H microstructure (Level "0"): Reducing the C/S-ratio (as is the case for leaching) empties the interlayer void space of the C-S-H and affects their electronic charge which in turn reduces the cohesion. Mortars have a lower cohesion pressure than the paste which can be attributed to the influence of the ITZ.

By contrast, the degradation of the friction coefficient is more pronounced for the cement paste which loses 32% of its initial friction coefficient while it is only 21% for the mortar. This suggests that the influence of the ITZ on the friction coefficient of leached mortars is not as detrimental as the mere increase in porosity in these zones might suggest. The generally higher friction coefficient for mortar that is observed for both the leached and unleached materials is due to the advantageous presence of the aggregates: The ITZ is compressed under the increasing confinement and deactivated. The relatively larger difference in frictional capacity for the leached materials ($\frac{\delta_{paste}}{\delta_{mortar}} = 0.69$ for leached and 0.8 for unleached materials) shows that this is even more true for the leached materials in which the ITZ is particularly porous. Figure 5-5 recalls this with an SEM micrograph.

Effective Stress Concept and Undrained Strength

The drained tests with varying pore pressures show that the effective stress concept applies at failure. The level of pore pressure, p, determines how much of the applied mean stress is effectively acting on the material. The validity of the effective stress concept offers an explanation for the undrained results on the leached paste and mortar, displayed in Figure 5-4.

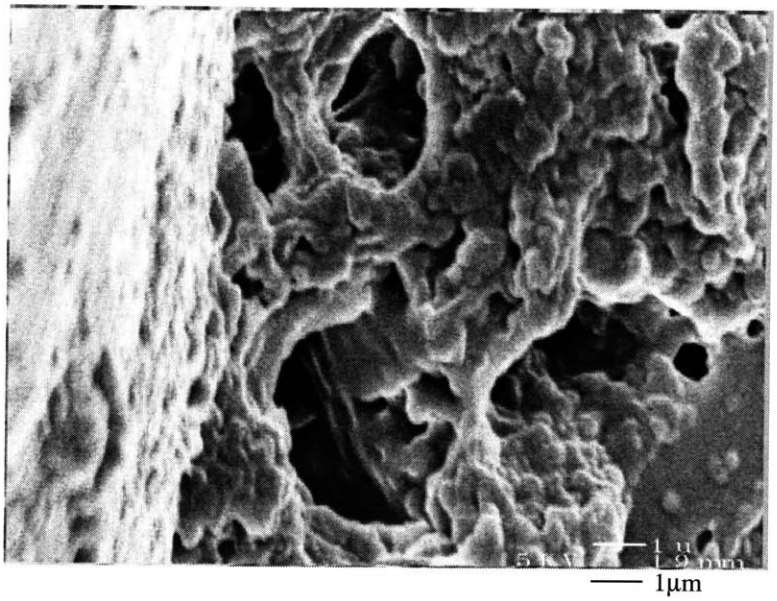

Figure 5-5: SEM Micrograph of the ITZ in a leached mortar.

The constant undrained deviatoric strength suggests that the pore pressure, p, in undrained tests, rises with the externally applied mean stress Σ_M such that the effective mean stress $\Sigma'_M = \Sigma_M + p = -1.5\,\mathrm{MPa}$ at all times. Figure 5-6 shows the Mohr plane of the undrained tests and the change in pore pressure associated with it. To illustrate the undrained behavior of the leached materials, we make a rough estimate of the pore pressure increase with applied external loading. A more refined analysis of the poromechanical properties of unleached and leached materials is developed in Chapter 7. In a very first approach, we consider a poroelastic material for which the state equations read (see e.g. [41]):

$$\Sigma_M = k_0 E_v - bp \tag{5.19}$$

$$\phi - \phi_0 = bE_v + \frac{p}{\mathtt{M}} \tag{5.20}$$

$$\mathbf{S} = 2\mu \mathbf{E}_d \tag{5.21}$$

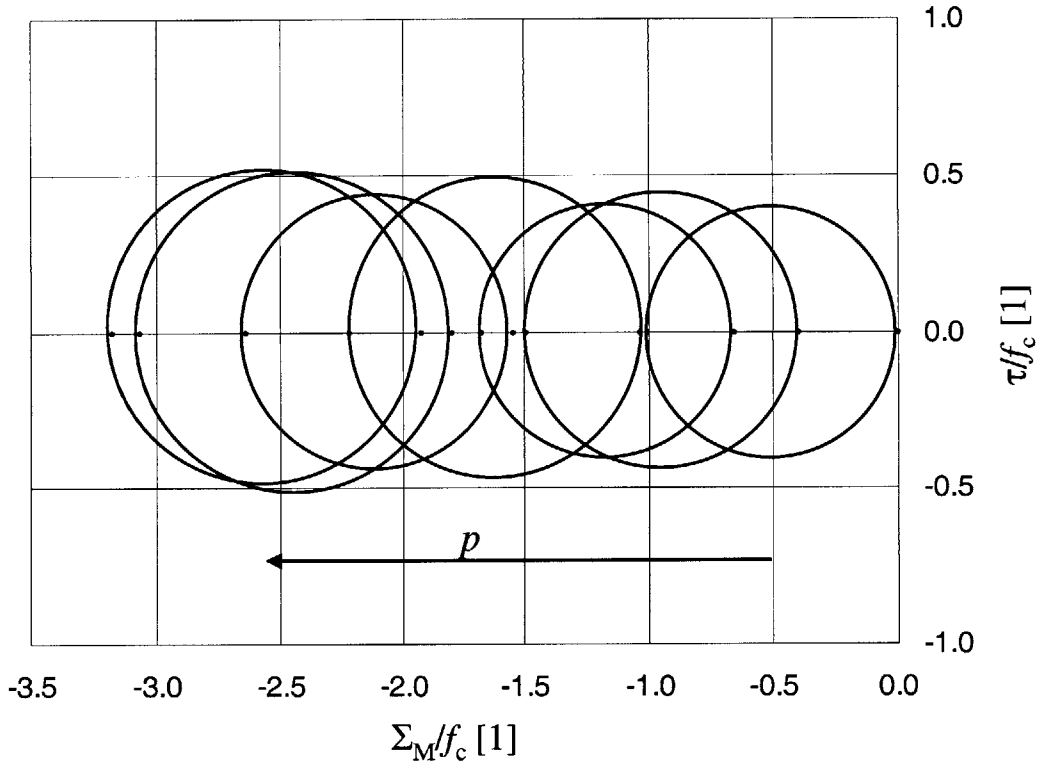

Figure 5-6: Representation of the undrained tests on cement paste in the Mohr plane. The circles correspond to the tests shown in Figure 5-3(a). Results normalized by the uniaxial compressive strength $f_c = 3.0\,\mathrm{MPa}$.

where b is the Biot coefficient which describes the relation between the stress and the pore pressure under constant deformation. Terzaghi's [143] effective stress concept corresponds to b=1. M is the Biot modulus which characterizes the relation between the pressure and the porosity change under constant deformation. k_0 is the drained bulk modulus of the porous medium. Both parameters, b and M, can be linked to the compressibility of the solid phase of the porous medium k_s [41]:

$$b = 1 - \frac{k_0}{k_s} \tag{5.22}$$

$$\frac{1}{\mathtt{M}} = \frac{b - \phi_0}{k_s} \tag{5.23}$$

In addition, the linearized state equation of the fluid reads:

$$\frac{p}{k_f} = \frac{\rho_f}{\rho_{f0}} - 1 \tag{5.24}$$

where k_f is the fluid bulk modulus and where we assume that ρ_{f0} is the reference density for which the pressure is zero. Combining (5.24) and (5.2) we can relate pressure, porosity change and mass change:

$$\frac{m_f - m_{f0}}{\rho_{f0}} = \frac{\rho_f \phi}{\rho_{f0}} - \phi_0 = \phi \left(\frac{p}{k_f} + 1 \right) - \phi_0 \tag{5.25}$$

which we can rewrite for the change in porosity:

$$\phi - \phi_0 = \frac{m_f - m_{f0}}{\rho_{f0}} - \phi \frac{p}{k_f} \tag{5.26}$$

In the case of an undrained experiment, $m_f - m_{f0} = 0$. The relation between porosity change and pressure then reads:

$$m_f \equiv m_{f0} : \phi - \phi_0 = -\phi \frac{p}{k_f} \tag{5.27}$$

Finally, a combination of (5.20) and (5.27) yields the following expression for the volume strain in the undrained experiment:

$$m_f \equiv m_{f0} : E_v = -\frac{p}{b} \left(\frac{\phi}{k_f} + \frac{1}{\mathtt{M}} \right) \tag{5.28}$$

Inserting (5.28) into (5.19) delivers the following ratio of mean stress to fluid pressure:

$$\frac{-\Sigma_M}{p} = \frac{k_0}{b}\left(\frac{\phi}{k_f} + \frac{1}{\mathtt{M}}\right) + b \tag{5.29}$$

The inverse of this expression is known as the Skempton coefficient [135, 20, 22] and is denoted by $B = -p/\Sigma_M$, which quantifies the amount of the macroscopically applied mean stress Σ_M which is carried in an undrained test by the saturating fluid pressure. To evaluate B further, and thus the pressure sensitivity of the material, we employ the homogenization theory that Kendall et al. [75] applied to the Young's modulus of porous materials:

$$k_0 = k_s(1-\phi)^3 \tag{5.30}$$

A combination of Equations (5.29) and (5.30) yields:

$$\frac{1}{B} = 1 - \left(1 - \frac{k_s}{k_f}\right)\frac{\phi(1-\phi)^3}{1-(1-\phi)^3} \tag{5.31}$$

Figure 5-7 shows B versus porosity for two different k_s/k_f-ratios. The lower value, $k_s/k_f = 2$ (with $k_f = 2.3\,\mathrm{GPa}$ and $k_s = 2.7\,\mathrm{GPa}$ from [37]), corresponds roughly to the value of a degraded cement paste, while the upper value $k_s/k_f = 7$ (with $k_s = 16\,\mathrm{GPa}$ from [37]) to the one of the intact cement paste. The figure presents the two parameters which govern the pressure sensitivity of cementitious materials: the porosity ϕ (taken here as total porosity because Kendall's model does not distinguish different porosities) and its increased value through leaching, and the skeleton-to-fluid bulk modulus ratio k_s/k_f which reflects the strong chemical softening. This analysis is only a first approach, but it offers an explanation for the observed strength behavior in undrained test, which is highly pressure sensitive.

5.3 Tensile Tests

This section presents original results from tensile tests on leached and unleached cement pastes and mortars. The tensile tests complete the construction of the strength domain for the leached materials.

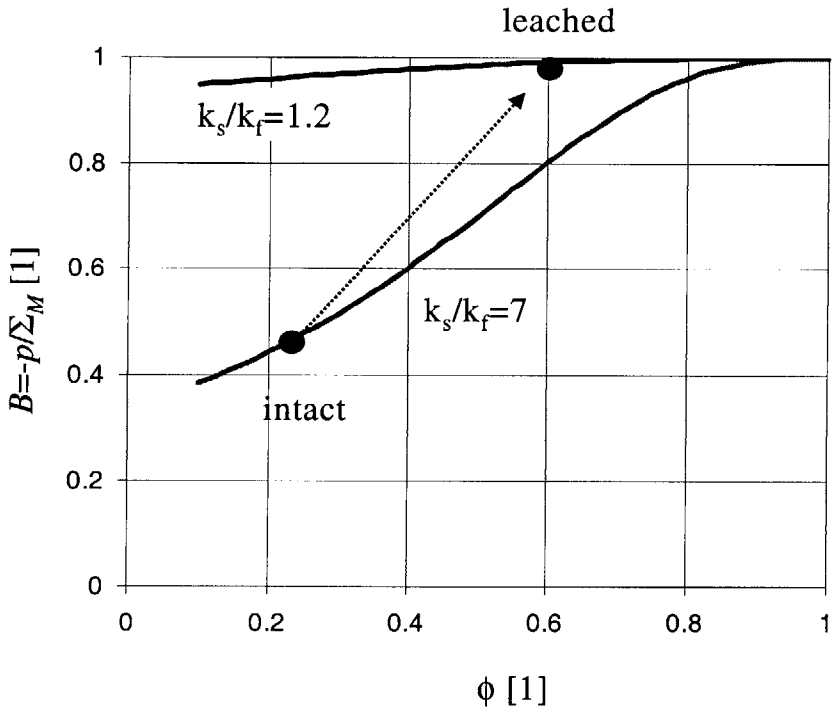

Figure 5-7: Evolution of the Skempton coefficient with porosity and bulk moduli ratio.

5.3.1 Tensile Test Design

Tensile tests on cementitious materials are particularly difficult to perform. In general, three different types of tests are used:

1. Brazilian test, which is also known as "Standard Test Method for Splitting Tensile Strength of Cylindrical Concrete Specimens" [6]. In this test, a cylindrical specimen is compressed by a lineload along its longitudinal axis. It is then supposed to fail in tension. Under an elastic material law assumption, the tensile stress that leads to failure is determined. The test gives relatively consistent results but suffers from the need to assume an elastic material behavior: As cementitious materials behave non-elastically, the determined value is not a true material property [104]. Hence the explicit statement of the way the material was tested when the strength from such a test is reported.

2. Three-point or Four-point bending test [9], in which a beam that is supported on both ends and is loaded with either a load in the middle (three-point) or two loads (four-point), one at every third of the beam span. From the force that is required for the beam failure, a tensile strength is deduced, invoking beam theory and again an elastic material behavior. Therefore in the same way as for the Brazilian test, when the obtained strength value is reported, the way it was tested has to be mentioned.

3. Direct tension test, which is potentially the best way of testing the tensile strength of cementitious materials. As the name suggests, a specimen is held on two sides and a tensile stress is applied. However, the execution of this test is difficult as problems have to be overcome such as [104]: Connection of the ends that involve inhibited lateral displacements and/or energy dissipation and inhomogeneous stress states, due to unwanted bending.

In the selection of our own testing equipment, the problems of each of the described testing methods were considered. In addition, the limitation in specimen size, given by long time periods that are necessary for calcium leaching, was important. This second aspect and the desire to avoid assumptions about the material law lead to the development of our own direct tension equipment. Figure 5-8 shows the dimensions of the specimens. The critical size is the diameter in the middle where failure should occur. This diameter has to be carefully chosen

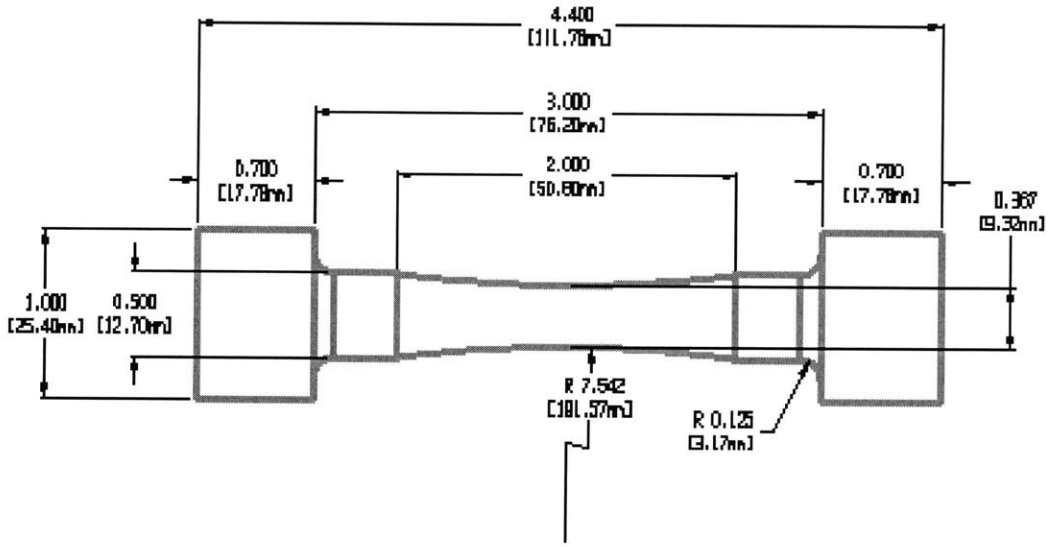

Figure 5-8: Dimensions of the used tensile specimen.

with respect to leaching time and homogeneity of the material. In our case, the dimension is about $D = 12.5\,\text{mm}$ which is close to the dimension of the cylinders used in the triaxial compression tests.

5.3.2 Specimen Preparation

To manufacture the specimens, a two part mold was produced from a two component epoxy[6]: An acrylic glass specimen of the desired shape for the final specimens was put in an aluminum cylinder, filled with the two component epoxy and hardened. Cutting the hardened epoxy in two halves then gave the mold. Figure 5-9 shows a picture of one part of such a mold. Before the specimens are cast, the molds are oiled and clamped in the two part aluminum hollow cylinder. Then the paste or mortar are poured carefully into the mold, vibrating slightly the mold on the vibration table to evacuate macropores from the material. During the hydration of cementitious materials, a reduction in volume of about 10% takes place. This phenomenon is also called the "Le Chatelier-effect" and is related to the incorporation of the water into the hydration products

[6]The two component epoxy was a 3120 RTV Silicone Rubber from Corning, supplied through Motion Industries, Inc., Birmingham, AL 35222.

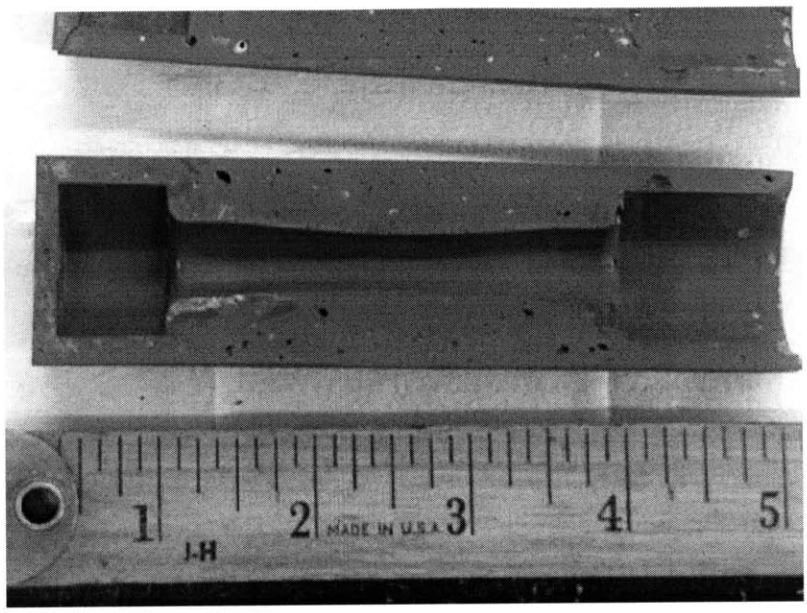

Figure 5-9: Photograph of one part of the tensile mold. The yard stick units are inches. 1 in=2.54 cm .

at a density higher than $1,000\,\mathrm{kg}\,/\,\mathrm{m}^3$ [141], [66]. The volume reduction translates in the given mold design to a contraction in the middle part of the specimens, resulting in tensile stresses as the ends are not free to move. If no additional measures were taken, the tensile stresses would exceed the tensile strength and the specimen would fail. To avoid this, a curing procedure was designed that consists of 18 hours curing of the specimen with a small compressive load applied after 5 hours, and further curing in a lime solution. The 18 hour curing time was chosen to have specimens sufficiently cured that they can be removed from the mold, but also to avoid maximum tensile stresses which develop after this time, as a finite element based calculation of the curing process showed[7]. The compressive load is applied after 5 hours in three steps to 200 N which corresponds to a compressive stress of 1.6 MPa . After the demolding process, the specimens are cured for at least 28 days in the lime solution, just as for the compressive test cylinders. The leaching procedure for the tensile specimens was identical to the cylindrical specimens. No protection was put on the specimen to avoid interfaces between leached and

[7]The finite element code "Heat"[125] was used to perform this calculation.

Device	Range	Resolution	Stability
Axial Strain LVDT	5 cm	$\pm 1 \times 10^{-4}$(0.1 mV)	$\pm 1 \times 10^{-3}$(1 mV)
Clip on extensometer	2.5 cm	$\pm 5 \times 10^{-6}$(0.1 mV)	$\pm 5 \times 10^{-5}$(1 mV)
Load Cell	892.7 N	0.013 N(0.001 mV)	0.13 N(0.01 mV)

Table 5.4: Transducer characteristics as measured by the data acquisition system for the tensile test.

unleached material which would have become preferred places of failure.

5.3.3 Test Equipment

The tension test equipment is shown in Figures 5-10 and 5-11. It is composed of two aluminum ends that each consist of two pieces that receive the specimen (Figure 5-11), which are closed by a set screw. The aluminum ends are bigger than the specimen and hence do not clamp laterally the specimen. The aluminum ends are connected to a universal joint[8], guaranteeing an automatically centered alignment of the specimen. In this way, one of the problems mentioned above (that is inhibited lateral displacements and energy dissipation if specimens were glued), is minimized. In addition, the three dimensionally curved specimens have no abrupt changes in diameter which avoids stress peaks. Hence failure takes place in the middle zone. The tensile force is measured through a 890 N-load cell in which one of the universal joints is screwed. The displacements are measured at the end of the lower universal joint with an LVDT transducer and in addition with a clip on extensometer that has a 2.5 cm base length (see Figure 5-10). The characteristics of theses three devices is shown in Table 5.4. The tests are conducted displacement driven at a strain rate of $2 \times 10^{-6}\,s^{-1}$ based on the extensometer reading. The testing machine operates at a constant rate and no feedback between the extensometer reading and the machine was given. Failure takes place therefore abruptly in a brittle manner without the softening behavior that is often reported for cementitious materials after the peak load [104].

[8]Standard catalogue piece from McMaster-Carr, N.J.

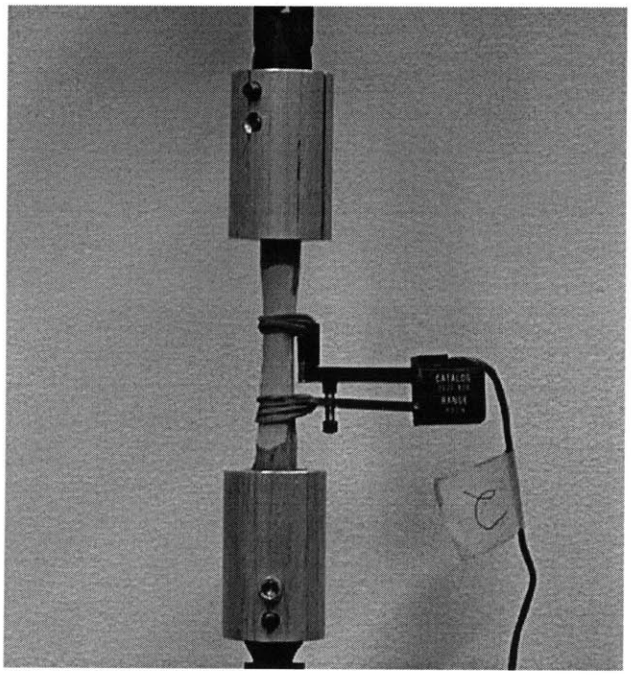

Figure 5-10: Tensile testing equipment: Aluminum ends, univeral joint and clip on extensometer.

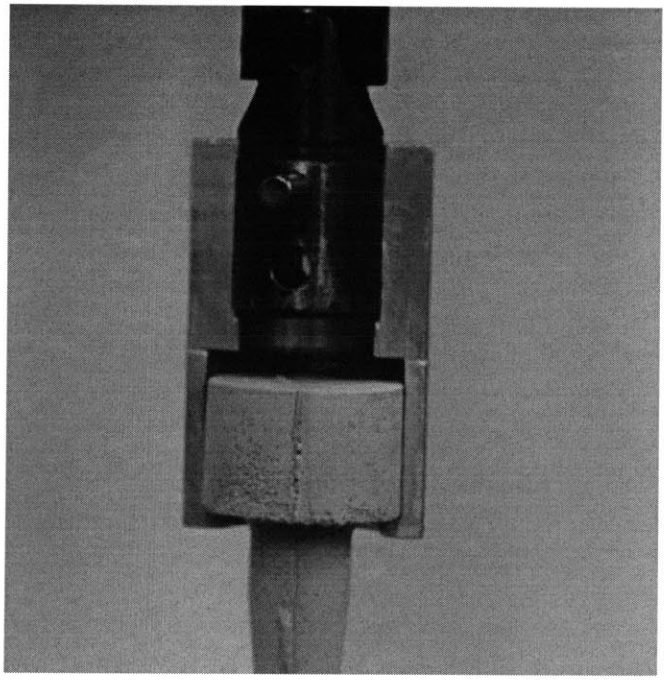

Figure 5-11: Detail of the aluminum ends connected to the universal joint. Note the horizontally free movement of the specimen in the end.

	Mortar		Paste	
Test Results	Intact	Degraded	Intact	Degraded
(a) Tensile Strength [MPa]	3.48	0.94	1.87	0.87
(b) Standard Deviation [MPa]	0.26	0.19	0.31	0.04
(c) Variation (=b/a)[-]	0.075	0.203	0.165	0.042
Number of tests	10	8	7	9

Table 5.5: Tensile test results.

5.3.4 Results

The results of the tensile tests are given in Table 5.5. The tensile strength is determined by dividing the maximum tension force by the measured area of the failure surface. The average tensile strength of the undegraded mortar is 3.48 MPa which is a typical value for mortars [104]. The variation of 7.5% is very good for tensile tests and reflects a well working test set-up. The undegraded paste has a tensile strength of 1.87 MPa, which is considerably smaller than the mortar. In the degraded state, the paste has a tensile strength that is reduced by 50%. Interestingly, the strength variation is reduced to around 4% which is very low for tensile tests on cementitious materials. Finally, the degraded mortar has virtually the same tensile strength as the degraded paste but a much higher variation.

5.3.5 Discussion

The difference in tensile strength for the unleached materials (cement paste versus mortar) is caused by the presence of the sand grains in the mortar that increase the strength through crack arresting and deviation. The energy required for crack growth is increased. Figures 5-12(A) and (C) show through an optical microscope the failure surface of the undegraded paste and mortar, respectively. The much rougher texture of the mortar failure surface can be recognized easily and confirms the suggested crack deflections around the grains as sources of higher tensile strength. This effect, in unleached materials, is apparently more important than the presence of the ITZ, which is a preferred origin of crack initiation. The variability of the test results on undegraded paste is more than twice as high as on the mortar which reflects a higher variability of the microstructure. Failure in both mortar and paste does not always occur exactly in the middle of the specimen. However, the variation in failure loci is of the same magnitude as the strength variations. This suggests that the failure locus variations are associated with actual

material variations and not associated with testing errors [99].

Figure 5-12(B) shows the failure surface of a leached paste and underscores that the leaching process leads to a more homogeneous material at Level II. The tensile strength of the degraded mortar is very similar to the paste strength, although the failure surface texture is much rougher (Figure 5-12(D)). The similar strength of the leached paste and mortar suggests that the ITZ dominates the mortar strength in the leached state: The beneficial presence of the aggregates has disappeared. It seems that the crack propagation is not hampered by the sand grains due to the already weak surrounding interface. The fact that the decrease in tensile strength through leaching is stronger for the mortar than for the paste shows that besides a general chemical softening of the material, a different failure mode through the particular porous ITZ is at work.

5.4 Combined Compression - Tension Strength Domain and Concluding Remarks

From the triaxial compression tests and the tension test we retain the strength domain for leached cement pastes and mortars. In the compression zone, the Drucker-Prager surface with the values summarized in Table 5.3 describes the strength domain. The extrapolation of the compressive triaxial strength results (Table 5.3) into the tensile domain ($\Sigma_M > 0$) would predict higher tensile strengths than measured. This leads us to conclude that a single criterion is not sufficient to describe the complete strength domain in the deviator-mean stress space. Instead, we propose a second Drucker-Prager surface which covers the compression - tension transition zone. This includes all stress states for which the mean stress is greater than in uniaxial compression. Figure 5-13 shows the two surface combination in a $\sqrt{J_2}/c_i \times \Sigma_M/c_i$ plot for the undegraded paste and mortar The parameters of this second Drucker-Prager surface are summarized in Table 5.6. They are based on a linear interpolation between the uniaxial compression and tensile strength using:

$$c = \frac{2}{\sqrt{3}} \frac{f'_c f'_t}{f'_c + f'_t} \quad \delta = \sqrt{3} \frac{f'_c - f'_t}{f'_c + f'_t} \tag{5.32}$$

In addition to obtaining the strength domain for leached pastes and mortars some other

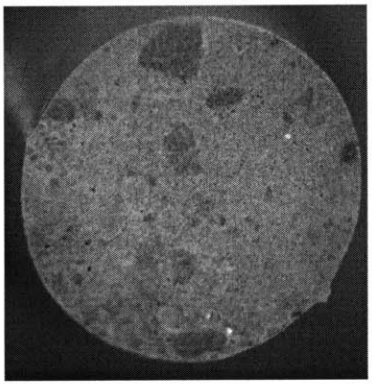

(A) Undegraded Paste

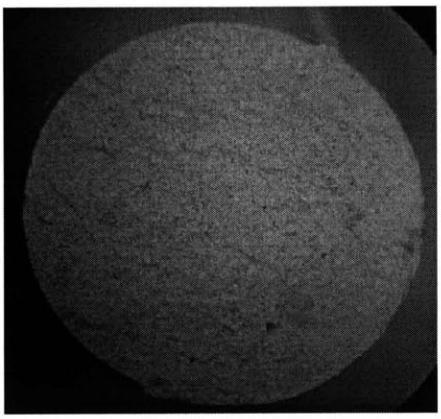

(B) Degraded Paste

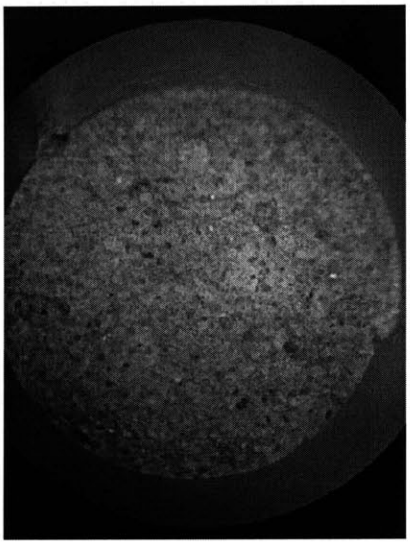

(C) Undegraded Mortar

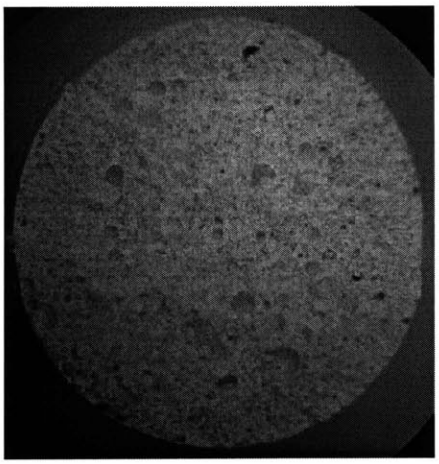

(D) Degraded Mortar

Figure 5-12: Optical microscope images of the failure surfaces from tensile tests. The diameters are roughly 9 mm.

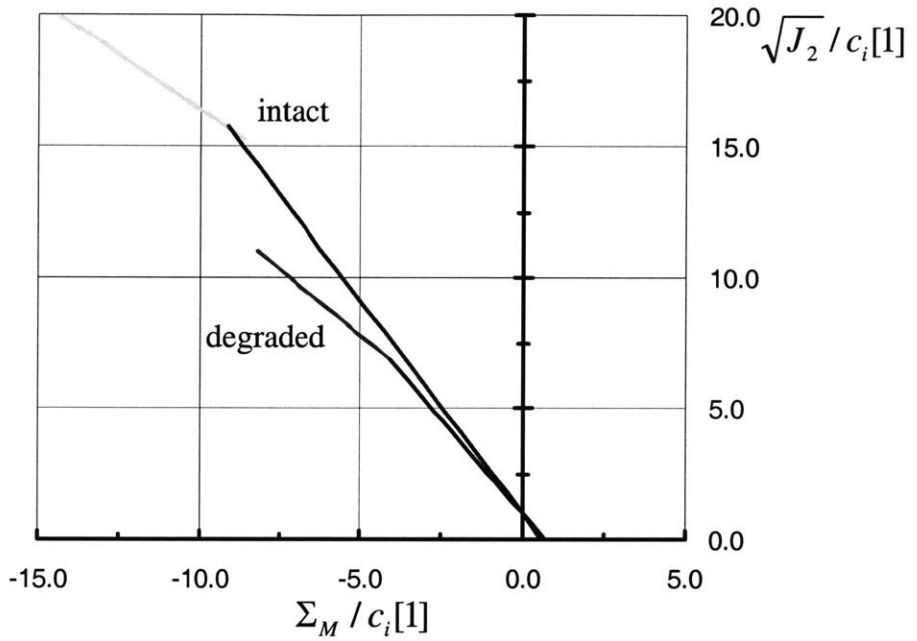

Figure 5-13: The combination of the two Drucker-Prager failure surfaces for the undegraded paste and mortar, stress normalized by the cohesion c_i, i=mortar or cement paste.

	Paste		Mortar	
	Initial	Degraded	Initial	Degraded
Uniaxial Tensile Strength f'_t [MPa]	1.87	0.87	3.48	0.94
Uniaxial Compressive Strength f'_c [MPa]	54.1	3.2	36.6	3.0
Friction Coefficient δ [1]	1.62	0.99	1.43	0.91
Cohesion c [MPa]	2.09	0.79	3.67	0.83
Cohesion pressure $\rho = \frac{c}{\delta}$ [MPa]	1.29	0.80	2.57	0.91

Table 5.6: Drucker-Prager strength parameters for the compression-tension transition zone.

conclusions can be drawn from the strength results:

- The strong reduction of the frictional capacity through leaching shows that in structural applications, the mechanical performance of leached parts will deteriorate significantly. At the same time, the changes for mortars and pastes are not identical, pointing towards the influence of the aggregates.

- The pressure sensitivity at failure and the pore pressure build-up in undrained tests lead to a vanishing frictional performance. This means that for practical purposes in any fast loading application, say undrained conditions, on leached pastes no friction can be considered.

- The combination of a lower cohesion value for the leached mortars compared to the pastes and a higher friction coefficient suggests that the role of the ITZ on the mechanical properties changes with the level of confinement. While the cohesion describes the strength performance at low confinement levels for which the ITZ is significant, the frictional behavior which characterizes the strength in higher confinements is less influenced by the ITZ which might have already been crushed. This will be further investigated in Chapter 6.

Chapter 6

Deformation Behavior

This Chapter is devoted to the experimental study of the deformational behavior of asymptotically leached cement pastes (Level II) and mortars (Level III). The deformational behavior on Level II and III complements the knowledge about the strength domain of leached materials from Chapter 5 in view of a complete material description. We present the results from triaxial compression tests and the uniaxial tension tests, this time with a focus on deformational properties. The operation of the testing devices is exactly as described in Section 5.1 and the same relations and physical quantities are employed in the discussion of the test results.

6.1 Loading Path in Triaxial Compression Tests

For the deformational behavior, only drained tests are performed because the measurement of the fluid mass change in the specimen is necessary to evaluate the volumetric strains . In addition to the deviatoric compression tests presented in the strength study, two other types of tests are performed with the objective to obtain a good picture of the inelastic deformation properties. The three types of tests that are performed are:

1. Hydrostatic compression test; in which $\Sigma_I = \Sigma_{II} = \Sigma_{III} = \Sigma_M$;

2. Deviatoric loading tests at increasing confinement. In these tests, the deviatoric stress ($\sqrt{J_2} \propto |\Sigma_{zz} - \Sigma_{rr}|$) is increased at the same time as the confinement, expressed as the negative mean stress, $\overline{p} = -\Sigma_M = -\frac{1}{3}\mathrm{tr}\boldsymbol{\Sigma}$, is decreased. This type of test was also used

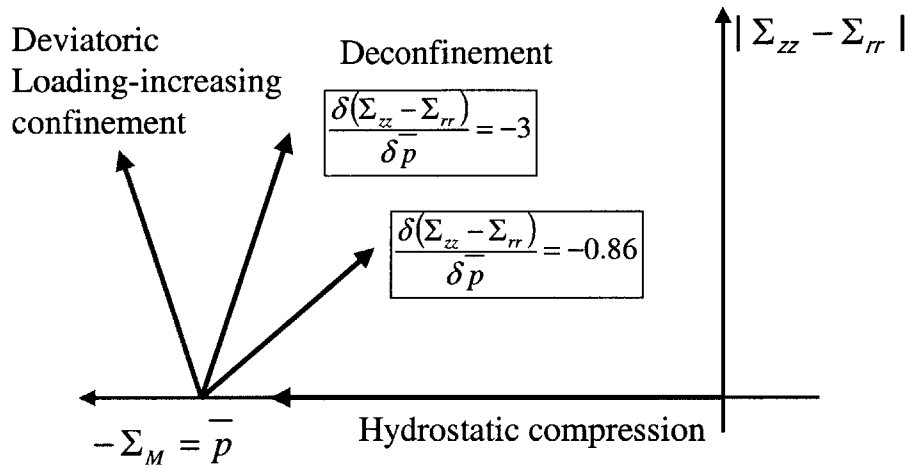

Figure 6-1: Schematic representation of the different loading paths for the drained tests.

in the strength investigation.

3. Deviatoric loading tests at decreasing confinement, $\overline{p}$. In this kind of test, after a hydrostatic loading, the deviatoric stress is increased, while at the same time the confinement, $\overline{p}$, is reduced.

Figure 6-1 gives a schematic view of the three test types and their loading paths in the $|\Sigma_{zz}-\Sigma_{rr}| \times \Sigma_M$ halfplane. The strain measurements and stress calculations are made using the relations developed in Section 5.1. The loading steps in the different tests types are the following:

- In the hydrostatic compression tests, the pore pressure (if any) is prescribed first, and kept constant during subsequent hydrostatic loading. The loading rate is $\left|\dot{\Sigma}_m\right| \simeq 5$ kPa/s,

which corresponds to strain rates close to the required $\left|\dot{E}_{zz}\right| = 5 \times 10^{-6}\,\mathrm{s}^{-1}$, which was determined in Section 5.2.2 based on drainage times. The maximum applied cell pressure is $\Sigma_M = -10$ MPa.

- The deviatoric loading tests with increasing confinement are performed as described in Chapter 5 and involve first the hydrostatic loading phase, followed by the application of the deviatoric stress through the additional force $\delta F < 0$ (δ denotes the change of a parameter after the hydrostatic loading phase) until failure of the specimen.

- In the deviatoric loading test at decreasing confinement, first a hydrostatic pressure, Σ_M^{hyd}, is applied along with a pore pressure p, identical to the deviatoric loading test at increasing confinement. In the second loading phase, however, a deviatoric load is applied at the same time as the confinement is reduced. This is achieved in a combined deformation-stress controlled test, in which the stress ratio $\gamma = \delta(\Sigma_{zz} - \Sigma_{rr})/\delta\overline{p}$ is kept constant. The change in deviatoric stress is provoked by an axial displacement at a rate of $\left|\dot{E}_{zz}\right| = 5 \times 10^{-6}\,\mathrm{s}^{-1}$, and the radial stress is adjusted via the computer controlled system to remain on the prescribed loading path. Two stress paths are followed after the hydrostatic compression to $\Sigma_M^{hyd} \approx -10\,\mathrm{MPa}$: In the first, the deconfinement ratio is $\gamma = -0.86$; in the second, $\gamma = -3$.

Based on the partition of the infinitesimal external work increment in Eq. (5.10), we present the results in the following three type of result plots:

1. The natural axial strain, $\delta E_{zz}^{\ln} = \ln(L_t/L_{ref})$, over the natural volumetric strain, $\delta E_v^{\ln} = \ln(1+\phi-\phi_{ref})$. These results provide insight into the importance of the shear work term in Eq. (5.10).

2. The deviatoric stress, $\Sigma_{zz} - \Sigma_{rr} = \delta\Sigma_{zz}$, over the natural deviatoric strain, $\delta E_{zz}^{\ln} - \frac{1}{3}\delta E_v^{\ln}$. These results provide evidence of the deviatoric deformation patterns of the calcium leached materials.

3. The change in mean stress, $\delta\Sigma_M = \Sigma_M - \Sigma_M^{hyd} = \delta\Sigma_{zz}/3$, over the change in porosity $\delta\phi = \phi - \phi_{ref}$, where ϕ_{ref} is the porosity at the end of the hydrostatic loading phase.

These results provide insight into the volumetric deformation behavior, featuring either contracting ($d\phi < 0$) or dilating behavior ($d\phi > 0$). In addition, these results give an evaluation of the volumetric work term in relation (5.10).

6.2 Hydrostatic Compression Tests

6.2.1 Results

The results from a typical drained hydrostatic compression test on a leached mortar and paste are displayed in Figure 6-2 in the form of the mean stress Σ'_M versus the change in Lagrangian porosity $\phi - \phi_0$. At low confinement pressure, the mortar has a higher deformability than the cement paste, but for high confinement it is the inverse:

- The cement paste follows an $s-$shaped hardening: after an initial elastic phase, the tangent stiffness decreases first. Then, at higher confinement pressure, the material stiffens (increase of tangent stiffness).
- The mortar stiffens continuously from above, meaning that the tangent stiffness $d\Sigma_M/d\phi$ increases continuously in hydrostatic compression.

Figures 6-3(a) and 6-3(b) show results from a series of hydrostatic loading and unloading tests. They illustrate that the overall stiffening of both materials is irreversible: the slopes of elastic loading-unloading increase for both materials with increasing confinement.

6.2.2 Discussion

SEM Micrographs show the expansion of the solid into the pore space[1]. The deformation behavior under hydrostatic compression can be illustrated with SEM micrographs on compressed specimens (Figs. 6-4 (a) - (c) and Figs. 6-5 (a) and (b)). Before loading, the microstructure of leached pastes is characterized by large pores created by the Portlandite dissolution and a relatively homogeneous microstructure composed of C-S-H (Level I) that dissolves and reprecipitates at a low C/S-ratio close to 1 (see Sections 2.3.2 and 4.3). Figures 6-4 (a) through

[1] *Throughout the discussion, the main idea of a paragraph is stated in italics to facilitate the reading.*

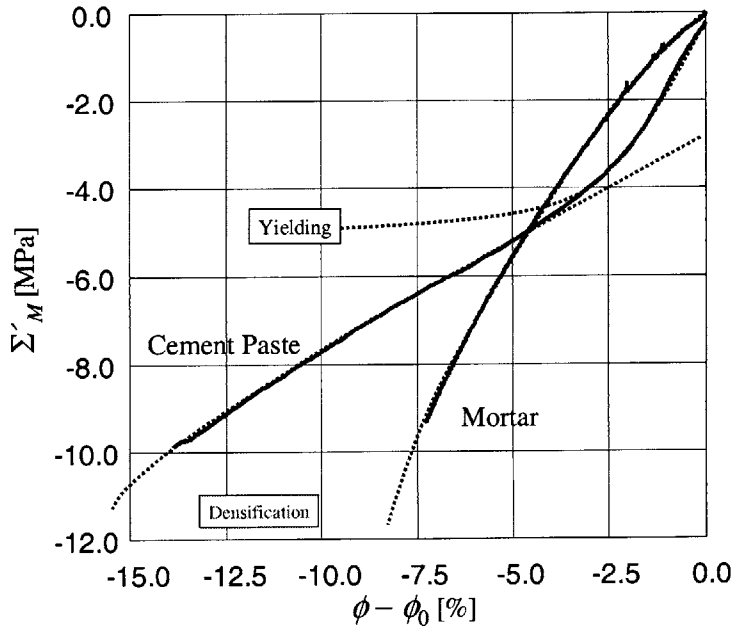

Figure 6-2: Results from drained hydrostatic compression tests. The constant pore pressure in these tests is $p = 0.5\,\mathrm{MPa}$. The dotted lines correspond to the extrapolated individual physical deformation mechanisms discussed

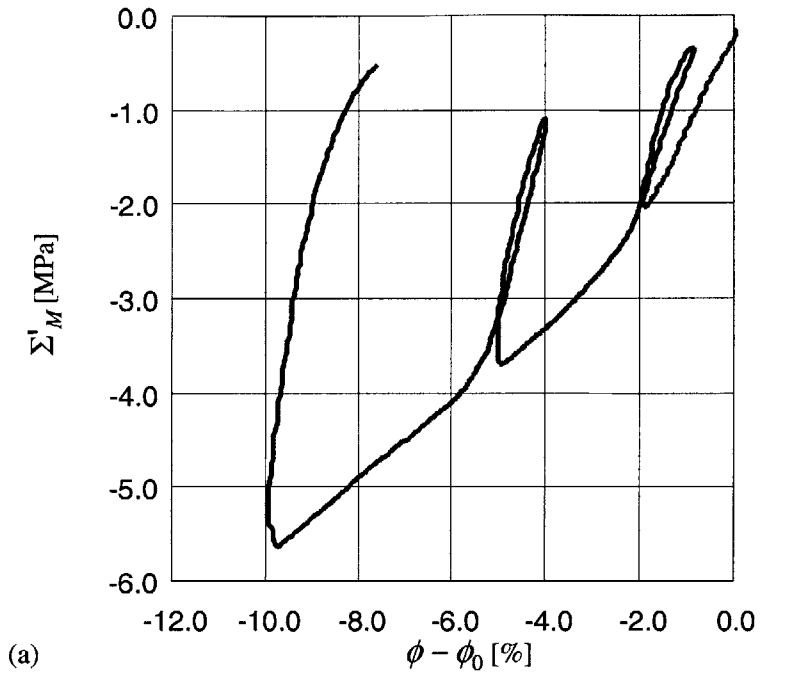

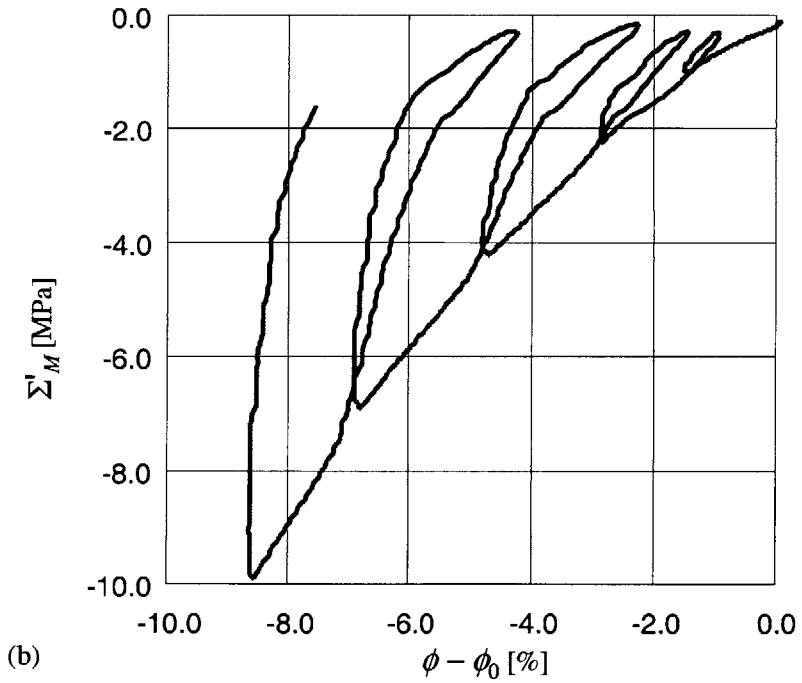

Figure 6-3: Hydrostatic compression loading-unloading cycles on (a) cement paste and (b) mortar. The pore pressure is constant at $p = 0.5\,\mathrm{MPa}$.

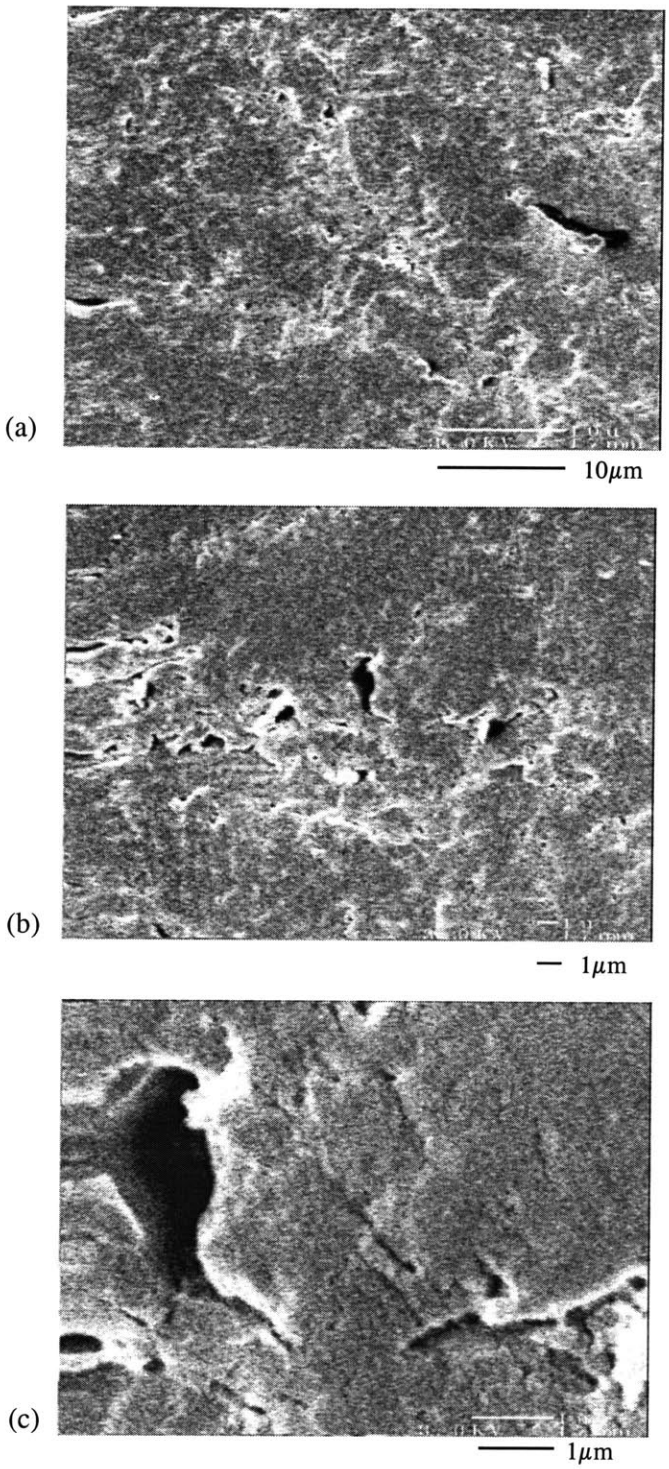

Figure 6-4: SEM micrographs of a hydrostatically compressed leached cement paste. $\Sigma'_M = -9\,\mathrm{MPa}$. $p = 0.5\,\mathrm{MPa}$.

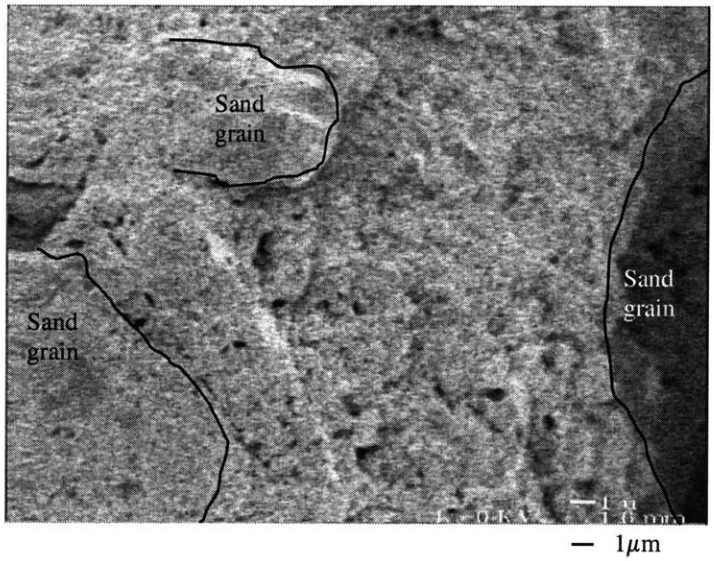

(a)

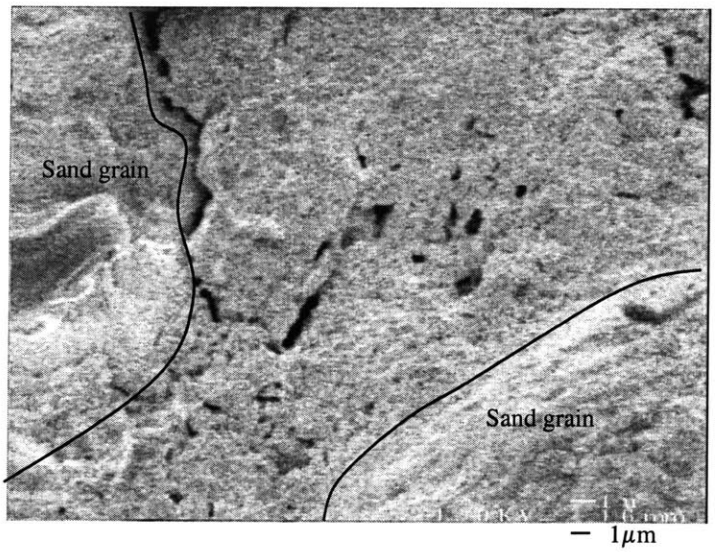

(b)

Figure 6-5: SEM micrograph of hydrostatically compressed leached mortar. $\Sigma'_M = -9\,\mathrm{MPa}$, $p = 0.5\,\mathrm{MPa}$. The marked regions correspond to sand grain locations. Note that some grains are losened during the polishing process.

(c) show three SEM micrographs of a hydrostatically compressed leached paste after unloading. The micrographs reveal that the large pore space created by the Portlandite dissolution is reduced during the hydrostatic loading (see Figures 4-8 and 4-9 for appearance before loading). More particularly, it appears that the surrounding solid expanded during loading into the pore space, thus reducing the porosity. Some zones show large localized shear deformation, for example in Figure 6-4(b). Moreover, large pores, the remnants of the Portlandite dissolution, may collapse from an initially rather circular shape into flat pores of elliptical shape (Figure 6-4(a)).

The ITZ is crushed through the confinement. In the case of mortars, the deformation of the ITZ creates a different deformation behavior compared with the cement paste. The porosity in the ITZ of leached mortars is particularly high, due to the higher Portlandite concentrations in the ITZ of an intact mortar. This has an effect on the deformation response under hydrostatic compression. Figures 6-5 (a) and (b) show the grain-matrix interface of a leached mortar after hydrostatic compression to $\Sigma'_M = -9\,\mathrm{MPa}$. The SEM micrographs show that the micrometer size porosity in the ITZ vanishes (to be compared with Figure 4-11 (a) through (d)) under stress application. At the same time, the matrix is squeezed into the space between the sand grains and no shear bands or dramatic changes in the pore morphology are observed.

Two main elements that control the deformation behavior of the leached materials can be extracted from the hydrostatic test results and the SEM micrographs:

1. *Decalcified C-S-H deform at constant volume into the pore space.* The plastic deformability of the solid of the cement paste matrix, which is composed, after leaching, mostly of low C/S−C-S-H (Level I): The expansion of the solid into the macropores (Fig. 6-4(c)) indicates that low C/S−C-S-H at yield deform either at constant volume (incompressible) or under microscopic dilatation, merging in some places into shear bands of concentrated plastic deformation as observed in Figure 6-4(b). The plastic yield of the solid into the macropores explains the first part of the $s-$shaped overall contractive hardening behavior of the cement paste occurring at decreasing tangent stiffness (see Figure 6-2). Once the solid has filled a large part of the pores, the free yield of the solid material is restrained leading to a stiffening of the material.

2. *Collapse of macropores leads to geometrical hardening.* The new pore size family generated by leaching of Portlandite-clusters, is an order of magnitude larger than typical pore sizes encountered in intact cement paste materials. In the cement-paste matrix, the large pores offer free expansion space for the plastic deformation of the low C/S−solid. At high confinements, these pores collapse, which contributes to the second part of the $s-$shaped compaction behavior of the cement paste, associated with a *geometrical hardening* (change in pore morphology). In contrast to the paste, the continuous stiffening of mortar indicates that the mortar's response is dominated by geometrical hardening of the leached ITZ porosity alone. At the given level of hydrostatic compaction, the main change in porosity of the mortar results from the compaction of the ITZ porosity.

6.3 Deviatoric Loading at Increasing Confinement

6.3.1 Results

The confinement level at the beginning of the deviatoric loading has a strong influence on the deformation behavior of leached pastes and mortars. We therefore show results for a low ($\Sigma_M^{hyd} = -1.5\,\text{MPa}$) and a high ($\Sigma_M^{hyd} = -6.5\,\text{MPa}$ or $\Sigma_M^{hyd} = -7.6\,\text{MPa}$) confinement level where Σ_M^{hyd} is the mean stress applied during the initial hydrostatic loading phase. The pore pressure is kept constant at $p = 0.5\,\text{MPa}$ during the tests. Figures 6-6 plot the (logarithmic) volume strain $\delta E_v^{\ln}$ in the triaxial test at increasing confinement, driven by the (natural) axial strain, $\delta E_{zz}^{\ln} = \ln(L_t/L_{hydro})$. Figures 6-7(a) and 6-7(b) show the corresponding deviatoric stress development, $\Sigma_{zz} - \Sigma_{rr}$, over the associated (energy conjugated) strain quantity, $\delta E_{zz}^{\ln} - \delta E_v^{\ln}/3$; and Figures 6-8(a) and 6-8(b) display the change in mean stress, Σ_M versus the change in Lagrangian porosity ϕ recorded during deviatoric loading. In all deviatoric loading tests at increasing confinement the same typical picture emerges:

- *While the initial deformational behavior for both materials is similar, at higher strains the rigid inclusions limit the mortar deformability.* The initial almost linear relation between the axial strain and the volumetric strain (Figs. 6-6) is independent of the type of material and confinement pressure. This indicates, in accord with the work increment (Eq. (5.10)), that the initial shear deformation of cement pastes and mortars is the same. Since the

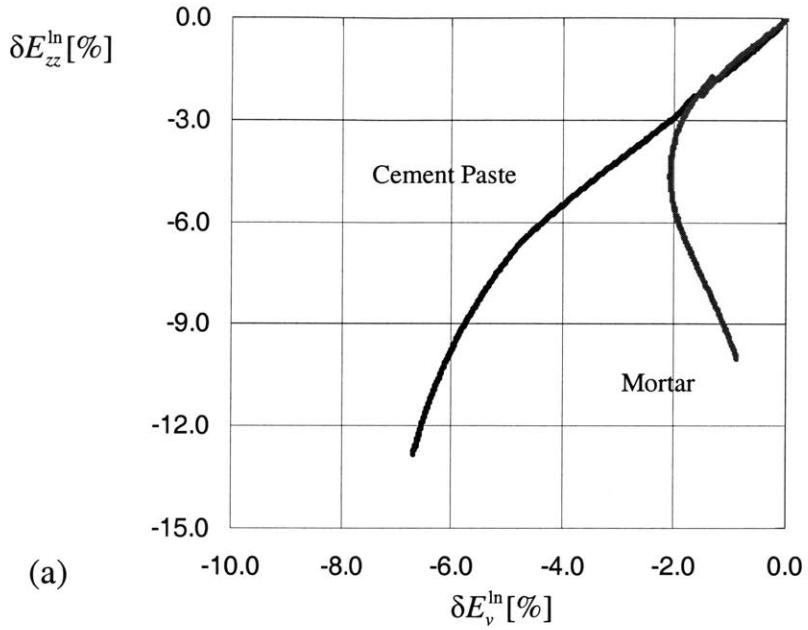

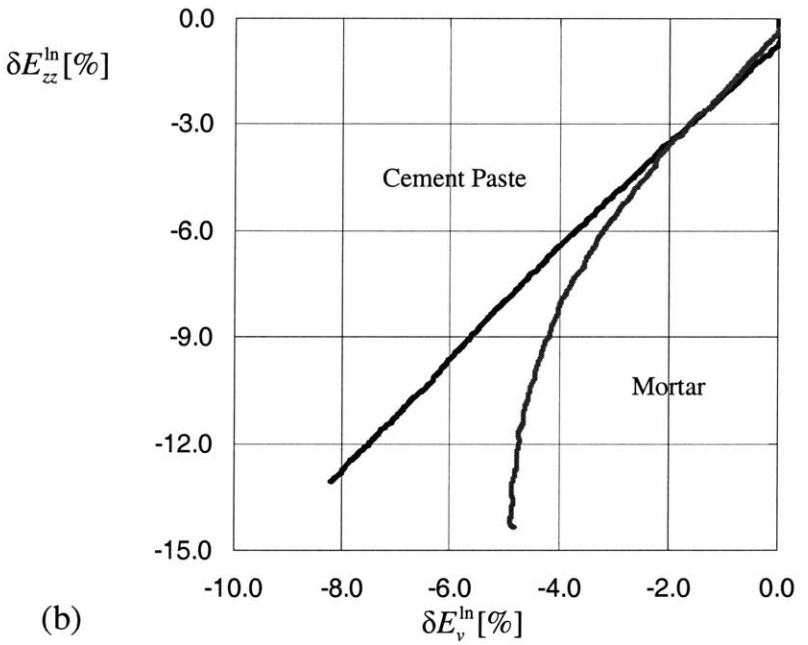

Figure 6-6: Axial over volumetric (natural) strain for (a) low confinement, $\Sigma_M^{hyd} = -1.5\,\text{MPa}$ and (b) high confinement, $\Sigma_M^{hyd} = -6.5\,\text{MPa}$ for the paste and $\Sigma_M^{hyd} = -7.6\,\text{MPa}$ for mortar. $p = 0.5\,\text{MPa}$ in all tests.

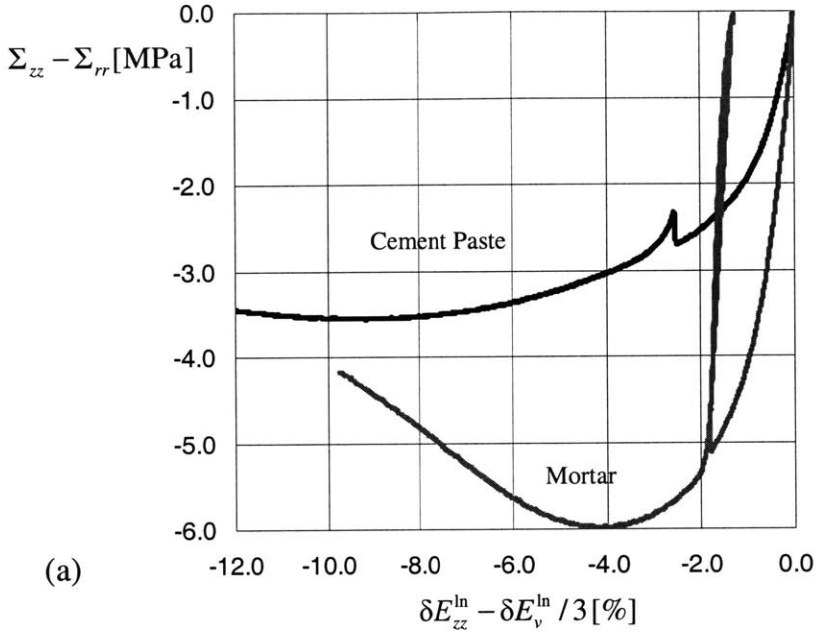

(a)

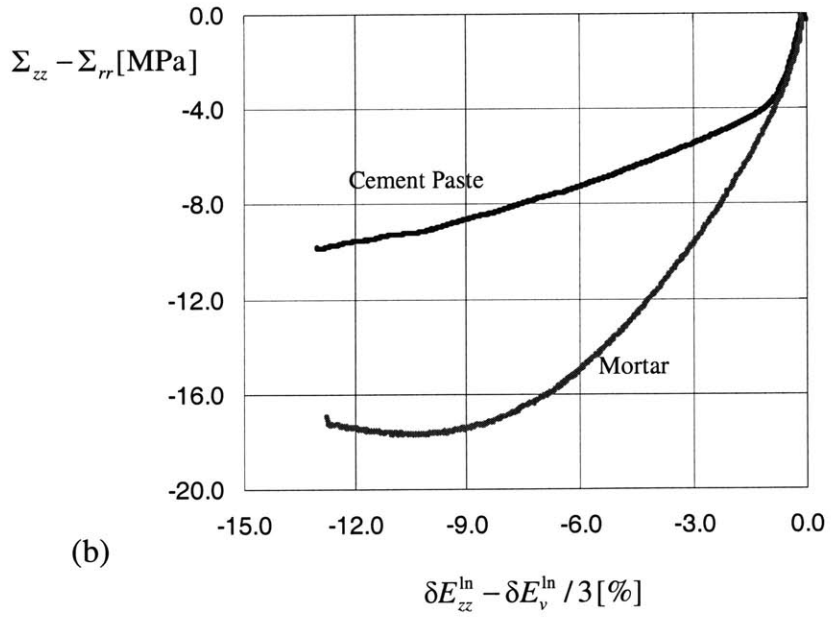

(b)

Figure 6-7: Deviatoric stress and strain evolution for (a) low confinement, $\Sigma_M^{hyd} = -1.5\,\text{MPa}$ and (b) high confinement, $\Sigma_M^{hyd} = -6.5\,\text{MPa}$ for the paste and $\Sigma_M^{hyd} = -7.6\,\text{MPa}$ for mortar. $p = 0.5\,\text{MPa}$ in all tests.

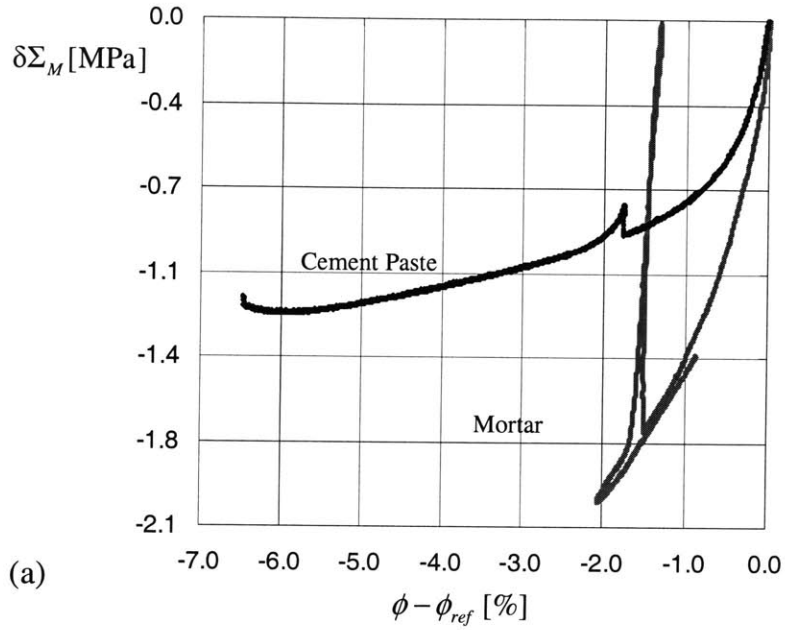

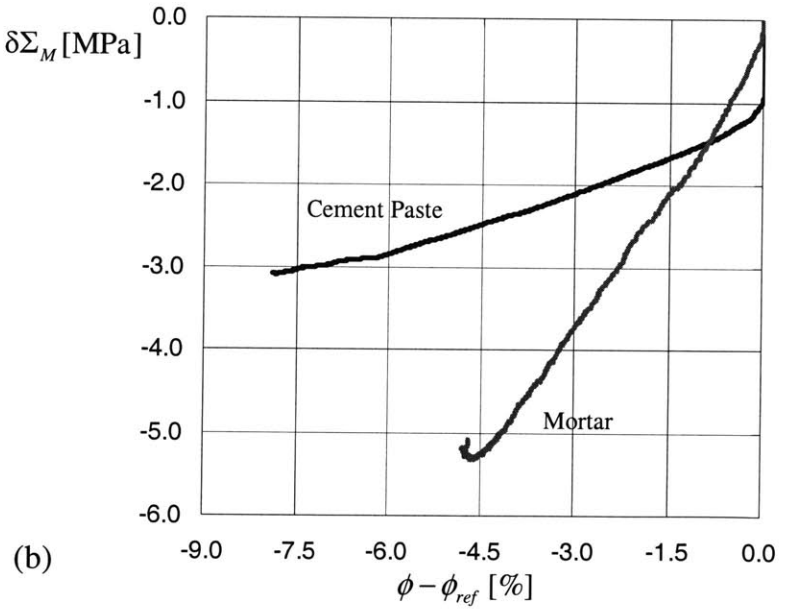

Figure 6-8: Change in mean stress and Lagrangian porosity for (a) low confinement, $\Sigma_M^{hyd} = -1.5\,\text{MPa}$ and (b) high confinement, $\Sigma_M^{hyd} = -6.5\,\text{MPa}$ for the paste and $\Sigma_M^{hyd} = -7.6\,\text{MPa}$ for mortar. $p = 0.5\,\text{MPa}$ in all tests.

inclusions are almost rigid, this shear deformation is the one of the cement paste matrix, including for mortar the ITZ. The lower overall deformability of the mortar due to the presence of rigid inclusions, leads to higher deviatoric stresses $\Sigma_{zz} - \Sigma_{rr}$ in the mortar than in the cement paste (Figs. 6-7(a) and 6-7(b)).

- *Cement pastes show a stronger contracting behavior. Failure in both materials is associated with zero volumetric deformations.* Cement pastes show a stronger contracting behavior than mortars (higher deformability) (Figs. 6-12), and, while cement pastes continue to contract, mortars have an early tendency to develop a dilating behavior ($dE_v^{\ln} > 0$), leading to failure (Figs. 6-12). The point at which the macroscopic contracting behavior switches into a macroscopic dilating behavior, corresponds to the maximum deviatoric stress the materials can support (Figs. 6-7(a) and 6-7(b)). Below this point, that is during contraction, the material hardens continuously. Beyond this point, softening takes place. Hence, a pure shear deformation characterizes this point. The zero volumetric deformation can be associated with what is known as "critical state"[2], at which calcium leached materials lose their capacity to support higher loads. This is consistent with the found shear planes along which the materials fail. Figure 6-9 shows a typical failure surface of a leached paste specimen.

6.3.2 Discussion

The solid material of the paste expands into the void space. Shear band development limits the strength for low confinements. The large compressibility of cement pastes is clearly a consequence of the large plastic deformation the low C/S-solid, can develop, in compression, and which is even enhanced by deviatoric loading. In fact, for the same confinement level the overall compaction expressed as the change in porosity in deviatoric loading is larger than in hydrostatic compression (compare Figs. 6-2 and 6-12). This supports that the low C/S-solid (Level I) expands into the large pore space, when subjected to shear deformation, leading to an additional reduction of the overall porosity, in addition to deformation caused by pure

[2]The Critical State concept was originally developed in Soil Mechanics and charcterizes a state of pure shear deformation. See for example [131].

Figure 6-9: Typical leached cement paste specimen fragment after failure on the shear plane.

hydrostatic compression. Furthermore, the shear deformation of the solid enhances the creation of shear bands in the cement paste, which ultimately exhausts the volume deformability at low confinement leading to failure. Failure is not achieved for the highly confined cement pastes. The material continues to contract quasi linearly with the prescribed vertical strain (Fig. 6-6(b)). Both the deviatoric stress-strain curve (Fig. 6-7(b)) and the mean stress-porosity curve (Fig. 6-8(b)) have a distinct yield point, which is associated with the onset of plastic yielding of the solid, and beyond which the material exhibits continuous hardening, and this up to large strains of 10% and more.

The ITZ limits the shear deformation capacity of mortars. The early tendency of the mortar to develop a dilating behavior can be attributed to the ITZ: At low confinement, the deviatoric loading generates shear in the ITZ, which favors the coalescence of the ITZ into continuous shear bands between inclusions, leading to failure. The low volume contraction at low confinement (Fig. 6-8(a)), appears as a consequence of the shear deformation at constant volume of the solid phase of the matrix, which fills a part of the ITZ-porosity, thus geometrically hardening the material. On the other hand, at high confinement, the solid phase first expands into the ITZ-porosity, leading to a continuous geometrical hardening of the composite (Fig. 6-8(b)), for which –in contrast to the cement paste– no distinct yield point is observed. Once the pores in the ITZ are filled or crushed, it is likely that frictional dilatation developing at the densified matrix-grain interface leads to failure of the mortar. In all cases, the onset of the overall dilating behavior defines the critical state of the material, beyond which material softening occurs. The contracting behavior and the tendency towards a critical state suggest that the yield surface is closed on the hydrostatic axis. The deformation measurements show that the strength surface presented in Chapter 5 coincides with zero volume deformations. In other words, the Drucker-Prager criterion that was introduced in Chapter 5 for the ultimate strength of the leached cementitious materials describes the critical state line. The material description can be improved by adding the closure on the hydrostatic axis.

6.4 Deviatoric Loading at Decreasing Confinement

The series of deviatoric loading tests with decreasing confinement is intended to illustrate the effects of a strong initial confinement, as it is relaxed, on the deviatoric deformation behavior. Particularly, the question about the persistence of the stabilizing effect of the hydrostatically induced geometrical hardening is of interest.

6.4.1 Results

Figures 6-10(a) to 6-12(a) show the results at the controlled deviator-to-confinement ratio $\gamma = \delta(\Sigma_{zz} - \Sigma_{rr})/\delta\overline{p} = -0.86$. Figures 6-10(b) to 6-12(b) show the same type of results for the deconfinement ratio $\gamma = -3$. In both cases, the leached paste and mortar have been hydrostatically precompressed to $\Sigma_M^{hyd} \approx -10\,\text{MPa}$ and the pore pressure is kept constant at $p = 0.5\,\text{MPa}$.

- *Depending on the stress path dilating or contracting behavior is encountered.* The extend to which the confinement is reduced leads to some important differences in the material behavior: In the $\delta E_{zz}^{\ln}$ vs. $\delta E_v^{\ln}$ plot, a high deconfinement ($\gamma = -0.86$) leads to a dilating behavior (Fig. 6-10(a)), while a low de-confinement ($\gamma = -3$) preserves a contracting behavior despite the reduction in confinement (Fig. 6-10(b)). For the high deconfinement, after an initial elastic part dominated by the axial deformation, the dilatation becomes dominant in the shear deformation, $\delta E_{zz}^{\ln} - \frac{1}{3}\delta E_v^{\ln}$. This sensitivity to dilatation is more pronounced for the mortar than for the cement paste. By contrast, at low deconfinement, the overall contraction behavior tends towards a minimum, beyond which dilatation takes place, which is similar to behavior observed in deviatoric loading at increasing confinement.

- *High deconfinement first leads to unloading before softening occurs. Low deconfinement immediately leads to hardening.* The deviatoric response captured in Figure 6-11(a) for high deconfinement, $\gamma = -0.86$, shows a clear yield point at a deviatoric stress of around $-4.5\,\text{MPa}$ for both cement paste and mortar. Below this point, the incremental work associated with shear deformation $dW_{ext} \propto (\Sigma_{zz} - \Sigma_{rr})(dE_{zz}^{\ln} - dE_v^{\ln}/3) < 0$ (from Eq. (5.10)), meaning that this loading phase corresponds effectively to an unloading. Beyond

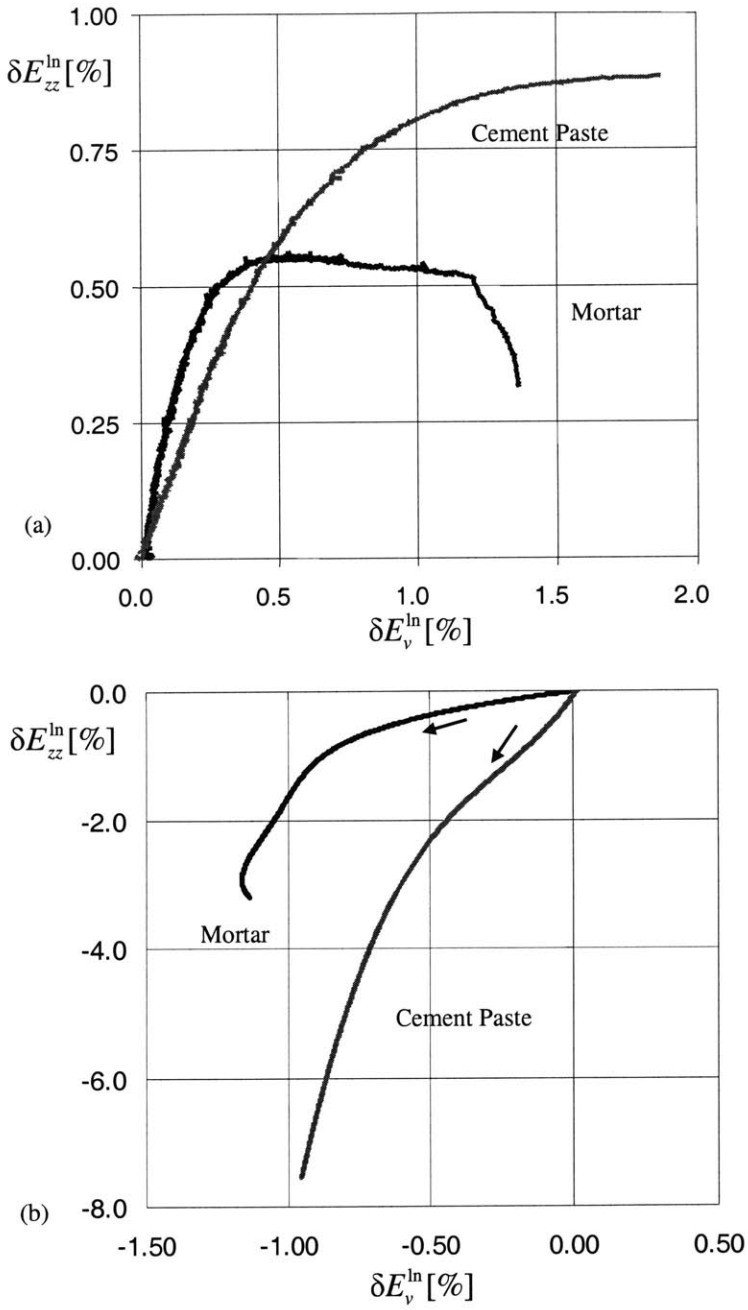

Figure 6-10: Change in the axial and logarithmic strains under deviatoric loading at decreasing confinement: (a) $\gamma = -0.86$, (b) $\gamma = -3$. The arrows denote the directon of the test. Note that an initial hydrostatic loading of $\Sigma_M^{hyd} \approx -10\,\text{MPa}$ took place before. $[p = 0.5\,\text{MPa}]$.

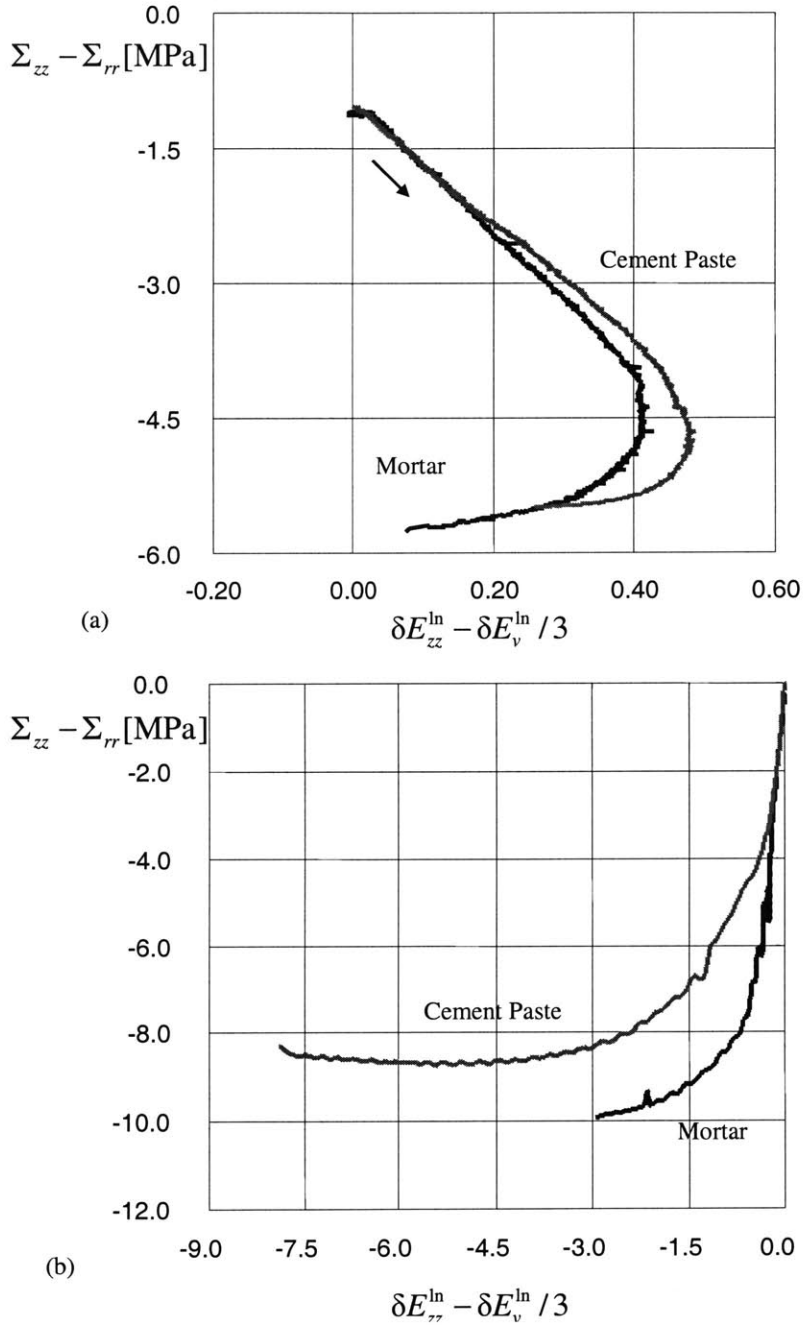

Figure 6-11: Evolution of the deviatoric stress vs. natural deviatoric strains: (a) $\gamma = -0.86$, (b) $\gamma = -3$. The arrows denote the directon of the test. Note that an initial hydrostatic loading of $\Sigma_M^{hyd} \approx -10\,\text{MPa}$ took place before. [$p = 0.5\,\text{MPa}$].

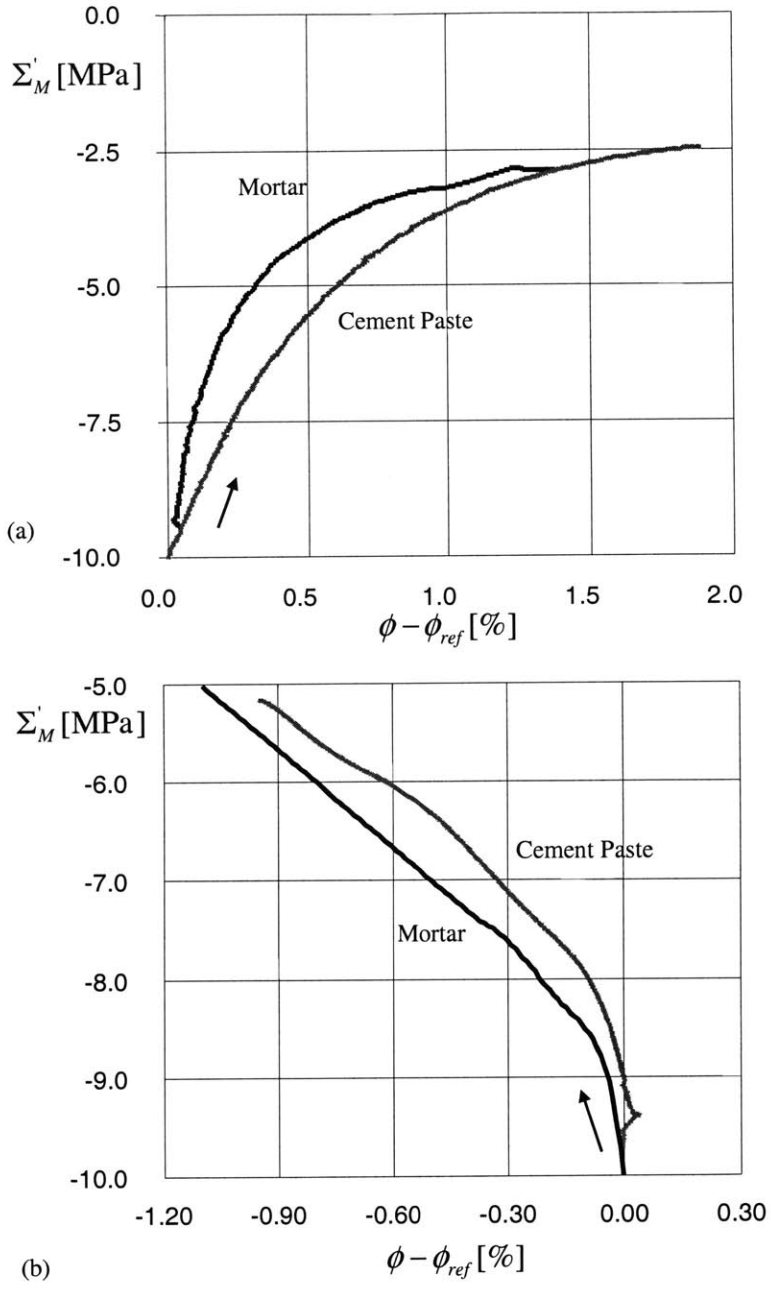

Figure 6-12: Evolution of the effective mean stress vs. Lagrangian porosity change: (a) $\gamma = -0.86$, (b) $\gamma = -3$. The arrows denote the directon of the test. Note that an initial hydrostatic loading of $\Sigma_M^{hyd} \approx -10\,\text{MPa}$ took place before. [$p = 0.5\,\text{MPa}$].

this point, $(\Sigma_{zz} - \Sigma_{rr})(dE^{\ln}_{zz} - dE^{\ln}_{v}/3)$ increases (Figure 6-11(a)), leading to some limited hardening, given that $dE^{\ln}_{zz} - dE^{\ln}_{v}/3 \to 0$. By contrast, at low de-confinement $\gamma = -3$, the incremental shear work is positive from above, leading to the elastoplastic hardening behavior shown in Figure 6-11(b).

- *In high deconfinement tests, the materials dilate while in low deconfinement tests the materials contract towards the critical state.* The high deconfinement ($\gamma = -0.86$) provokes a progressive dilatation of the material (Fig. 6-12(a)), for which the volumetric work $\Sigma'_m d\phi < 0$. By contrast, $\Sigma'_m d\phi > 0$ at low de-confinement ($\gamma = -3$), for which the material contracts almost linearly as the confinement is reduced (Fig. 6-12(b)).

6.4.2 Discussion

Shear bands lead to failure. In both loading cases, an increasing deviatoric loading induces shear deformations in the highly compacted matrix. The large dilatation that occurs in the high deconfinement test indicates that the solid in this loading case has little space left to expand in the free pore space. Indeed, this space has been crushed during the initial hydrostatic loading to $\Sigma_M^{hyd} \approx -10\,\text{MPa}$. In the cement paste, the solid deforms, eventually at constant volume, into the shear bands leading to the failure of the material along shear plans. The failure mechanism is similar for the mortar: as the cement paste matrix deforms, it activates the compacted ITZ, leading to shear failure along shear bands connecting almost rigid inclusions.

In low deconfinement the shear deformation dominates the total deformation. At low de-confinement, the initial elastic dilatation of the material generates sufficient pore space for the solid phase to deform, without creation of shear bands in the cement paste matrix. Given that the porosity overall decreases (Fig. 6-12(b)), the volume required by the shear deformation of the solid is larger than the porosity generated by elastic dilatation. This leads to an overall compaction, and to the pronounced plastic behavior of both cement paste and mortar shown in Figure 6-11(b). Once the volume deformability is exhausted, the materials fail in a similar fashion as specimens in deviatoric loading at increasing confinement.

In high deconfinement tests, softening is observed leading to final stress states on the critical state line. In high deconfinement tests, after reaching the maximum deviatoric stress (Figure 6-11(a)) a strong softening is observed, associated with dilating deformation. This is not depicted

on Figure 6-11(a) because the test control cannot keep the stress path on the $\gamma = -0.86$ trajectory, precisely because of the strong softening behavior. The stable stress state after softening takes place is on the critical state line and associated with zero volumetric deformation. The fact that dilating softening occurs in a high deconfinement test at increasing deviatoric load suggests that the yield surface is not only closed on the hydrostatic axis in compression but also closed on the tension side of the hydrostatic axis, with the critical state line dividing zones of dilating and contracting behavior.

6.5 Effective Stress Concept During Deformation

In section 5.2.4, it was shown that the effective stress concept applies at failure for the leached cement pastes and mortars. During the experimental investigation, different pore pressures where used to check whether the concept applies also to the deformation behavior. Figure 6-13 displays two typical mean stress-porosity curves of a drained triaxial compression test on mortars, one carried out at a fluid pressure of $p = 1\,\text{MPa}$, the other at a fluid pressure of $p = 5\,\text{MPa}$, for which the mean stress was corrected following the effective stress concept, $\Sigma'_M = \Sigma_M + p$. The good agreement between the two tests shows that the effective stress concept is valid throughout the loading process. The same is true for the leached paste as Figure 6-14 shows with a comparison of a test at $p = 6\,\text{MPa}$ and $p = 0\,\text{MPa}$. The validity of the effective stress concept during the loading process confirms the assumption made in Section 5.1, Eq. (5.5), that the solid phase is (almost) incompressible, and justifies a posteriori the assumptions made for determining the volume strains from the change in Lagrangian porosity that is:

$$E_v^{\ln} = \ln \frac{V}{V_0} = \ln\left(1 - (\phi - \phi_0)\right) \tag{6.1}$$

On the other hand, the leached materials show some non elastic deformation almost immediately after load application. This makes it difficult to conclude on the validity of the effective stress concept in the elastic range. This aspect will be analyzed in some more details in Chapter 7 by means of a micromechanical approach.

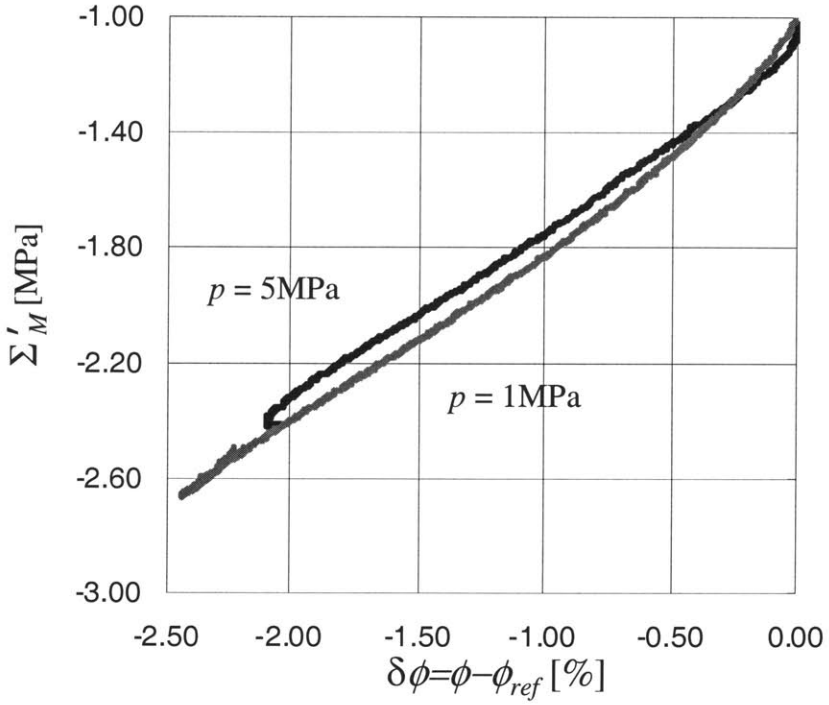

Figure 6-13: Effective mean stress over porosity change plot for different pore pressures shows that the effective stress concept also applies for the deformations.

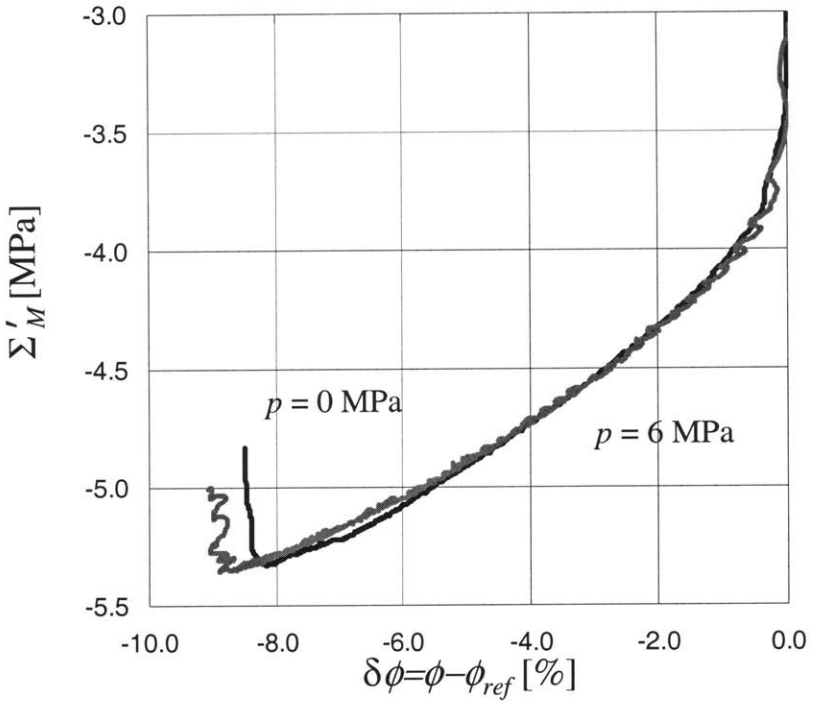

Figure 6-14: Comparison of two tests on leached pastes. Black solid curve for $p = 0$ MPa pore pressure, the grey curve correpsonds to $p = 6$ MPa pore pressure.

6.6 Deformation Behavior in Uniaxial Tension

The deformation behavior in tension complements the material information. Specifically, the change in ductility associated with leaching is studied.

6.6.1 Results

The uniaxial tensile tests equipment (equipment description in Section 5.3.1) limits the deformational behavior investigation in tension to axial deformations and stresses. Figures 6-15 (a) and (b) show a typical set of stress-strain curves for the paste and the mortar. The strains are measured with the clip-on extensometer and the stresses are calculated at the level where failure took place. The measured force is divided by the measured surface area[3]. In all cases, the materials show an almost linear stress-strain relation before failure takes place abruptly. Hardening, if any is negligible. A possible softening after the peak stress is not accessible with the equipment. The reduction of the Young's modulus, defined here as a secant modulus at failure, through leaching is more important than the tensile strength degradation so that the deformation at failure increases with the leaching process. This agrees well with the Young's modulus measurements by Constantinides [37] which were presented in Section 2.3.4.

6.6.2 Discussion - Ductility

Definitions of ductility exist for metals: Either the strain at failure or the area reduction (necking) in a uniaxial tension test are considered ductility measurements for metals [7]. For cementitious materials, deformation at failure is certainly an important characteristic of ductility. As the Young's modulus decreases more by leaching than the uniaxial tensile strength for both paste and mortar, the deformation at failure increases with leaching and hence the leaching process is expected to increase the ductility. The same is true in compression: Carde [28] who based his ductility definition on the deformation at failure in uniaxial compression, found that it increases with leaching. A second way to estimate the change in ductility can be based on an energy comparison. Assuming a perfect brittle material, the externally supplied that is $1/2 \times F_{\max} \times u^d$ is entirely dissipated during fracture in heat form. This provides a

[3] Two measurements of the diameter of the sections are taken with a caliper 90° rotated.

G_f [N / mm]	Mortar	Paste
intact	5.03×10^{-3}	4.53×10^{-3}
leached	6.35×10^{-3}	7.35×10^{-3}

Table 6.1: Fracture energy assuming perfect brittle behavior

means of estimating the fracture energy G_f from [148]:

$$G_f = \frac{F_{\max} \times u^d}{2A_f} = \frac{1}{2}\Sigma_{zz}^{\max} \times E_{zz}^{\max} \times l \tag{6.2}$$

where $l = 25.4\,\text{mm}$ (1 in) in our tests. Using the results from Figures 6-15 (a) and (b) yields the results displayed in Table 6.1. The determined values for the fracture energy suggest that the fracture energy increases with the leaching process, expressing a more ductile respons of the leached materials.

However, this approach neglects any additional source of dissipation related e.g. to frictional or plastic mechanisms. Such a combined plastic-fracture process is taken into account by the following approach based on a ductile fracture reasoning [13]. The size of the fracture process zone (fpz), l_{ch}, is compared to a characteristic lengthscale of the studied structure $\mathcal{L}$. The ratio

$$\mathcal{I} = \frac{\mathcal{L}}{l_{ch}} = \frac{\mathcal{L} f_t^2}{E G_f} \tag{6.3}$$

is known as Irwin's number and describes the ductility ($\mathcal{I} \to 0$) or brittleness ($\mathcal{I} \to \infty$) respectively. Comparing $\mathcal{I}$ before and after leaching for the paste yields (values from Tables 5.5 and 2.5):

$$\frac{\mathcal{I}^\infty}{\mathcal{I}^0} = \left(\frac{f_t^2}{E G_f}\right)_\infty \times \left(\frac{E G_f}{f_t^2}\right)_0 = 1.5 \times \frac{G_f^0}{G_f^\infty} \tag{6.4}$$

while for the mortar (values from Tables 5.5 and 2.5) we have:

$$\frac{\mathcal{I}^\infty}{\mathcal{I}^0} = \left(\frac{f_t^2}{E G_f}\right)_\infty \times \left(\frac{E G_f}{f_t^2}\right)_0 = 0.4 \times \frac{G_f^0}{G_f^\infty} \tag{6.5}$$

If we use the estimates for the fracture energy presented before, it is $\mathcal{I}^\infty < \mathcal{I}^0$ for paste and mortar, which suggests an increase in ductility. On the other hand, measurements of the change in fracture energy with leaching were performed for partially leached mortar beams

by Le Bellego [80]. Le Bellego found that the fracture energy was roughly 50% of the initial value after 98 days of leaching. This would imply $\mathcal{I}^{\infty} > \mathcal{I}^{0}$ for the cement paste (Level II), and $\mathcal{I}^{\infty} < \mathcal{I}^{0}$ for the mortar (Level III). By way of conclusion, it appears that the ductility of mortar increases in the course of leaching. In turn, for cement paste, a fracture energy test is necessary to conclude.

6.7 Summary

6.7.1 Summary of Physical Observations

The study of the deformation behavior gives additional understanding of the material and clarifies some questions raised in the strength investigation.

- Large plastic deformations are encountered and show that the matrix of the cement paste (Level II), consisting mainly of C-S-H with a low C/S ratio, is highly plastically deformable. This is consistent with the increase in polymerization that accompanies a reduction in the C/S ratio [117] and takes place on Level I , as was shown in Chapter 2. For unleached pastes, these large deformations are unlikely to occur as they are inhibited by the presence of Portlandite on Level II and the different C-S-H properties at high C/S ratio on Level I.

- The validity of the effective stress concept at failure can be linked to a purely cohesive solid phase as was shown by de Buhan and Dormieux [27]. Now with the deformational behavior study showing the validity of the effective stress concept during the entire loading process there is strong evidence that additionally the solid is incompressible. The high compaction capacity of calcium leached materials, then, appears as a consequence of the shear deformation of the pure cohesive heterogeneous solid, which expands into the macroporosity, in order to preserve its volume. The large pores created by the dissolution of CH-clusters provide expansion space for the incompressible plastically deformable solid during deviator loading. Once this porosity is filled, further volume contraction is restrained, which leads to generation of shear bands and macroscopic dilatation, which ultimately governs the failure of the cement paste.

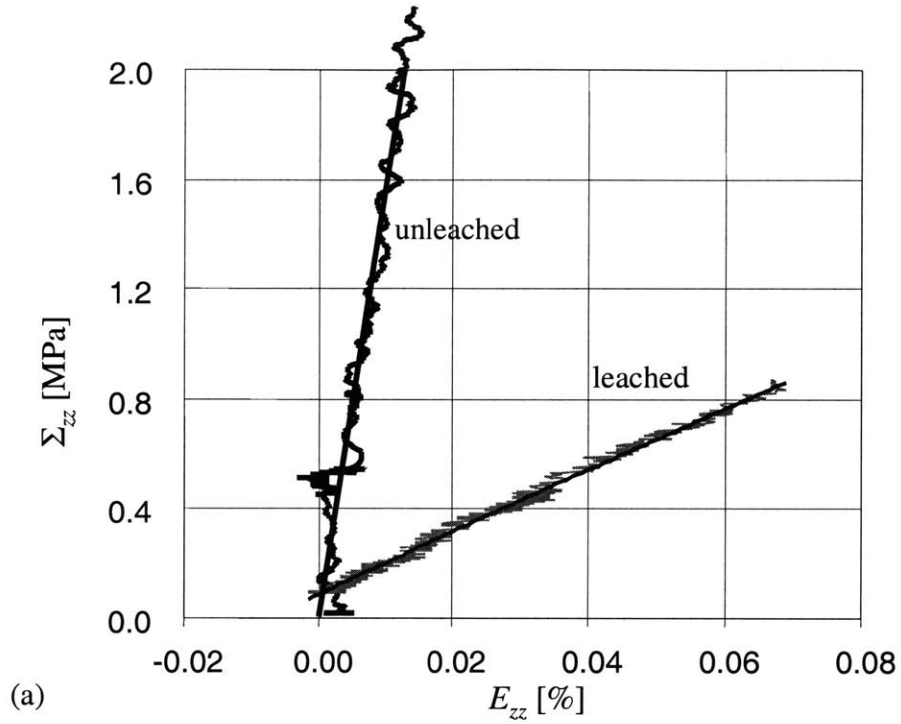

(a)

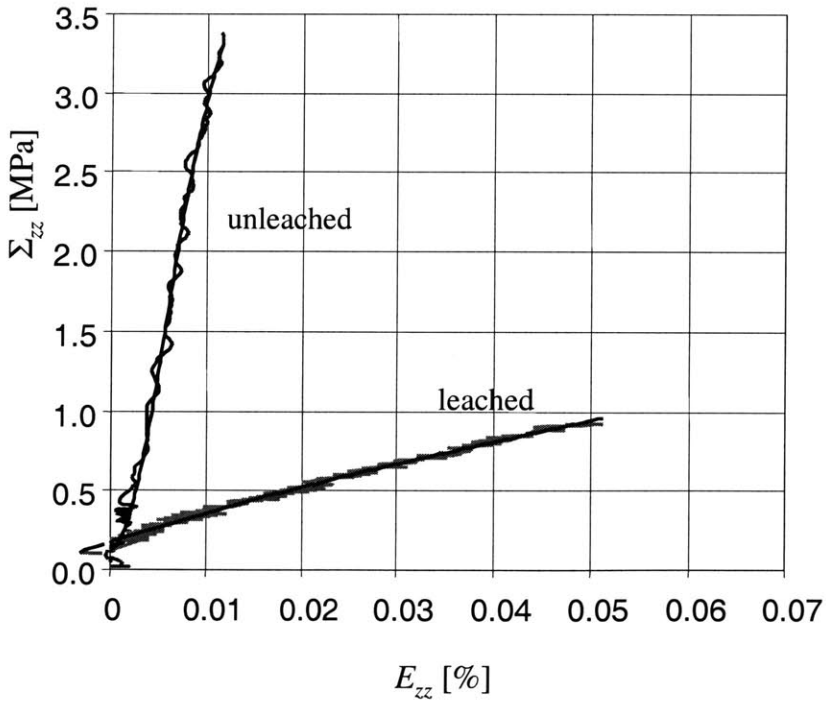

(b)

Figure 6-15: Stress-strain curves in tension for (a) leached and intact cement pastes and leached and intact mortar and (b).

- In mortars, a competition between plastic material behavior and porosity controlled microstructural deformation takes place. In hydrostatic compression, the mortar's response is governed by geometrical hardening of the ITZ, which crushes the large pores in the ITZ. As shear deformation increases, in compression, the intrinsic plastic deformation properties of the paste dominate first, leading to a pronounced deviatoric hardening as the solid is squeezed into the pore space. With increasing deviator stress, at low confinements, the incompletely filled ITZ-porosity merges into shear bands through the cement paste along which the material fails. At high confinement, a saturation of the porosity by the solid phase exhausts the volume contraction capacity of the material. Additional shear deformation of the solid triggers frictional dilatation mechanisms at the densified matrix-grain interface that lead to the observed bulk failure of calcium leached mortars. These observations confirm the strength analysis from which the important role of the ITZ in low confinement stress states emerged in contrast to high confinement stress states where the ITZ is crushed and thus mechanically deactivated.

- In tension, the deformation at failure increases through leaching for both the cement paste and the mortar. For the paste, this increase of deformation at failure points to an increased ductility while a fracture mechanics reasoning suggests an increase of brittleness of the material. In turn for mortar, calcium leaching increases the ductility.

6.7.2 Improved Yield Surface

The additional observations on the material deformation suggests the following enhanced description of the yield surface that emerged from the strength investigation:

- From the deviatoric loading cases with increasing confinement it emerges that failure of the tested specimens takes place at zero volume deformation, after prior contracting deformations. Moreover, in hydrostatic compression tests, the porosity change is important (strong contraction under increasing pressure) and characteristic of the material state.

- At the same time we note that a dilating behavior can occur when the deconfinement is high enough and in such a case, after a strong softening, failure again takes place on the strength surface proposed in Section 5.2.

To incorporate the additional information in the material description, we propose a modified Cam-Clay model, originally developed for clays by researchers affiliated with the University of Cambridge [131]. In the stress space, it incorporates a critical state that separates a contracting from a dilating domain. In addition, the hardening is governed by the change is porosity which very much reflects the leached cementitious materials. Figure 6-16 shows the elliptical strength surface of a Cam Clay model. Algebraically, it is described by

$$2f_{CC} = \frac{3J_2}{M^2} + [\Sigma_M + p + (p_c - p_t)]^2 - (p_c + p_t)^2 \leq 0 \tag{6.6}$$

where $2p_c$ and $2p_t$ are the closing pressures of the ellipse on the hydrostatic axis. M is close to a constant the slope of the critical state line, that were described in the strength investigation by a Drucker-Prager. More precisely, as the maximum strength coincides with the critical state, the Drucker-Prager line and the critical state line are identical and M can be determined. The critical state is defined for:

$$f_{cc} = 0 : \frac{\partial f_{cc}}{\partial \Sigma'_M} = 0 \Rightarrow \Sigma'_{M,crit} = p_t - p_c \tag{6.7}$$

Substituting (6.7) in (6.6) leads to the following expression that describes all critical states:

$$\frac{3J_2}{M^2} - \left(2p_t - \Sigma'_m\right)^2 = 0 \Rightarrow \sqrt{J_2} + \frac{M}{\sqrt{3}}\Sigma'_m - \frac{2M}{\sqrt{3}}p_t = 0 \tag{6.8}$$

Thus from a comparison with Eq.(5.17),

$$\delta = \frac{M}{\sqrt{3}};\ c = \frac{2M}{\sqrt{3}}p_t \tag{6.9}$$

The material description in the compression - tension zone is not changed and the material strength in the tensile domain is describe with the Drucker-Prager surface presented in Section 5.4. Figure 6-16 shows the combination of the two strength surfaces in the $\sqrt{J_2} \times \Sigma'_M$ halfplane. Figure 6-17 shows the strength domain in the three dimensional stress space consisting of the Cam Clay ellipsoid and the Drucker-Prager cone in the principal stress space $\Sigma_I \times \Sigma_{II} \times \Sigma_{III}$.

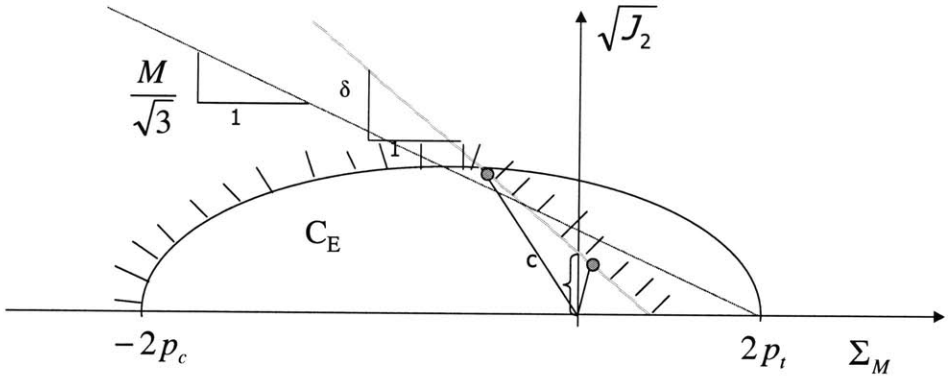

Figure 6-16: Schematic depiction of the combined Cam-Clay Drucker-Prager model. C_E denotes the elasticity domain.

6.8 Summary of the Experimental Part

The experimental part of this study has provided information on asymptotically leached cement pastes and mortars. Besides the physical appearance of the leached materials at Levels I through III as observed in the SEM and quantified through porosity and density measurements, the mechanical properties in the leached state have been obtained. These include the strength domain in the $\sqrt{J_2} \times \Sigma'_M$ space for both compressive and tensile stress states. In addition, the deformation behavior has been accessed which leads to a detailed description of the plastic loading surface of the cement paste and mortar through a combination of the Cam-Clay and the Drucker-Prager plasticity models. The validity of the effective stress concept during the entire loading process was proven experimentally. The consequences in undrained loading situations is a frictional capacity that vanishes. Together, a complete picture of the material properties of the intact and asymptotically leached pastes (Level II) and mortars (Level III) emerges. What is left are the properties of the intermediate states, which cannot be determined experimentally. They will be accesses by means of micromechanical modeling (Chapters 7 and 8) and constitutive modeling (Chapter 9).

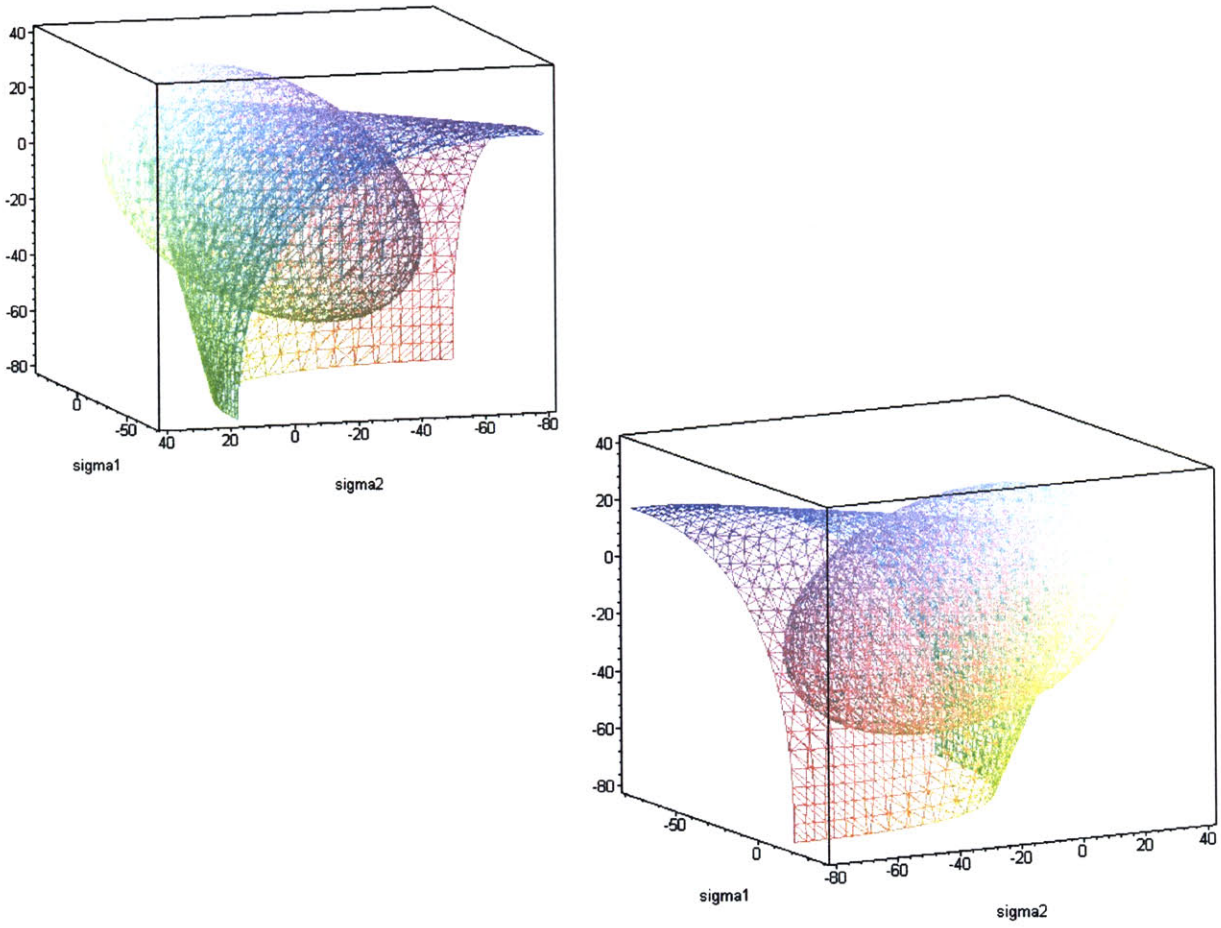

Figure 6-17: Representation of the two-surface strength domain in the principal stress space $\Sigma_I \times \Sigma_{II} \times \Sigma_{III}$.

Part III

A Micro-to-Macro Chemomechanics Approach

Chapter 7

Micromechanical Analysis of Poroelastic Properties

This third part of the study is devoted to the development of a chemomechanical theory that shall make it possible to bridge between the asymptotic states of calcium leaching, that is between the intact and completely leached materials. To this end, the first two chapters in this part revisit the experimental observations by means of Continuum Micromechanics. The objective is twofold: (1) To understand in a quantitative manner how the elasticity and strength properties in the two asymptotic leaching states which were tested experimentally scale between microstructural levels. (2) To quantitatively model the strength and stiffness degradation of the intermediate leaching state. This Chapter focuses on the poroelastic properties: First we present some basic elements of Continuum Micromechanics and show its applications to the modeling of the elastic properties of leached and unleached cementitious materials[1]. In a second step, we study the homogenization of some poroelastic properties, that is the Biot coefficient, which describes the effect of the pore pressure on the macroscopic stress state, and the Biot modulus which concerns the effect of the pore pressure on the porosity change in a deformation free experiment. The homogenization model for the elasticity properties developed in this Chapter is a natural extension of the model of Constantinides and Ulm [38] to Level III of the microstructure, where we account for the effect of the ITZ on the elasticity properties.

[1] More advanced readers might directly want to turn to the second section of this chapter.

The homogenization model for the Biot parameters, b and $\mathtt{M}$, first encountered in section 7.3, is based on the micromechanics derivation of Dormieux [45] and Lemarchand [84]. It aims at a refined analysis of the pressure sensitivity of unleached and leached materials found in our experiments. These micromechanical concepts developed around the homogenization of poroelastic properties will be further developed in Chapter 8 for the application to strength of cement based materials. Both, poroelastic and strength properties, are the input for the chemomechanical model developed in Chapter 9. It will allow us to model the evolution of the mechanical performance between the asymptotic states.

7.1 Basic Aspects of Continuum Micromechanics of Cement-Based Materials

The field of micromechanics has become of great importance over the last fifty years, in particular in the context of the development of new materials with complex microstructures that requires mechanical techniques to predict macroscopic properties. As experimental tools for microstructural treatments at the nanometer scale become available, the demands towards predictive mechanical techniques increase. Continuum micromechanics represents the systematic approach to obtain mechanical properties at a larger length scale based on the properties of the material below this length scale. Most of the developments in this field focused until recently primarily on linear elastic properties in small deformations [161]. More recent contributions, among them the developments presented in Chapter 8, extend the approach to the micromechanical analysis of strength properties [84, 139]. An excellent review paper has been presented recently by Zaoui [161].

7.1.1 The Representative Volume Element (RVE) at the Three-Level Microstructure

A prerequisite for the application of continuum micromechanics is the existence of a Representative Volume Element (RVE). If we characterize its length scale by l, the following two conditions must be met to guarantee its existence:

1. $l \ll L$, where L is the length scale of the macroscopic structure in which the considered

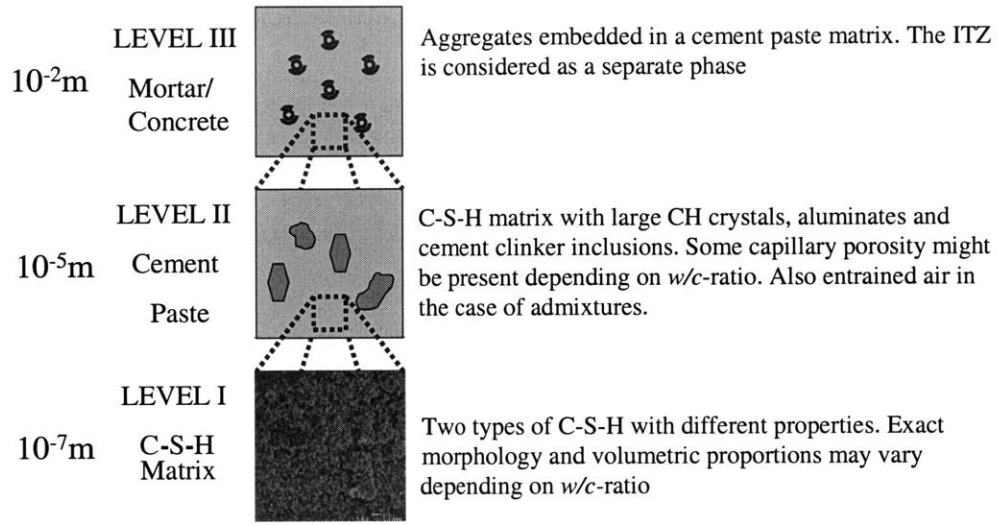

Figure 7-1: Recall of the three-level microstructure of cementitious materials and the characteristic length scale l. Adapted from [37].

material exists. This condition assures that the continuum mechanics techniques can be applied and continuous stress and deformation fields can be determined.

2. $l \gg d$, where d is the length scale of the heterogeneities considered in the micromechanical analysis. This condition is necessary to assign homogeneous properties to the macroscopic scale.

These two conditions are also called separability-of-scales conditions. The three-level microstructure we consider respects these conditions (see Figure 7-1): At Level I, the length scale l is on the order of 10^{-7} m, which is on the one hand considerably larger than the nanometer scale inhomogeneities of C-S-H and on the other hand much smaller than the characteristic length scale of Level II, that is roughly 10^{-5} m. In turn, the characteristic length scale of Level III is 10^{-2} m. This shows that the proposed microstructure division respects the separation of scales.

7.1.2 The Three Steps in Continuum Micromechanics

A micromechanical analysis can be broken down into three steps [160]:

- Representation: This is the choice of material elements that are considered and their respective mechanical properties.
- Localization: This is the analysis of the microscopic stress and deformation response to the macroscopically applied boundary conditions.
- Homogenization: This last step refers to the averaging procedure that leads to the macroscopic behavior. Here particularly the type of average to be chosen is of importance.

7.1.3 Representation

The representation deals with the description of the considered system. Simplifications in the geometrical description are necessary to deal with complex microstructures. Different *phases* need to be identified with their mechanical properties and their geometrical nature. Phases in continuum micromechanics are, as will become clearer in the following steps, domains with constant material properties. Depending on the considered material, this leads to the distinction between matrix and fibers, matrix and aggregates, and so on. The phases are defined by volume fractions. An alternative to the use of volume fractions is the use of a statistical representation of different equivalent RVEs. Then the probability to find a certain mechanical property at a point in space becomes the descriptive variable of the representation. An underlying hypothesis in Continuum Micromechanics is the ergodicity, that is the equivalence between spacial and ensemble averages [78]. This is expressed by the volume average of a spatially varying microscopic property, say $y = y(x)$, in the form:

$$\langle y \rangle_\Omega = \frac{1}{|\Omega|} \int_\Omega y(\mathbf{x})\, d\Omega \tag{7.1}$$

where Ω refers to the domain over which the quantity is averaged.

For the considered cement based materials, we consider the following phases:

- At Level I there are two phases: the C-S-H$_\alpha$ and the C-S-H$_\beta$ with volume fractions f_α

and f_β, respectively. Because of the much larger volume fraction of C-S-H_α, the C-S-H_β are represented as inclusions in the C-S-H_α matrix.

- At Level II, we consider the Portlandite, the unhydrated clinker and voids, all imbedded in the homogeneous C-S-H matrix as spherical inclusions.
- At Level III, the cement paste is considered as a matrix phase with aggregates as inclusions. The ITZ is considered as a separate phase depending on the confinement level, which will be developed later.

7.1.4 Localization

The next step is the mechanical analysis of the RVE subjected on its boundary to two types of boundary conditions called Hashin conditions:

- *Homogeneous stresses applied on the boundary*; that is:

$$\text{On } \partial\Omega_{\mathbf{T}^d} : \mathbf{T}^d = \boldsymbol{\Sigma} \cdot \mathbf{n} \tag{7.2}$$

where $\boldsymbol{\Sigma}$ is the macroscopically applied stress tensor and $\mathbf{n}$ is the outward normal vector to the boundary $\partial\Omega$ of the RVE. With this boundary condition, the macroscopic stress is then the volume average of the microscopic stress $\boldsymbol{\sigma} = \boldsymbol{\sigma}(\mathbf{x})$:

$$\boldsymbol{\Sigma} = \langle \boldsymbol{\sigma} \rangle_\Omega = \frac{1}{|\Omega|} \int_\Omega \boldsymbol{\sigma}(\mathbf{x})\, d\Omega \tag{7.3}$$

- *Homogeneous deformations applied on the boundary*; that is:

$$\text{On } \partial\Omega_{\boldsymbol{\xi}^d} : \boldsymbol{\xi}^d = \mathbf{E} \cdot \mathbf{x} \tag{7.4}$$

where $\mathbf{E}$ is the homogeneous macroscopic strain and $\mathbf{x}$ the coordinate vector, locating the material point in the microstructure. Macroscopic strain and microscopic strain $\boldsymbol{\varepsilon}(\mathbf{x})$ are then related by the following volume average:

$$\mathbf{E} = \langle \boldsymbol{\varepsilon} \rangle_\Omega = \frac{1}{|\Omega|} \int_\Omega \boldsymbol{\varepsilon}(\mathbf{x})\, d\Omega \tag{7.5}$$

The localization properly speaking consists in determining the microscopic stresses and strains as functions of the macroscopically applied boundary conditions. In the simplest case, that is for linear elastic problems, the microscopic and macroscopic stresses and strains are linked linearly through localization relations of the type:

$$\boldsymbol{\varepsilon}(\mathbf{x}) = \mathbb{A}(\mathbf{x}) : \mathbf{E};\ \langle \mathbb{A}(\mathbf{x}) \rangle = \mathbb{I} \tag{7.6}$$

$$\boldsymbol{\sigma}(\mathbf{x}) = \mathbb{B}(\mathbf{x}) : \boldsymbol{\Sigma};\ \langle \mathbb{B}(\mathbf{x}) \rangle = \mathbb{I} \tag{7.7}$$

where $\mathbb{A}(\mathbf{x})$ and $\mathbb{B}(\mathbf{x})$ represent the 4th order strain localization tensor, respectively stress localization tensor and $\mathbb{I}$ is the 4th order unit tensor. $\mathbb{A}(\mathbf{x})$ and $\mathbb{B}(\mathbf{x})$ can be evaluated in some (rare) cases through the solution of an elastic boundary value problems (BVP). In other cases they can be approximated by variational methods. The most commonly encountered case is the estimation of the localization tensor through consideration of the Eshelby inclusion problem [48]: An ellipsoidal inclusion embedded in an elastic reference medium subjected to constant strain at infinity[2]. This reference solution provides an estimate for the localization tensor of a phase r [160]:

$$\langle \mathbb{A} \rangle_{\omega_r} \equiv \mathbb{A}_r^{est} = \left[\mathbb{I} + \mathbb{S}_r^{Esh} : \left(\mathbb{C}_0^{-1} : \mathbb{C}_r - \mathbb{I} \right) \right]^{-1} : \left\langle \left[\mathbb{I} + \mathbb{S}_r^{Esh} : \left(\mathbb{C}_0^{-1} : \mathbb{C}_r - \mathbb{I} \right) \right]^{-1} \right\rangle^{-1} \tag{7.8}$$

where $\langle \mathbb{A} \rangle_{\omega_r}$ stands for the volume average of the localization tensor over material volume of phase r, ω_r. $\mathbb{C}_0$ is the fourth order elasticity tensor of the reference medium, $\mathbb{C}_r$ is the fourth order elasticity tensor of phase r and $\mathbb{S}_r^{Esh}$ is the Eshelby tensor of phase r which depends on the reference medium (through $\mathbb{C}_0$) and the geometry and orientation of r. According to the choice of the reference medium, we distinguish:

- The Mori-Tanaka (MT) scheme [108], in which the reference medium is taken to be the matrix phase, i.e. $\mathbb{C}_0 \equiv \mathbb{C}_m$.

[2] Eshelby, in his 1957 landmark paper, considered the response of an ellipsoidal particle in an infinite elastic solid subjected to constant strain at infinity and showed that the stress and strain state in the particle is uniform. This solution is used in many localization schemes. This is expressed by (7.8) which is the solution for such an inclusion phase. In turn, for any other phase r (than the inclusion) in which the strain varies, (7.8) provides an estimate for the on-average constant phase-localization tensor $\langle \mathbb{A} \rangle_{\omega_r}$.

- The Self-Consistent scheme [34], in which the REV is chosen as reference medium, that is $\mathbb{C}_0 \equiv \mathbb{C}_{\text{hom}}$. Both schemes will be employed for different levels in the sequel.

7.1.5 Homogenization

The last step in Continuum Micromechanics is the homogenization step by which the properties of the equivalent homogeneous material are determined. This involves expressing the macroscopic strains and stresses as functions of the microscopic stresses and strains. For the determination of homogeneous elastic properties the stress average (7.3) is evaluated. With the strain localization condition (7.6), the microscopic stress can be written as $\boldsymbol{\sigma}_r(\mathbf{x}) = (\mathbb{C} : \mathbb{A}) : \mathbf{E}$ which leads to the following expression of the macroscopic elasticity tensor:

$$\boldsymbol{\Sigma} = \mathbb{C}_{\text{hom}} : \mathbf{E};\ \mathbb{C}_{\text{hom}} = \langle \mathbb{C} : \mathbb{A} \rangle_\Omega = \sum_r f_r \mathbb{C}_r : \mathbb{A}_r^{est} \tag{7.9}$$

where $f_r = \omega_r / \Omega$ is the volume fraction of phase r. It is important to note that linear homogenization methods such as Equation (7.9) contain only a simple volume average or what is called the first moment of the local strains. Higher order averages could be defined too; and will be introduced in Chapter 8 for non-linear strength homogenization.

7.2 Estimation of the Elastic Properties in the Three-Level Microstructure

In this section we apply the presented micromechanical techniques to the homogenization of the elastic properties. This procedure takes place in the framework of the three level microstructure and is partly based on the work of Constantinides [37]. For the homogenization steps, two different schemes are used. The Mori-Tanaka (MT) scheme [108], which considers a matrix with reinforcing inclusions and the Hervé-Zaoui (HZ) scheme [65] which considers a *n+1* spheres composite, and which belongs to the family of Self-Consistent schemes. The MT scheme will be used to homogenize the elasticity properties of Levels I and II. The HZ scheme will be used to homogenize the properties at Level III.

7.2.1 Mori-Tanaka Scheme

The MT scheme considers inclusions in a continuos matrix. The estimate of the localization tensor $\mathbb{A}_r^{est}(\mathbf{x})$ for phase r in the Mori Tanka scheme is obtained from the Eshelby inclusion solution (7.8) by considering the matrix as the reference medium ($\mathbb{C}_0 \equiv \mathbb{C}_m$). Every inclusion phase is considered individually in the MT scheme. Taking into account the random microstructure, we assume spherical inclusions and isotropic elasticity. For the case of isotropic elasticity, the elasticity tensors of inclusion and matrix are written as the sum of a deviatoric and a volumetric part:

$$\mathbb{C}_I = 3k_I\mathbb{K} + 2\mu_I\mathbb{J};\ \mathbb{C}_m = 3k_m\mathbb{K} + 2\mu_m\mathbb{J} \tag{7.10}$$

where k_I, μ_I, k_m and μ_m are the bulk moduli and shear moduli of the inclusion and matrix, respectively; $\mathbb{J}$ and $\mathbb{K}$ are the deviatoric and volumetric part of the fourth order unit tensor[3]. In addition the assumption of spherical inclusions implies for the Eshelby tensor:

$$\mathbb{S}_I^{Esh} = \beta^m\mathbb{J} + \alpha^m\mathbb{K} \tag{7.11}$$

where

$$\beta^m = \frac{6\,(k_m + 2\mu_m)}{5\,(3k_m + 4\mu_m)};\ \alpha^m = \frac{3k_m}{3k_m + 4\mu_m} \tag{7.12}$$

A combination of (7.8), (7.9), (7.10) and (7.11) for each inclusion phase leads to an isotropic macroscopic elasticity tensor which can be expressed through the following estimates for the

[3]This partition is based on the partition of the fourth order unit tensor $\mathbb{I} = \mathbb{J}+\mathbb{K}$ with $\mathrm{I}_{ijkl} = \frac{1}{2}\left(\delta_{ik}\delta_{jl} + \delta_{il}\delta_{jk}\right)$ and $\mathrm{K}_{ijkl} = \frac{1}{3}\delta_{ij}\delta_{kl}$. Then the following relations hold: $\mathbb{K} : \mathbf{1} = \mathbf{1}$, $\mathbb{J} : \mathbf{1} = \mathbf{0}$, $\mathbf{K} : \mathbf{D} = \mathbf{0}$, $\mathbb{J} : \mathbf{D} = \mathbf{D}$, where $\mathbf{D}$ is the deviator of a symetric second order tensor [160].

homogenized bulk and shear moduli (see Table 7.1):

$$k_{\text{hom}}^{est} = \sum_r f_r k_r \left\langle A^{v,est} \right\rangle_{\omega_r} = \sum_r f_r k_r \left(1 + \alpha^m \left(\frac{k_r}{k_m} - 1\right)\right)^{-1} \times \left[\sum_r f_r \left(1 + \alpha^m \left(\frac{k_r}{k_m} - 1\right)\right)^{-1}\right]^{-1} \tag{7.13}$$

$$\mu_{\text{hom}}^{est} = \sum_r f_r \mu_r \left\langle A^{d,est} \right\rangle_{\omega_r} = \sum_r f_r \mu_r \left(1 + \beta^m \left(\frac{\mu_r}{\mu_m} - 1\right)\right)^{-1} \times \left[\sum_r f_r \left(1 + \beta^m \left(\frac{\mu_r}{\mu_m} - 1\right)\right)^{-1}\right]^{-1} \tag{7.14}$$

where $\left\langle A^{v,est} \right\rangle_{\omega_r}$ and $\left\langle A^{d,est} \right\rangle_{\omega_r}$ are the volumetric and the deviatoric part of the localization tensor $\langle \mathbb{A} \rangle_{\omega_r} = \left\langle A^{v,est} \right\rangle_{\omega_r} \mathbb{K} + \left\langle A^{d,est} \right\rangle_{\omega_r} \mathbb{J}$, which are estimated by $\left\langle A^{v,est} \right\rangle_{\omega_r} = a_r^{v,est}$ and $\left\langle A^{d,est} \right\rangle_{\omega_r} = a_r^{d,est}$, developed in Table 7.1. The previous relation simplifies in the case of only one inclusion embedded in a matrix phase to:

$$\frac{k_{\text{hom}}^{est}}{k_m} = 1 + f_I \frac{k_I - k_m}{1 + \alpha^m (1 - f_I)(k_I/k_m - 1)} \tag{7.15}$$

$$\frac{\mu_{\text{hom}}^{est}}{\mu_m} = 1 + f_I \frac{\mu_I - \mu_m}{1 + \beta^m (1 - f_I)(\mu_I/\mu_m - 1)} \tag{7.16}$$

where f_I is the volume fraction of the inclusions. Finally, from the homogenized bulk and shear moduli, the Young's modulus and Poisson's ratio can be determined from:

$$E_{\text{hom}}^{est} = \frac{9 k_{\text{hom}}^{est} \mu_{\text{hom}}^{est}}{3 k_{\text{hom}}^{est} + \mu_{\text{hom}}^{est}}; \quad \nu_{\text{hom}}^{est} = \frac{3 k_{\text{hom}}^{est} - 2 \mu_{\text{hom}}^{est}}{6 k_{\text{hom}}^{est} + 2 \mu_{\text{hom}}^{est}} \tag{7.17}$$

7.2.2 Elastic Properties on Levels I and II

On Level I, the two types of C-S-H are considered with volume fractions f_α and f_β. The elastic properties of both types of C-S-H, E_α, E_β, ν_α and ν_β, respectively, were measured by Constantinides [37] in the leached and unleached state. Their values are reported as input parameters for a $w/c = 0.5$ cement paste in Tables 7.2 and 7.3 along with the values for the volume fractions. The stiffness difference between the two C-S-H types and the difference in

Determination of the localization tensor for the MT scheme with isotropic phases and spherical inclusions.

$\mathbb{A}_r^{est} = \left[\mathbb{I} + \mathbb{S}_r^{Esh} : \left(\mathbb{C}_0^{-1} : \mathbb{C}_r - \mathbb{I}\right)\right]^{-1} : \left\langle \left[\mathbb{I} + \mathbb{S}_r^{Esh} : \left(\mathbb{C}_0^{-1} : \mathbb{C}_r - \mathbb{I}\right)\right]^{-1} \right\rangle^{-1}$

The matrix is the reference medium: $\mathbb{C}_0 = \mathbb{C}_m$;

All phases are considered isotropic: $\mathbb{C}_m = 3k_m\mathbb{K} + 2\mu_m\mathbb{J}$; $\mathbb{C}_r = 3k_r\mathbb{K} + 2\mu_r\mathbb{J}$

Therefore the inverse reads: $\mathbb{C}_m^{-1} = \frac{1}{3k_m}\mathbb{K} + \frac{1}{2\mu_m}\mathbb{J}$

And $\mathbb{C}_0^{-1} : \mathbb{C}_r = \frac{k_r}{k_m}\mathbb{K} + \frac{\mu_r}{\mu_m}\mathbb{J}$; $\mathbb{C}_0^{-1} : \mathbb{C}_r - \mathbb{I} = \left(\frac{k_r}{k_m} - 1\right)\mathbb{K} + \left(\frac{\mu_r}{\mu_m} - 1\right)\mathbb{J}$
In the case of spherical inclusions: $\mathbb{S}_r^{Esh} = \beta^m\mathbb{J} + \alpha^m\mathbb{K}$

Therefore: $\mathbb{S}_r^{Esh} : \left(\mathbb{C}_0^{-1} : \mathbb{C}_r - \mathbb{I}\right) = \alpha^m\left(\frac{k_r}{k_m} - 1\right)\mathbb{K} + \beta^m\left(\frac{\mu_r}{\mu_m} - 1\right)\mathbb{J}$

and $\mathbb{I} + \mathbb{S}_r^{Esh} : \left(\mathbb{C}_0^{-1} : \mathbb{C}_r - \mathbb{I}\right) = \left(1 + \alpha^m\left(\frac{k_r}{k_m} - 1\right)\right)\mathbb{K} + \left(1 + \beta^m\left(\frac{\mu_r}{\mu_m} - 1\right)\right)\mathbb{J}$

the inverse of which is: $\left(1 + \alpha^m\left(\frac{k_r}{k_m} - 1\right)\right)^{-1}\mathbb{K} + \left(1 + \beta^m\left(\frac{\mu_r}{\mu_m} - 1\right)\right)^{-1}\mathbb{J}$

Given that the properties are constant in space, the volume average of this expression reads:
$\left\langle \left[\mathbb{I} + \mathbb{S}_r^{Esh} : \left(\mathbb{C}_0^{-1} : \mathbb{C}_r - \mathbb{I}\right)\right]^{-1} \right\rangle = \sum_r f_r \left[\left(1 + \alpha^m\left(\frac{k_r}{k_m} - 1\right)\right)^{-1}\mathbb{K} + \left(1 + \beta^m\left(\frac{\mu_r}{\mu_m} - 1\right)\right)^{-1}\mathbb{J}\right]$

The inverse of which reads:
$\left[\sum_r f_r\left(1 + \alpha^m\left(\frac{k_r}{k_m} - 1\right)\right)^{-1}\right]^{-1}\mathbb{K} + \left[\sum_r f_r\left(1 + \beta^m\left(\frac{\mu_r}{\mu_m} - 1\right)\right)^{-1}\right]^{-1}\mathbb{J}$

The localization tensor $\mathbb{A}_r^{est}$ for isotropic phases and spherical inclusions
reduces to: $\mathbb{A}_r = a_r^{v,est}\mathbb{K} + a_r^{d,est}\mathbb{J}$
where $a_r^{v,est} = \left(1 + \alpha^m\left(\frac{k_r}{k_m} - 1\right)\right)^{-1}\left[\sum_r f_r\left(1 + \alpha^m\left(\frac{k_r}{k_m} - 1\right)\right)^{-1}\right]^{-1}$
and $a_r^{d,est} = \left(1 + \beta^m\left(\frac{\mu_r}{\mu_m} - 1\right)\right)^{-1}\left[\sum_r f_r\left(1 + \beta^m\left(\frac{\mu_r}{\mu_m} - 1\right)\right)^{-1}\right]^{-1}$

Table 7.1: Localization tensor for the Mori-Tanaka scheme with spherical inclusions and isotropic phases.

	Undegraded	Output	
	Input [GPa]	MT Loc. Factors	Elastic Prop. [GPa]
Level I	$E_\alpha = 21.7, E_\beta = 29.4$	$a_\alpha^{v,est} = 1.051$	$E^{est}_{\text{C-S-H}} = 23.8$
	$\nu_\alpha = \nu_\beta = 0.24$	$a_\alpha^{v,est} = 0.881$	$\nu^{est}_{\text{C-S-H}} = 0.24$
	$f_\alpha = 0.3, f_\beta = 0.7$	$a_\alpha^{d,est} = 1.047$	$k^{est}_{\text{C-S-H}} = 15.2$
	$k_\alpha = 13.9, k_\beta = 18.8$	$a_\alpha^{d,est} = 0.891$	$\mu^{est}_{\text{C-S-H}} = 9.6$
	$\mu_\alpha = 8.8, \mu_\beta = 11.9$		
Level II	$E_{\text{C-S-H}}, E_{CH} = 38$	$a^{v,est}_{\text{C-S-H}} = 1.008$	$E^{est}_{Paste} = 23.5$
	$\nu_{\text{C-S-H}}, \nu_{CH} = 0.31$	$a^{v,est}_{\text{CH}} = 0.612$	$\nu^{est}_{Paste} = 0.25$
	$f_{\text{C-S-H}} = 0.86, f_{CH} = 0.11$	$a^{v,est}_{\text{voids}} = 2.208$	
	$k_{\text{CH}} = 33.3$	$a^{d,est}_{\text{C-S-H}} = 0.993$	$k^{est}_{Paste} = 15.4$
	$\mu_{\text{CH}} = 14.5$	$a^{d,est}_{\text{CH}} = 0.793$	$\mu^{est}_{Paste} = 9.4$
		$a^{d,est}_{\text{voids}} = 1.952$	

Table 7.2: Results from the micromechanical modeling of the elastic properties in the unleached state for Levels I and II [37].

Asymptotically Degraded		Output	
	Input[GPa]	MT Loc. Factors	Elastic Prop.[GPa]
Level I	$E_\alpha = 3.0, E_\beta = 12.0$	$a_\alpha^{v,est} = 1.229$	$E^{est}_{\text{C-S-H}} = 4.3$
	$\nu_\alpha = \nu_\beta = 0.24$	$a_\alpha^{v,est} = 0.467$	$\nu^{est}_{\text{C-S-H}} = 0.24$
	$f_\alpha = 0.3, f_\beta = 0.7$	$a_\alpha^{d,est} = 1.218$	$k^{est}_{\text{C-S-H}} = 2.7$
	$k_\alpha = 13.9, k_\beta = 18.8$	$a_\alpha^{d,est} = 0.492$	$\mu^{est}_{\text{C-S-H}} = 1.7$
	$\mu_\alpha = 8.8, \mu_\beta = 11.9$		
Level II	$E_{\text{C-S-H}}$	$a^{v,est}_{\text{C-S-H}} = 0.802$	$E^{est}_{Paste} = 2.8$
	$\nu_{\text{C-S-H}}$	$a^{v,est}_{\text{voids}} = 1.744$	$\nu^{est}_{Paste} = 0.23$
	$f_{\text{C-S-H}} = 0.79, f_{voids} = 0.21$	$a^{d,est}_{\text{C-S-H}} = 0.831$	$k^{est}_{Paste} = 1.73$
		$a^{d,est}_{\text{voids}} = 1.636$	$\mu^{est}_{Paste} = 1.1$

Table 7.3: Results from the micromechanical modeling of the elastic properties in the leached state for Levels I and II [37].

volume fractions, makes the application of the MT scheme attractive. Application of (7.15) through (7.17) delivers the estimates for the homogeneous elasticity parameters of the C-S-H matrix given in Table 7.2 and 7.3.

On Level II, we consider a C-S-H matrix with Portlandite inclusions and voids. The C-S-H matrix becomes the reference medium for the MT scheme while the Portlandite inclusions and the voids are treated individually as inclusions. Tables 7.2 and 7.3 report the input data for the leached and unleached material state. The elastic properties of Portlandite are based on measurements by Beaudoin [14] and Wittmann [155]. The volume fractions were estimated by Constantinides [37] for the cement paste tested in this study. The change in volume fraction of the C-S-H in the degraded state corresponds to the creation of a macroporosity associated with the C-S-H decalcification (see Section 2.3.2). Application of (7.13), (7.14) and (7.17) yields estimates for the Young's modulus of the intact and homogeneously leached cement paste reported in Tables 7.2 and 7.3. These estimates compare well to the experimentally obtained values (see Table 2.5)[4]. With the micromechanical techniques in place and a good comparison with the experimental data, Constantinides also estimated the elastic properties of a cement paste in which only the Portlandite has been dissolved but the C-S-H are intact [37]. In such a case the homogenization of Level I remains unchanged as in the undegraded case. On Level II, the volume fraction of Portlandite becomes zero and the void volume fraction increases correspondingly. Table 7.4 summarizes the input data and the result for the Young's modulus as Equations (7.15) through (7.17) are applied.

7.2.3 Hervé-Zaoui Scheme

At Level III, the representation of the material as individual inclusions in a matrix is no more adequate. The ITZ is expected to influence considerably the homogenized elastic properties. To enhance the representation, we use the Hervé-Zaoui (HZ) scheme. The HZ scheme describes an infinite domain consisting of $n+1$ inclusions. In the case of cement-based materials at Level III, n is equal to three. The three inclusions are the aggregate, the surrounding ITZ and the cement paste matrix. The $n+1=4$th layer corresponds to the homogenized material, which is

[4]A difference to the model originally presented by Constantinides & Ulm exists with respect to the fluid: In contrast to Constantinides & Ulm, we determine drained elastic properties and neglect the stiffness of the water phase.

	Only CH dissolved	Output	
	Input [GPa]	MT Loc. Factors	Elastic Prop. [GPa]
Level I	$E_\alpha = 21.7, E_\beta = 29.4$	$a_\alpha^{v,est} = 1.051$	$E_{\text{C-S-H}}^{est} = 23.8$
	$\nu_\alpha = \nu_\beta = 0.24$	$a_\alpha^{v,est} = 0.881$	$\nu_{\text{C-S-H}} = 0.24$
	$f_\alpha = 0.3, f_\beta = 0.7$	$a_\alpha^{d,est} = 1.047$	$k_{\text{C-S-H}}^{est} = 15.2$
		$a_\alpha^{d,est} = 0.891$	$\mu_{\text{C-S-H}}^{est} = 9.6$
Level II	$E_{\text{C-S-H}}$	$a_{\text{C-S-H}}^{v,est} = 0.857$	$E_{Paste}^{est} = 17.9$
	$\nu_{\text{C-S-H}}$	$a_{\text{voids}}^{v,est} = 1.878$	$\nu_{Paste}^{est} = 0.23$
	$f_{\text{C-S-H}} = 0.86, f_{voids} = 0.14$	$a_{\text{C-S-H}}^{d,est} = 0.881$	$k_{Paste}^{est} = 11.2$
		$a_{\text{voids}}^{d,est} = 1.732$	$\mu_{Paste}^{est} = 7.3$

Table 7.4: Results from the micromechanical modeling of the elastic properties for the intermediate leaching state in which only Portlandite dissolved [37]

the reference material in this scheme. Accordingly, the HZ scheme belongs to the family of Self Consistent schemes. The representation is shown in Figure 7-2. The different spheres are characterized by their radius, R_θ ($\theta \in [1,3]$ is the subscript used in this section for the different phases, 1 = Aggregate, 2 = ITZ, 3 = matrix); and the volume fractions of the different phases are given by:

$$f_\theta = \frac{R_\theta^3 - R_{\theta-1}^3}{R_3^3};\ \frac{R_\theta}{R_3} = \sqrt[3]{\sum_{i=1}^{\theta} f_i};\ \ \theta \in [1,3] \tag{7.18}$$

where $V = \frac{4}{3}\pi R_3^3$ is the reference volume. To determine the localization tensors $\mathbb{A}_\theta(\mathbf{x})$ (Equation (7.6)), a boundary value problem (BVP) has to be solved which yields the microscopic strains as functions of the macroscopically applied strains. The BVP is different from Eshelby's problem because several layered inclusions are considered in the infinite domain.

Hervé-Zaoui's Solution of the BVP

We briefly recall here the solution elements provided by Hervé & Zaoui [65]. We consider the homogeneous deformation condition (7.4) at infinity in spherical coordinates:

$$\begin{aligned} \partial\Omega_{\boldsymbol{\xi}^d} : \boldsymbol{\xi}^d = \mathbf{E}\cdot\mathbf{x} \ &= \ \left(r\frac{\lambda_0}{3} + \gamma r \sin^2\psi\cos 2\phi\right)\mathbf{e}_r + \gamma r \sin\psi\cos\vartheta\cos 2\phi\mathbf{e}_\psi \\ &- \ \gamma r \sin\psi \sin 2\phi \mathbf{e}_\phi \end{aligned} \tag{7.19}$$

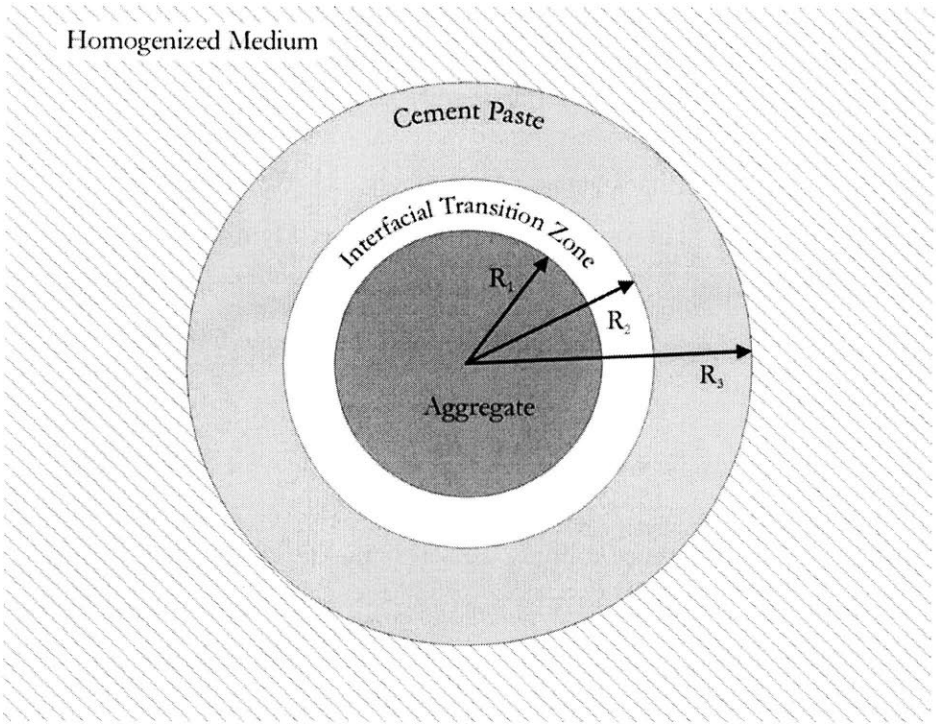

Figure 7-2: Geometrical representation of Hervé-Zaoui scheme applied to Level III (mortar, concrete).

For the volumetric displacement at infinity, the displacement field is purely radial and reads:

$$\xi_r^{(\theta)} = F_\theta r + \frac{G_\theta}{r^2}$$

The constants F_θ and G_θ are determined from the displacement and stress continuity between the phases. This can be written in the following compact form:

$$\mathbf{J}_\theta(R_\theta)\,\mathbf{V}_\theta = \mathbf{J}_{\theta+1}(R_\theta)\,\mathbf{V}_{\theta+1}$$

where $\mathbf{V}_\theta = [F_\theta\ G_\theta]^T$, and$\mathbf{J}_\theta(R_\theta)$ is given by:

$$\mathbf{J}_\theta(R_\theta) = \begin{bmatrix} r & \frac{1}{r^2} \\ 3k_\theta & -\frac{4\mu_\theta}{r^3} \end{bmatrix}$$

The previous relations allow the successive determination of the constants in phase $\theta+1$ from the ones determined before in phase θ :

$$\mathbf{V}_{\theta+1} = \mathbf{N}_\theta^{(\theta)}\mathbf{V};\ \mathbf{N}^{(\theta)} = \mathbf{J}_{\theta+1}^{-1}(R_\theta)\,\mathbf{J}_\theta(R_\theta)$$

which gives the possibility to express all unknown coefficients with respect to the first phase:

$$\mathbf{V}_{\theta+1} = \mathbf{Q}^{(\theta)}\mathbf{V};\ \mathbf{Q}^{(\theta)} = \prod_{j=1}^{\theta}\mathbf{N}_j$$

Carrying out this operation for the considered three phase representation yields:

$$\mathbf{V}_\theta = \begin{pmatrix} F_\theta \\ G_\theta \end{pmatrix} = \frac{F_4}{Q_{11}^{(3)}} \begin{pmatrix} Q_{11}^{(\theta-1)} \\ Q_{21}^{(\theta-1)} \end{pmatrix};\ F_4 = \frac{\lambda_0}{3}$$

Table 7.5: Hervé-Zaoui's solution for a volumetric displacement [65].

in which the first term is purely volumetric with λ_0 a constant, and where $\mathbf{e}_r$ is the radial unit vector. The other terms correspond to a purely deviatoric displacement. Tables 7.6 and 7.5 recall the solution of the BVP due to Hervé and Zaoui [65].

With these solutions for the displacements in each phase in hand, the microscopic strain in phase θ is evaluated from the standard strain-displacement relation:

$$\epsilon_\theta(\underline{x}) = \frac{1}{2}\left(\boldsymbol{\nabla}\cdot\boldsymbol{\xi}^{(\theta)} + {}^t\boldsymbol{\nabla}\cdot\xi^{(\theta)}\right) \tag{7.20}$$

In the volumetric loading case, application of (7.20) yields the volumetric localization coefficients for the Hervé-Zaoui-scheme

$$\langle A^v\rangle_{\omega_\theta} \equiv A_\theta^{v,est} = \frac{F_\theta}{F_4} \tag{7.21}$$

and for the deviatoric loading, the deviatoric localization factor reads:

$$\left\langle A^d\right\rangle_{\omega_\theta} \equiv A_\theta^{d,est} = \bar{a}_\theta - \frac{21}{5}\frac{R_\theta^5 - R_{\theta-1}^5}{(1-2\nu_\theta)\left(R_\theta^3 - R_{\theta-1}^3\right)}\bar{b}_\theta \tag{7.22}$$

For the deviatoric loading case, the components of the displacement field in the REV read in spherical coordinates

$$\xi_r^{(\theta)} = U_r^{(\theta)}(r)\sin^2\psi\cos 2\phi$$
$$\xi_\psi^{(\theta)} = U_\psi^{(\theta)}(r)\sin\psi\cos\psi\cos 2\phi$$
$$\xi_\phi^{(\theta)} = U_\phi^{(\theta)}(r)\sin\psi\sin 2\phi,$$

with

$$\begin{pmatrix} U_r^{(\theta)} \\ U_\psi^{(\theta)} \\ U_\phi^{(\theta)} \end{pmatrix} = \begin{bmatrix} r & -\frac{6\nu_\theta}{1-2\nu_\theta}r^3 & \frac{3}{r^4} & \frac{5-4\nu_\theta}{1-2\nu_\theta}\frac{1}{r^2} \\ r & -\frac{7-4\nu_\theta}{1-2\nu_\theta}r^3 & -\frac{2}{r^4} & \frac{2}{r^2} \\ -r & \frac{7-4\nu_\theta}{1-2\nu_\theta}r^3 & \frac{2}{r^4} & -\frac{2}{r^4} \end{bmatrix} \begin{pmatrix} a_\theta \\ b_\theta \\ c_\theta \\ d_\theta \end{pmatrix}$$

The constants a_θ, b_θ, c_θ and d_θ are determined through four independent displacement and stress continuity conditions between the phases. These conditions are written in the compact form: $\mathbf{L}_\theta(R_\theta)\cdot\mathbf{W}_\theta = \mathbf{L}_{\theta+1}(R_{\theta+1})\cdot\mathbf{W}_{\theta+1}$

where $\mathbf{W}_\theta = \begin{bmatrix} a_\theta & b_\theta & c_\theta & d_\theta \end{bmatrix}^T$, and $\mathbf{L}_\theta(r)$ is given by:

$$\mathbf{L}_\theta(r) = \begin{bmatrix} r & -\frac{6\nu_\theta}{1-2\nu_\theta}r^3 & \frac{3}{r^4} & \frac{5-4\nu_\theta}{1-2\nu_\theta}\frac{1}{r^2} \\ r & -\frac{7-4\nu_\theta}{1-2\nu_\theta}r^3 & -\frac{2}{r^4} & \frac{2}{r^2} \\ \mu_\theta & \frac{3\nu_\theta}{1-2\nu_\theta}\mu_\theta r^2 & -\frac{12}{r^5}\mu_\theta & \frac{2(\nu_\theta-5)}{1-2\nu_\theta}\frac{\mu_\theta}{r^3} \\ \mu_\theta & -\frac{7+2\nu_\theta}{1-2\nu_\theta}\mu_\theta r^2 & \frac{8}{r^5}\mu_\theta & 2\frac{1+\nu_\theta}{1-2\nu_\theta}\frac{\mu_\theta}{r^3} \end{bmatrix}$$

The previous relations allow the successive determination of the constants in layer $\theta+1$ from the one determined before in layer θ:

$$\mathbf{W}_{\theta+1} = \mathbf{M}^{(\theta)}\cdot\mathbf{W}_\theta;\ \mathbf{M}^{(\theta)} = \mathbf{L}_{\theta+1}^{-1}(R_\theta)\cdot\mathbf{L}_\theta(R_\theta)$$

This gives the possibility to express all unknown coefficients with respect to phase 1:

$$\mathbf{W}_{\theta+1} = \mathbf{P}^{(\theta)}\cdot\mathbf{W}_1;\ \mathbf{P}^{(\theta)} = \prod_{j=1}^{\theta}\mathbf{M}^{(j)}(R_j)$$

Carrying out this operation for the three layered inclusion delivers the following explicit solution for the sought constants:

$$\mathbf{W}_\theta = \begin{pmatrix} a_\theta \\ b_\theta \\ c_\theta \\ d_\theta \end{pmatrix} = \frac{\gamma}{\sqrt{2}\left(P_{22}^{(3)}P_{11}^{(3)} - P_{12}^{(3)}P_{21}^{(3)}\right)}\mathbf{P}^{(\theta-1)}\cdot\begin{pmatrix} P_{22}^{(3)} \\ -P_{21}^{(3)} \\ 0 \\ 0 \end{pmatrix}$$

Given the linearity of $\mathbf{W}_\theta$ with respect to γ, it is convenient to work with the normalized constants $\overline{\mathbf{W}}_\theta = \mathbf{W}_\theta/\gamma = \begin{bmatrix} \bar{a}_\theta & \bar{b}_\theta & \bar{c}_\theta & \bar{d}_\theta \end{bmatrix}^T$.

Table 7.6: Hervé-Zaoui's solution for deviatoric displacement loading [65].

The coefficients F_θ, $\overline{a}_\theta$ and $\overline{b}_\theta$ are given in Table 7.5 and 7.6. In their original paper, Hervé and Zaoui determined the homogenized elastic properties by enforcing the equivalence of the average strains with the results for phase $n+1$. This can equivalently be expressed through the stress averages. The volumetric part of the macroscopic stress reads:

$$\Sigma_M = \frac{1}{3}\mathrm{tr}\boldsymbol{\Sigma} = \left\langle \frac{1}{3}\mathrm{tr}\boldsymbol{\sigma} \right\rangle = \langle k_\theta \mathrm{tr}\boldsymbol{\varepsilon}_\theta \rangle = \sum_\theta f_\theta k_\theta \langle \mathrm{tr}\boldsymbol{\varepsilon}_\theta \rangle_{\omega_\theta} = \sum_\theta f_\theta k_\theta A_\theta^{v,est} \mathrm{tr}\mathbf{E} = k_{\mathrm{hom}} \mathrm{tr}\mathbf{E} \quad (7.23)$$

which yields for the macroscopic bulk modulus:

$$k_{\mathrm{hom}} = \sum_\theta f_\theta k_\theta A_\theta^{v,est} \quad (7.24)$$

The deviatoric part of the macroscopic stress reads:

$$\mathbf{S} = \boldsymbol{\Sigma} - \Sigma_M \mathbf{1} = \langle \mathbf{s}_\theta \rangle = \langle 2\mu_\theta \boldsymbol{\epsilon}_\theta \rangle = \sum_\theta 2 f_\theta \mu_\theta \langle \boldsymbol{\epsilon}_\theta \rangle_{\omega_\theta} = \sum_\theta 2 f_\theta \mu_\theta A_\theta^{d,est} \mathbf{E}^d = 2\mu_{\mathrm{hom}} \mathbf{E}^d \quad (7.25)$$

where $\boldsymbol{\epsilon}_\theta = \boldsymbol{\varepsilon}_\theta - \frac{1}{3}\varepsilon_\theta^v \mathbf{1}$ is the microscopic strain deviator, with $\varepsilon_\theta^v = \mathrm{tr}\boldsymbol{\varepsilon}_\theta$, while $\mathbf{E}^d = \mathbf{E} - \frac{1}{3}\mathrm{tr}\mathbf{E}\mathbf{1}$ is its macroscopic equivalent. For the macroscopic shear modulus it follows:

$$\mu_{\mathrm{hom}} = \sum_\theta f_\theta \mu_\theta A_\theta^{d,est} \quad (7.26)$$

7.2.4 Elastic Properties on Level III

The HZ-scheme is used to upscale the elastic properties of Level III. In contrast to Levels I and II, on Level III the elastic properties of the ITZ are unknown. We therefore attempt to determine these properties by an inverse analysis comparing the micromechanical results with the experimental values obtained for mortars by Constantinides [37]. Similar attempts, but for different representations, have been made before by Ramesh et al. [119], Lutz and Zimmerman [88], Lutz et al. [87], Li et al. [86] and more recently by Hashin and Monteiro [62].

The volume fractions of the phases are the following: The aggregates (sand) make up for roughly 50% of the volume. For the ITZ, based on the SEM micrographs of the ITZ (Figure 7-3), we assume a thickness of $D = 20\,\mu$m which corresponds to typically observed sizes of the ITZ [96, 107]. Assuming a constant thickness of the ITZ for all aggregates, the volume fraction

	Unleached				Leached			
	E [GPa]	ν [1]	k [GPa]	μ [GPa]	E [GPa]	ν [1]	k [GPa]	μ [GPa]
Mortar (from [38])	25.1	0.22	15.1	10.2	4.8	0.20	2.6	1.9
Sand	62.5	0.21	35.9	25.8	62.5	0.21	35.9	25.8
Paste	23.5	0.25	15.4	9.4	2.8	0.23	1.7	1.1
ITZ (inverse analysis)	9.4	0.25	6.0	3.7	1.3	0.23	0.8	0.5

Table 7.7: Results from the homogenization at Level III for the ITZ stiffness

of the ITZ can be determined using the grading curve of the sand (Figure 4-1) from:

$$\frac{f_{ITZ}}{f_I} = \int_0^1 \frac{V_{ITZ}}{V_I} dm = \int_0^1 \left[\left(1 + \frac{D}{r(m)} \right)^3 - 1 \right] dm \tag{7.27}$$

where f_I is the total volume fraction of the aggregates. Application of (7.27) yields 30% for the ITZ volume fraction. Application of (7.24) and (7.26) with the determined volume fractions and the known elastic properties of paste (Tables 7.2 and 7.3) and the aggregates (Table 7.7) leads to the elastic properties of the ITZ. Table 7.7 shows the obtained values. In the case of the unleached mortar, the ITZ has 40% of the paste's stiffness, while in the leached case this ratio is 45%. This difference is small and suggests that the ITZ undergoes a degradation during leaching process similar to the paste, as far as the elasticity is concerned, despite the higher Portlandite content in the ITZ (Section 2.3.4).

7.3 Homogenization of the Biot Coefficient

Given the porous structure of unleached and leached materials, the determination of the Biot coefficients at the different levels of the microstructure is of interest. In section 6.5, we showed that leached materials become extremely pressure sensitive, such that their behavior obeys the effective stress concept. The question, however, is whether the effective stress concept is related to the validity of the effective stress concept in the elastic range or whether it is due to the pressure sensitivity related to plastic deformation. The first would correspond to a Biot coefficient close to one. The second to a Coussy coefficient $\beta = 1$ (see Eq. (5.18)). In this section, we want to apply the micromechanical techniques presented before to estimate the Biot coefficient at the different levels of the microstructure. This approach will allow us also

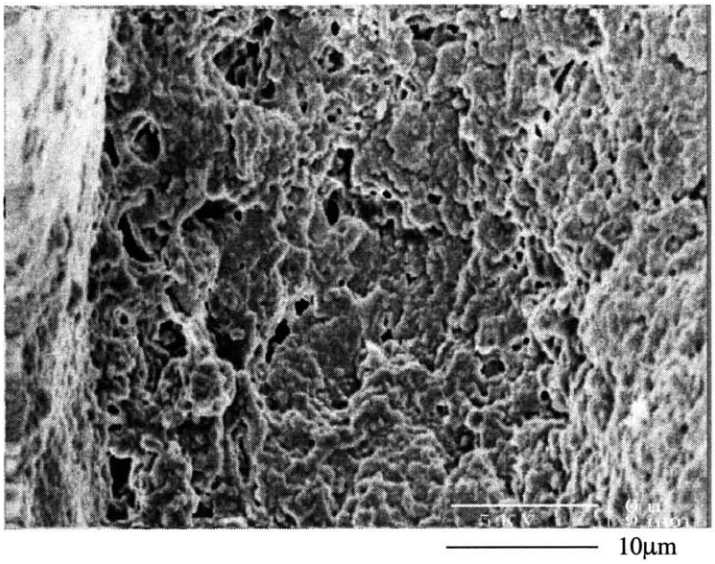

Figure 7-3: SEM micrograph of the Interfacial Transition Zone (ITZ) of a calcium depleted mortar, with sand inclusion (left) and matrix (right).

(1) to trace the influence of the leaching process and (2) to evaluate the influence of aggregates. To this end we first develop a general micromechanical approach for an n- phase solid with a saturated porosity. In a second step, we specify the representation as we apply the approach to the different levels of the microstructure.

7.3.1 Introduction

The theory of porous media in which the Biot coefficients have their place, deals with the interaction of the fluid pressure in the pore space and the solid phase. We have evoked this theory throughout the experimental part of this study, particularly in Section 5.2.4. The effect of the pore pressure on behavior of the porous medium has been addressed first by Terzaghi [143] in the context of a consolidation theory and was expanded by Biot [19], Gassmann [55] and Skemtpon [135]. The micromechanical treatment of poromechanical problems is more recent and due to Dormieux [45] and Lemarchand [84].

Building on these works, we consider an REV that is composed of the pore space with Lagrangian porosity ϕ and N solid phases of volume fractions $f_\theta, \theta = 1, N$ and the respective

volumes ω_θ. The REV is subjected to the regular displacement boundary condition (7.4). Furthermore, at the interface between the fluid phase and a solid phase, the stress continuity reads:

$$\text{on } \partial\omega_f : \boldsymbol{\sigma} \cdot \mathbf{n} = -p\mathbf{n} \tag{7.28}$$

where $\partial\omega_f$ is the boundary of the fluid phase with outward unit normal vector $\mathbf{n}$ and p is the fluid pressure. The microscopic stress in the REV can be written in the form:

$$\boldsymbol{\sigma}_\theta = (1-\eta)\,\mathbb{C}_\theta : \boldsymbol{\varepsilon}_\theta - \eta p\mathbf{1} \tag{7.29}$$

where $\eta = 1$ in ω_f and $\eta = 0$ in the solid volume $\omega_{\theta=1,N}$.

7.3.2 Decomposition of the Poroelastic Problem

Following Lemarchand's proposal [84], we decompose the poroelastic problem in two sub-problems:

1. In the first sub-problem denoted with $'$, we consider an empty porous system ($p = 0$) subjected to the macroscopic deformation at the boundary (7.4). Taking the stress average of (7.29) in this case gives:

$$\boldsymbol{\Sigma}' = \langle \boldsymbol{\sigma}' \rangle_\Omega = \frac{1}{\Omega}\int_\Omega (1-\eta)\,\mathbb{C}_\theta : \boldsymbol{\varepsilon}_\theta \, dV = \sum_{\theta=1}^{N} f_\theta \mathbb{C}_\theta : \langle \mathbb{A} \rangle_{\omega_\theta} : \mathbf{E} \tag{7.30}$$

   where we use the linear strain localization relation (7.6), and where $\langle \mathbb{A} \rangle_{\omega_\theta}$ is the volume average of the localization tensor over the individual solid volume ω_θ, that can be approximated by Eshelby's solution (7.8), i.e. $\langle \mathbb{A} \rangle_{\omega_\theta} \simeq \mathbb{A}_\theta^{est}$

2. In the second sub-problem, the REV is considered to be subjected to a zero-strain ($\mathbf{E} = 0$) and to a pore pressure p, for which the stress average of (7.29) yields:

$$\boldsymbol{\Sigma}'' = \langle \boldsymbol{\sigma}'' \rangle_\Omega = \sum_{\theta=1}^{N} f_\theta \langle \boldsymbol{\sigma}'' \rangle_{\omega_\theta} - \phi p\mathbf{1} \tag{7.31}$$

   Since p is the only loading of the micromechanical system, and since the system is assumed

to behave linear elastic, it follows that $\boldsymbol{\sigma}''$ is linearly related to p, as is the volume average $\langle\boldsymbol{\sigma}''\rangle_\Omega$. This is expressed by introduction of the Biot tensor $\mathbf{B}$:

$$\langle\boldsymbol{\sigma}''\rangle_\Omega = -p\mathbf{B} \tag{7.32}$$

Superposition of (7.30) and (7.31) leads to the classical poroelastic state equation [41]:

$$\boldsymbol{\Sigma} = \langle\boldsymbol{\sigma}'\rangle_\Omega + \langle\boldsymbol{\sigma}''\rangle_\Omega = \mathbb{C}_{\text{hom}} : \mathbf{E} - p\mathbf{B};\ \mathbb{C}_{\text{hom}} = \sum_{\theta=1}^{N} f_\theta \mathbb{C}_\theta : \langle\mathbb{A}\rangle_{\omega_\theta} \tag{7.33}$$

where $\mathbb{C}_{\text{hom}}$ is the drained elasticity tensor which we determined in Section 7.2 for cement-based materials.

7.3.3 Determination of the Biot Tensor

The remaining task to determine the Biot tensor requires to clarify the link between Biot tensor and the microscopic stresses. To this end, we use a result obtained by Levin in the context of thermal stresses [85], that links a microscopic 'prestress', here $\boldsymbol{\sigma}^p = -\eta p\mathbf{1}$ in Eq. (7.29), to a macroscopic 'prestress', here $\boldsymbol{\Sigma}^p = -p\mathbf{B}$ in Eq. (7.33):

$$\boldsymbol{\Sigma}^p = -p\mathbf{B} \equiv \langle\boldsymbol{\sigma}^p : \mathbb{A}\rangle_\Omega = -\langle\eta p\mathbf{1} : \mathbb{A}\rangle_\Omega = -p\mathbf{1} : \phi\langle\mathbb{A}\rangle_{\omega_f} \tag{7.34}$$

In addition, use in (7.34) of the consistency condition $\langle\mathbb{A}\rangle_\Omega = \mathbb{I} \Leftrightarrow \phi\langle\mathbb{A}\rangle_{\omega_f} = \mathbb{I} - \sum_{\theta=1}^{N} f_\theta \langle\mathbb{A}\rangle_{\omega_\theta}$, yields the Biot tensor in the form:

$$\mathbf{B} = \mathbf{1} : \phi\langle\mathbb{A}\rangle_{\omega_f} = \mathbf{1} : \left(\mathbb{I} - \sum_{\theta=1}^{N} f_\theta \langle\mathbb{A}\rangle_{\omega_\theta}\right) \tag{7.35}$$

In the isotropic case for which $\langle\mathbb{A}\rangle_{\omega_\theta} = \langle A^v\rangle_{\omega_\theta}\mathbb{K} + \langle A^d\rangle_{\omega_\theta}\mathbb{J}$, expression (7.35) simplifies to:

$$\mathbf{B} = b\mathbf{1};\ b = \phi\langle A^v\rangle_{\omega_f} = 1 - \sum_{\theta=1}^{N} f_\theta \langle A^v\rangle_{\omega_\theta} \tag{7.36}$$

where b is the Biot coefficient. Expressions (7.35) and (7.36) reduce the determination of the Biot tensor to the determination of the strain localization tensors of N elastic solid phases. The

application to the three-level microstructure of cement-based materials is shown next.

7.4 Estimation of the Biot Coefficients of Cement-Based Materials

In the context of cement-based materials, only material levels need to be considered at which the material has a porosity filled with water that exerts a pressure. This is the case for Levels II and III. By contrast at Level I no consideration is necessary as the intrinsic C-S-H porosity is of a size that only a few water molecules are present between the C-S-H sheets. The water in the gel porosity of the C-S-H is neglected because it is chemically or physically bound to the solid (see Section 2.2.5 and Table 4.3).

7.4.1 Level II: Cement paste

At Level II, the cement paste is composed of the four unhydrated clinker phases (if the water-cement ratio is low), the C-S-H matrix, the Portlandite, and the saturated porosity.

Volume fractions

In the undegraded state, the volume fractions are:

$$\phi_0 = 1 - f^0_{\text{C-S-H}} - f_{\text{CH}} - \sum_{i=1}^{4} f_i \tag{7.37}$$

where the sum is over the unhydrated clinker phases. In turn, in the asymptotically leached state, the Portlandite is entirely dissolved and the volume it occupied is entirely added to the porosity as chemical porosity, along with some porosity created by the decalcification of the C-S-H (see Section 2.3.2), $\phi^c_\infty = f_{\text{CH}} + f^0_{\text{C-S-H}} - f^\infty_{\text{C-S-H}}$, we have:

$$\phi_\infty = \phi_0 + \phi^c_\infty = 1 - f^\infty_{\text{C-S-H}} - \sum_{i=1}^{4} f_i \tag{7.38}$$

Representation and Localization

The initial and the chemical porosity are assumed to belong to the same pore family, that is they have the same morphology (spherical pores). Assuming isotropy of all involved phases, the volume strain localization of the different phases obey the following relation; in the undegraded state:

$$\phi_0 \langle A^v \rangle_{voids} = 1 - f^0_{\text{C-S-H}} \langle A^v \rangle_{\omega_{\text{C-S-H}}} - f_{\text{CH}} \langle A^v \rangle_{\omega_{\text{CH}}} - \sum_{i=1}^{4} f_i \langle A^v \rangle_{\omega_i} \tag{7.39}$$

and in the degraded state:

$$(\phi_0 + \phi^c_\infty) \langle A^v \rangle_{voids} = 1 - f^\infty_{\text{C-S-H}} \langle A^v \rangle_{\omega_{\text{C-S-H}}} - \sum_{i=1}^{4} f_i \langle A^v \rangle_{\omega_i} \tag{7.40}$$

where $\langle A^v \rangle_{\omega_j}, j = f, \text{C}-\text{S}-\text{H}, i = 1,4$ denote the volume averages of the volumetric strain localization factors of the involved solid phases. The C-S-H phase has by far the largest volume fraction and considerably poorer elastic properties than the other phases. Consistent with the homogenization of the elasticity properties (see Section 7.2). We apply the MT scheme.

Poroelastic Properties

The two poroelastic properties at stake at Level II are the drained homogenized bulk modulus, k_{hom}, and the Biot coefficient b. The first is given by (7.33) the second by (7.35), and read here:

- In the undegraded state (superscript 0):

$$k^0_{\text{hom}} = k^0_{\text{C-S-H}};\ f^0_{\text{C-S-H}} \langle A^v \rangle_{\omega_{\text{C-S-H}}} + k_{\text{CH}} : f_{\text{CH}} \langle A^v \rangle_{\omega_{\text{CH}}} + \sum_{i=1}^{4} f_i k_i \langle A^v \rangle_{\omega_i} \tag{7.41}$$

$$b^0 = 1 - f^0_{\text{C-S-H}} \langle A^v \rangle_{\omega_{\text{C-S-H}}} - f_{\text{CH}} \langle A^v \rangle_{\omega_{\text{CH}}} - \sum_{i=1}^{4} f_i \langle A^v \rangle_{\omega_i} \tag{7.42}$$

- In the degraded state (superscript ∞):

$$k^\infty_{\text{hom}} = k^\infty_{\text{C-S-H}};\ f^\infty_{\text{C-S-H}} \langle A^v \rangle_{\omega_{\text{C-S-H}}} + \sum_{i=1}^{4} f_i k_i \langle A^v \rangle_{\omega_i} \tag{7.43}$$

$$b^{\infty} = 1 - f^{\infty}_{\text{C-S-H}} \langle A^v \rangle_{\omega_{\text{C-S-H}}} - \sum_{i=1}^{4} f_i \langle A^v \rangle_{\omega_i} \tag{7.44}$$

The bulk modulus of the unleached and leached paste was estimated in Section 7.2, by approximating the volumetric strain localization factors $\langle A^v \rangle_{\omega_i}$ by the Eshelby estimate developed in Table 7.1, that is $\langle A^v \rangle_{\omega_\theta} \equiv a^{v,est}_{\theta}$. The same is employed here for the determination of the Biot coefficients of the leached and unleached cement paste. More precisely, for a high $w/c-$cement paste, for which all clinker phases have been hydrated (i.e. $f_i = 0, i = 1..4$). A combination of the bulk modulus expressions (7.41) and (7.43) with respectively (7.42) and (7.44) delivers:

$$b^0 = 1 - \frac{k_{\text{hom}}}{k^0_{\text{C-S-H}}} - a^v_{\text{CH}} f_{\text{CH}} \left(1 - \frac{k_{\text{CH}}}{k^0_{\text{C-S-H}}} \right) \tag{7.45}$$

$$b^{\infty} = 1 - \frac{k_{\text{hom}}}{k^{\infty}_{\text{C-S-H}}} \tag{7.46}$$

where a^v_{CH} is the volumetric localization coefficient estimated from the MT scheme (see Table 7.1). Use of the numerical values of Table 7.2 and 7.3 delivers:

$$b^0 = 1 - \frac{15.4}{15.2} - 0.612 \times 0.11 \left(1 - \frac{33.33}{15.2} \right) = 0.07 \tag{7.47}$$

$$b^{\infty} = 1 - \frac{1.7}{2.7} = 0.37 \tag{7.48}$$

The homogenization scheme predicts a strong increase of the Biot coefficient through the degradation process. The value indicates also that in elasticity some strong interaction between fluid pressure and macroscopic stress takes place. By contrast, the homogenization procedure does not deliver a Biot coefficient close to one. This supports the analysis in section 5.2.4, stating that the validity of the effective stress concept is rather a statement about strength properties than elastic properties.

Finally, we are interested in the evolution of the Biot coefficient between its initial state and the asymptotically leached state. When the Portlandite dissolves (while the C-S-H remains intact), the poroelastic properties in this intermediate state are obtained analogous to (7.43) and (7.44),

$$k^{\rightarrow \text{CH}}_{\text{hom}} = (1 - (\phi_0 + \phi^c_{\infty}))\, k^0_{\text{C-S-H}} \langle A^v \rangle_{\omega_{\text{C-S-H}}} \tag{7.49}$$

$$b^{\rightarrow \mathrm{CH}} = 1 - \frac{k_{\mathrm{hom}}^{\rightarrow \mathrm{CH}}}{k_{\mathrm{C-S-H}}^{0}} = 1 - \frac{11.2}{15.2} = 0.26 \tag{7.50}$$

where superscript $\rightarrow$ CH stands for the dissolution of Portlandite. The evaluation shows that the Portlandite dissolution accounts for the larger part of the increase of the Biot coefficient in the leaching process.

7.4.2 Level III: Mortar and Concrete

At Level III, we consider the REV composed of a cement-paste matrix, inclusions, and the ITZ, hence as a three solid phase composite material without a distinct porosity. Focus of this section is the effect of the inclusions on the Biot coefficient. In a first step, we reduce the problem to a two-phase solid system, composed of a porous cement-paste matrix and inclusions, ignoring the effect of the ITZ. In second step, we will include the ITZ.

Effect of Inclusions on the Biot Coefficient of Mortar and Concrete

We return to the very definition of the Biot coefficient, starting from (7.29):

$$\boldsymbol{\sigma}_\theta = (1-\eta)\,\mathbb{C}_\theta : \boldsymbol{\varepsilon}_\theta + \boldsymbol{\sigma}^p;\ \boldsymbol{\sigma}^p = -\eta p \mathbf{1} \tag{7.51}$$

where $\eta = 0$ in any solid phase, and $\eta = 1$ in any pore space. Decomposing the poroelastic problem into the two sub-problems yields:

1. For the empty porous system ($p = 0 \rightarrow \boldsymbol{\sigma}^p = 0$) subjected to $\boldsymbol{\xi}^d = \mathbf{E}\cdot\mathbf{x}$ at the boundary of Level III, the stress average is given still by (7.30), and leads to the homogenized stiffness tensor:

$$\boldsymbol{\Sigma}' = \langle \boldsymbol{\sigma}' \rangle_\omega = \mathbb{C}_{\mathrm{hom}}^{III} : \mathbf{E};\quad \mathbb{C}_{\mathrm{hom}}^{III} = \sum_{\theta=1}^{N} f_\theta \mathbb{C}_\theta : \langle \mathbb{A} \rangle_{\omega_i} \tag{7.52}$$

   This stiffness tensor can be determined by using the concentration factors and stiffness tensors of the phases defined at Level III:

$$f_m \langle \mathbb{A} \rangle_{\omega_M} + f_I \langle \mathbb{A} \rangle_{\omega_I} = \mathbb{I} \tag{7.53}$$

   where we determine the localization tensors through application of the solution from the

HZ scheme given in Table 7.6.

2. The unstrained material system subjected in the porosity of the matrix phase to a pore pressure p:

$$\boldsymbol{\Sigma}'' = (1 - f_I) \left\langle \boldsymbol{\sigma}'' \right\rangle_{\omega_M} + f_I \left\langle \boldsymbol{\sigma}'' \right\rangle_{\omega_I} \tag{7.54}$$

Considering (7.51) in (7.54) we find:

$$\boldsymbol{\Sigma}'' = (1 - f_I) f_s^{II} \left\langle \boldsymbol{\sigma}'' \right\rangle_{\omega_s} + f_I \left\langle \boldsymbol{\sigma}'' \right\rangle_{\omega_I} - (1 - f_I) \phi^{II} p \mathbf{1} = - p \mathbf{B} \tag{7.55}$$

where f_I is the inclusion volume fraction and stress $\boldsymbol{\Sigma}''$ is the macroscopic eigenstress at level III.

Taking Levin's formula (7.34), to relate the macroscopic eigenstress $-p\mathbf{B}$ and the microscopic eigenstress $\boldsymbol{\sigma}^p = -\eta p \mathbf{1}$, we find for $\mathbf{B}$:

$$\mathbf{B} = \langle \eta \mathbf{1} : \mathbb{A} \rangle_\Omega = (1 - f_I) \langle \eta \mathbf{1} : \mathbb{A} \rangle_{\omega_M} + f_I \langle \eta \mathbf{1} : \mathbb{A} \rangle_{\omega_I} = (1 - f_I) \mathbf{1} : \langle \eta \mathbb{A} \rangle_{\omega_M} \tag{7.56}$$

Equation (7.56) provides a means to estimate the effect of the aggregates on the Biot tensor. There are different ways of evaluating (7.56). We choose to assume that the strain localization tensor in the matrix is constant, that is, it is the same in the solid and the porosity of the matrix. This is, in other words, a mixture rule employed at Level II of the matrix but respects the separation-of-scale-condition[5]. The hypothesis reads:

$$\mathcal{H} : \langle \eta \mathbb{A} \rangle_{\omega_M} = \langle \eta \rangle_{\omega_M} \mathbb{A}_M = \phi^{II} \mathbb{A}_M \tag{7.57}$$

where $\phi^{II} = \phi^{III} / (1 - f_I)$ is the porosity at level II. Using this hypothesis in (7.56) yields for $\mathbf{B}$:

$$\mathbf{B} = (1 - f_I) \phi^{II} \mathbf{1} : \mathbb{A}_M = \phi^{II} \mathbf{1} : \left(\mathbb{I} - f_I \langle \mathbb{A} \rangle_{\omega_I} \right) \tag{7.58}$$

Equation (7.58) reveals two points of particular interest:

[5] That is, given the difference in size between Level II and Level III, it is appropriate on Level III, to consider in a first approximation, the same strain in the solid phase and the porosity, particularly for the small porosity in the undegraded state.

- It leads, if we assume the mixture rule for all involved phases, that is $\langle \mathbb{A} \rangle_{\omega_\theta} = \mathbb{I}$, to the easily checked lower bound estimate of the Biot tensor:

$$\forall \theta : \langle \mathbb{A} \rangle_{\omega_\theta} = \mathbb{I} \Rightarrow \mathbf{B} = \phi^{II} (1 - f_I) \mathbf{1} \tag{7.59}$$

This result involves two strong assumptions, i.e. (7.57) and (7.59) but reproduces clearly the increasing effect of a porosity on level II; and the inverse for the effects of aggregates on Level III on the Biot tensor.

- With (7.57), the homogenized stiffness tensor reads for the two-phase system:

$$\mathbb{C}^{III}_{\text{hom}} = \mathbb{C}_m + f_I (\mathbb{C}_I - \mathbb{C}_m) : \langle \mathbb{A} \rangle_{\omega_I} \tag{7.60}$$

which allows one to recast (7.58) in the form:

$$\mathbf{B} = \boldsymbol{\phi}^{\mathbf{II}} \mathbf{1} : \left(\mathbb{I} - (\mathbb{C}_I - \mathbb{C}_m)^{-1} : (\mathbb{C}^{III}_{\text{hom}} - \mathbb{C}_m) \right) \tag{7.61}$$

This expression is of a very similar format as the standard expressions of the two-phase system and reduces in the isotropic case to[6]:

$$\mathbf{B} = b\mathbf{1}; b =: \phi^{II} \left(1 - \frac{k^{III}_{\text{hom}} - k_m}{k_I - k_m} \right) \tag{7.62}$$

Evaluating (7.62) numerically yields for the intact state:

$$b^0_{mortar} = \phi^{II} \left(1 - \frac{k^0_{\text{hom}} - k^0_m}{k_I - k^0_m} \right) = 0.03 \times \left(1 - \frac{15.1 - 15.4}{35.9 - 15.4} \right) = 0.03 \tag{7.63}$$

and in the asymptotically degraded state:

$$b^\infty_{mortar} = \phi^{II} \left(1 - \frac{k^\infty_{\text{hom}} - k^\infty_m}{k_I - k^\infty_m} \right) = 0.21 \times \left(1 - \frac{2.6 - 1.7}{35.9 - 1.7} \right) = 0.20 \tag{7.64}$$

[6] Eq. (7.61) reduces to (7.59), if we employ the mixture formula $\mathbb{C}^{III}_{\text{hom}} = \mathbb{C}_m + f_I (\mathbb{C}_I - \mathbb{C}_m)$.

while for the case where only the Portlandite has been leached:

$$\mathbf{B}_{mortar}^{\rightarrow \mathrm{CH}} = \phi^{II}\left(1 - \frac{k_{\mathrm{hom}}^{\rightarrow \mathrm{CH}} - k_m^{\rightarrow \mathrm{CH}}}{k_I - k_m^{\rightarrow \mathrm{CH}}}\right) = 0.14 \times \left(1 - \frac{11.83 - 11.2}{35.9 - 11.2}\right) = 0.14 \qquad (7.65)$$

These values show a strong influence of the aggregates on the Biot coefficient. Compared with the paste, the mortar shows roughly 50% of the value of the paste's Biot coefficient, both for the leached and unleached case. In addition, the effect of the Portlandite dissolution is found to dominate the evolution of the Biot coefficient. The leaching process has some effect on the Biot coefficient, an increase from 0.03 to 0.2 is predicted. In general, however, in the mortars/concrete the effect of the pore pressure on the elastic macroscopic stress appears to be small, given the large inclusion volume fraction.

Effect of the ITZ on the Biot Coefficient of Mortar and Concrete

To refine the analysis, we want to study the influence of the ITZ on the Biot coefficient. The porosity in the ITZ is given by $\phi^{ITZ} = \omega_{f,ITZ}/\omega_{ITZ}$ and the matrix porosity $\phi^{II} = \omega_{f,M}/\omega_{II}$. This leads us back to the originally considered three-phase composite system (Matrix, ITZ, Inclusion), of which two-phases are porous solid phases with a porosity that manifests itself at a lower scale. The homogenized elasticity tensor for this system has been determined in Section 7.2 from:

$$\mathbb{C}_{\mathrm{hom}}^{III} = \mathbb{C}_m + f_{ITZ}\left(\mathbb{C}_{ITZ} - \mathbb{C}_m\right) : \langle \mathbb{A} \rangle_{\omega_{ITZ}} + f_I\left(\mathbb{C}_I - \mathbb{C}_m\right) : \langle \mathbb{A} \rangle_{\omega_I} \qquad (7.66)$$

where $\mathbb{C}_{ITZ}$ is the stiffness tensor of the ITZ which occupies the volume fraction $f_{ITZ} = \omega_{ITZ}/\Omega = 1 - (f_m + f_I)$ in the REV Ω; and $\langle \mathbb{A} \rangle_{\omega_{ITZ}}$ is the strain localization tensor of the ITZ which was given through the solution of the HZ scheme.

For the derivation of the Biot tensor we assume that the pressure developing in the ITZ-porosity is the same as in the matrix porosity. Under this assumption, the Biot tensor is obtained analogously to reads (7.56) from:

$$\mathbf{B}^{III} = \mathbf{1} : \langle \eta \mathbb{A} \rangle_{\Omega} = \mathbf{1} : \left[f_m \langle \eta \mathbb{A} \rangle_{\omega_M} + f_{ITZ} \langle \eta \mathbb{A} \rangle_{\omega_{ITZ}} \right] \qquad (7.67)$$

Employing an analogous hypothesis as (7.57), that is:

$$\mathcal{H}\text{: } \langle \eta \mathbb{A} \rangle_{V_M} = \phi^{II} \langle \mathbb{A} \rangle_{\omega_M} \text{ ; } \langle \eta \mathbb{A} \rangle_{\omega_{ITZ}} = \phi^{ITZ} \langle \mathbb{A} \rangle_{\omega_{ITZ}} \tag{7.68}$$

we can rewrite (7.67) with the help of the consistency condition $\langle \mathbb{A} \rangle_{\Omega} = \mathbb{I}$ in the form:

$$\mathbf{B}^{III} = \mathbf{1} : \left[\phi^{II} \left(\mathbb{I} - f_I \langle \mathbb{A} \rangle_{\omega_I} \right) + f_{ITZ} \left(\phi^{ITZ} - \phi^{II} \right) \langle \mathbb{A} \rangle_{\omega_{ITZ}} \right] \tag{7.69}$$

Finally, if we express $f_I \langle \mathbb{A} \rangle_{\omega_I}$ in (7.69) by the expression given by (7.66), the Biot tensor can be developed in the form:

$$\mathbf{B}^{III} = \mathbf{B}^0_{mortar} + f_{ITZ} \left(\mathbf{B}^{II}_{ITZ} + \phi^{ITZ} \mathbf{1} \right) : \langle \mathbb{A} \rangle_{\omega_{ITZ}} \tag{7.70}$$

where $\mathbf{B}^0_{mortar}$ is the expression of the Biot tensor (7.61), developed for the two phase system, and $\mathbf{B}^{II}_{ITZ}$ is of a similar form as (7.61) reading:

$$\mathbf{B}^{II}_{ITZ} = \phi^{II} \mathbf{1} : \left[\mathbb{I} - \left(\mathbb{C}_I - \mathbb{C}_m \right)^{-1} : \left(\mathbb{C}_{ITZ} - \mathbb{C}_m \right) \right] \tag{7.71}$$

For the case of an isotropic material with isotropic phases, (7.70) simplifies to:

$$\mathbf{B}^{III} = b^{III} \mathbf{1};\ b^{III} = b^0_{mortar} + f_{ITZ} \left(b^{II}_{ITZ} + \phi^{ITZ} \right) \langle A^v \rangle_{\omega_{ITZ}} \tag{7.72}$$

with

$$b^0_{mortar} = \phi^{II} \left(\frac{k_I - k^{III}_{\text{hom}}}{k_I - k_m} \right) ;\ b^{II}_{ITZ} = \phi^{II} \left(\frac{k_{ITZ} - k_m}{k_I - k_m} \right) \tag{7.73}$$

Expressions (7.72) and (7.73) is used to evaluate the Biot coefficients for the unleached and leached mortar. Employing the values from Table 7.2 and 7.3 and the localization factor for the ITZ from the HZ scheme, (see Table 7.8) yields for the Biot coefficients in the intact and degraded state $b^{III}_0 = 0.04$ and $b^{III}_\infty = 0.35$, respectively. A comparison with the values obtained for the two phase system (i.e. $b^{III}_0 = 0.03$ and $b^{III}_\infty = 0.20$) shows that the influence of the ITZ is considerable in relative terms. However, the total value of the Biot coefficient for mortars remains small. On the other hand, the Biot coefficient of the mortar in the asymptotically degraded state is virtually the same as for the paste. Finally, for purpose of completeness, the

	Input [GPa]	HZ Loc. Factors	Output
Undegraded	$\phi^{II} = 0.03, f_{ITZ} = 0.3$	-	$b^{II}_{ITZ} = -0.014$
	$k_I = 35.9$	-	$b^{0}_{mortar} = 0.03$
	$k^{III}_{\text{hom}} = 15.1$	-	$b^{III}_{0} = 0.04$
	$k^{0}_{ITZ} = 6.0$	$\langle A^v \rangle^{0}_{\omega_{ITZ}} = 1.846$	
	$k_m = 15.4$	-	
Degraded	$\phi^{II}_{\infty} = 0.21, f_{ITZ} = 0.3$	-	$b^{II,\infty}_{ITZ} = -0.006$
	$k^{\infty}_{I} = 35.9$	-	$b^{\infty}_{mortar} = 0.204$
	$k^{III,\infty}_{\text{hom}} = 2.6$	-	$b^{III}_{\infty} = 0.35$
	$k^{\infty}_{ITZ} = 0.8$	$\langle A^v \rangle^{\infty}_{\omega_{ITZ}} = 2.310$	
	$k^{\infty}_{m} = 1.7$	-	
Intermediate	$\phi^{II}_{\rightarrow CH} = 0.14, f_{ITZ} = 0.3$		$b^{II,\infty}_{ITZ} = -0.038$
	$k^{\rightarrow CH}_{I} = 35.9$		$b^{\rightarrow CH}_{mortar} = 0.134$
	$k^{III,\rightarrow CH}_{\text{hom}} = 12.3$		$b^{III}_{\rightarrow CH} = 0.19$
	$k^{\rightarrow CH}_{ITZ} = 4.5$	$\langle A^v \rangle^{\rightarrow CH}_{\omega_{ITZ}} = 1.946$	
	$k^{\rightarrow CH}_{m} = 11.2$		

Table 7.8: Biot coefficients for Level III, considering the ITZ.

Biot coefficient for the intermediate leaching state is $b^{III}_{\rightarrow CH} = 0.19$.

7.5 Homogenization of the Biot Modulus for Cementitious Materials

In the elastic theory of porous media [41], besides the drained elasticity tensor $\mathbb{C}_{\text{hom}}$ and the Biot coefficient tensor $\mathbf{B}$, the Biot Modulus $\mathtt{M}$ is a third important material property that affects the change in porosity [41]:

$$\phi - \phi_0 = \mathbf{B} : \mathbf{E} + \frac{p}{\mathtt{M}} \tag{7.74}$$

State equation (7.74) is a generalization of (5.20). The micromechanical background of expression (7.74) was provided by Dormieux [45], by considering an REV with a fluid phase (volume ω_f) and a solid phase (volume $\omega_s = \Omega - \omega_f$) for which:

$$\phi - \phi_0 = \phi \mathbf{1} : \langle \boldsymbol{\varepsilon} \rangle_{voids} \tag{7.75}$$

The Biot modulus $\mathtt{M}$ is obtained by considering, analogously to Section 7.3, superposition of the following two sub-problems:

1. For the empty porous system ($p = 0$) subjected to the regular displacement boundary condition (7.4), using the strain localization condition (7.6), and the general definition of the Biot tensor (7.35), yields:

$$p = 0; \;\; (\phi - \phi_0)' = \phi \mathbf{1} : \langle \boldsymbol{\varepsilon}' \rangle_{voids} = \phi \mathbf{1} : \langle \mathbb{A} \rangle_{voids} : \mathbf{E} = \mathbf{B} : \mathbf{E} \tag{7.76}$$

2. The second sub-problem, that is the zero-deformation boundary value problem ($\mathbf{E} = \mathbf{0}$) subjected at the solid-fluid interface to the pressure boundary condition (7.28), leads to the definition of the Biot modulus $\mathtt{M}$:

$$\mathbf{E} = \mathbf{0}; \;\; (\phi - \phi_0)'' = \phi \mathbf{1} : \langle \boldsymbol{\varepsilon}'' \rangle_{voids} = \frac{p}{\mathtt{M}} \tag{7.77}$$

   To determine $\mathtt{M}$, we note that $\phi \langle \boldsymbol{\varepsilon}'' \rangle_{voids} = -f_s \langle \boldsymbol{\varepsilon}'' \rangle_{\omega_s}$, with $f_s = \omega_s / \Omega$, in this sub-problem ($\mathbf{E} = \mathbf{0}$), and that $\langle \boldsymbol{\varepsilon}'' \rangle_{\omega_s} = \mathbb{C}_s^{-1} : \langle \boldsymbol{\sigma}'' \rangle_{\omega_s}$. Furthermore, relations (7.31) and (7.32) deliver $f_s \langle \boldsymbol{\sigma}'' \rangle_{\omega_s} = -p (\mathbf{B} - \phi \mathbf{1})$; and we can write for the Biot modulus:

$$\frac{1}{\mathtt{M}} = \mathbf{1} : \mathbb{C}_s^{-1} : (\mathbf{B} - \phi \mathbf{1}) \tag{7.78}$$

   Eq. (7.78) holds for the classical two phase (solid-fluid) porous material only. In the case of isotropic behavior of the phases it reads:

$$\frac{1}{\mathtt{M}} = \frac{b - \phi}{k_s} \tag{7.79}$$

   where b is the Biot coefficient and k_s the bulk modulus of the solid phase.

The presented concept can be extended to $N-$ solid phases (with index θ), by considering that the porosity change reads in such a situation:

$$\mathbf{E} = \mathbf{0}; \;\; (\phi - \phi_0)'' = -\mathbf{1} : \sum_{\theta=1}^{N} f_\theta \langle \boldsymbol{\varepsilon}'' \rangle_{\omega_\theta} = -\mathbf{1} : \sum_{\theta=1}^{N} f_\theta \mathbb{C}_\theta^{-1} : \langle \boldsymbol{\sigma}'' \rangle_{\omega_\theta} \tag{7.80}$$

Relations (7.31) and (7.32) together with expression (7.35) of the Biot coefficient tensor for $N-$solid phases deliver a means of expressing $\langle \boldsymbol{\sigma}'' \rangle_{\omega_\theta}$ in (7.80); that is:

$$p\left[\mathbf{B}-\phi\mathbf{1}\right]=p\mathbf{1}:\left[\sum_{\theta=1}^{N} f_\theta\left(\mathbb{I}-\langle\mathbb{A}\rangle_{\omega_\theta}\right)\right]=-\sum_{\theta=1}^{N} f_\theta\langle\boldsymbol{\sigma}''\rangle_{\omega_\theta}\Rightarrow\langle\boldsymbol{\sigma}''\rangle_{\omega_\theta}=p\mathbf{1}:\left(\langle\mathbb{A}\rangle_{\omega_\theta}-\mathbb{I}\right) \quad (7.81)$$

Using (7.81) in (7.80) yields the Biot modulus for the $N-$solid phase porous material in the form:

$$\frac{1}{\mathtt{M}}=\mathbf{1}:\sum_{\theta=1}^{N} f_\theta\mathbb{C}_\theta^{-1}:\left(\mathbf{1}:\left(\mathbb{I}-\langle\mathbb{A}\rangle_{\omega_\theta}\right)\right) \quad (7.82)$$

This expression reduces to (7.79) for $N=1$; and $1/\mathtt{M}\rightarrow 0$ for the application of a mixture rule ($\langle\mathbb{A}\rangle_{\omega_\theta}=\mathbb{I}$). In the case of isotropic phases, (7.82) reads:

$$\frac{1}{\mathtt{M}}=\sum_{\theta=1}^{N} f_\theta\frac{1-\langle A^v\rangle_{\omega_\theta}}{k_\theta} \quad (7.83)$$

7.5.1 Application to Level II

For the unleached paste, application of (7.83) reads:

$$\left(\frac{1}{\mathtt{M}}\right)_0^{II}=f_{\mathrm{CH}}\frac{1-\langle A^v\rangle_{\omega_{\mathrm{CH}}}}{k_{\mathrm{CH}}}+f_{\mathrm{C-S-H}}\frac{1-\langle A^v\rangle_{\omega\mathrm{C-S-H}}}{k_{\mathrm{C-S-H}}} \quad (7.84)$$

which yields, using the values from Table 7.2 including the MT scheme solution for the localization factors:

$$\mathtt{M}_0^{II}=\left(0.11\frac{1-0.612}{33.33}+0.86\frac{1-1.008}{15.2}\right)^{-1}=1170\,\mathrm{GPa} \quad (7.85)$$

Applying (7.79) to a leached cement paste, we find:

$$\mathtt{M}_\infty^{II}=\frac{2.7}{0.79\times(1-0.831)}=20\,\mathrm{GPa} \quad (7.86)$$

Finally, in the case where only the Portlandite has been leached we find in the same way:

$$\mathtt{M}_{\rightarrow\mathrm{CH}}^{II}=\left(f_{\mathrm{C-S-H}}\frac{1-\langle A^v\rangle_{\omega\mathrm{C-S-H}}}{k_{\mathrm{C-S-H}}}\right)^{-1}=\left(0.86\frac{1-0.857}{15.2}\right)^{-1}=124\,\mathrm{GPa} \quad (7.87)$$

These results show that the Biot modulus decreases strongly with leaching, and particularly that the main change of $\mathtt{M}$ is associated with the dissolution of the Portlandite.

7.5.2 Application to Level III

For an application at Level III, the estimation for the Biot modulus needs to be adapted slightly. We consider as phases the aggregates, ITZ and the porous matrix. The total porosity change is due to the porosity change in the matrix and in the ITZ. Generalizing (7.77) this change in porosity in sub-problem 2 is expressed by:

$$\mathbf{E}=\mathbf{0};\ \ (\phi-\phi_0)''_{III}=\mathbf{1}:\langle\eta\varepsilon''\rangle_{\Omega}=\mathbf{1}:\left[f_m\langle\eta\varepsilon''\rangle_{\omega_m}+f_{ITZ}\langle\eta\varepsilon''\rangle_{\omega_{ITZ}}\right]=\frac{p}{\mathtt{M}^{III}} \tag{7.88}$$

where $\eta=1$ in any pore (in the matrix or ITZ), and $\eta=0$ elsewhere. The change in porosity at the scale of the matrix (Level II) and at the level of the ITZ can be related to the Biot moduli at these scales, that is:

$$\langle\eta\varepsilon''\rangle_{\omega_m}=\frac{p}{\mathtt{M}^{II}};\ \ \langle\eta\varepsilon''\rangle_{\omega_{ITZ}}=\frac{p}{\mathtt{M}^{ITZ}} \tag{7.89}$$

Use of (7.89) in (7.88) provides a means of evaluating the Biot modulus on Level III:

$$\frac{1}{\mathtt{M}^{III}}=\frac{f_m}{\mathtt{M}^{II}}+\frac{f_{ITZ}}{\mathtt{M}^{ITZ}} \tag{7.90}$$

Relation (7.90) is based on the assumption that the same pressure prevails in the matrix porosity and in the ITZ-porosity, and appears therefore as some sort of Reuss-bound. The drawback of this expression is that it requires as input the unknown Biot modulus for the ITZ. In a first approach, we may neglect the ITZ and evaluate the Biot modulus on Level III from the one of the matrix, that is:

$$\mathtt{M}^{III}=\frac{\mathtt{M}^{II}}{1-f_I} \tag{7.91}$$

This expression is used for evaluation purposes. In this case, using the values from (7.85), and $f_I = 0.5$, we obtain:

$$\begin{aligned} \mathtt{M}_0^{III} &= \frac{1169.7}{1-0.5} = 2340\,\text{GPa} \\ \mathtt{M}_\infty^{III} &= \frac{20.2}{1-0.5} = 40\,\text{GPa} \\ \mathtt{M}_{\rightarrow\text{CH}}^{III} &= \frac{123.5}{1-0.5} = 247\,\text{GPa} \end{aligned} \tag{7.92}$$

While these values are upper bounds they follow the same degradation pattern as the Biot modulus of the paste, which is where the actual changes occur.

7.6 Discussion: Refined Estimate of the Skempton Coefficient

With the estimates for Biot coefficient and Biot modulus at hand, we can return to the discussion of section 5.2.4 where we evaluated the Skempton coefficient B, defined as the ratio between pore pressure increase and applied mean stress in an undrained experiment, that is:

$$B = -\frac{p}{\Sigma_M} \tag{7.93}$$

From this definition, we derived the expression for the Skempton coefficient (5.31):

$$\frac{1}{B} = -\frac{\Sigma}{p} = \frac{k_{\text{hom}}}{b}\left(\frac{\phi_0}{k_f} + \frac{1}{\mathtt{M}}\right) + b \tag{7.94}$$

where k_{hom} is the drained bulk modulus of the porous medium and k_f is the fluid bulk modulus (2.3 GPa). For the cement paste, we evaluate (7.94) for the three degradation states:

$$B_0^{II} = \left(\frac{15.4}{0.07} \times \left(\frac{1}{1169.7} + \frac{0.03}{2.3}\right) + 0.07\right)^{-1} = 0.32 \tag{7.95}$$

$$B_{\rightarrow\text{CH}}^{II} = \left(\frac{11.2}{0.26} \times \left(\frac{1}{123.5} + \frac{0.14}{2.3}\right) + 0.26\right)^{-1} = 0.32 \tag{7.96}$$

$$B_\infty^{II} = \left(\frac{1.7}{0.37} \times \left(\frac{1}{20.2} + \frac{0.21}{2.3}\right) + 0.37\right)^{-1} = 0.98 \tag{7.97}$$

and for the mortar we find[7]:

$$B_0^{III} = \left(\frac{15.1}{0.03} \times \left(\frac{1}{2340} + \frac{0.03}{2.3}\right) + 0.03\right)^{-1} = 0.15 \tag{7.98}$$

$$B_{\rightarrow \mathrm{CH}}^{III} = \left(\frac{12.3}{0.14} \times \left(\frac{1}{247} + \frac{0.14}{2.3}\right) + 0.14\right)^{-1} = 0.17 \tag{7.99}$$

$$B_\infty^{III} = \left(\frac{2.6}{0.20} \times \left(\frac{1}{40.4} + \frac{0.21}{2.3}\right) + 0.2\right)^{-1} = 0.61 \tag{7.100}$$

It is interesting to note that the Skempton coefficient is most affected by the C-S-H decalcification, while the Portlandite dissolution has little effect (in contrast to the evolution of b and M). This confirms the trends of the preliminary results of Section 5.2.4: The leaching process leads to a significant increase of the Skempton coefficient. While close to one for the leached cement paste, it is close to B =0.6 for the mortar. This means that the material behavior in undrained loading situation changes: For the cement paste, before leaching only 28% of the applied stress are converted into pore pressure, reducing the confinement. After degradation, almost the entire applied mean stress is converted into pore pressure, hence no confinement is acting. The refined model developed here is in good agreement with the rough estimate in Section 5.2.4. The consequence of this is that in undrained loading (fast loading) no frictional enhancement of the material strength can be activated. The addition of aggregates reduces this effect. But still, roughly 60% of the confinement pressure in an undrained experiment is carried by the fluid pressure; thus reducing the activation of friction in mortar and concrete.

7.7 Chapter Summary

This chapter introduced some micromechanical techniques that focus on the estimation of poroelastic properties of leached and unleached cement-based materials. These techniques were adapted for the considered three-level microstructure of cement based materials. Concerning the elastic properties the following results were obtained:

- The elastic stiffness of the ITZ is estimated to be 40% of the paste's in the undegraded and

[7]For purpose of consistency, with the values for the Biot modulus, the employed values for mortar refer to the representation without considering the ITZ. Estimates for a mortar representation are expected still to be higher. The values (7.98) and (7.100) can be considered to be lower bounds.

45% in the degraded state. The value for undegraded materials matches experimental data and similar estimates by other authors, giving confidence in the micromechanical method. The degradation of ITZ and bulk paste seem similar for the elastic properties.

- Based on the model for the homogeneous elastic properties of a paste, which reproduces well the experimental data by Constantinides [37], the effect of the leaching of Portlandite alone was estimated (Table 7.4). The reduction in stiffness is relatively small, underscoring the importance of the C-S-H properties for the stiffness of the paste.

The estimation of the Biot coefficient for the cement pastes and mortars was developed, based on the techniques introduced in the context of elastic properties. The evaluation of the Biot coefficients showed:

- Undegraded cement based materials have values for the Biot coefficient that are very small. The values of 0.07 and 0.05 for respectively pastes and mortars, respectively indicates that the effect of the pore pressure on the elastic material behavior can almost be neglected. This evaluation is a first quantitative assessment for undegraded cement based materials.

- For cement pastes and mortars, the increase of the Biot coefficient through leaching is considerable and mostly associated with the Portlandite dissolution. The final values of 0.37 for the paste and 0.35 for the mortar show that in the asymptotically degraded state, the pore pressure has an effect on the elastic deformation behavior. However, the Biot coefficient is still far from one. This provides an answer to the question raised in section 6.5 concerning the effective stress concept: The observed validity of the effective stress concept is rather a consequence related to the strength behavior, not the elastic properties.

- The effect of aggregates on the Biot coefficient is shown to be strong. If no ITZ is considered, mortars show strongly reduced values and the increase with leaching albeit present still leads to maximum values of only 0.2. When the ITZ is considered, this value is 0.35, showing that the ITZ is important for the mortar behavior, although the total value of the Biot coefficient is still far from 1.

Properties	Intact	Intermediate	Leached
Level I			
k^{I}_{hom} [GPa]	15.2	15.2	2.7
μ^{I}_{hom} [GPa]	9.6	9.6	1.7
Level II			
k^{II}_{hom} [GPa]	15.4	11.2	1.7
μ^{II}_{hom} [GPa]	9.4	7.3	1.1
b^{II} [1]	0.07	0.26	0.37
$\mathtt{M}^{II}$ [GPa]	1169.7	123.5	20.2
B^{II} [GPa]	0.32	0.32	0.98
Level III			
k^{III}_{hom} [GPa]	15.1	12.3	2.6
μ^{III}_{hom} [GPa]	10.2	8.6	1.9
b^{III} [1]	0.04	0.19	0.35
$\mathtt{M}^{III}$ [GPa]	2340	247	40.4
B^{III} [GPa]	0.15	0.17	0.61

Table 7.9: Summary of the values for the poroelastic properties developed in this Chapter

The Biot modulus estimations shown in this chapter are extensions from the estimation of the Biot coefficient. The developed estimates show that the effect of leaching on the Biot modulus of paste and mortar is very strong. The values are reduced by more than a factor of 50 and 30, respectively, which is more than for uniaxial compressive strength (factor 10) or the Young's modulus. This strong reduction explains the experimentally observed behavior in undrained loading situations - shown through the Skempton coefficient which is close to one in degraded cement pastes and 60% for degraded mortar. Table 7.9 summarizes the values for the poroelastic properties obtained in this Chapter, for the undegraded state, the intermediate state (after Portlandite dissolution), and the asymptotically leached state.

Chapter 8

Micromechanical Analysis of Strength Properties

The experimental strength investigation on leached pastes and mortar showed that mortar (Level III), in high confinement (Table 5.3), has a higher friction coefficient than the paste (Level II). Similarly, in low confinement (see Table 5.6), the cohesion of the paste was found to be smaller than the cohesion of the mortar. This has been observed for both the unleached and leached state. In the same spirit as for the elastic properties, we want to use micromechanical techniques to explain this difference in strength properties. These techniques are based on an extension of the linear micromechanical techniques employed for the homogenization of elastic properties to strength properties. This Chapter is structured as follows: First, the necessary modifications of the linear micromechanical approach of Chapter 7 are introduced. In a second step, the application to strength properties of cement-based materials at the three levels of the microstructure is presented. Depending on the level of confinement, we distinguish two approaches: The first approach which is due to Lemarchand et al. [83], focuses on the frictional behavior of leached/unleached cementitious materials which dominates high levels of confinement. The second approach focuses on the cohesive strength of cementitious materials, which dominates low levels of confinement.

8.1 Extension of the Micromechanical Approach to Strength Properties

In this section the necessary changes to the linear micromechanical approach of Chapter 7 are discussed. These extensions follow the three-step structure of continuum micromechanics: Representation, Localization and Homogenization.

8.1.1 Material Representation for Strength Properties

For the homogenization of strength properties, the representation of the phases has to include, in addition to the volume fractions, geometry and elastic properties, information about the strength. For each phase a microscopic strength criterion is applied:

$$f(\boldsymbol{\sigma}_\theta) \leq 0 \tag{8.1}$$

For the cement-based materials considered in this study, this local strength criterion is given by the experimental results reported in Chapter 5. The Drucker-Prager criterion of a phase reads:

$$f(\boldsymbol{\sigma}_\theta) = \sqrt{j_2} + \delta_\theta \, \sigma_M^\theta - c_\theta \leq 0 \tag{8.2}$$

where j_2 is the second invariant of the deviatoric stress $\mathbf{s}_\theta = \boldsymbol{\sigma}_\theta - \sigma_M^\theta \mathbf{1}$, with σ_M^θ the microscopic mean stress; δ_θ and c_θ are the friction coefficient and cohesion. Moreover, microscopic nonlinear stress-strain relations need to be specified. A common way of describing local nonlinear behavior in the context of strength homogenization is the nonlinear elastic representation:

$$\boldsymbol{\sigma}_\theta = 2\mu_\theta\left(\epsilon_\theta, \varepsilon_\theta^v\right)\boldsymbol{\epsilon}_\theta + k_\theta\left(\epsilon_\theta, \varepsilon_\theta^v\right)\varepsilon_\theta^v \mathbf{1} \tag{8.3}$$

where $\varepsilon_\theta^v = \mathrm{tr}\boldsymbol{\varepsilon}_\theta$ is the volumetric microscopic strain, $\boldsymbol{\epsilon}_\theta = \boldsymbol{\varepsilon}_\theta - \frac{1}{3}\varepsilon_\theta^v \mathbf{1}$ is the microscopic deviatoric strain tensor and $\epsilon_\theta = \sqrt{\boldsymbol{\epsilon}_\theta : \boldsymbol{\epsilon}_\theta}$ is the invariant of the deviatoric strain tensor. $\mu_\theta\left(\epsilon_\theta, \varepsilon_\theta^v\right)$ and $k_\theta\left(\epsilon_\theta, \varepsilon_\theta^v\right)$ are strain dependent shear and bulk secant moduli which give this approach the name "secant method" [139].

8.1.2 Localization and Homogenization for Strength Properties

The general idea of the localization, that is determining the microscopic stresses and strains as a response to the macroscopic load, remains unchanged. However, the material representation with a nonlinear stress-strain relation changes the determination of the local strains. Phases are domains of constant properties. Failure in a phase may not necessarily occur in a homogeneous fashion in the phase, and strains close to failure may therefore vary. A common way to account for locally varying strains is the introduction of effective strains, a concept due to Suquet [139]. These effective strains are defined as moments of the microscopic strains per phase. The first moment corresponds to the strain localization used in the classical homogenization of elastic properties, that is:

$$\varepsilon_\theta^{eff} = \langle \boldsymbol{\varepsilon}_\theta \rangle_{V_\theta} = \frac{1}{V_\theta} \int_{V_\theta} \boldsymbol{\varepsilon}_\theta (\mathbf{x})\, d\Omega \tag{8.4}$$

where V_θ is the volume of phase θ. This first-order moment definition carries the name "classical" method. Definition (8.4) leads to the following invariants of the "effective" strains:

$$\epsilon_\theta^{eff} \equiv \overline{\epsilon}_\theta = \sqrt{\langle \boldsymbol{\epsilon}_\theta \rangle_{V_\theta} : \langle \boldsymbol{\epsilon}_\theta \rangle_{V_\theta}} \tag{8.5}$$

$$\varepsilon_\theta^{eff} \equiv \overline{\varepsilon}_\theta^{v} = \langle tr\,(\boldsymbol{\varepsilon}_\theta) \rangle_{V_i} \tag{8.6}$$

For isotropic materials, expressions (8.5) and (8.6) can be expressed as functions of the localization factors:

$$\overline{\epsilon}_\theta = \overline{A}_\theta^d E_d \tag{8.7}$$

$$\overline{\varepsilon}_\theta^{v} = \overline{A}_\theta^v E_v \tag{8.8}$$

where $E_d = \sqrt{\mathbf{E}_d : \mathbf{E}_d}$ is the macroscopic deviatoric invariant $\mathbf{E}_d = \mathbf{E} - \frac{1}{3} E_v \mathbf{1}$, and $E_v = \mathrm{tr}\mathbf{E}$ is the macroscopic volumetric strain. The single horizontal bar indicates the first moment definition[1]. The localization coefficients need to be specified for a given scheme. For the MT

[1] The localization factors in the "classical" method obey the consistency condition: $\sum_\theta f_\theta \overline{A}_\theta^v = \sum_\theta f_\theta \overline{A}_\theta^d$.

scheme for isotropic materials, the effective strains read:

$$(\overline{\epsilon}_\theta)^{MT} = a_\theta^d E_d \tag{8.9}$$

$$(\overline{\varepsilon}_\theta^v)^{MT} = a_\theta^v E_v \tag{8.10}$$

where a_θ^d and a_θ^v are given in Table 7.1. For the HZ scheme, the localization factors are directly given by Eqs. (7.21) and (7.22):

$$(\overline{\epsilon}_\theta)^{HZ} = A_\theta^d E_d \tag{8.11}$$

$$(\overline{\varepsilon}_\theta^v)^{HZ} = A_\theta^v E_v \tag{8.12}$$

A first refinement of the "classical" theory consists in considering a second moment definition for the effective strains which is referred to as "modified" secant method [139]. The effective shear strain invariant reads in the second moment definition:

$$\epsilon_\theta^{eff} \equiv \overline{\overline{\epsilon_\theta}} = \sqrt{\left\langle (\epsilon_\theta)^2 \right\rangle_{V_\theta}} = \sqrt{\langle \boldsymbol{\epsilon}_\theta : \boldsymbol{\epsilon}_\theta \rangle_{V_i}} \tag{8.13}$$

or equivalently:

$$\overline{\overline{\epsilon_\theta}}^2 = \left(\overline{\overline{A}}_\theta^{dd}\right)^2 E_d^2 + \left(\overline{\overline{A}}_\theta^{dv}\right)^2 E_v^2 \tag{8.14}$$

where $\overline{\overline{A}}_\theta$ stands for concentration factors. In contrast to the classical method, the modified method involves a priori a coupling in the localization between shear and volume strain. This is the case for the MT-scheme as developed in Table 8.1. For the HZ-scheme there are no cross terms between volumetric and deviatoric invariants:

$$\left(\overline{\overline{\epsilon_\theta}}^2\right)^{HZ} = \left(\overline{\overline{A}}_\theta^{d}\right)^2 E_d^2 \tag{8.15}$$

The localization coefficient of the modified secant method for the HZ-scheme is given in Table 8.2. :

Modified Strain Localization Factors for the MT scheme

The higher moment definition is based on an energy approach in which the effective strains are obtained as the derivatives of the macroscopic elastic strain energy ([46], [77])

The elastic energy of the REV is: $2\mathcal{E}=\langle \boldsymbol{\varepsilon} : \mathbb{C} : \boldsymbol{\varepsilon} \rangle_\Omega = \mathbf{E} : \mathbb{C}_{\text{hom}} : \mathbf{E}$

Assuming isotropic behavior of the phases we have:

$$\mathcal{E} = \left\langle \tfrac{1}{2} k \left(\varepsilon^v\right)^2 + \mu \epsilon : \epsilon \right\rangle_\Omega$$

Following Kreher[77] displacements $\boldsymbol{\xi}$ and strains are considered functions of the elastic moduli. This leads to expressing the derivatives of the elastic energy in the form:

$$\frac{\partial \mathcal{E}}{\partial k_\theta} = f_\theta \left(\tfrac{1}{2} \overline{\overline{\varepsilon_\theta}}^2 + \left\langle \sigma : \frac{\partial \varepsilon}{\partial k_\theta} \right\rangle_V \right)$$

$$\frac{\partial \mathcal{E}}{\partial \mu_\theta} = f_\theta \left(\tfrac{1}{2} \overline{\overline{\epsilon_\theta}}^2 + \left\langle \sigma : \frac{\partial \varepsilon}{\partial \mu_\theta} \right\rangle_V \right)$$

where $V = \Omega - \omega_\theta$

This expression serves as a definition for $\overline{\overline{\varepsilon_\theta}}^2$ and $\overline{\overline{\epsilon_\theta}}^2$

In the case of a two phase material with rigid or empty inclusion I and matrix m we have: $\left\langle \sigma : \frac{\partial \varepsilon}{\partial \mu_m} \right\rangle_{\omega_I} = 0 = \left\langle \sigma : \frac{\partial \varepsilon}{\partial k_m} \right\rangle_{\omega_I}$

Finally this yields for the effective shear strain:

$$\overline{\overline{\epsilon_m}}^2 = \frac{2}{f_m} \frac{\partial \mathcal{E}}{\partial \mu_m} = \frac{1}{f_m} \frac{\partial}{\partial \mu_m} \left(\mathbf{E} : \mathbb{C}_{\text{hom}} : \mathbf{E} \right) = \frac{1}{f_m} \left(\frac{\partial k_{\text{hom}}}{\partial \mu_m} E_v^2 + \tfrac{1}{2} \frac{\partial \mu_{\text{hom}}}{\partial \mu_m} E_{dv}^2 \right)$$

so that: $\left(\overline{\overline{A_m}}^{dd} \right)^2_{MT} = \frac{1}{2f_m} \frac{\partial \mu_{\text{hom}}}{\partial \mu_m}$; $\left(\overline{\overline{A_m}}^{dv} \right)^2_{MT} = \frac{1}{f_m} \frac{\partial k_{\text{hom}}}{\partial \mu_m}$

For voids we have: $\left(\overline{\overline{A_m}}^{dv} \right)^2_{MT} = \frac{12 f_I k_{\text{hom}}^2}{\left(4\mu_{\text{hom}} + 3 f_I k_{\text{hom}}\right)^2}$;

$\left(\overline{\overline{A_m}}^{dd} \right)^2_{MT} = \frac{k_{\text{hom}}^2 \left(81 - 27 f_I (1-2f_I) - 48 k_{\text{hom}} \mu_{\text{hom}} f_i (1-2f_I) + 32 \mu_{\text{hom}}^2 (2 + f_I (1-3f_I))\right)}{2 f_m \left[k_{\text{hom}} (9 + 6 f_I) + \mu (8 + 12 f_I)\right]^2}$

For rigid inclusions: $\left(\overline{\overline{A_m}}^{dv} \right)^2_{MT} = \frac{4 f_I k_{\text{hom}}}{3 (1-f_I)^2}$; $\left(\overline{\overline{A_m}}^{dd} \right)^2_{MT} = \frac{(6+9f_I) k_{\text{hom}} + \mu_{\text{hom}} (1+\mu_{\text{hom}}) (24+16 f_I)}{12 (1+2\mu_{\text{hom}})^2 f_m^2}$

Table 8.1: Localization coefficients for the MT scheme based on the 2nd moment strain average

Modified Method Strain Localization Factors for the HZ scheme

With the displacement solution from Tables 7.6 and 7.5
the local strains are calculated:

$$\varepsilon^{\theta}(\mathbf{x}) = \tfrac{1}{2}\left(\boldsymbol{\nabla}\boldsymbol{\xi}^{(\theta)} + {}^{t}\boldsymbol{\nabla}\boldsymbol{\xi}^{(\theta)}\right)$$

This leads to the following expressions of the localization coefficients:

$$\left(\frac{\overline{\overline{=}}^{d}}{A_{\theta}}\right)^{2} = \left(\bar{\bar{\epsilon}}_{\theta}/E_{d}\right)^{2} = \frac{1}{(1-2\,\nu_{\theta})^{2}}\left[3\bar{b}_{\theta}^{2}(8\nu_{\theta}^{2}+35)\frac{R_{\theta}^{7}-R_{\theta-1}^{7}}{R_{\theta}^{3}-R_{\theta-1}^{3}} + 42\bar{a}_{\theta}\,\bar{b}_{\theta}\,(2\,\nu_{\theta}-1)\frac{R_{\theta}^{5}-R_{\theta-1}^{5}}{R_{\theta}^{3}-R_{\theta-1}^{3}}\right.$$

$$+5\bar{a}_{\theta}^{2}\,(1-2\,\nu_{\theta})^{2} + 24\,\bar{b}_{\theta}\,\bar{d}_{\theta}\,\nu_{\theta}(5-7\,\nu_{\theta})\frac{R_{\theta}^{2}-R_{\theta-1}^{2}}{R_{\theta}^{3}-R_{\theta-1}^{3}} + 8\bar{d}_{\theta}^{2}\,(7\,\nu_{\theta}^{2}-10\,\nu_{\theta}+10)\,\frac{1}{R_{\theta}^{3}\,R_{\theta-1}^{3}}$$

$$\left. + 144\,\bar{c}_{\theta}\,\bar{d}_{\theta}\,(1-2\,\nu_{\theta})\frac{R_{\theta}^{5}-R_{\theta-1}^{5}}{R_{\theta}^{5}R_{\theta-1}^{5}(R_{\theta}^{3}-R_{\theta-1}^{3})} + 120\,\bar{c}_{\theta}^{2}(1-2\,\nu_{\theta})^{2}\frac{R_{\theta}^{7}-R_{\theta-1}^{7}}{R_{\theta}^{7}R_{\theta-1}^{7}(R_{\theta}^{3}-R_{\theta-1}^{3})}\right]$$

Table 8.2: Localization coefficients for the HZ-scheme based on the 2nd moment strain average

8.2 Strength Homogenization at High Confinement: Friction Coefficient

In this first part of the homogenization of strength properties, we focus on the frictional behavior of cementitious materials originally proposed by Lemarchand et al. [83]. The frictional capacity is expressed in e.g. the Drucker-Prager strength criterion, through the friction coefficient δ. It characterizes the strength of the cementitious materials particularly for high confinement levels for which $\delta_{\theta}\,\sigma_{M}^{\theta} \gg c_{\theta}$. In these stress domains, the experimental results of (Chapters 5 and 6) showed that the ITZ plays only a small role. Indeed it was found that the ITZ is crushed under the confinement (see for instance Figure 6-5). An appropriate representation of this microstructure on Level III is an inclusion phase (aggregate) embedded into a matrix phase (paste). The MT scheme is used for localization and homogenization.

8.2.1 Friction Enhancement at Level III: Representation

The representation includes for the paste (subsrcipt $\theta = m$) the Drucker-Prager strength criterion for the matrix (Level II):

$$f(\boldsymbol{\sigma}_m) = \sqrt{j_2} + \delta_m \, \sigma_M^m - c_m \leq 0 \tag{8.16}$$

where δ_m and c_m are the friction coefficient and the cohesion of the matrix (see Table 5.3). For $f(\boldsymbol{\sigma}_m) = 0$, the shear strength $s_m = \sqrt{2j_2} = \sqrt{2} \, |c_m - \delta_m \, \sigma_M^m|$, can be seen as an asymptotic value in a deviatoric compression test:

$$\lim_{\epsilon^m \to \infty} s^m = \sqrt{2} \, |c_m - \delta_m \, \sigma_M^m| \tag{8.17}$$

Making use of the nonlinear elastic representation of the stress-strain relation (8.3) the secant shear modulus $\mu_m(\epsilon_m)$ in the equivalent non-linear elastic constitutive law must comply with,

$$\lim_{\epsilon^m \to \infty} \mu_m(\epsilon_m) \, \epsilon_m = \frac{1}{\sqrt{2}} \, |c_m - \delta_m \, k_m \varepsilon_m^v| \tag{8.18}$$

In the case of high confinement $c_m \ll \mu_m(\epsilon_m) \, \epsilon_m$, and (8.18) can be solved for the local friction coefficient:

$$\delta_m = -\sqrt{2} \lim_{\epsilon^m \to \infty} \left(\frac{\mu_m(\epsilon_m)}{k_m(\epsilon_m)} \times \frac{\epsilon_m}{\varepsilon_m^v} \right) \tag{8.19}$$

Macroscopically, that is for the mortar (Level III), a Drucker-Prager criterion is used to the describe the strength domain:

$$F(\boldsymbol{\Sigma}) = \sqrt{J_2} + \delta_{\text{hom}} \, \Sigma_M - c_{\text{hom}} \leq 0 \tag{8.20}$$

where δ_{hom} and c_{hom} are respectively the friction coefficient and the cohesion of the mortar, see Table 5.3. The equivalent macroscopic deviator stress is $S = \sqrt{\underline{\underline{S}} : \underline{\underline{S}}} = \sqrt{2J_2}$. It follows at failure:

$$F(\boldsymbol{\Sigma}) = 0 \Leftrightarrow S = \sqrt{2} \, |c_{\text{hom}} - \delta_{\text{hom}} \, \Sigma_M| \tag{8.21}$$

With the nonlinear elastic representation of the 'real' behavior of the mortar, S and Σ_M are related to E_d and E_v by:

$$S = 2\mu_{\text{hom}} E_d \quad ; \quad \Sigma_M = k_{\text{hom}} E_v \tag{8.22}$$

where μ_{hom} and k_{hom} are the macroscopic secant moduli (i.e. the one of the mortar). For high values of the shear strain E_d corresponding to the limit case, the macroscopic counterpart of (8.18) reads:

$$\lim_{E_d \to \infty} \mu_{\text{hom}} E_d = \frac{1}{\sqrt{2}} \left| c_{\text{hom}} - \delta_{\text{hom}}\, k_{\text{hom}}\, E_v \right| \tag{8.23}$$

or equivalently, noting that $c_{\text{hom}} \ll \mu_{\text{hom}}\, E_d$ in the case of high confinement:

$$\delta_{\text{hom}} = -\sqrt{2} \lim_{E_d \to \infty} \left(\frac{\mu_{\text{hom}}}{k_{\text{hom}}} \times \frac{E_d}{E_v} \right) \tag{8.24}$$

Finally, a combination of (8.19) and (8.24) delivers the ratio of the macroscopic to microscopic friction coefficient in the form:

$$\frac{\delta_{\text{hom}}}{\delta_m} = \lim_{\substack{E_d \to \infty \\ \epsilon^m \to \infty}} \left(\frac{\rho_{\text{hom}}}{\rho_m} \times \frac{E_d}{E_v} \times \left(\frac{\epsilon_m}{\varepsilon_m^v} \right)^{-1} \right) \tag{8.25}$$

where $\rho_{\text{hom}} = \frac{\mu_{\text{hom}}}{k_{\text{hom}}}$ and $\rho_m = \frac{\mu_m}{k_m}$. The limit of infinite deviatoric deformations is respected when the shear deformation is much larger than the volumetric deformation, $E_d \gg E_v$, and when the bulk modulus is much larger than the shear modulus, such that $\rho_m \to 0$. These conditions are used in the evaluation of (8.25).

8.2.2 Localization and Homogenization

For the localization and homogenization we use the MT scheme. In the absence of an ITZ it should describe well the influence of the aggregates (Index I) on the homogenized properties. The volume fraction of the aggregates is $f_I = 0.5$. To evaluate (8.25) we need to determine the effective strains in the matrix and the ratio $\frac{\rho_{\text{hom}}}{\rho_m}$.

For the classical definition of the strain average we have:

$$\overline{\left(\frac{\delta_{\text{hom}}}{\delta_m}\right)} = \lim_{\substack{\rho_m \to 0 \\ E_d/E_v \to \infty}} \left(\frac{\rho_{\text{hom}}}{\rho_m} \times \frac{E_d}{E_v} \times \left(\frac{\bar{\epsilon}_m}{\bar{\epsilon}_m^v} \right)^{-1} \right) \tag{8.26}$$

$$= \lim_{\substack{\rho_m \to 0 \\ E_d/E_v \to \infty}} \left(\frac{\rho_{\text{hom}}}{\rho_m} \times \frac{A_m^v}{A_m^d} \right) \tag{8.27}$$

Injecting (8.9) and (8.10) in (8.26), while assuming, in (7.15) and (7.16), that the inclusions are rigid, we obtain:

$$\overline{\left(\frac{\delta_{\text{hom}}}{\delta_m}\right)} = 1 + \frac{3}{2} f_I \tag{8.28}$$

The classical method predicts a frictional enhancement that is a linear function of the inclusion volume fraction. Figure 8-1 illustrates this estimate, and displays the experimental data. The first moment approach overestimates the increase in frictional capacity.

To improve the estimation, we use the 2nd moment definition of the effective shear strains in the matrix while keeping the 1st moment definition for the volumetric strains, as proposed by Lemarchand [83]. This combination yields the following modified estimate for the frictional enhancement:

$$\overline{\overline{\left(\frac{\delta_{\text{hom}}}{\delta_m}\right)}} = \lim_{\substack{\rho_m \to 0 \\ E_d/E_v \to \infty}} \left(\frac{\rho_{\text{hom}}}{\rho_m} \times \frac{E_d}{E_v} \times \left(\frac{\bar{\bar{\epsilon}}_m}{\bar{\epsilon}_m^v} \right)^{-1} \right) \tag{8.29}$$

Expression (??) can be evaluated with the help of (8.9), (8.10), (7.15) and (7.16) and the value for the 2nd moment localization coefficient from Table 8.1. This yields:

$$\overline{\overline{\left(\frac{\delta_{\text{hom}}}{\delta_m}\right)}} = \sqrt{1 + \frac{3}{2} f_I} \tag{8.30}$$

Figure 8-1 shows for the case of unleached materials that the modified method gives an excellent estimate of the friction enhancement. For the case of leached materials, the method predicts a priori the same value, as the only variable of the frictional enhancemnet in (8.30) is the inclusion volume fraction. However, large compressive deformations were observed during the triaxial tests with increasing deviatoric stress (Section 6.3). The actual volume fraction of inclusions is therefore certainly higher than 0.5 which would improve the estimate. An excellent estimate is obtained with an effective volume fraction of $f_I^{eff} = f_I^0 \times \phi^\infty / \phi_0 = 0.7$.

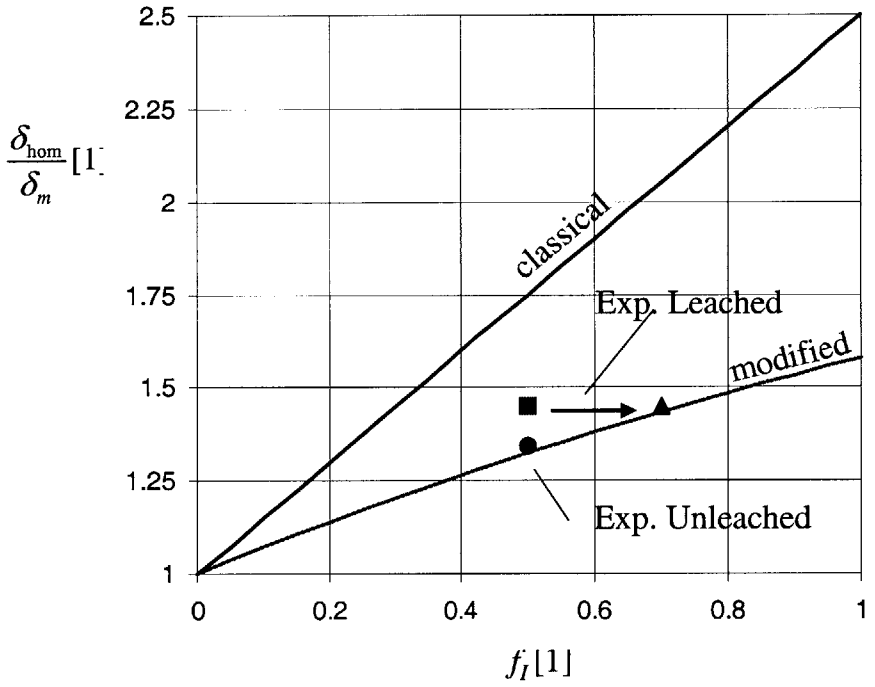

Figure 8-1: Evolution of the predicted friction coefficient ratio $\delta_{\mathrm{hom}}/\delta_{\mathrm{m}}$ versus inclusion volume fraction f_I for the classical and the modified secant method. Figure adapted from [83].

8.2.3 Friction Coefficient at Level II: Effect of Portlandite

The developed micromechanical technique allows an estimation of the effect of Portlandite on the friction coefficient of the paste. To this end we consider the paste as the REV, composed of a matrix (unleached C-S-H) and voids. These voids are due to the leaching of Portlandite. We use the MT scheme for localization and homogenization, and evaluate (8.26) by injecting (8.9) and (8.10), in (8.26) and by assuming in (7.15) and (7.16) that the inclusions are voids. This yields for the classical method:

$$\overline{\left(\frac{\delta_{\rightarrow \mathrm{CH}}}{\delta_{\mathrm{C-S-H}}}\right)} = 1 - \phi_{\rightarrow \mathrm{CH}} \tag{8.31}$$

where ϕ is the porosity of the paste created through the Portlandite leaching and $\delta_{\rightarrow \mathrm{CH}}$ is the friction coefficient of the Portlandite free cement paste. Equation (8.31) is a predictive formula for the loss of friction that goes along with the dissolution of Portlandite. Application of the mixed method yields with the 2nd moment localization coefficient from Table 8.1:

$$\overline{\overline{\left(\frac{\delta_{\rightarrow \mathrm{CH}}}{\delta_{\mathrm{C-S-H}}}\right)}} = \frac{1 - \phi_{\rightarrow \mathrm{CH}}}{\sqrt{1 + \frac{2}{3}\phi_{\rightarrow \mathrm{CH}}}} \tag{8.32}$$

which gives in the domain of interest for $\phi_{\rightarrow \mathrm{CH}} \in [0; 0.15]$ values that are very close to (8.31). For $\phi_{\rightarrow \mathrm{CH}} = 0.14$, the decrease in friction coefficient is $\overline{\left(\frac{\delta_{\rightarrow \mathrm{CH}}}{\delta_{\mathrm{C-S-H}}}\right)}$ =0.86 and $\overline{\overline{\left(\frac{\delta_{\rightarrow \mathrm{CH}}}{\delta_{\mathrm{C-S-H}}}\right)}} = 0.90$. The friction coefficient of the C-S-H matrix can be estimated analogously from the intact paste:

$$\overline{\left(\frac{\delta_m}{\delta_{\mathrm{C-S-H}}}\right)} = 1 - \phi_0; \quad \overline{\overline{\left(\frac{\delta_m}{\delta_{\mathrm{C-S-H}}}\right)}} = \frac{1 - \phi_0}{\sqrt{1 + \frac{2}{3}\phi_0}} \tag{8.33}$$

where ϕ_0 is the initial porosity at Level II (=0.03). Combining (8.31) and (8.33), we can estimate the reduction of the friction coefficient of the paste caused by the Portlandite dissolution to be:

$$\overline{\left(\frac{\delta_{\rightarrow \mathrm{CH}}}{\delta_m}\right)} = \frac{(1 - \phi_{\rightarrow \mathrm{CH}})}{1 - \phi_0}; \quad \overline{\overline{\left(\frac{\delta_{\rightarrow \mathrm{CH}}}{\delta_m}\right)}} = \frac{1 - \phi_{\rightarrow \mathrm{CH}}}{\sqrt{1 + \frac{2}{3}\phi_{\rightarrow \mathrm{CH}}}} \times \frac{\sqrt{1 + \frac{2}{3}\phi_0}}{1 - \phi_0} \tag{8.34}$$

which yields assuming the 14% porosity $\overline{\left(\frac{\delta_{\rightarrow CH}}{\delta_m}\right)} = 0.88$ and $\overline{\overline{\left(\frac{\delta_{\rightarrow CH}}{\delta_m}\right)}} = 0.86$. The total reduction of the friction coefficient for the cement paste through leaching is roughly 32% (Table 5.3) so that the effect of the Portlandite dissolution accounts for almost half of it, the other half being associated with the C-S-H decalcification.

8.3 Strength Homogenization at Low Confinement: Cohesion

The second part of the homogenization of strength properties focuses on low confinement stress states. These are stress states in which the cohesion dominates the strength of materials. In a similar fashion as for the frictional capacities, we apply the micromechanical techniques for strength homogenization presented in this Chapter. In low confinement stress states, the ITZ has to be taken into account when considering the Level III representation. In contrast to high confinement situations, the ITZ is not crushed, but plays an important role for the macroscopic material strength. We therefore choose the HZ scheme for the homogenization at Level III. The strength properties of the ITZ are unknown. Some microhardness measurements were reported by different authors which show hardness values between 25% to 40% of the bulk paste, but no experimental data on the strength properties of the ITZ are available. In addition, these hardness measurements vary strongly in absolute values ([103], [159], see also Section 2.2.4). The object of the cohesion homogenization therefore is first to deduce the properties of the ITZ from the homogenization at Level III. In a second step we study the cohesion homogenization problem at Level II to estimate the influence of Portlandite leaching.

8.3.1 Representation for the Cohesion Homogenization

We consider the geometrical representation of the HZ scheme (see Fig. 7-2) with the aggregates (index 1), the ITZ (index 2) and the paste (index 3). The microscopic strength is described by (8.2) and the non-linear elastic representation by the stress-strain relation (8.3). We consider a macroscopically purely deviatoric loading for which the solution of the BVP for the microscopic strains is given in Table 7.6. In the HZ scheme, a macroscopic deviatoric deformation leads to microscopically deviatoric strains only. In this situation the microscopic strength criteria can

be rewritten in the case of failure as:

$$f(\boldsymbol{\sigma}_\theta) = 0 \Leftrightarrow \lim_{\epsilon_\theta \to \infty} s^\theta = \sqrt{\frac{1}{2}}\, c_\theta \Rightarrow c_\theta = \sqrt{2} \lim_{\epsilon_\theta \to \infty} \left[\mu_\theta(\epsilon_\theta)\, \epsilon_\theta\right] \tag{8.35}$$

Analogously, the macroscopic (mortar) strength criterion delivers at failure:

$$F(\boldsymbol{\Sigma}) = 0 \Leftrightarrow \lim_{E_d \to \infty} S = \sqrt{\frac{1}{2}}\, c_{\text{hom}} \Rightarrow c_{\text{hom}} = \sqrt{2} \lim_{E_d \to \infty} \left[\mu_{\text{hom}} E_d\right] \tag{8.36}$$

Finally, a combination of (8.35) and (8.36) delivers:

$$\frac{c_{\text{hom}}}{c_\theta} = \lim_{\substack{E_d \to \infty \\ \epsilon_\theta \to \infty}} \left[\frac{\mu_{\text{hom}}}{\mu_\theta(\epsilon_\theta)} \times \frac{E_d}{\epsilon_\theta}\right] \tag{8.37}$$

The limits of infinite microscopic and macroscopic deviatoric strains are assured by letting $\rho_\theta = \mu_\theta / k_\theta$ for the ITZ and matrix tend towards zero.

8.3.2 Localization and Homogenization

Equation (8.37) is being evaluated in the context of the HZ scheme by injecting (7.26) and (8.11) or (8.15) in (8.37). This yields the ratio of mortar to paste cohesion:

$$\frac{c_{\text{hom}}}{c_3} = \lim_{\substack{\rho_3 \to 0 \\ \rho_2 \to 0}} \left(\frac{(\eta_2 - \eta_1)\, f_2 A_2^d + (1 - \eta_1)\, f_3 A_3^d}{A_3^{d,eff}} \right) = \mathcal{F}(\eta_1; \eta_2; f_\theta) \tag{8.38}$$

where $\eta_\theta = \mu_\theta / \mu_3$ denotes the shear modulus ratio with respect to the matrix shear modulus. $A_3^{d,eff}$ is the localization coefficient which depends on the definition of the effective strains. Expression (8.38) depends only on the shear modulus ratios and the volume fractions. An analogous expression can be derived for the ratio of homogenized cohesion and ITZ cohesion so that the interface-to-matrix cohesion ratio, $\chi = c_2/c_3$, can be expressed as:

$$\chi = \frac{c_2}{c_3} = \eta_2 \times \lim_{\substack{\rho_m \to 0 \\ \rho_i \to 0}} \left(\frac{A_2^{d,eff}}{A_3^{d,eff}} \right) \tag{8.39}$$

This expression shows that η_2 can be directly related to χ so that we can formally rewrite (8.38):

$$\frac{c_{\text{hom}}}{c_3} = \mathcal{F}(\eta_1; \eta_2 \rightarrow \chi; f_\theta) = \mathcal{G}(\eta_1; \chi; f_\theta) \tag{8.40}$$

Expressions (8.38) to (8.40) are evaluated numerically using MAPLE®. A typical input file is shown in Appendix C.

8.3.3 Parameter Study: Effect of the ITZ Cohesion on the Mortar Cohesion

In a first application of the developed micromechanical model we want to gain insight into the quantitative effect of the ITZ on the mortar cohesion. To this end we evaluate expressions (8.38) to (8.40) for the aggregate volume fractions $f_1 = 0.5$ (assumed to be rigid, $\eta_1 \rightarrow 0$) while the ITZ volume fraction f_2 takes the values 0.15; 0.30 and 0.45, scanning a range of possible ITZ volume fractions. The results are given for both the classical and the modified definition of the effective strains, and are displayed in Figures : 8-2, 8-3 and 8-4:

- The "a"–figures display the cohesion ratio as a function of the shear-modulus ratio $\eta_2 \in [0, 1]$, that is the result of (8.38). It is interesting to note that the classical and modified definition do not deliver the same solution, and diverge even for high interface volume fractions (see Figure 8-4a). When the ITZ volume fraction tends toward 0.5, the paste vanishes and the representation as a three phase model becomes obsolete.

- The "b"–figures display the relation between η_2 and χ, that is the result of (8.39). It is interesting to note here, that for low values of $\eta_2 \leq 0.2$, both methods deliver almost identical values. Note also that the interface-to-matrix cohesion range of practical interest is $\chi \in [0, 1]$, meaning that the interface is the weaker material. This corresponds to η_2−values roughly smaller than 0.5. Higher values for χ are irrelevant for cement based materials in which the ITZ, if it exists, is always weaker than the matrix.

- Finally, the "c"– figures display the final result of the homogenization procedure, that is c_{hom}/c_3 as a function of the interface-to-matrix cohesion ratio $\chi \in [0, 1]$, obtained by the variable change $\eta_2 \rightarrow \chi$, that is the solution of (8.40) In all the considered cases, it appears that the macroscopic (mortar) cohesion ratio on Level III is a nonlinear increasing

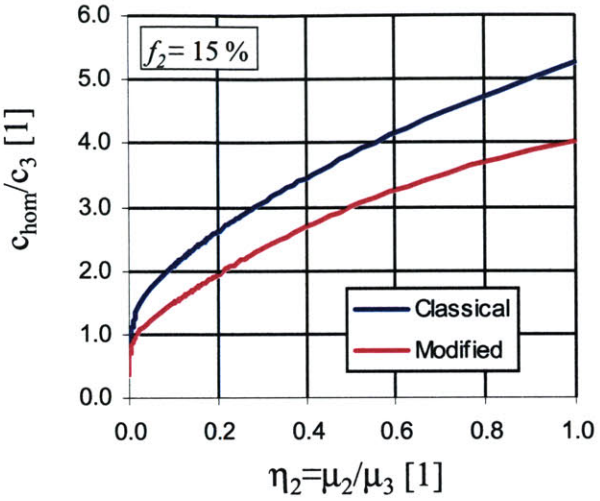

(a)

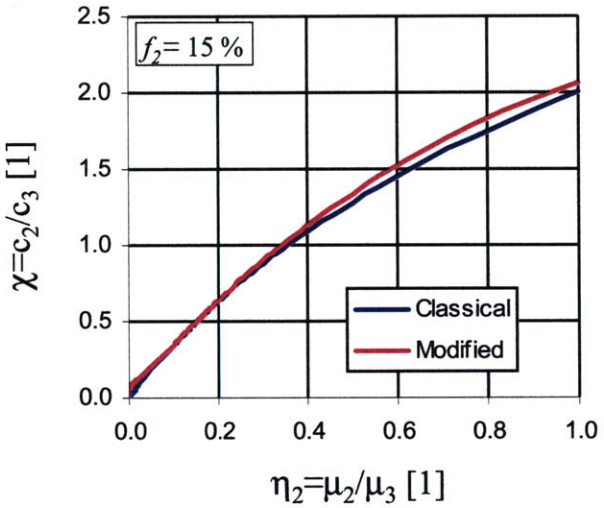

(b)

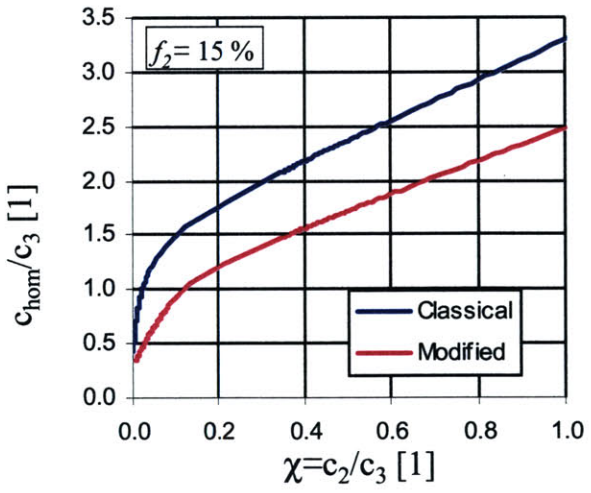

(c)

Figure 8-2: Strength homogenization procedure for $f_2 = 0.15$ and $f_1 = 0.5$: (a) c_{hom}/c_3 vs. η_2; (b) χ vs. η_2; (c) c_{hom}/c_3 vs. $\chi = c_2/c_3$.

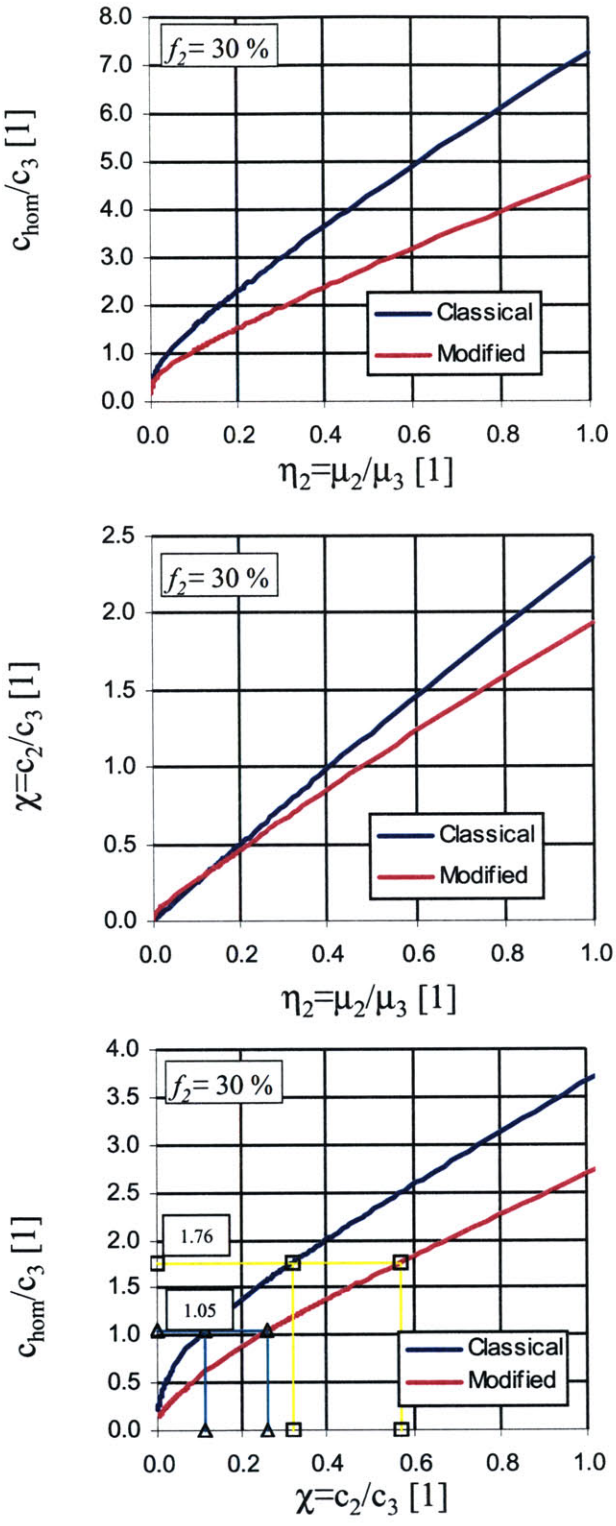

Figure 8-3: Strength homogenization procedure for $f_2 = 0.3$ and $f_1 = 0.5$: (a) c_{hom}/c_3 vs. η_2; (b) χ vs. η_2; (c) c_{hom}/c_3 vs. $\chi = c_2/c_3$.

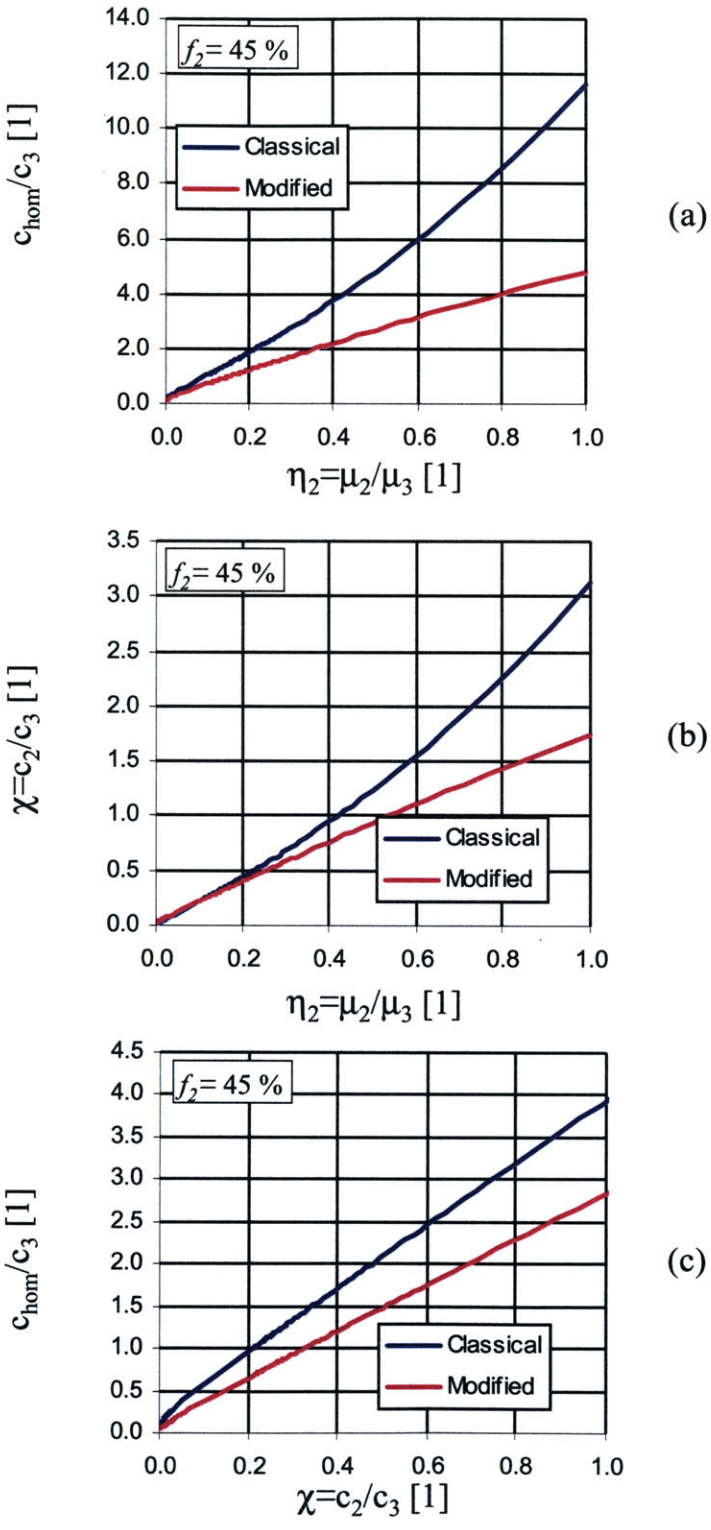

Figure 8-4: Strength homogenization procedure for $f_2 = 0.45$ and $f_1 = 0.5$: (a) c_{hom}/c_3 vs. η_2; (b) χ vs. η_2; (c) c_{hom}/c_3 vs. $\chi = c_2/c_3$.

function of the interface-to-matrix cohesion ratio. The classical strain definition generally predicts a higher mortar cohesion than the modified method.

A characteristic parameter in the cohesion homogenization is the critical value of the interface-to-matrix cohesion ratio χ, below which the composite cohesion, c_{hom}, is smaller than the one of the matrix, i.e. $c_{\text{hom}}/c_3 < 1$; and above it is the inverse. Figure 8-5 this critical interface-to-matrix cohesion ratio, $\chi^{crit} \Leftrightarrow c_{\text{hom}}/c_3 = 1$, as a function of the interface volume fraction f_2 for an inclusion volume fraction of $f_1 = 0.5$. As expected, a higher interface volume fraction requires compensation by a higher $\chi^{crit}-$ value to deliver the same performance $c_{\text{hom}}/c_3 = 1$. Interestingly, the modified method delivers, for moderate interface volume fractions, an almost linear $\chi^{crit} - f_2$ relation , with values that are much greater than the one predicted by the classical method. This underscores that the modified method is more sensitive to the interface properties than the classical secant method.

8.3.4 Inverse Analysis: Chemical Softening of the ITZ Cohesion

An application of special interest of the model is the determination of the ITZ properties. In a similar fashion as for the elastic properties of the ITZ (see Section 7.2.4), we determine the cohesion properties by matching experimental results and model predictions. The input parameters to the inverse application of the model are the following:

1. The volume fractions of the aggregates and the ITZ: The aggregate volume fraction is $f_1 = 0.5$. The ITZ volume fraction was determined in Section 7.2.4 and is $f_2 = 0.3$.

2. The experimental mortar-to cement paste cohesion ratio is $c_{\text{hom}}/c_3 = 1.76$ for the undegraded material, and $c_{\text{hom}}/c_3 = 1.05$ for the asymptotically leached material (Table 5.6).

Using these values in Figure 8-3c ($f_2 = 0.3; f_1 = 0.5$) provides a means of estimating the interface-to-matrix cohesion ratio $\chi = c_2/c_3$. For the nondegraded material, we obtain:

$$\left(\frac{c_{\text{hom}}}{c_3}\right)^0 = 1.76 \Rightarrow \chi^0 \in [0.32; 0.57] \tag{8.41}$$

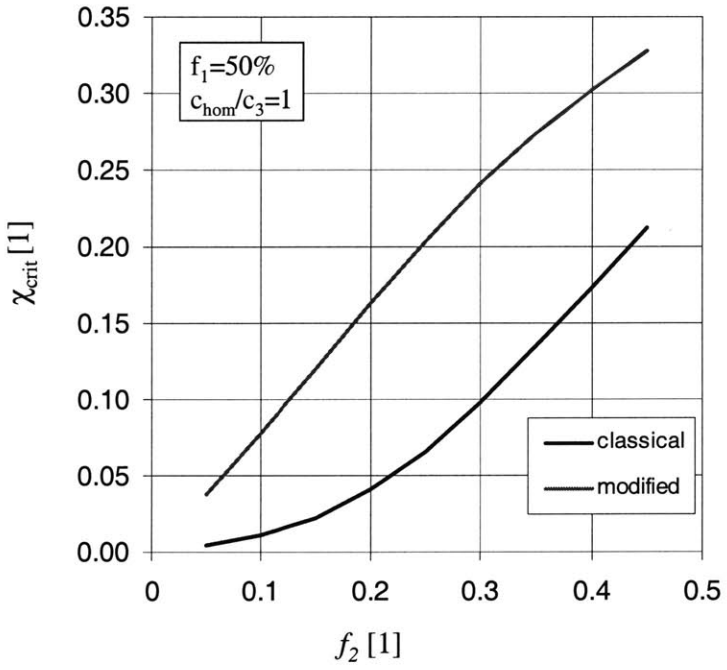

Figure 8-5: Critical interface-to-matrix cohesion ratio $\chi_{crit} \Leftrightarrow c_{\mathrm{hom}}/c_3 = 1$ vs. interface volume fraction (for an inclusion volume fraction $f_1 = 0.5$).

where the lower value corresponds to the classical method and the upper value to the modified method. Analogously, for the degraded material we find:

$$\left(\frac{c_{\text{hom}}}{c_3}\right)^{\infty} = 1.05 \Rightarrow \chi^{\infty} \in [0.11; 0.26] \tag{8.42}$$

The values for the nondegraded material (8.41) are on the same order as the reported microhardness measurements of the ITZ ([103], [159]). But, in addition, the model provides a means of estimating the effect of calcium leaching on the interface cohesion, for which both methods converge to a residual interface cohesion of approximately 15% of the initial cohesion:

$$\frac{c_2^{\infty}}{c_2^0} = \frac{\chi^{\infty}}{\chi^0} \times \frac{c_3^{\infty}}{c_3^0} \in [0.13; 0.17] \tag{8.43}$$

This value needs to be compared to the chemical softening of the matrix (Level II), $c_3^{\infty}/c_3^0 = 0.38$. It shows that the chemical softening of the ITZ in terms of cohesion is more severe than for the matrix. This is in contrast to the chemical damage of the elasticity properties discussed in Section 7.2.4 which was found to be on the same order (40-45%) for both ITZ and matrix. For mortars this means that beyond the overall strength loss due to calcium leaching, a particularly weak interface exists in chemically softened cement-based materials which dominates the cohesion of the composite material (Level III).

8.3.5 Limit Case: Empty Inclusion - Application for Portlandite leached Materials

Another application of interest in the context of calcium leaching is the limit case of empty inclusions, for which $c_2 = 0$, or $\eta_2 = \chi = 0$. This configuration represents a cement paste (Level II) from which the Portlandite has been dissolved. In this case, the only mechanically active phase is the matrix of volume fraction $1 - \phi_{\rightarrow \text{CH}}$. For this two phase composite, (8.38) reduces to:

$$\frac{c_{\rightarrow \text{CH}}}{c_{\text{C-S-H}}} = (1 - \phi_{\rightarrow \text{CH}}) \lim_{\rho_3 \rightarrow 0} \left(\frac{A_3^d}{A_3^{d,eff}}\right) \tag{8.44}$$

where $c_{\rightarrow \text{CH}}$ is the cohesion of the Portlandite free paste. The classical method ($A_3^{d,eff} = \overline{A}_3^d$) delivers a linear relation between the cohesion ratio $c_{\rightarrow \text{CH}}/c_{\text{C-S-H}}$ and the solid volume fraction

$1-\phi_{\rightarrow \mathrm{CH}}$. By contrast, the modified method delivers a non-linear relation between the cohesion ratio and the matrix volume fraction:

$$\chi = 0 : \frac{\overline{\overline{c_{\rightarrow \mathrm{CH}}}}}{c_3} = (1-\phi_{\rightarrow \mathrm{CH}}) \lim_{\rho_3 \rightarrow 0} \left(\frac{A_3^d}{\overline{\overline{A}}_3^d} \right) = \mathcal{H}(1-\phi_{\rightarrow \mathrm{CH}}) \tag{8.45}$$

Both estimates are displayed in Figure 8-6. The difference between the two is small, and similar to the friction coefficient (8.31), a linear porosity dependence is obtained for the cohesion in the case of Portlandite dissolution. To estimate the relative cohesion of the cement paste before and after Portlandite dissolution we estimate the C-S-H cohesion and obtain:

$$\frac{\overline{c_{\rightarrow \mathrm{CH}}}}{c_3} = \frac{1-\phi_{\rightarrow \mathrm{CH}}}{1-\phi_0}; \quad \frac{\overline{\overline{c_{\rightarrow \mathrm{CH}}}}}{c_3} = \frac{\mathcal{H}(1-\phi_{\rightarrow \mathrm{CH}})}{\mathcal{H}(1-\phi_0)} \tag{8.46}$$

Expression (8.46) is a predictive formula for the cohesion reduction associated with the Portlandite dissolution. It yields for the cohesion ratio with the classical method 0.88 and with the modified method 0.85.

We can also determine the intrinsic chemical softening of the C-S-H matrix versus the chemical softening induced by an increase of the porosity of the cement paste. The volume fraction $1-\phi$ corresponds to the total porosity[2] and $c_{\mathrm{hom}} = c_3$ is the cement paste cohesion, and $c_3 = c_{\mathrm{C-S-H}}$ the cohesion of the matrix solid phase at Level II. For the classical method, using the values for the cement paste cohesion from Table 5.6, we obtain:

$$\frac{\overline{c^{\infty}_{\mathrm{C-S-H}}}}{c^0_{\mathrm{C-S-H}}} = \left(\frac{c_3^{\infty}}{c_3^0} \right) \times \frac{1-\phi_0}{1-\phi_{\infty}} = 0.46 \tag{8.47}$$

Analogously, for the modified secant method:

$$\frac{\overline{\overline{c^{\infty}_{\mathrm{C-S-H}}}}}{c^0_{\mathrm{C-S-H}}} = \left(\frac{c_3^{\infty}}{c_3^0} \right) \times \frac{\mathcal{H}(1-\phi_0)}{\mathcal{H}(1-\phi_{\infty})} = 0.48 \tag{8.48}$$

where $\mathcal{H}(1-\phi_0) = 0.97$ and $\mathcal{H}(1-\phi_{\infty}) = 0.76$ are the values taken by function $\mathcal{H}(1-\phi)$ displayed in Figure 8-6 for respectively the initial porosity $\phi_0 = 0.03$ and the asymptotic porosity

[2]Note that the macro-porosity is not the total porosity of the material but the porosity at Level II considered as a phase of the matrix in the sense of continuum micromechanics. This corresponds to the micrometer-range porosity of cement-based materials.

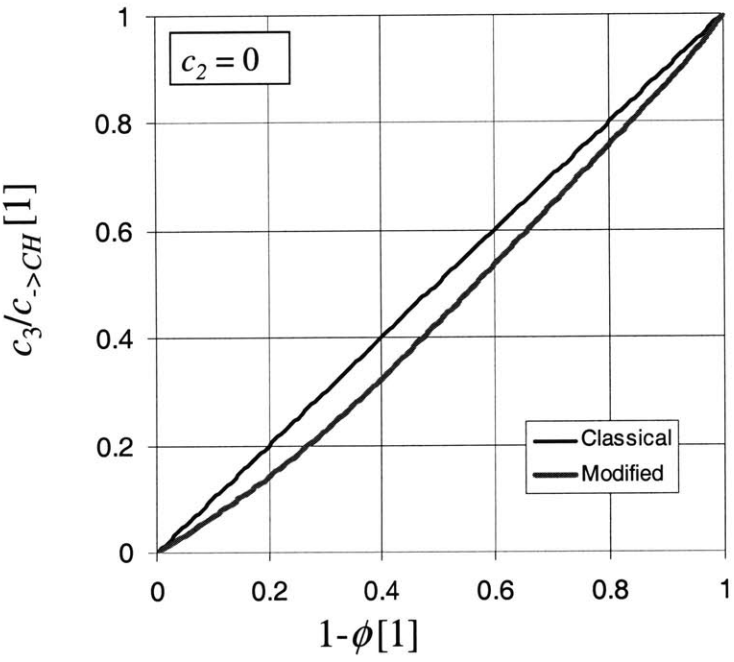

Figure 8-6: Limit Case of empty inclusions: $c_3/c_{\rightarrow \mathrm{CH}}$ vs. $1 - \phi$ (= solid volume fraction).

$\phi_\infty = 0.21$ of the cement paste (Level II). We obtain with both methods an estimated cohesion reduction through leaching of more than 50%. This means that calcium leaching does not only affect the strength properties of cement pastes or mortars by an increase of the porosity. There exists a second source of cohesion reduction which is an intrinsic softening of the solid material composing the Level II matrix. Such a change in intrinsic properties, particularly of the C-S-H matrix, was suggested by Adenot [3] from morphology measurements performed through Small Angle Neutron Scattering (SANS). It also is in accord with the statistical mechanics simulations by Pellenq et al. [113], who suggested that an increase of the C/S ratio which occurs during leaching should decrease the C-S-H cohesion. On the other hand, Beaudoin et al. [15] concluded from the extrapolation of elasticity measurements on C-S-H with different C/S ratios that no change in intrinsic properties should take place at Level I. Beaudoin's measurements however, did not consider the C/S ratio of interest (≤ 1), for which Adenot showed that precisely at C/S=1, a change in C-S-H morphology takes place. Hence, it seems likely that the extrapolation by Beaudoin is not appropriate.

8.4 Chapter Summary

In this Chapter we extended the micromechanical techniques to the homogenization of strength properties.

- In high confinement stress states, the frictional behavior is dominant and the ITZ can be neglected. Based on the approach by Lemarchand et al. [83] an estimate for the friction enhancement in mortars was given which predicts well the experimentally observed values. With the same approach, the effect of Portlandite dissolution on the friction coefficient of a paste was estimated. A linear relation of friction coefficient ratio and porosity created by Portlandite dissolution was obtained.

- At low confinement levels, the cohesion describes the material strength and the ITZ is of importance. The homogenization scheme for the cohesion involving the Hervé-Zaoui scheme is an original contribution to the field of micromechanics. The cohesion of the ITZ can be estimated by matching model predictions and experimental results for mortars. This revealed that the ITZ is more affected by the leaching process than the paste, a

result that is in line with microstructural observations. The developed homogenization scheme was also used for the estimate of the Portlandite dissolution effect on the cohesion. Similarly to the friction coefficient, a linear relation with the porosity increase was found. In particular, application of the homogenization model at Level II showed that the softening through calcium leaching is not only due to an increase in porosity but also due to a chemical softening of the Level II solid matrix.

The results derived in this Chapter on the one hand enhance the understanding of the strength scaling in cement based materials, here described through friction coefficient and cohesion. On the other hand, based on micromechanical approaches that are validated on experimental results of degraded and undegraded cementitious materials, we developed strength estimates for the experimentally non accessible degradation state in which only Portlandite is leached. These estimates are of importance for the constitutive model of cement based materials subjected to leaching. Table 8.3 summarizes the values for the friction coefficient and the cohesion for the three-level microstructure and the three reference states: Undegraded, Portlandite dissolution and asymptotically leached. Finally, while developed around the topic of cement-based materials, there are other composite materials for which the same approach could be used. They include filled epoxy resin [72], cemented soils [36], [73], frozen sand [121] and metal-ceramic composites [140].

Properties	Intact	Intermediate	Leached
High Confinement			
Level I			
δ [1]	0.85	0.85	0.71
c [GPa]	18.01	18.01	1.26
Level II			
δ [1]	0.82	0.71	0.56
c [GPa]	17.11	14.5	1.15
Level III			
δ [1]	1.02	0.94	0.81
c [GPa]	9.82	9.13	0.96
Low Confinement			
Level I			
δ [1]	1.67	1.67	1.26
c [GPa]	2.2	2.2	1.05
Level II			
δ [1]	1.62	1.39	0.99
c [GPa]	2.09	1.8	0.79
Level III			
δ [1]	1.43	1.34	0.91
c [GPa]	3.67	3.41	0.83

Table 8.3: Summary of the values for the strength properties. The asymptotic values correspond to the experimental data presented in Chapter 5.

Chapter 9

Chemomechanical Constitutive Model

So far, the investigation of the effects of calcium leaching on the mechanical behavior of cement pastes and mortars focused on the asymptotic states of leaching. Both experimentally and micromechanically strength properties and deformation behavior of the intact and asymptotically degraded state, have been analyzed. The objective of this Chapter is to develop the necessary means to bridge between these two asymptotic states by constitutive modeling. This includes for one part the constitutive modeling of the material behavior between the asymptotes; and secondly, intimately linked to the former, the modeling of the dissolution-diffusion process associated with leaching. This Chapter is organized as follows: In the first section we focus on the energy transformations of the solid phase of a cement based material subjected to leaching. Using a novel microchemomechanical theory we identify the sources of dissipation which need to be considered at a macroscopic scale. This macroscopic scale is considered in the second section, where an extended chemoporoplasticity model for leaching of cementitious materials is proposed. The third section presents the chemoplastic elements of the model, in combination with the experimental and micromechanical results presented in Chapters 5 to 8 of this study. Finally, the fourth section describes the dissolution-diffusion model that was developed in a one-dimensional setting in Section 3.1.2. Here, we develop the three-dimensional extension.

9.1 Micro-Chemomechanics of Calcium Leaching

The aim of this section is to identify the sources of dissipation of cement-based materials subjected to leaching *and* mechanical loading. Focusing on the behavior of the solid matrix, the thermodynamic system we consider is the solid at Level II of the microstructure of cement-based systems.

9.1.1 Kinematics and Mass Conservation

We consider an RVE composed of a solid phase[1] of volume V_s and a fluid phase of volume V_f. The RVE is subjected to the Hashin-type boundary condition (on $\partial V : \boldsymbol{\xi}_d = \mathbf{E} \cdot \mathbf{x}$). The initial volume of the RVE is denoted by V, and in the deformed configuration V_t so that the Lagrangian porosity reads:

$$\phi = \frac{V_f}{V} = \frac{V_t - V_s}{V} = J - \frac{V_s}{V} \tag{9.1}$$

where $J \simeq 1 + E_v$ is the Jacobian of deformation in infinitesimal deformation. The calcium leaching is considered to take place on the boundary of the solid phase, ∂V_s which is in contact with the fluid phase. A dissolution of calcium leads to displacement of this solid boundary. In addition, also the mechanical deformation of the solid phase can lead to a displacement of this boundary. Denoting by $\mathbf{U}^s \cdot \mathbf{n}_s$ the total normal velocity, it is decomposed in two terms:

$$\text{on } \partial V_s\text{: } \mathbf{U}^s \cdot \mathbf{n}_s = \mathbf{u}^s \cdot \mathbf{n}_s + \mathbf{u}^c \cdot \mathbf{n}_s \tag{9.2}$$

where $\mathbf{n}_s$ is the unit outward normal and $\mathbf{u}^s$ is the velocity associated with mechanical deformation, $\mathbf{u}^c$ is the velocity associated with the chemical dissolution. The change in solid volume can be expressed with (9.2) and $\mathbf{u}^c \cdot \mathbf{n}_s \leq 0$ in the form:

$$\frac{dV_s}{dt} = \int_{\partial V_s} \mathbf{U}^s \cdot \mathbf{n}_s da = \int_{\partial V_s} \left(\mathbf{u}^s \cdot \mathbf{n}_s + \mathbf{u}^c \cdot \mathbf{n}_s\right) da = \int_{V_s} \boldsymbol{\nabla} \cdot \mathbf{u}^s dV + \int_{\partial V_s} \mathbf{u}^c \cdot \mathbf{n}_s da \tag{9.3}$$

[1] For purpose of clarity, we omit here the difference between different solid phases at Level II and refer to all solid phases present as "solid phase".

The first term on the R.H.S. of (9.3) corresponds to the solid volume change induced by mechanical deformation. It is related to the microscopic volumetric strain rate by:

$$\boldsymbol{\nabla} \cdot \mathbf{u}^s = \frac{d\varepsilon_v^s}{dt} \tag{9.4}$$

where ε_v^s is the volume strain in the solid phase. In turn, the second term in (9.3) describes the volume change provoked by the moving solid boundary under chemical dissolution. Taking the total time derivative of (9.1) we obtain:

$$\begin{aligned} \frac{d\phi}{dt} &= \frac{dE_v}{dt} - \frac{1}{V}\left(\int_{V_s} \boldsymbol{\nabla} \cdot \mathbf{u}^s dV - \int_{\partial V_s} \mathbf{u}^c \cdot \mathbf{n}_s da\right) \\ &= \frac{dE_v}{dt} - \frac{V_s}{V}\left\langle \frac{d\varepsilon_v^s}{dt} \right\rangle_{V_s} - \frac{1}{V}\int_{\partial V_s} \mathbf{u}^c \cdot \mathbf{n}_s da \end{aligned} \tag{9.5}$$

where E_v is the macroscopic volumetric strain. From (9.5) we can identify two sources of porosity change:

$$\frac{d\phi}{dt} = \frac{d\phi^m}{dt} + \frac{d\phi^c}{dt};\ \frac{d\phi^m}{dt} = \frac{dE_v}{dt} - \frac{V_s}{V}\left\langle \frac{d\varepsilon_v^s}{dt} \right\rangle_{V_s};\ \frac{d\phi^c}{dt} = -\frac{1}{V}\int_{\partial V_s} \mathbf{u}^c \cdot \mathbf{n}_s da \tag{9.6}$$

ϕ^m is the change in porosity associated with the volumetric deformation of the solid phase, while ϕ^c is the change in porosity due to the calcium dissolution. It is the chemical porosity[2].

Analogously, the conservation of the solid mass reads, considering no solid mass supply from the outside:

$$\frac{dm_s}{dt} - \frac{1}{V}\int_{\partial V_s} \rho_s \mathbf{u}^c \cdot \mathbf{n}_s da = \frac{1}{V}\int_{V_s}\left(\frac{d\rho_s}{dt} + \rho_s \frac{d\varepsilon_v^s}{dt}\right) da \equiv 0 \tag{9.7}$$

where $m_s = \frac{1}{V}\int_{V_s} \rho_s dV$ is the apparent solid mass density and ρ_s is the real mass density.

[2] An alternative derivation [82] of the chemical porosity can be based on formulating the mass conservation at the solid boundary relative to the Langrangean configuration prior to leaching:

$$[[\mathbf{M} - m\mathbf{C}]] \cdot \mathbf{n} = 0$$

where $\mathbf{M}$ represents the Langrangean relative flux vector of the leached products, m is the total mass per unit inital volume; $C = \mathbf{C} \cdot \mathbf{n}$ is the Lagrangean velocity of the leaching front. On the intact side, $\mathbf{M} = 0$ and $m = m_0$. This leads then to the introduction of the chemical porosity as:

$$\frac{d\phi^c}{dt} = -\int_{\partial V_s} \frac{m_0}{\rho_0} \mathbf{C} \cdot \mathbf{n} dA$$

Finally, in the case of a Level III microstructure, the previous equations remain valid by considering V_s as the solid of the matrix. In this case the porosities defined by (9.6) are scaled by the matrix volume fraction $1 - f_I$:

$$\phi = (1 - f_I)\,\phi_M \tag{9.8}$$

where f_I is the aggregate volume fraction, and ϕ_M is the porosity of the matrix.

9.1.2 Energy Dissipation

The combination of the first and second law of thermodynamics leads to the Clausius-Duhem inequality, which states that the external energy supply to the thermodynamic system that is not stored as free energy is dissipated in form of heat [148]. Considering the solid phase as our thermodynamic system, and assuming isothermal and quasistatic evolutions, the Clausius-Duhem inequality reads:

$$\frac{d\mathcal{D}}{dt} = \frac{dW^s_{ext}}{dt} - \frac{dW^s}{dt} \geq 0 \tag{9.9}$$

where dW^s_{ext} is the external energy supply to the solid and dW^s is the free (Helmholtz) energy stored in the solid. The external energy supply can be divided into a mechanical and a chemical part:

- The mechanical energy supply is provided by surface tractions on the solid boundary and volume forces. The surface tractions read:

$$\text{on } \partial V_s : \mathbf{t}_s = \boldsymbol{\sigma} \cdot \mathbf{n}_s = -p\mathbf{n}_s \tag{9.10}$$

  with $\boldsymbol{\sigma}$ being the stress tensor in the solid, and p is the pore pressure assumed constant in the fluid phase. The volume forces in the solid are denoted by $\rho_s \mathbf{f} dV$ where ρ_s is the density of the solid phase and $\mathbf{f}$ is the acceleration vector. The surface tractions do work on the total normal velocity $\mathbf{U}^s \cdot \mathbf{n}_s$ while the volume forces only work on the solid velocity $\mathbf{u}^s$. The mechanical energy supply therefore reads:

$$\frac{dW^m_{ext}}{dt} = \int_{V_s} \mathbf{u}^s \cdot \rho_s \mathbf{f} dV + \int_{\partial V_s} \mathbf{U}^s \cdot (\boldsymbol{\sigma} \cdot \mathbf{n}_s)\, da = V_s \left\langle \boldsymbol{\sigma} : \frac{d\boldsymbol{\varepsilon}^s}{dt} \right\rangle_{V_s} - \int_{\partial V_s} p\mathbf{u}^c \cdot \mathbf{n}_s da \tag{9.11}$$

where we invoked the local equilibrium condition in the solid, $\boldsymbol{\nabla} \cdot \boldsymbol{\sigma} + \rho_s \mathbf{f} = \mathbf{0}$, the stress continuity condition (9.10) at the fluid-solid interface and the symmetry of both the stress tensor and the strain rate tensor, i.e. $\frac{d\boldsymbol{\varepsilon}^s}{dt} = \frac{1}{2}\left(\boldsymbol{\nabla} \cdot \mathbf{u}^s + {}^t\boldsymbol{\nabla} \cdot \mathbf{u}^s\right)$. In order to transform this relation into macroscopic stress variables, the Hill-Mandel lemma needs to be invoked. For porous media it reads [149]:

$$\boldsymbol{\Sigma} : \frac{d\mathbf{E}}{dt} = \frac{1}{V}\left[\int_{\partial V_s} \mathbf{u}^s \cdot (\boldsymbol{\sigma} \cdot \mathbf{n}_s)\, da + \int_{\partial V_f} \mathbf{u}^s \cdot (\boldsymbol{\sigma} \cdot \mathbf{n}_f)\, da\right] = \frac{V_s}{V}\left\langle \boldsymbol{\sigma} : \frac{d\boldsymbol{\varepsilon}^s}{dt}\right\rangle_{V_s} - p\frac{d\phi^m}{dt} \tag{9.12}$$

where $\mathbf{n}_f = -\mathbf{n}_s$ is the outward unit normal vector of the fluid phase, $\boldsymbol{\Sigma}$ and $\mathbf{E}$ are the macroscopic stress and strain tensors, respectively. Using (9.12) in (9.11), the mechanical energy supply can be rewritten in terms of macroscopic variables:

$$\frac{dW^m_{ext}}{dt} = V\left[\boldsymbol{\Sigma} : \frac{d\mathbf{E}}{dt} + p\left(\frac{d\phi^m}{dt} + \frac{d\phi^c}{dt}\right)\right] \tag{9.13}$$

- The chemical energy supply is provided by the "work" the chemical potential of the solute, $\mu_{\mathrm{Ca}^{2+}}$, does along the molar flux J_N. In the case of Portlandite dissolution, the molar flux is given by:

$$J_N = \frac{\rho_{\mathrm{CH}}}{\mathcal{M}_{\mathrm{CH}}}\mathbf{u}^c \cdot \mathbf{n}_s \tag{9.14}$$

where $\mathcal{M}_{\mathrm{CH}}$ is the molar mass of Portlandite (of dimension $[\mathcal{M}_{\mathrm{CH}}] = M \times mol^{-1}$). The chemical energy supply rate reads:

$$\frac{dW^c_{ext}}{dt} = \int_{\partial V_s} \mu_{\mathrm{Ca}^{2+}} \frac{\rho_{\mathrm{CH}}}{\mathcal{M}_{\mathrm{CH}}}\mathbf{u}^c \cdot \mathbf{n}_s da \tag{9.15}$$

which simplifies, for a constant chemical potential on the solid surface and with Eq. (9.6) to:

$$\frac{1}{V}\frac{dW^c_{ext}}{dt} = -\mu_{\mathrm{Ca}^{2+}} \frac{\rho_{\mathrm{CH}}}{\mathcal{M}_{\mathrm{CH}}}\frac{d\phi^c}{dt} \tag{9.16}$$

The free energy of the solid also reads as the sum of two components: A mechanical potential ψ_s^{el} and the chemical potential ψ_s^c associated with the minerals bound to the solid matrix:

$$W_s = \int_{V_s} \psi_s dV = \int_{V_s} \left(\psi_s^{el} + \psi_s^c\right) dV = \int_{V_s} \left(\psi_s^{el} + \frac{\rho_{\text{CH}}}{\mathcal{M}_{\text{CH}}}\mu_{\text{CH}}\right) dV \tag{9.17}$$

where μ_{CH} is the chemical potential of the Portlandite bound in the matrix, which is assumed constant in V_s. The total time derivative of the free energy reads:

$$\frac{dW^s}{dt} = \int_{V_s} \frac{\partial \psi_s^{el}}{\partial t} dV + \int_{\partial V_s} \left(\psi_s^{el} + \frac{\rho_{\text{CH}}}{\mathcal{M}_{\text{CH}}}\mu_{\text{CH}}\right) \mathbf{U}^s \cdot \mathbf{n}_s da \tag{9.18}$$

Using (9.2) and the divergence theorem, Eq. (9.18) is developed in the form

$$\frac{dW^s}{dt} = \int_{V_s} \frac{d\psi_s^{el}}{dt} dV + \int_{\partial V_s} \left(\psi_s^{el} + \frac{\rho_{\text{CH}}}{\mathcal{M}_{\text{CH}}}\mu_{\text{CH}}\right) \mathbf{u}^c \cdot \mathbf{n}_s da \tag{9.19}$$

Finally, assembling the different terms of the dissipation, that is (9.13) and (9.19), we rewrite (9.9):

$$\frac{1}{V}\frac{d\mathcal{D}}{dt} = \varphi^m + \varphi^c \tag{9.20}$$

- The first term of the dissipation rate, φ^m, is associated with the mechanical deformation of the matrix phase, and reads:

$$\varphi^m = \boldsymbol{\Sigma} : \frac{d\mathbf{E}}{dt} + p\frac{d\phi^m}{dt} - \frac{d\Psi_s^{el}}{dt};\ \frac{d\Psi_s^{el}}{dt} = \frac{V_s}{V}\left\langle \frac{d\psi_s^{el}}{dt} \right\rangle_{V_s} \tag{9.21}$$

  It is identical to the standard formulation in the poromechanics theory [41] if the total porosity ϕ in the original theory is replaced by the mechanical porosity. In consequence, modeling the mechanical deformations can be based on existing macroscopic material models for porous media.

- The second part of the dissipation rate, φ^c, is associated with the dissolution of the calcium and the corresponding increase in chemical porosity. It reads:

$$\varphi^c = -\frac{1}{V}\int_{\partial V_s} A \times J_N da \geq 0; A = \mu_{Ca^{2+}} - \mu_{CH} - \frac{\mathcal{M}_{\text{CH}}}{\rho_{\text{CH}}}\left(\psi_s^{el} + p\right) \geq 0 \tag{9.22}$$

where A is the chemical affinity, that is the driving force of the molar flux J_N. Following standard non-equilibrium thermodynamics [60], the kinetics of the local dissolution process is described by a kinetics law that relates the affinity A to the molar flux J_N:

$$J_N = J_N(A)\,; A \times J_N(A) \geq 0 \tag{9.23}$$

The difference in chemical potentials, $\Delta G = \mu_{Ca^{2+}} - \mu_{\mathrm{CH}}$ is the pure chemical driving force of the dissolution. However, both the elastic energy ψ_s^{el} and the fluid pressure p are driving the dissolution as well. Indeed, as both, ψ_s^{el} and p, are positive they always increase the dissolution process $J_N(A) \leq 0$ unless they are small compared to the chemical potential difference.

9.1.3 Estimate of the Effect of Strain and Pressure on the Dissolution Kinetics

We want to evaluate the order of magnitude of the elements of the affinity, and more precisely how the strain energy compares to the macroscopic chemical affinity $\Delta G = \mu_{\mathrm{Ca}^{2+}} - \mu_{\mathrm{CH}}$. A rough estimate of ΔG of Portlandite dissolution reaction, that is:

$$\mathrm{Ca}(OH)_2^s \rightarrow \mathrm{Ca}^{2+} + 2\mathrm{OH}^- \tag{9.24}$$

is provided by considering the change in the ionic activity product $IAP = \left\{\mathrm{Ca}^{2+}\right\}\left\{\mathrm{OH}^{-2}\right\}$ of the solution with regard to the solubility product K_{so} of the Portlandite, according to:

$$\Delta G = R\theta \ln\left(\frac{IAP}{K_{so}}\right) \tag{9.25}$$

where $\{...\}$ denote activities, $R = 8.31451\,\mathrm{J\,mol^{-1}\,K^{-1}}$ is the universal gas constant and $\theta = 293.15\,\mathrm{K}$ is a reference temperature. In unleached cementitious systems, $\Delta G = 0$, such that $K_{so} = IAP_{eq} = \left\{\mathrm{Ca}^{2+}\right\}_{eq}^{\mathrm{CH}}\left\{\mathrm{OH}^-\right\}_{eq}^2$. A rough estimate of ΔG can be obtained from (9.25) by considering the change in $\{OH^-\}$ and $\left\{\mathrm{Ca}^{2+}\right\}$ between the equilibrium states before and after Portlandite dissolution. Calculations from Adenot [3] provide numerical values for the

changes in concentration[3] of the different species in the fluid phase. The $[OH^-]$ concentration changes from $5\times10^{-2}\,\mathrm{mol}/\mathrm{l}$ to $6\times10^{-3}\,\mathrm{mol}/\mathrm{l}$, which corresponds to pH values of 12.7 and 11.8 respectively, while the $\left[\mathrm{Ca}^{2+}\right]$-concentration changes from $2.2\times10^{-2}\,\mathrm{mol}/\mathrm{l}$ to $3\times10^{-3}\,\mathrm{mol}/\mathrm{l}$. Evaluating (9.25), considering that the activity coefficients remain unchanged, we find:

$$\Delta G_{est} \simeq -15\,\mathrm{kJ\,mol^{-1}}; \Delta G_{est}\left(\frac{\rho}{M}\right) \simeq -450\,\mathrm{MPa} \tag{9.26}$$

where the Portlandite density was taken as $\rho_{\mathrm{CH}} = 2,240\,\mathrm{kg}/\mathrm{m}^3$ and the molar mass as $\mathcal{M}_{\mathrm{CH}} = 74.1\,\mathrm{g}/\mathrm{mol}$. The magnitude of the pure chemical driving force ΔG, needs to be compared to the elastic free energy and pressure. Given small deformations, the elastic free energy ψ_s^{el} is smaller than 1 MPa and the maximum pressure level in the interstitial pore solution never exceeds 10 MPa. It therefore appears that both strain energy and pressure are at least one order of magnitude smaller than the pure chemical driving force, and that their effect on the chemical affinity can be neglected[4]. This allows us to develop the chemical dissipation (9.22) with (9.6) in the form:

$$\varphi^c = \frac{1}{V}\int_{\partial V_s}\left(\mu_{\mathrm{Ca}^{2+}} - \mu_{\mathrm{CH}}\right)\frac{\rho_{\mathrm{CH}}}{\mathcal{M}_{\mathrm{CH}}}\mathbf{u}^c\cdot\mathbf{n}_s da = -\mathcal{A}\times\frac{d\phi^c}{dt} \tag{9.27}$$

$$\mathcal{A} = \left(\mu_{\mathrm{Ca}^{2+}} - \mu_{\mathrm{CH}}\right)\frac{\rho_{\mathrm{CH}}}{\mathcal{M}_{\mathrm{CH}}}\bigg|_{\partial V_s} \tag{9.28}$$

where we assumed a constant difference in chemical potential along the solid boundary ∂V_s. The quantity $\mathcal{A}$ can be regarded as a macroscopic affinity (of dimension stress) that drives the Portlandite dissolution. At equilibrium $\mathcal{A} = 0$. If the calcium concentration in the pore solution, $\left[\mathrm{Ca}^{2+}\right]$, is lower than the equilibrium concentration, $\left[\mathrm{Ca}^{2+}\right]_{eq}$, the macroscopic affinity is smaller than zero and the dissolution takes place, creating the chemical porosity $d\phi^c > 0$. The change in chemical porosity is expressed by kinetics laws. Most of the kinetics laws are either first or second order laws meaning that they depend to the power one or two on the

[3] This example refers to the case of deionized water for which Adenot developed his model [3]. The activities and concentrations are related by $\{A\} = \gamma_i[A]$ where γ is an activity coefficient. The ratio of the activities are evaluated under the asumption that the activity coefficients do not change.

[4] There are other applications where this effect cannot be neglected. In exploration engineering [63], there are situations in which the pressure level is so high that the pressure is the dominating driving force in the pressure-dissolution process.

affinity [137]. In the case of calcium leaching, the dissolution is instantaneous compared to the transport time scale. The instantaneous dissolution has been demonstrated by Adenot for leaching with deionized water [4] and was experimentally proven for leaching with ammonium nitrate (in Chapter 3, see Table 3.5). From (9.27), the following relations that must be satisfied simultaneously express the instantaneous dissolution:

$$\mathcal{A} \leq 0; d\phi^c \geq 0; \mathcal{A} \times d\phi^c = 0 \tag{9.29}$$

This last set of conditions can be reformulated in terms of the calcium concentrations. This is a more common way of expressing instantaneous dissolution conditions in the analysis of front propagations in concrete (see for example [149]). Furthermore, if we assume that the entire chemical porosity is created at a front i (i = CH, or C-S-H), the following relations hold:

$$\frac{\left[\mathrm{Ca}^{2+}\right]}{\left[\mathrm{Ca}^{2+}\right]^i_{eq}} - 1 \leq 0; d\phi^c_i \geq 0; \left(\frac{\left[\mathrm{Ca}^{2+}\right]}{\left[\mathrm{Ca}^{2+}\right]^i_{eq}} - 1\right) \times d\phi^c_i = 0 \tag{9.30}$$

In summary, the energy estimate presented in this section and the instantaneous dissolution kinetics justify a decoupling of the dissolution-diffusion process from any mechanical energy transformations. We keep this in mind for further developments in this Chapter.

9.2 Macro-Chemoporomechanics

The micro-chemomechanical approach highlights the sources of dissipation in the solid. This section complements these findings from a macroscopic viewpoint of chemically reactive porous media [41]. "Macroscopic" means here the solid *and* fluid phases.

9.2.1 Kinematics and Mass conservation

We adopt the kinematics of the classical Biot-Coussy theory of reactive porous media [41]; that is we consider as thermodynamic system the superposition of two continuous media, the fluid phase (subscript f) and the solid (subscript s). An elementary volume $d\Omega$ consisting of both phases deforms, and its current elementary volume is denoted $d\Omega_t$. These volumes correspond

to V and V_t in (9.1) and are related by the volume transport formula:

$$d\Omega_t = Jd\Omega \tag{9.31}$$

where $J \simeq 1 + E_v$ denotes the Jacobian of infinitesimal deformation. The Lagrangian porosity is still defined by (9.1), that is:

$$\phi = \frac{d\Omega_t^f}{d\Omega} \tag{9.32}$$

where $d\Omega_t^f$ corresponds to $V_f = V_t - V_s$ in the micromechanics notation.

The fluid phase is considered as an ideal mixture[5] of solvent (water, ammonium nitrate etc.) and a solute (Ca^{2+}-ions). To simplify the presentation, we will assume that the solvent is at rest such that the mass conservation reduces to the one of the solute phase (subscript '*sol*') and the solid phase (subscript '*s*'):

$$\frac{dm_{sol}}{dt} = -\boldsymbol{\nabla} \cdot \mathbf{w}_{sol} + m^{\circ}_{\rightarrow sol} \tag{9.33}$$

$$\frac{dm_s}{dt} = -m^{\circ}_{\rightarrow sol} \tag{9.34}$$

where $\mathbf{w}_{sol}$ is the solute outflux vector, that is the calcium mass that leaves per unit time the volume $d\Omega$ through the surface of $d\Omega$. This outflux will be developed in more details in Section 9.4; $m^{\circ}_{\rightarrow sol}$ is the rate of dissolved mass from the solid. This rate can be related to the porosity change of chemical origin:

$$m^{\circ}_{\rightarrow sol} = \frac{d}{dt}\left(\phi^c \rho_s\right) \tag{9.35}$$

Expression (9.34) is the macroscopic counterpart of expression (9.7) developed in Section 9.1.1, and ρ_s is the mass density of the solid phase, which in a first approach will be assumed to be constant (i.e. incompressible solid phase). Finally, the total change in mass of the porous medium (solid and solute) is only due to external solute supply; and yields:

$$\frac{dm_T}{dt} = -\boldsymbol{\nabla} \cdot \mathbf{w}_{sol}; \;\; \Rightarrow m^{\circ}_{\rightarrow sol} = \frac{dm_{sol}}{dt} - \frac{dm_T}{dt} \tag{9.36}$$

[5] Ideal mixture means here that solvent and solute occupy the same porosity ϕ. Furthermore, the total pressure of an ideal mixture is the sum of the pressures of the mixture components. Assuming that the solvent phase is at rest comes to assume that $p = p_{sol}$. We will use this assumption in Section 9.2.2.

Mass conservation law (9.36) reveals tat the dissolved mass rate is a time derivative which justifies a posteriori expression (9.35).

9.2.2 Macroscopic Dissipation

In the macroscopic approach, the thermodynamic system is the solid and the fluid phase. For such an open system, the sum of intrinsic solid dissipation and the dissipation associated with the calcium dissolution reads in isothermal conditions [41]:

$$\Phi_1 + \Phi_{\rightarrow} = \boldsymbol{\Sigma} : \frac{d\mathbf{E}}{dt} - g_{sol} \boldsymbol{\nabla} \cdot \mathbf{w}_{sol} - \frac{d\Psi}{dt} \geq 0 \tag{9.37}$$

The first term in (9.37) refers to the energy supply of the macroscopic stress ($\boldsymbol{\Sigma} : \frac{d\mathbf{E}}{dt}$ is the macroscopic strain energy rate). The second term represents the energy supply by the solute phase entering the macroscopic system, where g_{sol} (of dimension $[g_{sol}] = Energy \times mass^{-1}$) denotes the solute's Gibbs potential. Finally, the last term represents the change of total free energy of the macroscopic system. Among other state variables describing the energy states of the elementary system (strain $\mathbf{E}$, porosity ϕ, etc.), the solid mass m_s is part of the set of state variables. For the considered system, in which the solvent mass is assumed at rest, the following expression can be adopted:

$$\Psi = \Psi_s + m_s G \tag{9.38}$$

where G (of dimension $[G] = energy \times mass^{-1}$) is the specific energy of the minerals bound in the solid phase. The expression for Ψ_s will be specified later on. Using the mass conservation laws (9.33) and (9.34) together with (9.35), (9.38) and (9.6) in (9.37), allows us to develop the macroscopic dissipation in the form:

$$\Phi_1 + \Phi_{\rightarrow} = \boldsymbol{\Sigma} : \frac{d\mathbf{E}}{dt} + p\frac{d\phi^m}{dt} - \left[\rho_s \left(g_{sol} - G\right) - p\right] \frac{d\phi^c}{dt} - \frac{d\Psi_s}{dt} \geq 0 \tag{9.39}$$

where $p = g_{sol}/\rho_{sol}$ is the mixture pressure (solvent at rest), and $\rho_{sol} = m_{sol}/\phi$ is the apparent solute density in the mixture.

Expression (9.39) of the macroscopic dissipation needs to be compared with (9.20), (9.21)

and (9.22) and suggests the following identification:

- The intrinsic dissipation corresponds to the dissipation associated with solid deformation, given by (9.21). The comparison of (9.19) and (9.21) with (9.39) reads:

$$\frac{d\Psi_s}{dt} = \frac{d\Psi_s^{el}}{dt} + \frac{1}{V}\int_{\partial V_s} \psi_s^{el}\mathbf{u}^c \cdot \mathbf{n}_s da \tag{9.40}$$

Relation (9.40) together with (9.6) suggests that the free energy Ψ_s depends on the chemical porosity ϕ^c, in contrast to the solid strain energy Ψ_s^{el}. This dependency is implicitly incorporated in chemical damage models [56],[80], in which:

$$\Psi_s = (1-\phi^c)\,\Psi_s^{el} \tag{9.41}$$

The underlying assumption of these models is that the strain energy is constant in the solid phase, such that:

$$\frac{\partial \Psi_s}{\partial \phi^c}\frac{d\phi^c}{dt} = -\Psi_s^{el}\frac{d\phi^c}{dt} = \frac{1}{V}\int_{\partial V_s} \psi_s^{el}\mathbf{u}^c \cdot \mathbf{n}_s da \tag{9.42}$$

In the approach developed here, we will omit the linear chemoelastic coupling (9.41), and consider, at the macroscopic scale that:

$$\frac{\partial \Psi_s}{\partial \phi^c}\frac{d\phi^c}{dt} = \frac{1}{V}\int_{\partial V_s} \psi_s^{el}\mathbf{u}^c \cdot \mathbf{n}_s da \tag{9.43}$$

The dependence of Ψ_s on ϕ^c will be incorporated through the dependency of the poroelastic properties on the chemical porosity (see Chapter 7). The intrinsic dissipation associated with the solid deformation thus reads:

$$\varphi^m = \Phi_1 = \boldsymbol{\Sigma} : \frac{d\mathbf{E}}{dt} + p\frac{d\phi^m}{dt} - \left(\frac{d\Psi_s}{dt} - \frac{\partial \Psi_s}{\partial \phi^c}\frac{d\phi^c}{dt}\right) \geq 0 \tag{9.44}$$

- The difference between (9.39) and (9.44) corresponds to the chemical dissipation:

$$\Phi_{\rightarrow} = \left[-\rho_s\left(g_{sol} - G\right) + \frac{\partial \Psi_s}{\partial \phi^c} + p\right]\frac{d\phi^c}{dt} \geq 0 \tag{9.45}$$

Given the negligible effect of the strain energy and the pressure on the affinity, as shown in Section 9.1.3., the previous expression simplifies to:

$$\Phi_{\rightarrow} = -\rho_s \left(g_{sol} - G\right) \frac{d\phi^c}{dt} \geq 0 \tag{9.46}$$

This expression which is of the same format as (9.27) and (9.29) allows us to specify the link between the two different writings of the chemical potentials:

$$\rho_s g_{sol} \equiv \mu_{\mathrm{Ca}^{2+}} \frac{\rho_{\mathrm{CH}}}{\mathcal{M}_{\mathrm{CH}}};\ \rho_s G \equiv \mu_{\mathrm{CH}} \frac{\rho_{\mathrm{CH}}}{\mathcal{M}_{\mathrm{CH}}} \tag{9.47}$$

In summary, with (9.39), we have established an explicit link between the micro-chemomechanical theory and the macro-chemomechanical theory, developed in the framework of macroscopic poromechanics. This macroscopic framework will be further considered for the derivation of the state equations and the evolution laws.

9.2.3 Macroscopic Choice of Free energy and State Equations

The macroscopic free energy Ψ_s is expressed as a function of the state variables [162]. In the framework of poroelasticity these are the total strain $\mathbf{E}$, the plastic strain $\mathbf{E}^p$ and some hardening variables χ_i that account both for irreversible solid deformation, in addition to the mechanical change in porosity ϕ^m and the plastic porosity ϕ^p. Furthermore, following the identification in the previous section, also the chemical porosity needs to be considered in the set of macroscopic state variables, describing the energy states of the porous medium at the macroscopic scale. Thus formally:

$$\Psi_s = \Psi_s \left(\mathbf{E}, \mathbf{E}^p, \phi^m, \phi^c, \phi^p, \chi_i\right) \tag{9.48}$$

Following the classical poroplasticity theory [41], we postulate that the free energy is a quadratic function of all state variables, except the chemical porosity:

$$\begin{aligned} \Psi_s &= \frac{1}{2}\left(\mathbf{E} - \mathbf{E}^p\right) : \mathbb{C}_{\mathrm{hom}}\left(\phi^c\right) : \left(\mathbf{E} - \mathbf{E}^p\right) - \left(\phi^m - \phi^p\right) \mathtt{M}\left(\phi^c\right) \mathbf{B}\left(\phi^c\right) : \left(\mathbf{E} - \mathbf{E}^p\right) \\ &+ \frac{1}{2} \mathtt{M}\left(\phi^c\right) \left(\phi^m - \phi^p\right)^2 + U\left(\chi_i, \phi^c\right) \end{aligned} \tag{9.49}$$

where $\mathbb{C}_{\text{hom}}(\phi^c)$ is the fourth order elasticity tensor, $\mathtt{M}(\phi^c)$ is the Biot modulus and $\mathbf{B}(\phi^c)$ is the second order tensor of Biot coefficients. In Chapter 7, we developed the expressions for these poroelastic properties as functions of the chemical porosity ϕ^c (see Table 7.9). Furthermore, following the micromechanical analysis of strength properties, also the frozen energy $U = U(\chi_i, \phi^c)$ is assumed to depend on the chemical porosity, in addition to the plastic hardening variables χ_i. This concept is referred to as chemical hardening. It was originally proposed by Coussy and Ulm [42], and was applied to calcium leaching by Ulm et al. [150]. Use of (9.49) in (9.39) delivers:

$$\Phi_1 + \Phi_{\rightarrow} = \boldsymbol{\Sigma} : \frac{d\mathbf{E}}{dt} + p\frac{d\phi^p}{dt} + \sum_i \zeta_i \frac{d\chi_i}{dt} - \mathcal{A}\frac{d\phi^c}{dt} \geq 0 \tag{9.50}$$

together with the state equations:

$$\boldsymbol{\Sigma} = \frac{\partial \Psi_s}{\partial \mathbf{E}} = -\frac{\partial \Psi_s}{\partial \mathbf{E}^p} = \mathbb{C}_{\text{hom}}(\phi^c) : (\mathbf{E} - \mathbf{E}^p) - \mathbf{B}(\phi^c)(p - p_0) \tag{9.51}$$

$$p = \frac{\partial \Psi_s}{\partial \phi^m} = -\frac{\partial \Psi_s}{\partial \phi^p} = \mathtt{M}(\phi^c)\left(-\mathbf{B}(\phi^c) : (\mathbf{E} - \mathbf{E}^p) + (\phi^m - \phi^p)\right) \tag{9.52}$$

$$\zeta_i = -\frac{\partial U}{\partial \chi_i} \tag{9.53}$$

$$\mathcal{A} = \rho_s(g_{sol} - G) - \frac{\partial \Psi_s}{\partial \phi^c} - p \simeq \frac{\rho_{\text{CH}}}{\mathcal{M}_{\text{CH}}}(\mu_{\text{Ca}^{2+}} - \mu_{\text{CH}}) \tag{9.54}$$

where $\zeta_i(\chi_i, \phi^c)$ represent the chemoplastic hardening forces, which are the driving forces of plastic hardening evolutions. The dependence of the hardening force on the chemical porosity takes into account the dependence of the strength properties on the chemical degradation process. This was analyzed in Chapter 8.

9.2.4 Quantitative Evolution of the Chemical Porosity

The dissolution process in the porous medium creates a porosity that is of purely chemical origin which we introduced as the chemical porosity, ϕ^c. The chemical porosity change is related directly to the dissolution process modelled in the first part of this Chapter. In a cement paste, the largest contribution to the chemical porosity originates from the Portlandite dissolution. Portlandite accounts for approximately 20% of the solid volume [141] of a paste, which means that its dissolution creates a (Lagrangian) porosity of about 11%, considering the already existing porosity. An additional approximately 7% of porosity are created as the C-S-H

decalcify. These values hold for the OPC pastes at $w/c = 0.5$ and need to be slightly adapted for other cementitious materials[6]. As was mentioned in Chapter 2, the porosity created during C-S-H decalcification is not a nano-porosity.

The chemical porosity can be directly linked to the calcium concentration in the solid, which is a linear function of the calcium concentration in the fluid phase once the Portlandite is dissolved. The evolution of the chemical porosity is assumed to follow the same pattern. Using the two front approach introduced in Chapter 3, which will be further developed in Section 9.4., the chemical porosity reads for an OPC as tested in the experimental part:

$$\phi^c = \left\{ \begin{array}{c} \phi_0^c \\ \phi_{\rightarrow \mathrm{CH}}^c \\ \phi_\infty^c \end{array} \right\} = \left\{ \begin{array}{ll} 0; & \left[\mathrm{Ca}^{2+}\right]_{sol} \geq \left[\mathrm{Ca}^{2+}\right]_{eq}^{\mathrm{CH}} \\ 0.11 - \frac{\left[\mathrm{Ca}^{2+}\right]_{sol} - \left[\mathrm{Ca}^{2+}\right]_{eq}^{\mathrm{CH}}}{\left[\mathrm{Ca}^{2+}\right]_{eq}^{\mathrm{CH}} - \left[\mathrm{Ca}^{2+}\right]_{eq}^{\mathrm{C-S-H}}} \times 0.07; & \left[\mathrm{Ca}^{2+}\right]_{eq}^{\mathrm{C-S-H}} \leq \left[\mathrm{Ca}^{2+}\right]_{sol} \leq \left[\mathrm{Ca}^{2+}\right]_{eq}^{\mathrm{CH}} \\ 0.18; & \left[\mathrm{Ca}^{2+}\right]_{sol} \leq \left[\mathrm{Ca}^{2+}\right]_{eq}^{\mathrm{C-S-H}} \end{array} \right. \tag{9.55}$$

where $\left[\mathrm{Ca}^{2+}\right]_{sol}$ is the calcium concentration in the fluid phase; $\left[\mathrm{Ca}^{2+}\right]_{eq}^{\mathrm{CH}}$ and $\left[\mathrm{Ca}^{2+}\right]_{eq}^{\mathrm{C-S-H}}$ are the equilibrium concentrations for the Portlandite and the C-S-H at C/S=1, respectively. These three values of the chemical porosity are associated with the values of the poroelastic parameters of Table 7.9, and the values of the strength parameters of Table 8.3. A combination of Eq. (9.55) with these tables specifies the dependence of the properties on the chemical porosity.

9.3 Chemoplasticity of Calcium Leaching

To complete the constitutive model, we are left with specifying the plastic evolution laws.

9.3.1 Strength Criteria and Evolution Laws

The strength criteria or loading functions describe the onset of plasticity and the strength limit. In Section 6.7.2 a combination of a Cam-Clay and Drucker-Prager loading function was retained

[6]For example for Ultra High Performance concretes that contain usually no Portlandite at all.

for the leached cementitious materials. That is:

$$\boldsymbol{\Sigma} \in C_E \Longleftrightarrow \max\left(f_{cc}, f_{DP}\right) \leq 0 \tag{9.56}$$

$$\text{with: } 2f_{CC} = \frac{3J_2}{M^2} + \left[\Sigma_M + \beta p + (p_c - p_t)\right]^2 - (p_c + p_t)^2 \leq 0 \tag{9.57}$$

$$f_{DP} = \sqrt{J_2} + \delta\left(\Sigma_M + \beta p\right) - c \leq 0 \tag{9.58}$$

where $J_2 = \frac{1}{2}\mathbf{S} : \mathbf{S}$ is the second deviator invariant; $M = \sqrt{3}\delta$ is close to a constant the slope of the critical state line, which connects all points of zero volume dilatation (i.e. $\partial f/\partial \Sigma_M = 0$). The intersections of the Cam-Clay loading function (9.57) with the mean stress axis (see Figure 6-16) is given by $-2p_c$ and $2p_t$ respectively. p_c is also called consolidation pressure, and p_t and the cohesion are related by $2p_t = \sqrt{3}c/M$ (see derivation in Section 6.7.2). Finally, β is the Coussy coefficient [41] which was found to be close to 1 in Section 5.2.4. This result, $\beta = 1$, was substantiated through the micromechanical analysis of Sections 6.5 and 7.3. Thus, the effective stress concept will be considered for plastic evolutions and the effective mean stress in the loading functions will be denoted by

$$\beta = 1 : \Sigma_M^{'p} = \Sigma_M + p \tag{9.59}$$

where superscript 'p' stands for the fact that the effective stress only applies to plastic evolutions (and not poroelastic ones).

9.3.2 Loading Function Parameter Determination

For the Cam-Clay loading function the slope of the critical state line, $M = \sqrt{3}\delta$ and the pressure $2p_t = \sqrt{3}c/M$ can be determined from the high confinement values for δ and c summarized in Table 8.3. In turn, the consolidation pressure p_c is affected by a plastic hardening/softening process. In the modified Cam-Clay model, this pressure is an exponential function of the plastic strain and reads:

$$p_c = p_c^0 \exp\left(-\kappa\left(\phi^p - \phi_0^p\right)\right) \tag{9.60}$$

where p_c^0 is a reference pressure associated with the plastic porosity ϕ_0^p while κ is the recompression index in a hydrostatic loading test. The reference consolidation pressure is chosen as

	Paste			Mortar		
	Int.	CH Lea.	As. Lea.	Int.	CH Lea.	As. Lea.
Crit. State slope M [1]	1.42	1.22	0.97	1.77	1.63	1.40
p_t [MPa]	10.43	10.2	1.03	4.81	4.86	0.50
p_c^0 [MPa]	69.0	64.09	6.3	37.3	39.0	4.06
λ [1]	0.01	0.01	0.01	0.01	0.01	0.01
κ [1]	0.05	0.05	0.05	0.05	0.05	0.05

Table 9.1: Determined Cam-Clay strength parameters.

the onset of yielding so that the reference plastic porosity is zero. The reference consolidation pressure can be determined from either the hydrostatic test or a uniaxial compression test. Here, we use the uniaxial compression test for which experimental data are available for the the intact and the asymptotically degraded state. We assume that the uniaxial compressive strength f_c is reached as yield starts. From there p_c^0 can be determined:

$$p_c^0 = \frac{f_c}{3} + \frac{f_c^2}{M^2\left(\frac{f_c}{3} + p_t\right)} \tag{9.61}$$

The constant κ is determined from hydrostatic loading experiments. For the asymptotically leached specimens, the test results from Chapter 6 (see Section 6.2.1) are used. For intact cementitious materials, no hydrostatic tests were performed during this investigation. Available data in the open literature presented by Chen [32] and originally published by Green et al. [58], are used. From these data, κ is determined as the slope of the loading path beyond the consolidation pressure in a logarithmic plot of the $p-e$ graph of the hydrostatic tests, where $e = \phi/(1-\phi) \simeq \phi^p/(1-\phi_0)$ is the void ratio. This comes to assume that the elastic deformations are small compared to the elastic ones. An analogous constant, λ, can be determined from an unloading branch of a hydrostatic test, describing the relation between mean stress and void ratio. Figure 9-1 illustrates the procedure. Analyzing the experimental data for hydrostatic test in the case of intact material (concrete) and the asymptotically leached materials reveals that the parameters λ and κ are virtually the same, and thus not affected by chemical degradation. Hence, irrespective of loading, and of the chemical state of the material, the coefficients λ and κ are considered to be constant. Table 9.1 summarizes the values for the different parameters used in the Cam-Clay model.

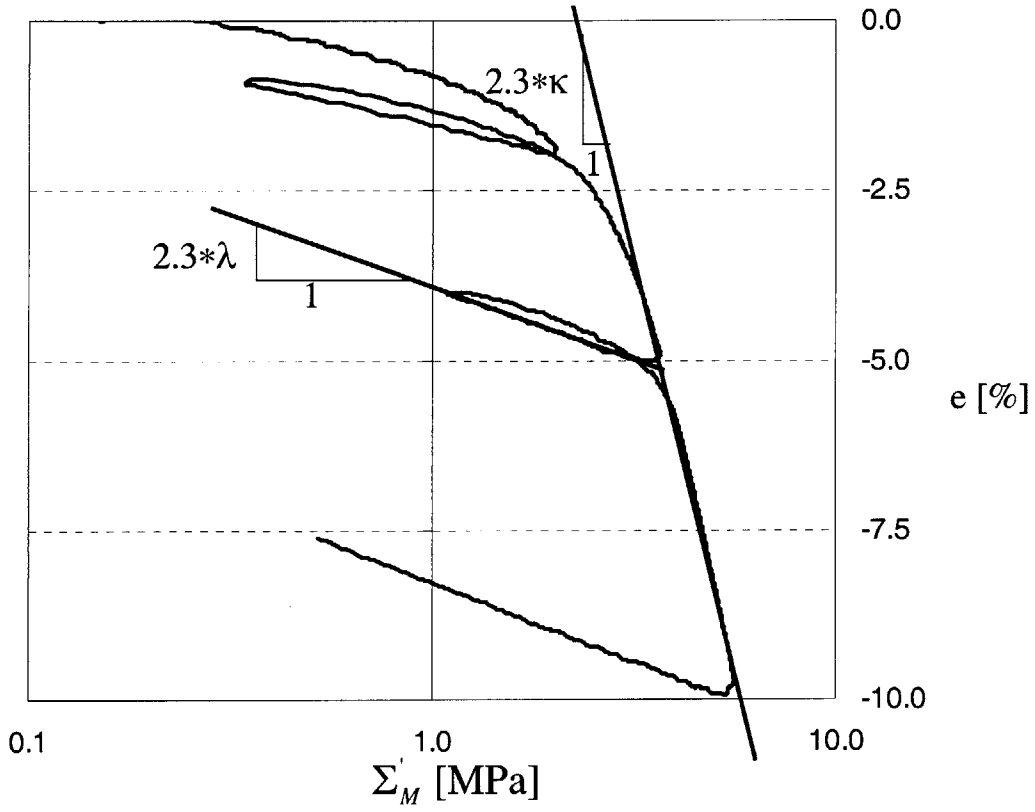

Figure 9-1: Examplary determination of λ and κ from a hydrostatic compression test carried out in this study.

9.3.3 Plastic Evolution Laws

In this subsection the remaining evolution laws for the plasticity model are presented. These are the flow rule and the hardening law for each of the loading surfaces. For both, the Cam-Clay and the Drucker-Prager loading function, we assume an associated plasticity.

Cam-Clay Flow Rule and Hardening Law

The Cam-Clay flow rule reads

$$d\mathbf{E}^p_{CC} = d\lambda_{CC}\frac{\partial f_{CC}}{\partial \boldsymbol{\Sigma}} = d\lambda_{CC}\left[\frac{3}{2M^2}\mathbf{S} + \frac{1}{3}\left(\Sigma'^p_M + (p_c - p_t)\right)\mathbf{1}\right] \tag{9.62}$$

where $d\lambda_{cc}$ is the plastic multiplier for the Cam-Clay model. As we assume isotropic plasticity, the plastic volume change reads:

$$dE^p_{v,CC} = d\lambda_{CC}\frac{\partial f_{CC}}{\partial \Sigma_M} = d\lambda_{CC}\left(\Sigma'^p_M + (p_c - p_t)\right) \equiv d\lambda_{CC}\frac{\partial f_{CC}}{\partial p} = d\phi^p_{CC} \tag{9.63}$$

The equality between volumetric plastic deformation and plastic porosity change results from $\beta = 1$ and the hypothesis of associated plasticity. The sign of the volume change depends on the sign of $\Sigma'^p_M + (p_c - p_t)$ as the plastic multiplier is always positive:

$$\text{sign}\left(dE^p_{v,CC}\right) = \text{sign}\left(\Sigma'^p_M + (p_c - p_t)\right) \tag{9.64}$$

In other words, if the effective plastic mean stress Σ'^p_M is smaller than the pressure difference $p_c - p_t$, the volume change is negative and contraction takes place. In the opposite case, dilatation occurs. The pressure difference $p_c - p_t$ marks the point of zero volume change and is therefore also called the critical pressure $p_{cr} = p_c - p_t$. In the absence of chemical dissolution, the consistency condition for the Cam-Clay model reads:

$$df_{CC} = 0 : \frac{3}{2M^2}dJ_2 + \left(\Sigma'^p_M + p_{cr}\right)d\Sigma'^p_M = d\lambda_{CC}H_{CC} \tag{9.65}$$

where H_{CC} is the hardening modulus. The hardening law describes how the elastic domain evolves as yielding occurs. The hardening force in the Cam-Clay model is $\zeta = p_c$, defined by

(9.60) and the associated hardening variable is $\chi_{CC} = E^p_{v,CC} = \phi^p$. It follows that

$$H_{CC} = \frac{\partial^2 U}{\partial \chi^2_{CC}} = -\frac{\partial p_c}{\partial \phi^p} \tag{9.66}$$

Drucker-Prager Flow Rule

The Drucker-Prager loading surface which is valid in the compression-tension transition zone, is also characterized by an associated flow rule. However, no hardening is considered - reflecting the virtually not existing hardening in the uniaxial compression and tension test (Section 6.6). The flow rule reads:

$$d\mathbf{E}^p_{DP} = d\lambda_{DP}\frac{\partial f_{DP}}{\partial \boldsymbol{\Sigma}} = d\lambda_{DP}\left[\frac{\mathbf{S}}{2\sqrt{J_2}} + \frac{\delta}{3}\mathbf{1}\right] \tag{9.67}$$

and the plastic volumetric strains read:

$$dE^p_{v,DP} = d\lambda_{DP}\frac{\partial f_{DP}}{\partial \Sigma_M} = d\lambda_{DP}\delta \equiv d\lambda_{DP}\frac{\partial f_{DP}}{\partial p} = d\phi^p_{DP} \tag{9.68}$$

where $d\lambda_{DP}$ denotes the plastic multiplier. Table 9.2 recapitulates the plasticity model elements.

9.3.4 Extension to Chemoplastic Evolutions

The evolution laws (9.62), (9.63) and (9.67), (9.68) are the standard poroplastic evolution laws that hold irrespective of any chemical changes that affect the strength domain at the same time as the porous material yields under load. However, simultaneous yielding and chemical dissolution changes the expression of the plastic multiplier [42]. This is due to the dependence of the hardening force on the chemical degradation state. To illustrate this phenomenon, let us rewrite the loading function $f\left(\boldsymbol{\Sigma}'^p = \boldsymbol{\Sigma} + p\mathbf{1}; \zeta\left(\chi, \phi^c\right)\right)$ in the form:

$$f = f\left(\boldsymbol{\Sigma}'^p, \chi, \phi^c\right) \leq 0 \tag{9.69}$$

Summary of the Poroplastic Constitutive Equations

State Equations:

$$\boldsymbol{\Sigma} = \Sigma_0 + \left(k_0\left(\phi^c\right) + \tfrac{2}{3}\mu\left(\phi^c\right)\right) tr\left(\mathbf{E} - \mathbf{E}^p\right)\mathbf{1} + 2\mu\left(\phi^c\right)\left(\mathbf{E} - \mathbf{E}^p\right) - b\left(\phi^c\right)\left(p - p_0\right)\mathbf{1}$$

$$p = p_0 + \mathtt{M}\left(\phi^c\right)\left(-b\left(\phi^c\right)\mathrm{tr}\left(\mathbf{E} - \mathbf{E}^p\right) + \left(\phi^m - \phi^p\right)\right)$$

$$\phi^c = f\left(\left[\mathrm{Ca}^{2+}\right]_m\right) \quad (9.55)$$

Loading Surfaces:

$$2f_{CC} = \tfrac{3J_2}{M(\phi^c)^2} + \left[\Sigma_M^{'p} + \left(p_c - p_t\right)\right]^2 - \left(p_c + p_t\right)^2 \leq 0$$

$$f_{DP} = \sqrt{J_2} + \delta\left(\phi^c\right)\Sigma_M^{'p} - c\left(\phi^c\right) \leq 0$$

Flow Rules:

$$d\mathbf{E}_{CC}^p = d\lambda_{CC}\left[\tfrac{3}{2M(\phi^c)^2}\mathbf{S} + \tfrac{1}{3}\left(\Sigma_M^{'p} + \left(p_c - p_t\right)\right)\mathbf{1}\right]$$

$$dE_{v,CC}^p = d\phi_{CC}^p = d\lambda_{CC}\left(\Sigma_M^{'p} + \left(p_c - p_t\right)\right)$$

$$d\mathbf{E}_{DP}^p = d\lambda_{DP}\left[\tfrac{\mathbf{S}}{2\sqrt{J_2}} + \tfrac{\delta(\phi^c)}{3}\mathbf{1}\right]$$
$$dE_{v,DP}^p = d\lambda_{DP}\delta\left(\phi^c\right)$$

Hardening Rule:

$$p_c = p_c^0\left(\phi^c\right)\exp\left(-\kappa\left(\phi^c\right)\left(\phi^p - \phi_0^p\right)\right)$$

Table 9.2: Summary of the poroplastic model equations.

The plastic consistency condition reads:

$$df = \frac{\partial f}{\partial \boldsymbol{\Sigma}'^p} : d\boldsymbol{\Sigma}'^p + \frac{\partial f}{\partial \chi} d\chi + \frac{\partial f}{\partial \phi^c} d\phi^c = 0 \tag{9.70}$$

In contrast to the standard poroplastic evolutions, a simultaneous change of the mechanical loading and a dissolution process becomes apparent. Since χ is a plastic hardening variable, the plastic hardening modulus is assumed to be solely associated with the evolution of $d\chi$, thus as in standard poroplasticity:

$$-\frac{\partial f}{\partial \chi} d\chi = d\lambda H; \; H = \frac{\partial^2 U}{\partial \chi^2} \tag{9.71}$$

In return, use of (9.71) in (9.70) delivers the following modified expression of the chemoplastic multiplier:

$$d\lambda = d\lambda|_{\phi^c} + \frac{1}{H} \frac{\partial f}{\partial \phi^c} d\phi^c \tag{9.72}$$

where $d\lambda|_{\phi^c} = \frac{1}{H} \frac{\partial f}{\partial \boldsymbol{\Sigma}'^p} : d\boldsymbol{\Sigma}'^p$ is the purely poroplastic multiplier. The additional term on the right hand side is due to a dissolution process that occurs simultaneously as plastic deformation takes place. H is readily obtained by using for f in (9.72) the Cam-Clay or the Drucker-Prager model, with the dependence of M, p_c, p_t and δ, c respectively on the chemical porosity change. These expressions are not developed here. Focus of the application part (Chapters 10 and 11) will be the residual strength capacity of structures at a given chemical degradation state. This does not require to consider chemoplastic evolutions.

9.4 Dissolution-Diffusion Problem

9.4.1 Motivation

The chemomechanical model developed in this chapter is based on a single macroscopic state variable for leaching, that is the chemical porosity ϕ^c. This chemical porosity is related to the calcium concentration by relation (9.55). To close the constitutive model, a dissolution-diffusion model is required that gives access to the calcium concentration. This will be achieved here by extending the one-dimensional two-front model of Chapter 3 to three dimensions.

The dissolution-diffusion model developed below is the three-dimensional version of the 1D two-front model of Chapter 3. This two-front approach has its significance in two aspects:

- The model is consistent with the micromechanical scales of cement-based materials. It takes into account the fundamentally different nature of the Portlandite and C-S-H leaching, which take place at two different scales of the microstructure: Level II for the Portlandite dissolution and Level I for the C-S-H decalcification.
- It simplifies the transport description for further practical applications of the model in model-based simulations; and limits the number of material states to the ones for which properties can be determined,either through experiments (see Chapter 5 and 6) or through an extension by micromechanical modeling (see Chapter 7 and 8).

9.4.2 Model Equations

The dissolution-diffusion model is a macroscopic model of a saturated porous medium of volume V consisting of a fluid phase V_f and a solid phase V_s. The considered porous medium corresponds to a Level II microstructure. The extension to mortars and concretes (Level III) is straightforward due to the inertness of the aggregates which do not alter the process. The solid phase is characterized by a calcium concentration $\left[Ca^{2+}\right]_s$ while in the fluid phase that occupies the total pore space, a calcium concentration $\left[Ca^{2+}\right]_{sol}$ prevails. As we consider two leaching fronts, leaching takes place only when either one of the equilibrium conditions is violated. The two fronts correspond to the leaching of the Portlandite and the decalcification of C-S-H at C/S = 1. The locations of these two fronts are denoted by $\mathbf{x}_{C-S-H}$ and $\mathbf{x}_{CH}$, respectively, where we consider the geometrical setting chosen such that both $\mathbf{x}_{C-S-H}$ and $\mathbf{x}_{CH}$ increase with time. Moreover, due to the equilibrium conditions, we always have: $|\mathbf{x}_{C-S-H}| \leq |\mathbf{x}_{CH}|$. The mass conservation of the calcium in the fluid phase (solvent), is obtained from (9.33) by considering that any dissolution occurs only on the dissolution fronts, thus:

$$\frac{\partial}{\partial t}\left(\phi\left[Ca^{2+}\right]_{sol}\right) + \boldsymbol{\nabla}\cdot\frac{\mathbf{w}_{sol}}{\mathcal{M}_{sol}} = 0 \tag{9.73}$$

where $\mathcal{M}_{sol}$ is the molar mass of calcium ions ($40\times10^3\,\mathrm{kg}\,/\,\mathrm{m}^3$), $\mathbf{w}_{sol}/\mathcal{M}_{sol}$ is ion flux vector in the fluid phase. This mass flux is considered to obey Fick's law and is written as :

$$\frac{\mathbf{w}_{sol}}{\mathcal{M}_{sol}} = -\phi D(\phi)\,\boldsymbol{\nabla}\left[\mathrm{Ca}^{2+}\right]_{sol} \tag{9.74}$$

where $D(\phi)$ is the diffusivity of the calcium in the pore solution, which depends on the porosity. The dependence of the diffusivity of cement-based materials on the porosity was studied in detail by Tognazzi [144]. Based on experimental results the following relation was proposed for porosities between 20% and 60%:

$$D(\phi) = a\exp(b\phi) \text{ with } a = 2.35\times10^{-13}\,\mathrm{m}^2\,/\,\mathrm{s} \text{ and } b = 9.95 \tag{9.75}$$

Relation (9.75) is adopted in this study. In addition to the mass conservation, initial and boundary conditions are specified. The initial condition is:

$$t \le 0, \forall \mathbf{x} : \left[\mathrm{Ca}^{2+}\right]_{sol} = \left[\mathrm{Ca}^{2+}\right]_0 \tag{9.76}$$

where $\left[\mathrm{Ca}^{2+}\right]_0$ is the initial calcium concentration. Boundary conditions are given either in terms of the calcium concentration or in terms of the flux:

$$\text{on } \Gamma = \Gamma_u + \Gamma_q \begin{cases} \Gamma_u : \left[\mathrm{Ca}^{2+}\right]_{sol} = \overline{\left[\mathrm{Ca}^{2+}\right]}_{sol} \\ \Gamma_q : D(\phi)\,\boldsymbol{\nabla}\left[\mathrm{Ca}^{2+}\right]_{sol}\cdot\mathbf{n} = \overline{q} \end{cases} \tag{9.77}$$

where Γ_u and Γ_q are the two complementary parts of the contour $\Gamma = \partial\Omega$ with outward normal vector $\mathbf{n}$.

At the two leaching fronts, the mass conservation leads to so called Rankine-Hugoniot jump conditions [120, 70], which were given for the 1-D model by equations (3.8) and (3.9). The 3-D extension of these jump conditions read:

$$\left(\left(\mathcal{M}_{\mathrm{Ca}^{2+}}\phi D\boldsymbol{\nabla}\left[\mathrm{Ca}^{2+}\right]_{sol}\right)_{\mathbf{x}^-_{\mathrm{C-S-H}}} - \left(\mathcal{M}_{\mathrm{Ca}^{2+}}\phi D\boldsymbol{\nabla}\left[\mathrm{Ca}^{2+}\right]_{sol}\right)_{\mathbf{x}^+_{\mathrm{C-S-H}}}\right)\cdot\mathbf{n} \tag{9.78}$$

$$-\ \Delta\phi^c_{\mathrm{C-S-H}}\rho_{Ca^{2+}}\mathbf{V}_{\mathrm{C-S-H}}\cdot\mathbf{n} = 0, \text{ for } \mathbf{x} = \mathbf{x}_{\mathrm{C-S-H}} :$$

$$\left(\left(\mathcal{M}_{\mathrm{Ca}^{2+}}\phi D\boldsymbol{\nabla}\left[\mathrm{Ca}^{2+}\right]_{sol}\right)_{\mathbf{x}^-_{\mathrm{CH}}} - \Delta\phi^c_{\mathrm{CH}}\rho_{\mathrm{CH}}\mathbf{V}_{\mathrm{CH}}\right)\cdot\mathbf{n} = 0, \text{ for } \mathbf{x} = \mathbf{x}_{\mathrm{CH}} : \tag{9.79}$$

Case	$[Ca^{2+}]^{eq}_{CH}$	$[Ca^{2+}]^{eq}_{C-S-H}$	m_{CH}	Δm_s
Deionized Water	22 mmol / l	2 mmol / l	182 kg / m^3	338 kg / m^3
Ammonium Nitrate [6M]	2.7 mol / l	0.5 mol / l	182 kg / m^3	338 kg / m^3

Table 9.3: Physical Parameters for leaching.

where $\Delta\phi^c_{C-S-H} = \phi^c_{C-S-H} - \phi^c_{\rightarrow CH}$ and $\Delta\phi^c_{CH} = \phi^c_{\rightarrow CH}$ denote the change in chemical porosity due to the C-S-H dissolution and Portlandite dissolution, respectively. These values are given by relations (9.55). $\mathbf{V}_{C-S-H}$ and $\mathbf{V}_{CH}$ are the velocities of the two leaching fronts. $\rho_{Ca^{2+}}$ and ρ_{CH} are real mass densities of the dissolved matter. They are different due to the different leaching mechanisms: For C-S-H, the calcium alone is dissolved from the structure while in the case of Portlandite, the complete crystal agglomeration goes into solution.

The equilibrium for the two minerals is described by two sets of equilibrium conditions which read [149]:

$$\frac{[Ca^{2+}]_{sol}}{[Ca^{2+}]^{C-S-H}_{eq}} - 1 \leq 0; \phi^c_{C-S-H} - \phi^c_{\rightarrow CH} \geq 0; \left(\frac{[Ca^{2+}]_{sol}}{[Ca^{2+}]^{C-S-H}_{eq}} - 1\right) \times \left(\phi^c_{C-S-H} - \phi^c_{\rightarrow CH}\right) = 0 \tag{9.80}$$

$$\frac{[Ca^{2+}]_{sol}}{[Ca^{2+}]^{CH}_{eq}} - 1 \leq 0; \phi^c_{\rightarrow CH} \geq 0; \left(\frac{[Ca^{2+}]_{sol}}{[Ca^{2+}]^{CH}_{eq}} - 1\right) \times \phi^c_{\rightarrow CH} = 0 \tag{9.81}$$

$[Ca^{2+}]^{CH}_{eq}$ and $[Ca^{2+}]^{C-S-H}_{eq}$ are the calcium equilibrium concentrations for Portlandite and C-S-H dissolution, determined in Chapter 3 for the ammonium nitrate and the deionized water leaching method. Table 9.3 recapitulates these values along with some typical values of the relative mass changes that go along with the leaching process.

9.4.3 Presence of Fractures

In the presence of fractures, the presented approach has to be extended. Considering a fracture channel with an advective flow, characterized by a velocity vector $\mathbf{v}_f$, the expression for the solute flux in the fracture channel reads [95]:

$$\frac{\mathbf{w}_{sol}}{\mathcal{M}_{sol}} = -D_f \nabla [Ca^{2+}]_f - [Ca^{2+}]_f \mathbf{v}_f \tag{9.82}$$

where D_f is the diffusion coefficient for calcium in water and $\left[Ca^{2+}\right]_f$ is the calcium concentration in the fracture channel. From a dimensional analysis of the invariants of equations (9.73) through (9.79) and (9.82) in a one-dimensional setting Mainguy et al. [95] showed that besides the Boltzmann diffusion variables ($\xi = \frac{x}{2\sqrt{D_f t}}$, i.e.(3.17)), a new invariant, related to the fracture presence appears:

$$\pi = \frac{x}{v_f t} \tag{9.83}$$

where x is the spacial variable along the axis of the fracture and $v_f = \mathbf{v}_f \cdot \mathbf{e}_x$ is the advection velocity along the x-direction. The other components of $\mathbf{v}_f$ are considered zero. The invariants ξ and π can be combined to a Péclet number, which quantifies the relative importance of the advective transport and the diffusive transport:

$$Pé = 4\frac{\xi^2}{\pi} = \frac{v_f x}{D_f} \tag{9.84}$$

For $Pe \gg 1$, the advective transport dominates; and for $Pe \ll 1$ it is the inverse. Based on the definition of the Péclet number, Mainguy et al. [95] showed that in the case of dominating diffusive transport in the fracture ($Pe \ll 1$), the time-space dependence is scaled by the quadratic root of time ($x(t) \propto t^{1/4}$); in contrast to the case of dominating advective transport in which it is scaled by the square root of time ($x(t) \propto t^{1/2}$). In other words, only in the case of dominating advective transport will the effect of the fracture be dominating. If this is not the case, the quadratic root of time dependency will slow down the diffusion and gives rise to a "fracture congestion phenomenon"[94]. While the detailed derivation of this phenomenon goes beyond the scope of our study, the result is important for us: Given the general small Péclet numbers in cracks in cement-based materials, the overall degradation process of the bulk material is little affected by the presence of cracks. Hence, coupling effects related to an apparent increase of the macroscopic diffusion coefficient D due to cracks can be neglected. In other words, irreversible skeleton evolutions (related to cracking) are uncoupled from the dissolution-diffusion problem, and vice versa.

9.5 Chapter Summary: Two Step Resolution

In this Chapter, we presented the elements of the constitutive model for cement-based materials subjected to calcium leaching. The model combines the experimentally and theoretically developed knowledge base about cement-based materials subjected to leaching. Through a micromechanical analysis we identified the sources of dissipation when both mechanical loading and chemical dissolution occur. Particularly the identification of the chemical porosity as a state variable is of importance. Through the chemical porosity, the interaction of calcium leaching and mechanical properties is given. On the other hand we showed that the influence of the mechanical loading on the dissolution process is negligible. This allows the solution of any combined leaching - mechanics problem in a two step process. First the dissolution-diffusion problem is solved, leading to a chemical porosity distribution. Then the mechanical problem can be treated, with material properties based on the chemical porosity.

The mechanical part of the constitutive model uses a poroelastoplastic description of the mechanical performance:

- The poroelastic part employs the micromechanical estimates of Biot coefficient, Biot modulus and Young's modulus, developed in Chapter 7 (see Table 7.9).
- A two surface plasticity model is used for the strength description. In addition to the experimental data for asymptotic leaching states, the micromechanical strength estimates developed in Chapter 8 (see Table 8.3) are used for the intermediate leaching state.

The dissolution-diffusion model for calcium leaching provides the extension to 3-D of the one-dimensional two-front modeling approach developed in Chapter 3. In addition, based on a dimensionless comparison of advective and diffusive transport through the fracture, the effect of cracks on the macroscopic degradation process can be shown to be generally negligible. This is an additional argument for a staggered treatment of the coupled chemomechanical problem: First a dissolution-diffusion part followed by a poroplastic analysis. This staggered scheme will be employed for model-based simulations.

Part IV

Chemomechanical Model-Based Simulations

Chapter 10

Validation of the Constitutive Model

10.1 Introduction

In the second and third part of this study, the mechanical behavior of cementitious materials subjected to leaching was studied both experimentally and theoretically from Levels I to III, which culminated in the development of the constitutive model in Chapter 9 that contains all the available information. It offers the possibility to numerically study the structural performance of inhomogeneously leached cement-based materials and structures. This is the focus of the third part of this study, which is composed of two chapters. This Chapter presents a validation of the chosen approach. Chapter 11 is devoted to a design application, using this approach.

The validation presented in this Chapter is a check of the relevance and quality of the chosen description of the material behavior in the presence of leaching. This includes both a validation of the dissolution-diffusion model and of the strength deformation model. The validation is performed through comparison of experimental data and model-based simulation results. A set of three validation cases is presented, each of which focuses on different aspects of the material description. In the first validation case, a uniaxial compression load case on a partially leached cement paste is studied, focusing on the strength description in the compressive loading domain. The second validation case deals with a partially leached notched mortar beam in bending, which involves the leaching prediction, the tensile strength domain and the deformation behavior both in tension and compression. The third validation case assesses the time-scales of the bending strength evolution of mortar beams in different degradation scenarios focusing on the change

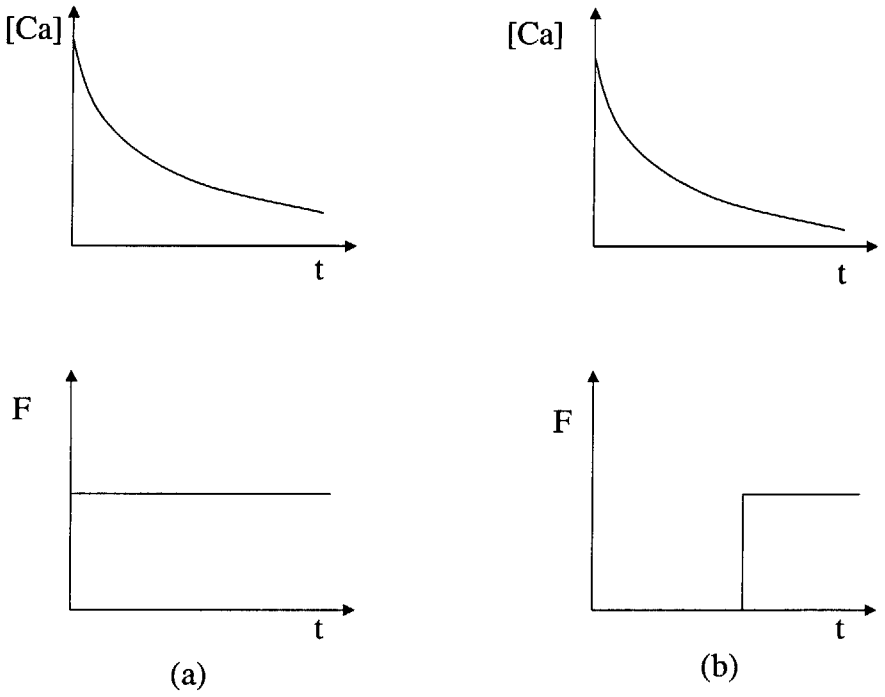

Figure 10-1: Schematic description of the two possible loading scenarios. In (a) a constant load F is applied as the leaching, expressed through [Ca] progresses. (b) shows the application of a load at a certain fixed degradation state.

in time-scales involved. The three validation cases are all examples of load cases in which the mechanical loading is applied for a given degradation state (Figure 10-1 (b)). The case in which a constant mechanical load is applied as leaching occurs (Figure 10-1 (a)) which would require a complete chemoplastic description (see Section 9.3.4), is not further considered in this study.

10.2 Finite Element Implementation

The model-based simulations are performed using a finite element implementation of the model equations in the finite-element code CESAR-LCPC [71]. Following the two-step resolution procedure described in Section 9.5, a staggered scheme of two consecutive calculation steps is chosen. The leaching calculations are preformed with the module LIXI [91], which includes a variable change so that the solid calcium concentration becomes the unknown. Figure 10-2

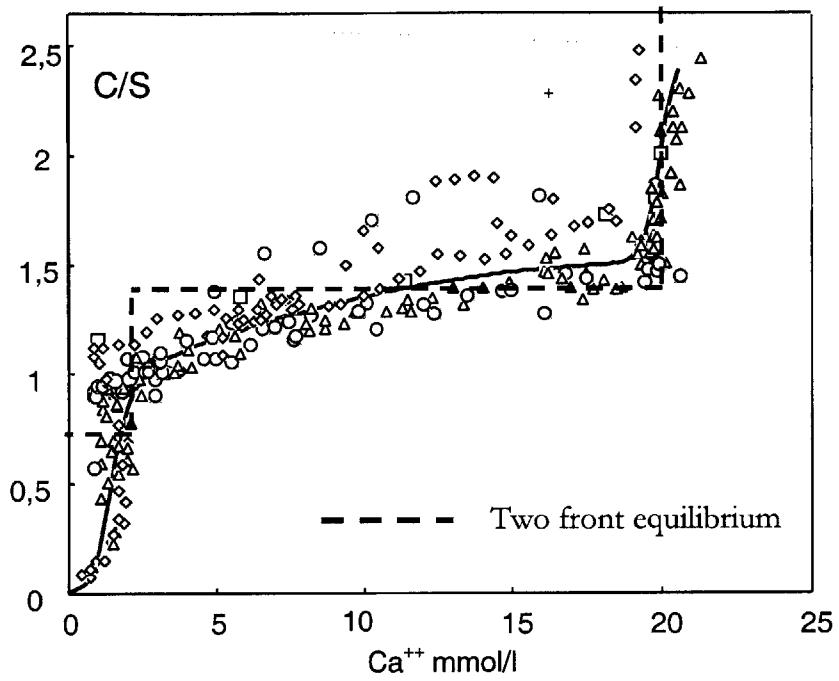

Figure 10-2: Modified Berner curve to account for the two-front approach in the solid-solute calcium equilibrium.

shows the connection between calcium concentration in the solute and the solid that is given by a modified Berner curve, reflecting the two-front approach. The mechanical calculations are performed with an enriched version of MPNL, a poroplasticity module. The description of the finite element algorithm, including the implemented return mapping algorithm, is given in Appendix D.

10.3 Validation I: Carde's Uniaxial Compression Tests on Partially Leached Cement Paste Cylinders

The first validation case is performed by comparing model-based predictions and experimental results of the compression of partially leached cement paste cylinders (Level II). The experimental data were provided by Carde [28]. With the study of this case, we specifically want to

validate:

- The use of the two front approach, to capture the non-homogeneous degradation mechanisms, and
- The micromechanical model of the strength properties at Level II, in particular for the intermediate leaching state.

The loading state is purely compressive in this validation case, which allows us to focus on the strength description in the low confinement compressive regime.

10.3.1 Experimental Configuration and Results

The experimental results are uniaxial compression tests by Carde [28] obtained on partially leached cylindrical cement paste specimens. The specimens have a diameter of 10, 12, 14, 20 and 30 mm and a height of twice the diameter. We focus here on the 30 mm specimens, because no size effects were reported by Carde. The cement paste specimens were prepared at a water-cement ratio of w/c =0.5 and were leached by Carde in a 6M Ammonium Nitrate solution bath, similar to the one presented in Chapter 3. The specimens for mechanical testing are leached radially only. For the characterization of the leaching process, Carde introduced the following surface ratio:

$$\gamma_{\rightarrow \mathrm{CH}} = \frac{A_{\rightarrow \mathrm{CH}}}{A_T} \tag{10.1}$$

where A_T is the total surface of the cylinder while $A_{\rightarrow \mathrm{CH}}$ is the leached surface. The leached surface corresponds to the area in which the Portlandite has been leached. This was measured by Carde through a visual inspection of the Portlandite dissolution front location. A second front was not considered by Carde. The surface ratio of $\gamma_{\rightarrow \mathrm{CH}} = 1$, which corresponds to a specimen in which the Portlandite front has reached the center, does not correspond to the end of the leaching process.

During the mechanical test, the load is applied through a described displacement and the total vertical force is recorded. The applied displacement rate was not reported by Carde. Carde's results are presented in Table 10.1. They contain the reference 28-day compressive strength f_c obtained on intact specimens of the same batch. The leached compressive strength, $f_{c,leached}$ refers to the total measured force divided by the total area of the cylinder, A_T.

$\gamma_{\rightarrow CH}[1]$	f_c[MPa]	$f_{c,leached}$[MPa]
0.25	54.2	45.1
0.39	54.2	38.1
0.54	54.2	34.0
0.72	56.5	28.3
1.00	56.5	14.6

Table 10.1: Experimental results by Carde on the 30mm cylindrical cement paste specimens

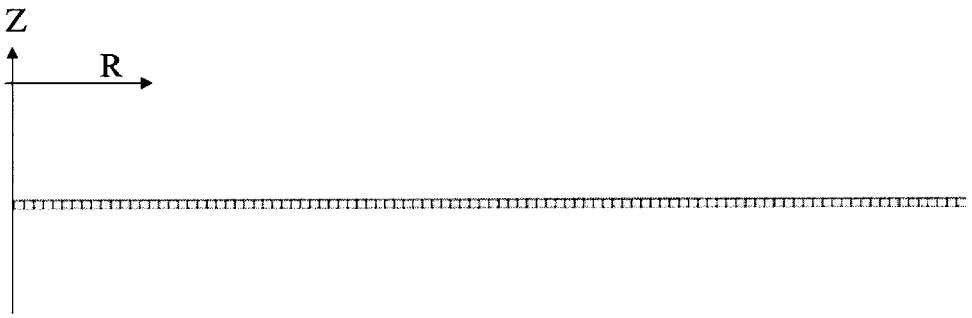

Figure 10-3: Mesh for the FE calculation.

10.3.2 Model-based Simulations and Results

Mesh

The mesh employed in the computations consists of one row of 100 rectangular elements with linear calcium concentration and displacement interpolation. The linear interpolation is chosen for a better representation of the sharp dissolution fronts. One row of elements is sufficient in this situation, as the leaching phenomenon is completely radial and the mechanical loading purely vertical. The elements are axisymmetric and have a radial length of 0.015cm. The element size was chosen after some study of different sizes so that even for short leaching times a good representation of the stress state is achieved. To check the mesh sensitivity of the results, a second, finer mesh consisting of 1,000 elements is used for comparison.

Leaching Simulation Input Data	
Portlandite Front	$\left[Ca^{2+}\right]_s = 8.0\,mol/l$; $\left[Ca^{2+}\right]_{sol} = 2.7\,mol/l$
C-S-H Front	$\left[Ca^{2+}\right]_s = 4.5\,mol/l$; $\left[Ca^{2+}\right]_{sol} = 0.5\,mol/l$
Initial porosity	$\phi_0 = 0.35$
Diffusion Coeff.	$D(\phi) = a\exp(b\phi)$ with $a = 2.35 \times 10^{-13} m^2/s$ and $b = 9.95$

Table 10.2: Input data for the leaching simulation.

Leaching Calculation

Boundary Conditions and Equilibrium Data

For the leaching calculation the following boundary conditions are used:

$$\left[Ca^{2+}\right]_s (R = 15\,mm, z, t) = 4.5\,mol/l \tag{10.2}$$

$$\overline{q}\,(R, z = \pm 0.075\,mm, t) = 0 \tag{10.3}$$

where $\left[Ca^{2+}\right]_s$ is the solid calcium concentration and $\overline{q}$ the calcium flux. The imposed solid calcium concentration of $4.5\,mol/l$ corresponds to the asymptotic calcium concentration after leaching[1]. The initial condition on the solid calcium concentration is given by:

$$\left[Ca^{2+}\right]_s (R, z, t \leq 0) = 14.7\,mol/l \tag{10.4}$$

The equilibrium data and the diffusion coefficient formulation used for the leaching calculation are given in Table 10.2. The shown equilibrium values correspond to the results presented in Section 3.2. The diffusion coefficient was determined from Tognazzi's formula [144], i.e. Eq. (9.75).

Results

The leaching of the cylinder is calculated for different time steps. The time steps are determined so that well spaced values for the surface ratio γ are obtained. Particularly for lower values,

[1]Given the relation between $\left[Ca^{2+}\right]_s$ and $\left[Ca^{2+}\right]_{sol}$, which is given by the modified Berner curve (Figure 10-2); it is numerically more stable to carry out the simulation using $\left[Ca^{2+}\right]_s$ as principal unknown. For details see Appendix D.2 and [91]. This asymptotic concentration is based on the experimental observation presented in Section 3.4.

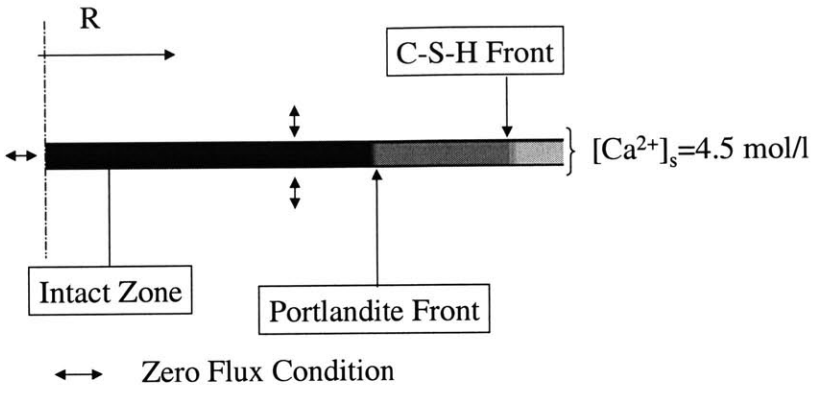

Figure 10-4: Results from the leaching calculation at $\gamma_{\rightarrow CH} = 0.69$. Note that double arrows indicate zero flux boundary conditions.

the effect of the leaching is expected to be strong. The $\gamma_{\rightarrow CH}$ values are 0.07, 0.19, 0.26, 0.31, 0.42, 0.54, 0.69, and 1.0. The time for the Portlandite front to reach the center ($\gamma_{\rightarrow CH} = 1$) is 45 days. This compares well to the analytical solution (Equation (3.73)) which predicts 44 days[2]. Figure 10-4 shows a plot of the calcium concentration distribution at $\gamma_{\rightarrow CH} = 0.69$, with the location of the Portlandite front and the C-S-H front.

Mechanical Calculation

Input Values

The displacement boundary conditions are:

$$u_z(R, z = 0.075\,\text{mm}, t) = u_d(t) \tag{10.5}$$

$$u_z(R, z = -0.075\,\text{mm}, t) = 0 \tag{10.6}$$

where $u_d(t)$ is the prescribed vertical displacement. The mechanical input values for the yield surfaces are given in Table 10.3. They are extracted from Tables 8.3 and 9.1. The properties for the intermediate leaching state are based on the application of the micromechanical estimates

[2]This time is readily calculated with the formulas presented in Chapter 3. In fact the leaching time scales with the square of the radius: $t_1 = (R_1/R_0)^2\, t_0$.

Input Parameters	Mechanical Calculation		
	Intact	CH leached	Asymp. leached
δ_{DP} [1]	1.62	1.39	0.99
c_{DP} [MPa]	2.09	1.80	0.79
M [1]	1.42	1.22	0.97
p_t [MPa]	10.43	10.2	1.03
p_c [MPa]	69.0	64.1	6.3
λ [1]	0.01	0.01	0.01
κ [1]	0.05	0.05	0.05

Table 10.3: Mechanical input data

given in sections 8.2 and 8.3. The calculations are performed completely drained so that no pore pressure effects occur.

Results

For the different leaching ratios γ the vertical stress distribution and total vertical force are determined. Figure 10-5 shows the distribution of the vertical stress, Σ_{zz} for three degradation states. The sharp dissolution fronts result in zones of distinct material properties and hence different stress states. The comparison with the experimental results of Carde is performed by calculating the stress ratio $\overline{\Sigma}$ which is defined as:

$$\overline{\Sigma} = \frac{1}{A} \frac{\int \Sigma_{zz}(r)\, dA}{f_{c,0}} \tag{10.7}$$

where $f_{c,0}$ is the reference uniaxial compressive strength, here 54.2 MPa. A comparison of the experimental and model-based results in Figure 10-6, shows that the model-based results are in very good agreement with the experimental results by Carde. The simplicity of the loading case gives the opportunity to check the performance of the following two model elements: The two front dissolution approach and the micromechanical strength models. The combination of both elements in model-based simulations performs rather well. Finally, the difference between the two meshes is negligible (see Figure 10-6). The results obtained with the coarser mesh almost coincide with the 10-times finer mesh. In this validation case, the mesh density has only an influence on the mechanical part of the calculation. For the leaching part, a mesh sensitivity of sharp dissolution front is known [95] in what concerns the location of the front in time.

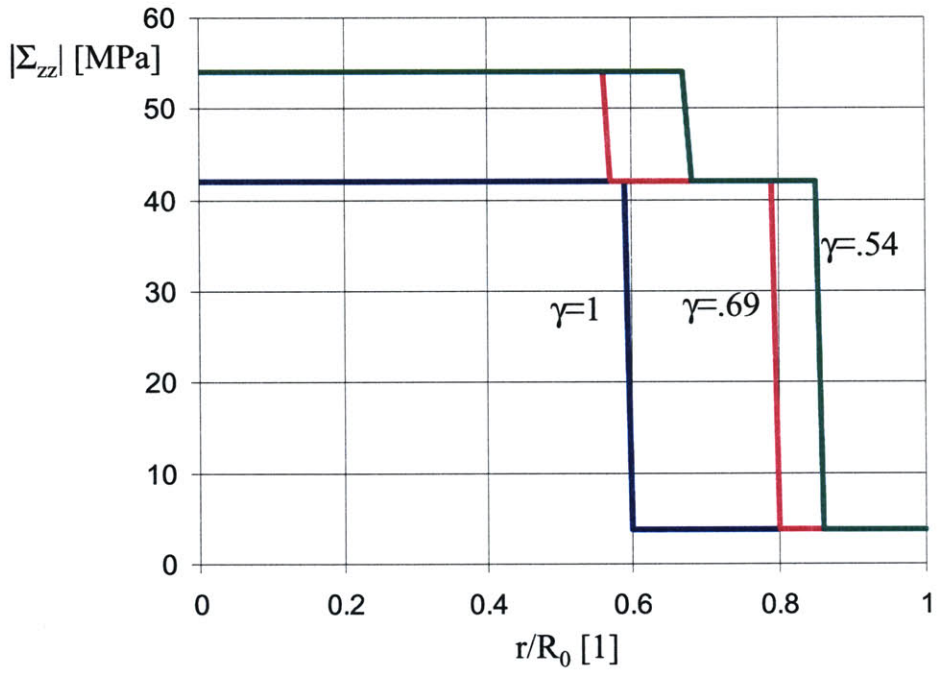

Figure 10-5: Results for the vertical stress distribution for three selected degradation states.

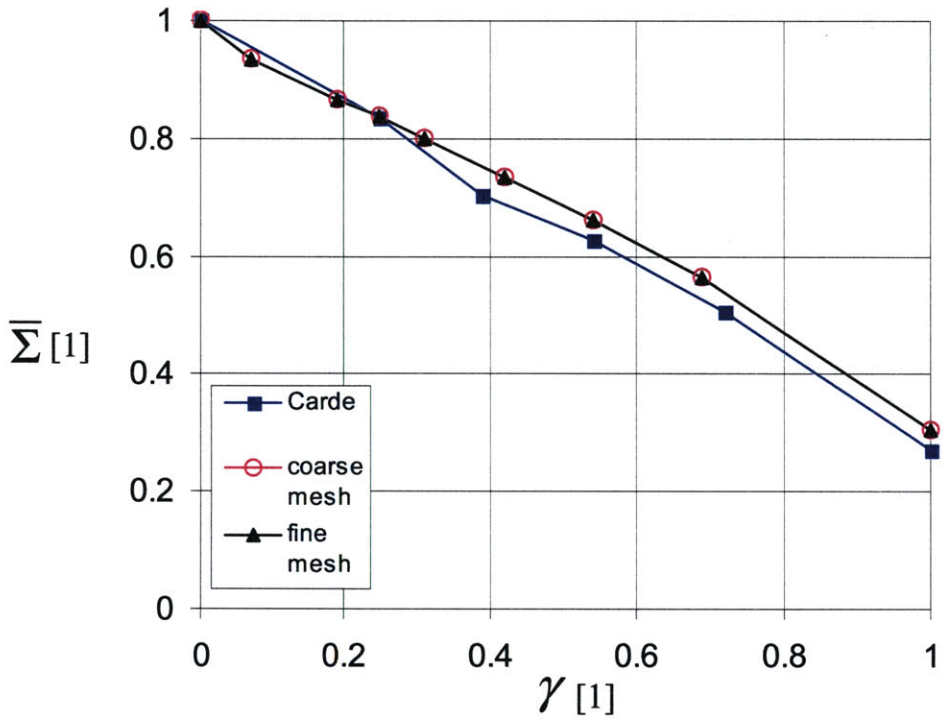

Figure 10-6: Comparison of the stress ratio $\overline{\Sigma}$ for different $\gamma_{\rightarrow CH}$ levels between the experiments by Carde and the model based simulations.

However, in this validation case the time plays no role because of the strength comparison as a function of the time independent surface ratio $\gamma_{\rightarrow CH}$.

10.4 Validation II: Le Bellego's Three-Point Bending Tests on Partially Leached Mortar Beams

The second validation case of the multiscale material model involves a mechanically more complex case: The three-point bending of a notched mortar beam for which the experimental data were provided by Le Bellego [80]. This validation case focuses on three main aspects:

- The leaching prediction in time, particularly the Portlandite front location.
- The strength description in the tensile domain.
- The deformation behavior in both the tension and compression domain.

10.4.1 Experimental Results by Le Bellego [80]

In her study of the chemical and mechanical couplings of calcium leaching in cementitious materials, Le Bellego conducted a large series of three-point bending tests of partially leached mortar beams [80]. In some cases, the beams were first leached and then mechanically tested. In other cases, the leaching took place under constant mechanical load. We consider here a case in which first the leaching occurs and then the beam is loaded mechanically. The considered beam has a size of 40 mm $\times$80 mm $\times$320 mm. The mortar was prepared at a water-cement ratio of $w/c = 0.5$. The beam is leached during 114 days in a 6M ammonium nitrate solution, comparable to the one presented in Chapter 3. Figure 10-7 (a) shows the leaching configuration of the beam. During the leaching period, the lateral surfaces of the beam and the top surface are covered with an RTV epoxy, preventing the ammonium nitrate from attacking the material. In addition, on the bottom surface a 60 mm long section at the corners of the beam is protected. The remaining surface open to the chemical attack is a 200 mm $\times$40 mm surface on the bottom of the beam. The degradation depth, corresponding to the Portlandite dissolution front, was measured by Le Bellego with Phenolphthalein on four beams. The average value after 114 days is 22 mm from the bottom of the beam.

(a)

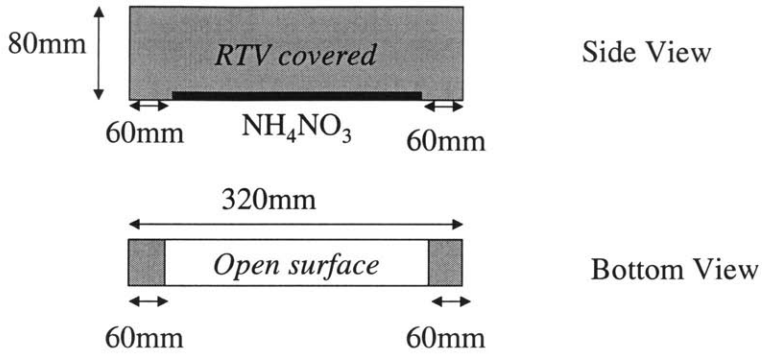

(b)

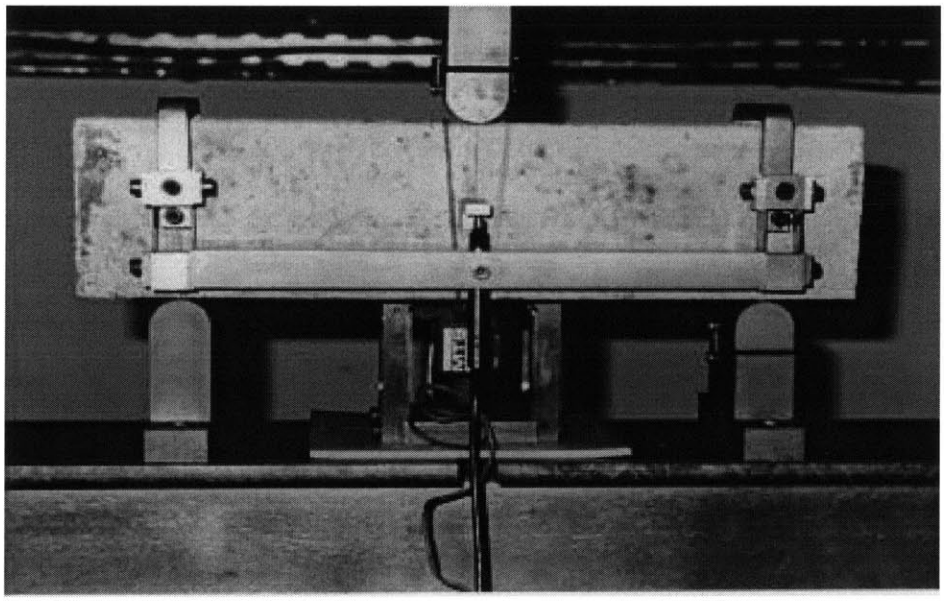

Figure 10-7: (a) Bottom and side view of the beam in its leaching configuration. (b) Mechanical loading configuration. Adapted from [80].

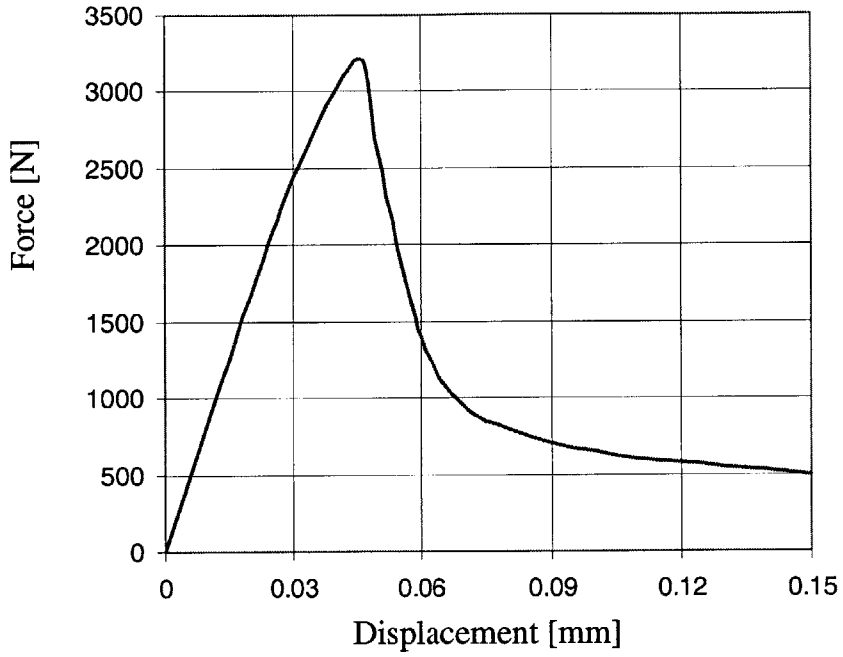

Figure 10-8: Averaged force displacement curve by Le Bellego for the three-point bending test. From Fig. 3-55 in [80].

After leaching, the beam was notched with a diamond saw. The 8 mm long and 3 mm wide notch is entirely in the leached section of the beam. The distance between supports is 240 mm. The three-point bending test was carried out displacement driven with a crack mouth opening displacement feedback control. The crack mouth opening rate was $0.25\,\mu\mathrm{m}/\mathrm{s}$, which corresponds roughly to a deformation rate of $8 \times 10^{-5}\,\mathrm{s}^{-1}$. Based on this rate drained conditions can be assumed. Figure 10-7 (b) shows a picture of the three-point bending loading configuration. The result presented by Le Bellego is a force-displacement curve shown in Figure 10-8. For the validation, the descending part of the curve will not be considered because it is controlled by the fracture properties of the structure, which are not included in our model. Comparing the results on leached and unleached notched beams, Le Bellego also reported a higher displacement at failure for the degraded beams. In addition, a smaller effect of the notch on the maximum force for degraded than for undegraded beams was found in the experiments.

10.4.2 Model-Based Simulations and Comparison

Leaching Calculation

Mesh, Boundary and Initial Conditions, Equilibrium Values

The mesh used for both the leaching and the bending calculation is shown in Figure 10-9. Making use of the symmetry of the problem, only half of the beam is modeled. The mesh consists of three-node linear elements around the notch and four-node linear elements in the middle part and around the supports. The initial condition is:

$$\left[Ca^{2+}\right]_s (x, y, t \leq 0) = 14.7\,\mathrm{mol}/\mathrm{l} \tag{10.8}$$

which corresponds to a $w/c = 0.5$ cement paste. The aggregates in the mortar have no influence on the leaching kinetics and can be neglected for the leaching process (see Section 3.4). The boundary conditions for the leaching calculation are:

$$\left[Ca^{2+}\right]_s (y = 0, 0 < x \leq 100\,\mathrm{mm}, t) = 4.5\,\mathrm{mol}/\mathrm{l} \tag{10.9}$$

$$\text{on } \Gamma_{\overline{q}} = \{x = 0, y;\ x, y = 80;\ x = 160, y;\ 100 < x \leq 160, y = 0\} : \overline{q} = 0 \tag{10.10}$$

The asymptotic solid calcium concentration of $4.5\,\mathrm{mol}/\mathrm{l}$ is imposed in the zone in contact with the ammonium nitrate solution. The notch is included in the leaching calculations to facilitate the portability of the mesh to the subsequent mechanical calculation. The change in leaching progress through the presence of the notch is small. The equilibrium values for the two leaching fronts are the same as in the first validation case and given in Table 10.2.

Results from Leaching Calculation

The result of the leaching calculation is the calcium concentration distribution in the solid displayed in Figure 10-10. The model-based simulations predict for the 114 days leaching period the location of the Portlandite front at 22 mm from the bottom of the beam. This is in very good agreement with Le Bellego's result. This underscores the prediction capability of the two-front leaching model.

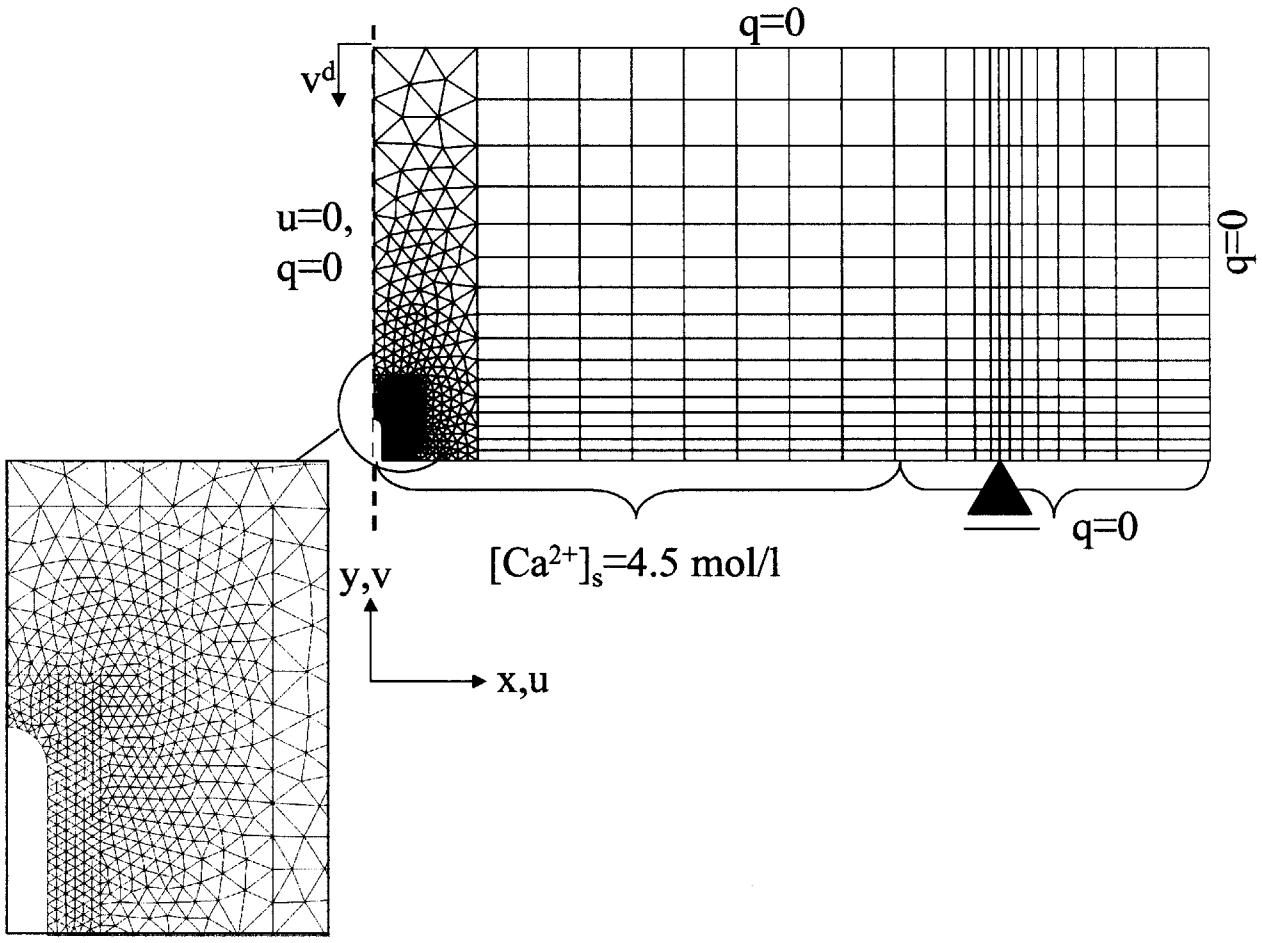

Figure 10-9: Mesh used for the simulation of the leaching and the bending.

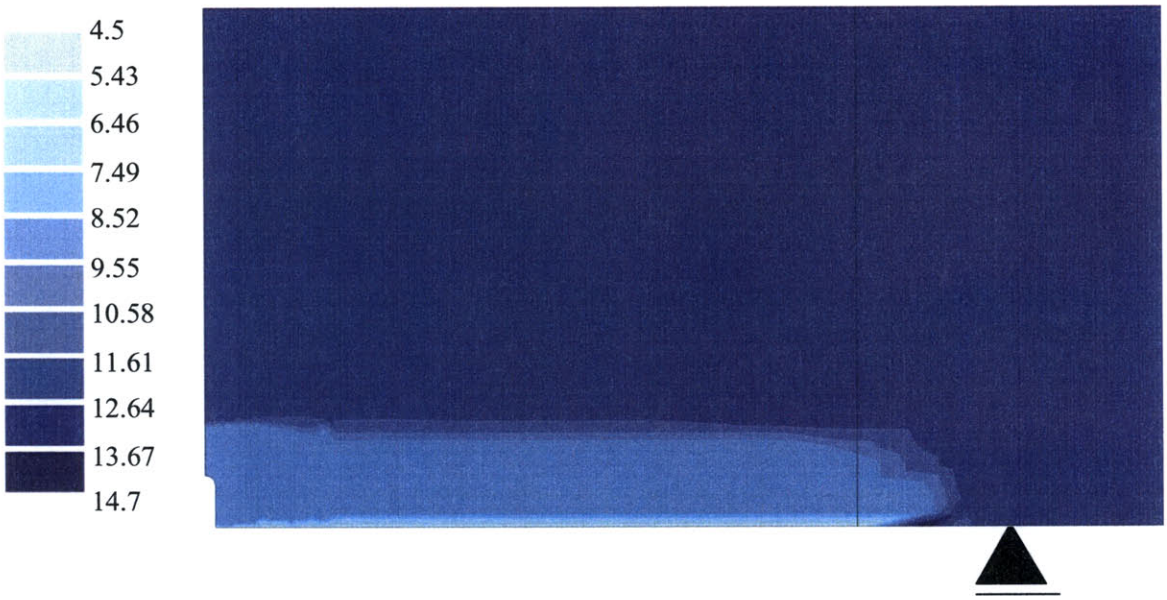

Figure 10-10: Results of the model based leaching calculations. Leaching takes place during 114 days.

Input Parameters	Mechanical Calculation		
	Intact	CH leached	Asymp. leached
δ_{DP} [1]	1.42	1.39	0.71
c_{DP} [MPa]	4.7	4.3	1.1
M [1]	1.77	1.64	1.29
p_t [MPa]	9.9	9.2	1.5
p_c [MPa]	40.9	38.0	6.2
λ [1]	0.01	0.01	0.01
κ [1]	0.05	0.05	0.05

Table 10.4: Mechanical input data for validation case 2

Boundary Conditions and Input Data for the Mechanical Calculation

The mechanical boundary conditions are the following:

$$u_y(x = 0, y = 80, t) = u_d(t) \tag{10.11}$$

$$u_y(x = 0, y, t) = 0 \tag{10.12}$$

$$u_y(x = 120, y = 0, t) = 0 \tag{10.13}$$

The vertical displacement $u_d = 0.05\,\text{mm}$ is applied in ten equal load steps. Boundary condition (10.12) is a symmetry condition in the symmetry axis (see Figure 10-9). The vertical displacement at the support (10.13) is set to zero on three nodes to avoid stress concentrations. The calculations are performed under isothermal and drained conditions.

The mechanical input data for the beams are largely based on the data provided by Le Bellego [80]. Table 10.4 summarizes the used values. From the reported uniaxial compressive strength on cylinders of 44.3 MPa and the uniaxial tensile strength (in direct tension) of 4.5 MPa the parameters δ_{DP} and c_{DP} are determined from (5.32). The slope of the critical state line M is assumed to have the same value as the tested mortars in our study. From the uniaxial compression strength and M follow the consolidation pressure p_c and p_t according to (9.61). For the values of the parameters in the asymptotically leached state, the same degradation scenario as for the mortars tested in this study is assumed. The parameters for the intermediate leaching state are calculated with the micromechanical estimates of sections 8.2 and 8.3 by using Eq. (8.31) and (8.44), respectively. The parameters λ and κ for the Cam-Clay hardening were derived in Section 9.3. The poroelastic properties are assumed to correspond to the values of

Table 7.9.

Results from Mechanical Analysis

Figure 10-11 shows a comparison of the experimental force-displacement curve (closed line) and the model-based simulations (square elements for each load step). The model-based simulations show a good agreement with the experimental curve until roughly 60% of the experimentally observed maximum load. From there on, the reproduction is still good albeit not perfect. At the maximum load of the experimental results, the model-based simulations suggest that the load could be increased further. The good agreement between the two results before failure indicates that the modeling of the material strength in tension and the deformation behavior is adequate. The fact that the failure load is not correctly predicted is due to the presence of the notch. Around the notch, close to the failure load, a strong stress concentration takes place which is typical for a fracture failure. The fracture behavior is not included in our model formulation.

Discussion

A second force displacement curve can be calculated with a beam of which the height is reduced by the leached part (22 mm). The triangle curve in Figure 10-11 shows that the bending capacity of such a beam is much smaller than the actual beam behavior. Inverting this argument means that the leached parts of the beam are still valuable for the bending resistance of the beam. A closer look at the stress and plastic strain distribution in the section confirms this finding that the leached parts are still important load carrying elements of the beam particularly because of the distance to the neutral axis, and the small but accountable asymptotic strength. The Σ_{xx} distribution along the height of the beam is shown in Figure 10-12 for a load level of 0.048 mm. In the lower part of the beam where the notch is situated, Σ_{xx} is zero. Above the notch, the tensile strength is the limiting factor for the stress distribution and a well developed zone of plastic deformation is obtained. Figure 10-13 shows the Σ_{xx} distribution along with the equivalent plastic strains at a prescribed vertical displacement of 0.048 mm (which is close to the peak load). The equivalent plastic strains are defined as the norm of the plastic strain tensor: $E_{eq}^{pl} = \sqrt{\mathbf{E}^p : \mathbf{E}^p}$. The figure shows that the plastic zones are the zones in tension. Moreover,

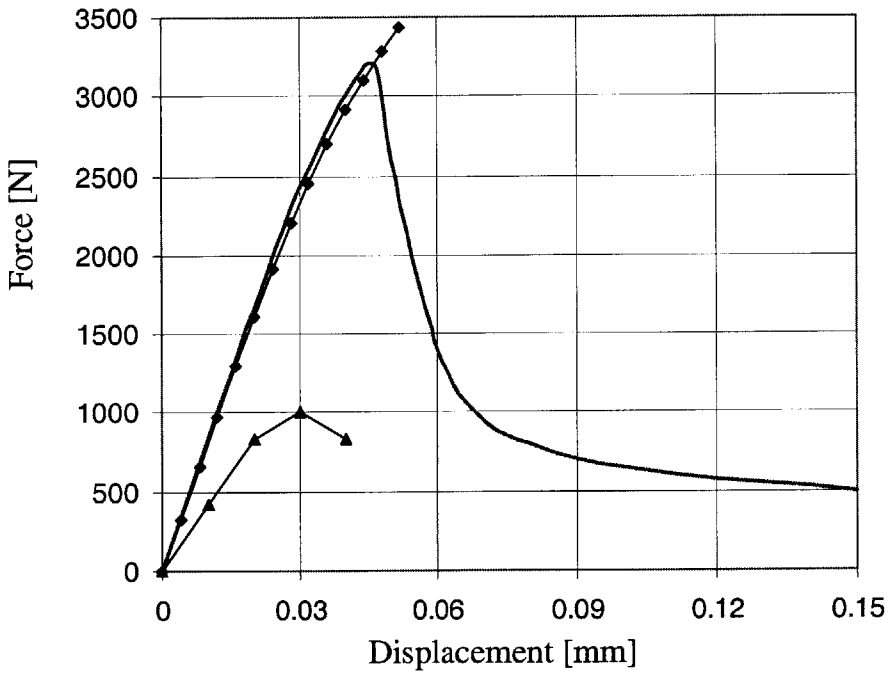

Figure 10-11: Comparison of the load - deflection curves from the experiments (closed line) and the model-based simulations. The squares indicate the notched beam simulation while the triangles correspond to a beam with a decreased height, corresponding to the leached zone.

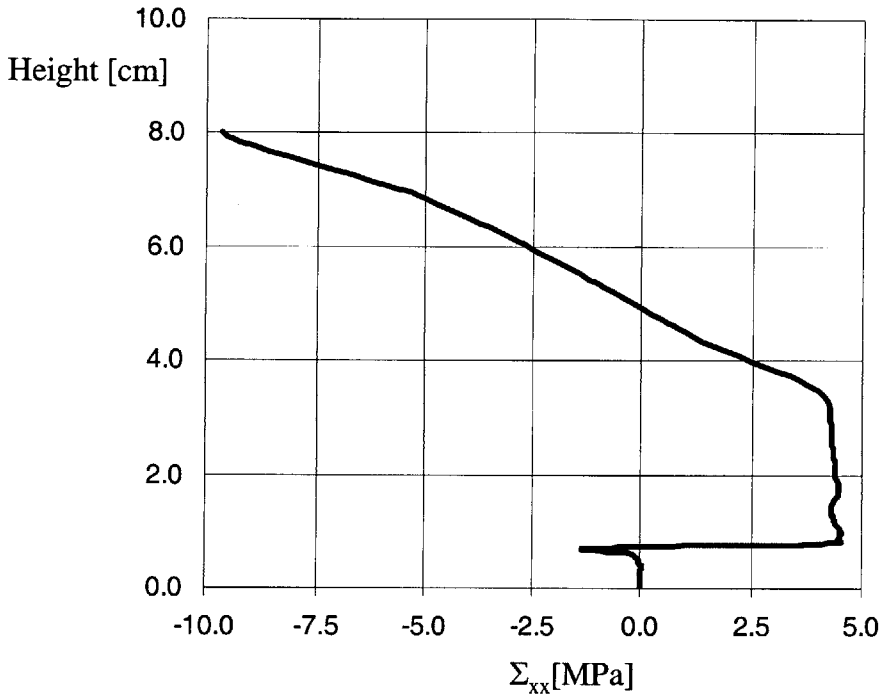

Figure 10-12: Σ_{xx} distribution in the notched beam at x=1.5mm at a displacement of 0.048 mm

the notch seems to shield the bulk of the beam: The plastic effects are very much confined to the proximity of the notch. The leached material concentrates the imposed deformation and in this way protects the intact material above from the effects of the notch. This observation might explain the less detrimental effects of a notch on leached beams that was noted by Le Bellego. This may explain how the material ductility which was discussed in Section 6.6.2 leads to beneficial structural effects: Instead of leading to brittle failure starting from the notch, the capacity of the leached material to plastically deform enhances the structural ductility performance. This is captured by the model-based simulation. It is suggested that this ductility increase is at the origin of higher displacements at failure in partially leached notch beams than in unleached beams as reported by Le Bellego. The effect of the notch and the role the leached material plays in it can be explained by comparing the stress distribution in an unnotched beam. Figure 10-14 shows the Σ_{xx} distribution along the height of the beam with and without

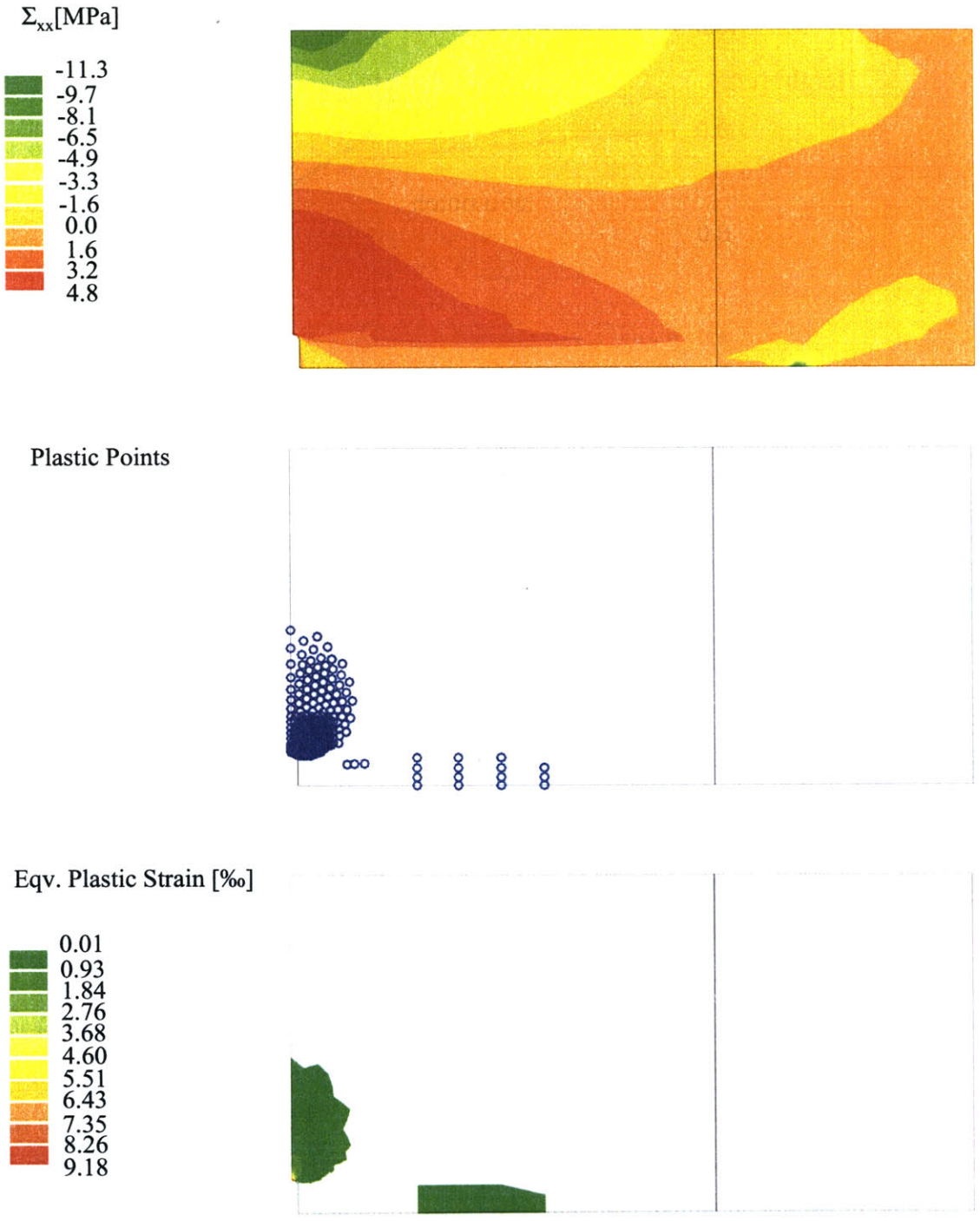

Figure 10-13: Stress Σ_{xx}, the plastic deformation zone and plastic strains for the notched beam at a displacement of 0.048 mm.

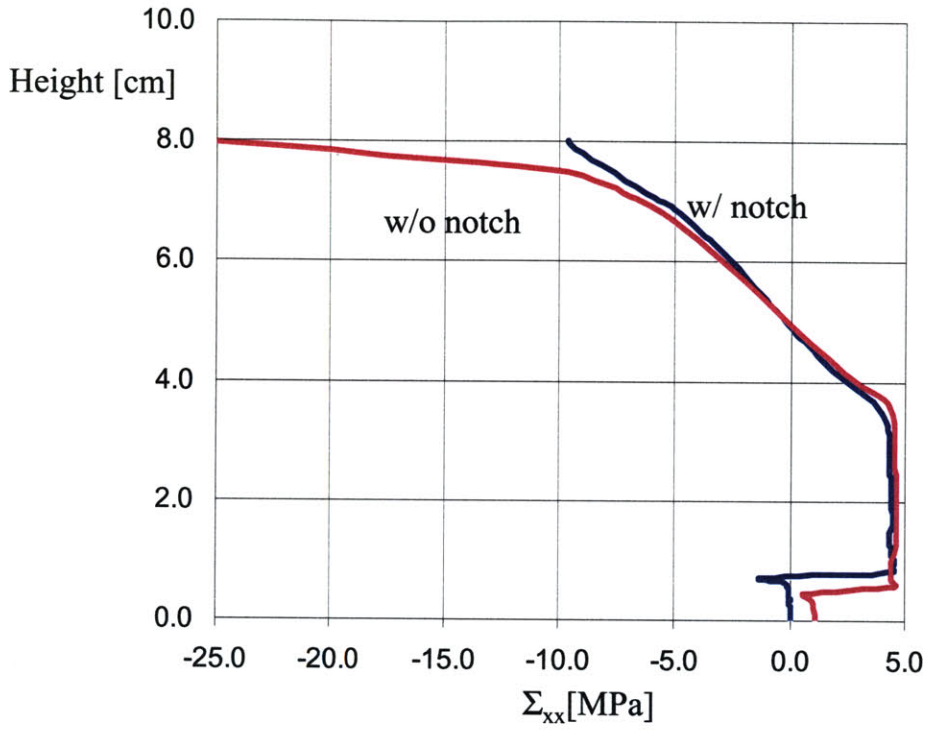

Figure 10-14: Comparison of the Σ_{xx} distribution in the notched and unnotched beam. Imposed displacement is 0.048 mm in both cases.

notch. The stress distribution in the middle part of the beam is very similar in both cases. The main difference is due to the notch that forces the stress to zero, while in the unnotched beam the residual tensile strength is reached. We also note from Figure 10-14 that at the top of the beam a higher compressive stress is reached when no notch is present. This shows that the notch through its stress concentrating effect prior to softening inhibits the beam rotation and leads to a stronger activation of the compressive zone. Figure 10-15 shows the complete Σ_{xx} distribution and the plastic points in the unnotched beam. The plastic zone is much increased compared to the notched beam and correspondingly the stress distribution is affected. The large area of plastic strains in the unnotched beam underscores the stress concentration effect of the notch in the degraded material zone. This limits the detrimental effect of the notch on the bending performance.

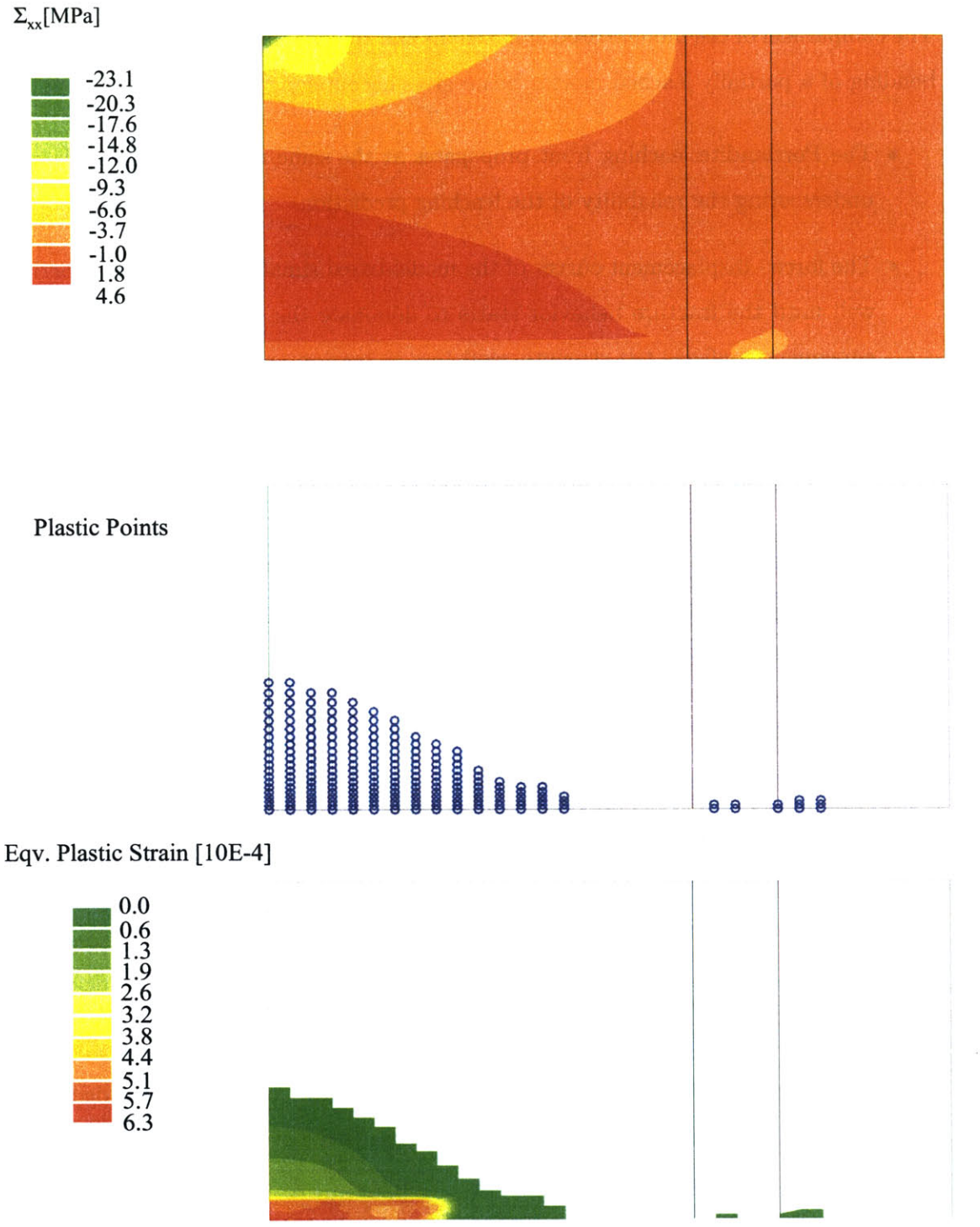

Figure 10-15: Stress distribution Σ_{xx}, plastic deformation zone and plastic strains in the leached beam without notch. The displacement is 0.048 mm.

10.4.3 Conclusion of the Validation Step

The comparison of the model-based simulations and the experimental results on the three-point bending of a partially leached mortar beam gives encouraging results:

- The Portlandite leaching front propagates at the same rate as measured by Le Bellego, underscoring the reliability of the leaching prediction.
- The force - displacement curves of the model-based simulations and the experiment agree well until the fracture behavior starts to dominate the experimental results. The good agreement confirms the strength modeling in tension and the micromechanical strength modeling for the intermediate degradation state in a very complex stress state around a notch.
- From the model-based simulation, the less detrimental effect of the notch on leached beams can be explained. In the leached material, the plastic deformations are localized close to the notch, shielding the bulk material. In addition, comparison with a beam reduced by the height of the leached zone shows that the residual strength in leached parts of the beam provide an important contribution to the bending capacity of a partially leached beam.

10.5 Validation III: Schneider's Time Evolution of Four-Point Bending Strength

The third validation case focuses on the evolution of the flexural performance in time. The validation case involves mortar beams that are leached for different durations before being tested in four-point bending. Experimental results for this case were provided by Schneider & Chen [129, 130]. The focus of this validation case is the evaluation of the time-scale of the flexural performance degradation.

10.5.1 Experimental Configuration and Results

Schneider and Chen performed tests on leached mortar beams as part of a research project on chemical corrosion and stress corrosion of high performance cementitious materials. The tests we consider in our validation case were performed on mortar beams produced at a water-cement ratio of w/c =0.5 from a Type I Portland cement and a fine sand. The beams have a size of 40 mm ×40 mm ×160 mm. The leaching takes place in a 10% ammonium nitrate solution. This corresponds to a concentration of 68 g NH_4NO_3 per kilogram of solution. The volume of the bath and the ratio of mortar volume and bath volume are not given in the experimental description. At different times between 7 days and 821 days, specimens are taken from the bath and tested in four-point bending. The results are reported by Schneider & Chen as a plot of the ratio β/β_{28} versus time. β is the maximum equivalent tensile stress in the beam calculated under the assumption of a linear stress distribution over the beam section:

$$\beta = \frac{6M}{bh^2} \tag{10.14}$$

where M is the bending moment, b and h are the width and height of the beam section, respectively. The index 28 refers to the strength measured on intact specimens after 28 days of curing. The β_{28} value is 8.3 MPa, corresponding to a bending moment of 88.53 Nm. Figure 10-16 shows the experimentally observed evolution of the flexural beam strength in time. The characterization of the leaching process with time complicates the validation process. In fact, time is not an objective variable to describe the leaching process: Depending on the boundary conditions in the leaching bath, very different states of degradation are obtained. A better way of characterizing the degradation state is the movement of a leaching front, for example the Portlandite leaching front, as shown in the first two validation cases. Schneider & Chen report the progress of this front for two times, one after 91 days, and a second after 365 days of leaching for which they give the value of 9.2 mm and 10.1 mm, respectively. Figure 10-17 shows these data values in a square root of time plot. The fact that the two measurements are not on a straight line through the origin indicates that the front propagation does not take place proportional to $\sqrt{t}$. This $\sqrt{t}$-dependency has been observed in leaching configurations with controlled ammonium nitrate concentration ([80], [28]). This suggests that the leaching

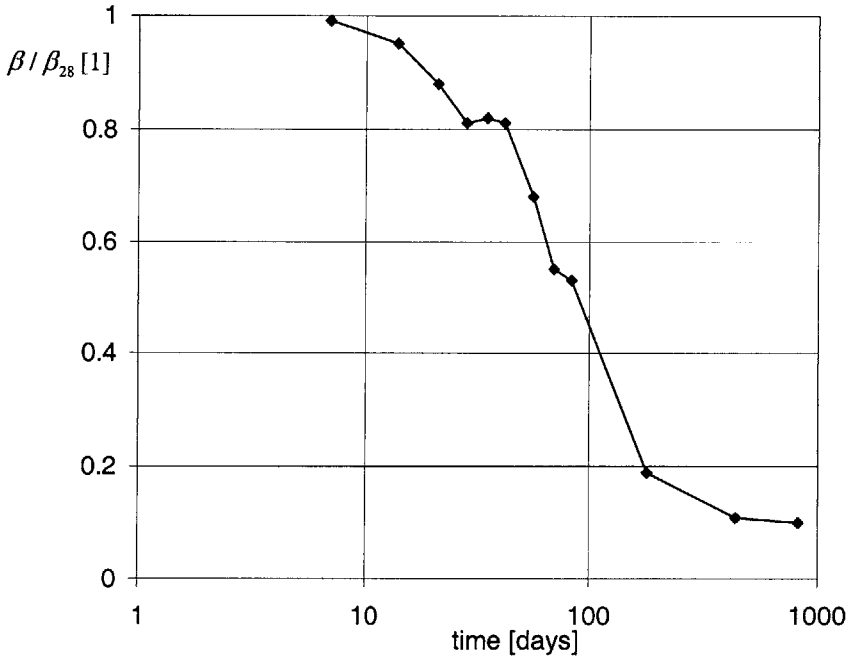

Figure 10-16: Evolution of the flexural strength as reported by Schneider & Chen [130].

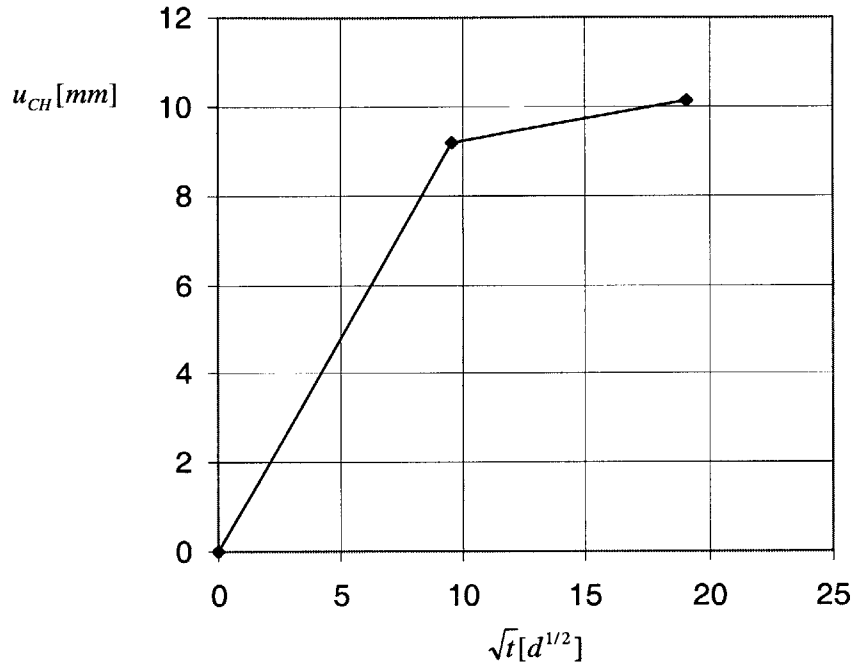

Figure 10-17: Measurement points of the Portlandite front propagation by Schneider & Chen [130].

conditions of Schneider & Chen are not constant in time and make a comparison difficult.

10.5.2 Model-Based Simulation of Leaching

Mesh, Initial and Boundary conditions

The combined leaching-bending problem is three-dimensional in nature. In the model-based simulation we choose to consider a section of the beam only, which as we will see later is possible because of the statically determined nature of the bending test. The details of the mechanical part of the model-based simulations are given in the next section. For the leaching simulation, considering symmetry, a 20 mm $\times$40 mm half section of the beam is discretized (Figure 10-18). A fine mesh is used consisting of 30$\times$60 four-node linear elements of constant length $l = 0.67$ mm. This small size is chosen in view of the leaching calculation which requires

Leaching Input Data		6 M solution	0.85 M solution
Portlandite Front	$\left[Ca^{2+}\right]_s = 8.0\,\mathrm{mol/l}$	$\left[Ca^{2+}\right]_{sol} = 2.7\,\mathrm{mol/l}$	$\left[Ca^{2+}\right]_{sol} = 0.43\,\mathrm{mol/l}$
C-S-H Front	$\left[Ca^{2+}\right]_s = 4.5\,\mathrm{mol/l}$	$\left[Ca^{2+}\right]_{sol} = 0.5\,\mathrm{mol/l}$	$\left[Ca^{2+}\right]_{sol} = 0.17\,\mathrm{mol/l}$
Initial porosity	$\phi_0 = 0.35$		
Diffusion Coeff.	$D(\phi) = a\exp(b\phi)$ with $a = 2.35 \times 10^{-13} m^2/s$ and $b = 9.95$		

Table 10.5: Input data for the leaching simulation of two leaching scenarios of Schneider and Chen's beams.

a precise determination of the leaching fronts for small differences in leaching times[3].

The boundary conditions for the leaching simulation are identical to the prior validation cases:

$$\text{On } \Gamma_{\overline{Ca}} = \left\{ \begin{array}{c} 0 \le x \le 20, y = 0;\ x = 20, 0 \le y \le 40; \\ 0 < x \le 20, y = 40 \end{array} \right\} : \left[Ca^{2+}\right]_s = 4.5\,\mathrm{mol/l} \qquad (10.15)$$

$$\text{on } \Gamma_{\overline{q}} = \{x = 0, 0 < y \le 40\} : \overline{q} = 0 \qquad (10.16)$$

The zero flux condition (10.16) is purely for symmetry reasons. The initial conditions read:

$$\left[Ca^{2+}\right]_s (x, y, t \le 0) = 14.7\,\mathrm{mol/l} \qquad (10.17)$$

Equilibrium parameters

The equilibrium parameters for the leaching simulation are not identical to the prior validation cases. Here we consider two different leaching scenarios. The first scenario corresponds to the $6M$ ammonium nitrate solution which was used before. The equilibrium parameters are unchanged and given in Table 10.5. The second scenario considers a $0.85M$ ammonium nitrate solution which yields a concentration of 68 g NH_4NO_3 per kilogram of solution, which corresponds to the conditions reported by Schneider & Chen. For this case the equilibrium values for the two leaching fronts need to be recalculated. The values obtained with the approach described in Section 3.2 are also given in Table 10.5.

[3] Given the short testing intervals of 7 days reported by Schneider & Chen.

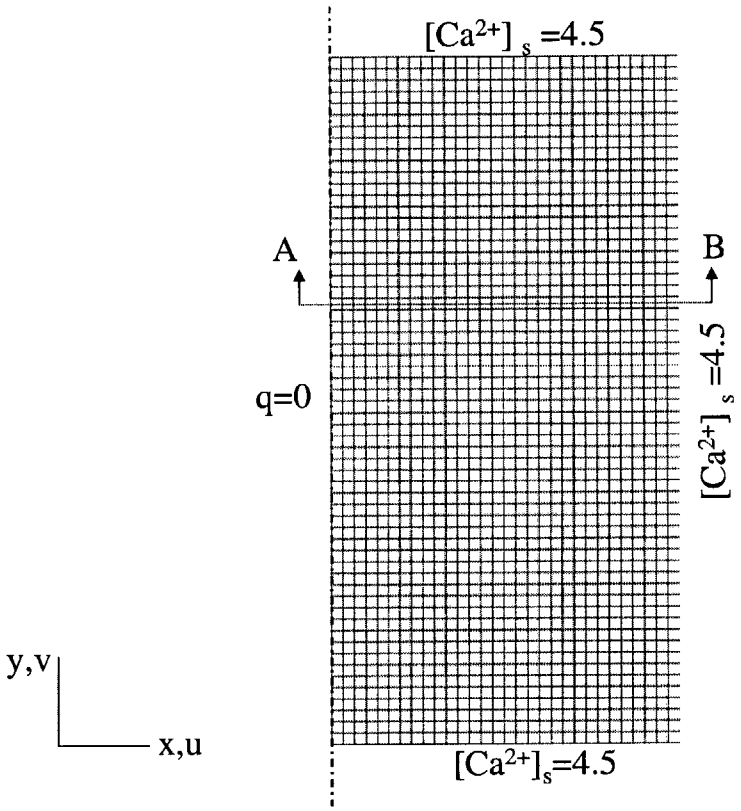

Figure 10-18: Mesh and leaching boundary conditions in the beam section.

Results of the Leaching Simulations

Figure 10-19 shows the leaching results in the case of the $6M$ ammonium nitrate solution at different times. Figure 10-20 shows the front movement along the A-B plane (See Figure 10-18). The Portlandite front reaches the center after roughly 100 days. The C-S-H front moves considerably slower, particularly as long as Portlandite is left for leaching. After the Portlandite front reached the center, the C-S-H front propagation accelerates. The specimen is homogeneously leached before 441 days, the next point at which Schneider&Chen had taken strength measurements. Together, the CH front moves considerably faster than the results reported by Schneider & Chen. Figures 10-21 and 10-22 show the equivalent results for the case of the $0.85M$ ammonium nitrate solution. Due to the lower equilibrium concentrations, the leaching takes much more time and the Portlandite front reaches the center after 441 days. The C-S-H front has not reached the center after 821 days, which corresponds to the end of the experimental observation. The C-S-H front moves slower as long as there is Portlandite available to leaching. After 84 days of leaching in the $0.85M$ solution, the Portlandite front has moved 5.5 mm into the specimen. This compares poorly to Schneider & Chen's value of 9.2 mm after 91 days of leaching. In fact Schneider & Chen's results are in between the two cases calculated.

10.5.3 Model-Based Simulation of Four-Point Bending Tests

2D Calculations

The four-point bending test is a statically determined system. That is the stress distribution in the section is entirely determined by the material law. Following the approach suggested by Ulm [147], we calculate the three-dimensional combined leaching and beam bending problem on a two-dimensional section. This reduces the calculation cost considerably. We assume the validity of the Bernoulli hypothesis, stating that the section remains plane. The strain in the longitudinal axis of the beam then reads:

$$\varepsilon_{zz} = \epsilon_z^0 + y\vartheta_x - x\vartheta_y \tag{10.18}$$

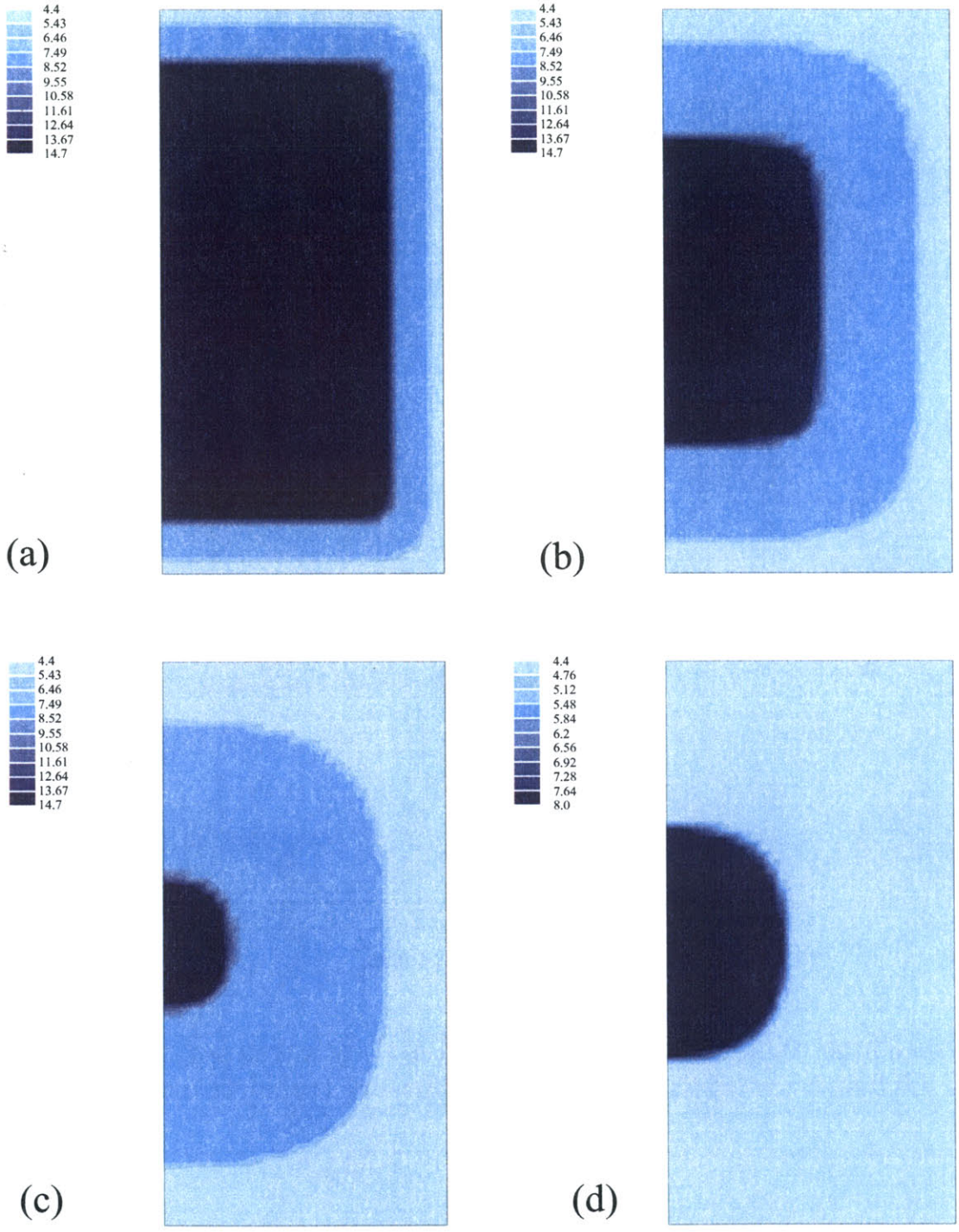

Figure 10-19: Results from the leaching calculation with the 6M ammonium nitrate solution. (a) 7days, (b) 35 days, (c) 84 days and (d) 182 days of leaching. The result values are solid calcium concentrations in mol / l.

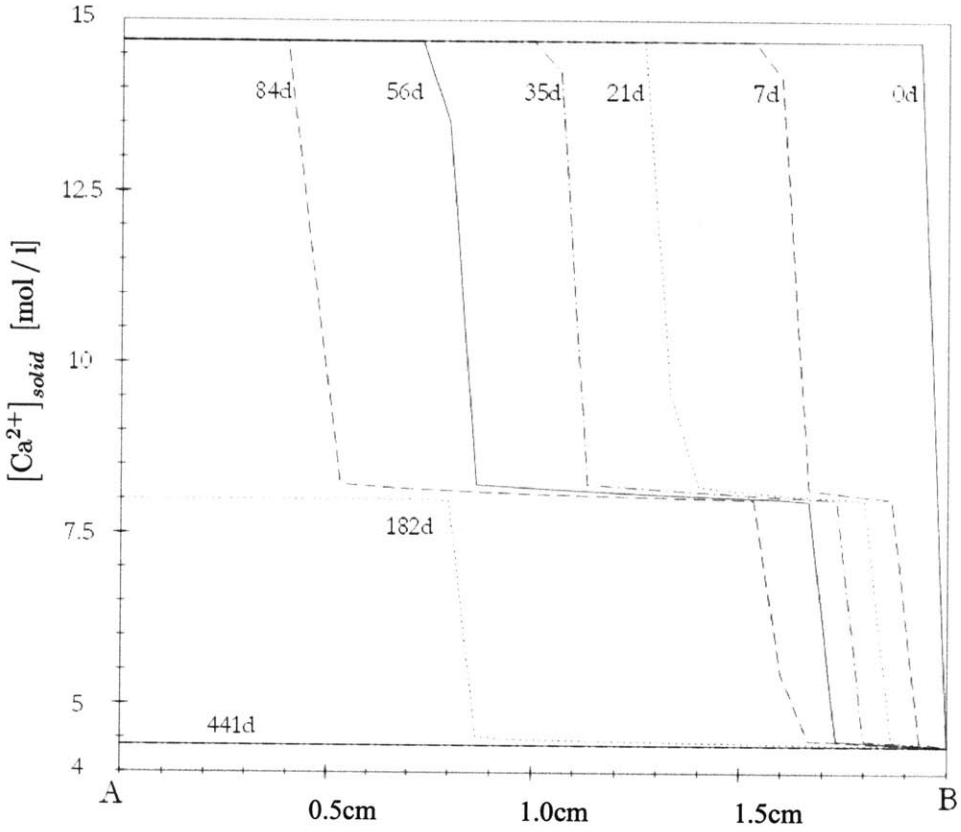

Figure 10-20: Movement of the two leaching fronts in the A-B plane for the 6 M solution. The C-S-H front moves faster once the Portlandite front has reached the center.

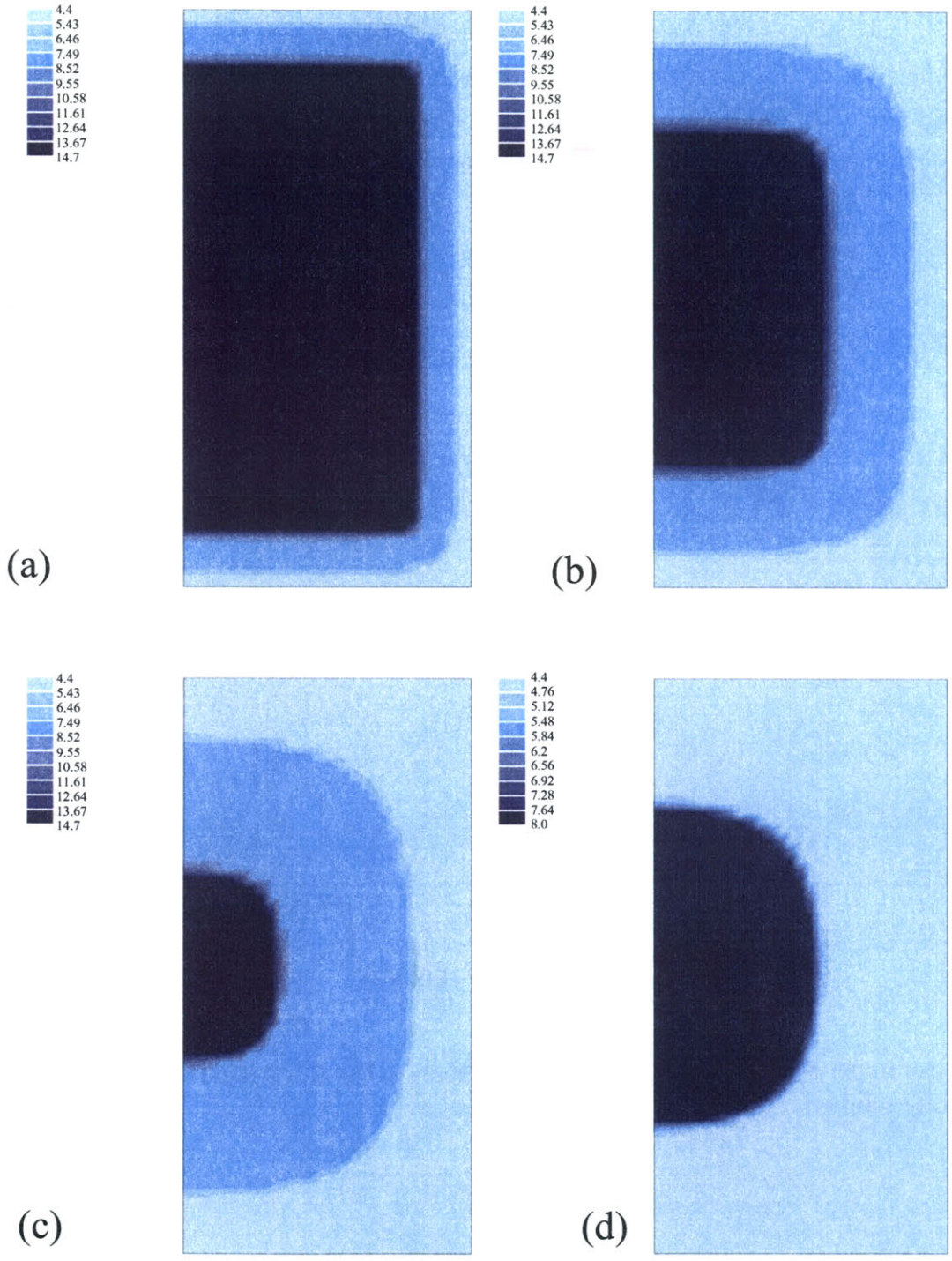

Figure 10-21: Results from the leaching calculation with the 10% ammonium nitrate solution. (a) 42days, (b) 182 days, (c) 441 days and (d) 821 days of leaching. The result values are solid calcium concentrations in mol/l.

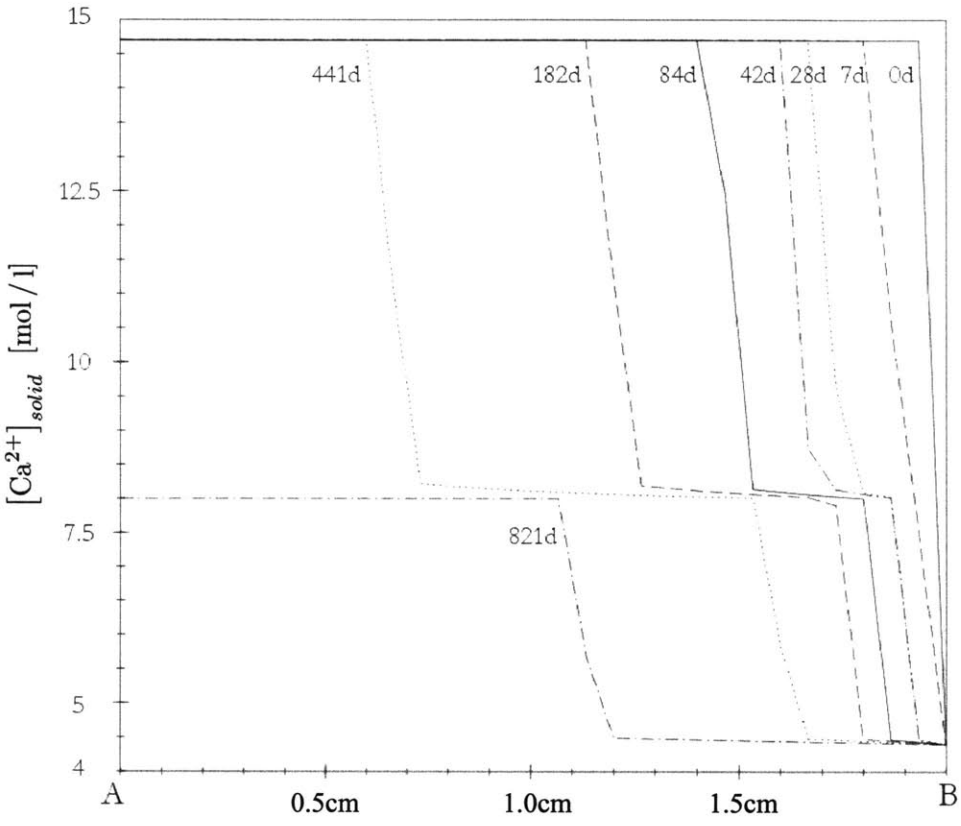

Figure 10-22: Movement of the two leaching fronts in the A-B plane for the 0.85 M ammonium nitrate solution.

where ϵ_z^0 is the deformation in the center of gravity of the section and ϑ_x and ϑ_y are the curvatures around the x and y-axis of the studied section, respectively. These three section unknowns need to be determined. To this end, the global equilibrium in the section is calculated, using the common definitions of the normal force and the bending moment:

$$N = \int_A \boldsymbol{\sigma} \cdot \mathbf{e}_z dA; \mathbf{M} = \int_A (x\mathbf{e}_x + y\mathbf{e}_y) \times (\boldsymbol{\sigma} \cdot \mathbf{e}_z)\, dA \tag{10.19}$$

where $\times$ denotes the cross product and A the section. The stress tensor in any part of the section can be written as:

$$\boldsymbol{\sigma} = \boldsymbol{\sigma}^{PS} + \varkappa \mathrm{diag}\begin{bmatrix} 1 & 1 & \frac{1-\nu}{\nu} \end{bmatrix} \varepsilon_{zz} \tag{10.20}$$

where $\boldsymbol{\sigma}^{PS}$ is the stress tensor corresponding plane strains ($\varepsilon_{zz} \equiv 0$)and $\varkappa = \nu E / [(1-2\nu)(1+\nu)]$. Use of (10.20) in (10.19) leads to expressing the section equilibrium in the following form:

$$\begin{pmatrix} N^{PS} - N^d \\ M_x^{PS} - M_x^d \\ M_y^{PS} - M_y^d \end{pmatrix} + \frac{1-\nu}{\nu} \begin{bmatrix} \int_S \varkappa dA & \int_S y\varkappa dA & -\int_S x\varkappa dA \\ \int_S y\varkappa dA & \int_S y^2\varkappa dA & -\int_S xy\varkappa dA \\ -\int_S x\varkappa dA & -\int_S xy\varkappa dA & \int_S x^2\varkappa dA \end{bmatrix} \begin{pmatrix} \epsilon_z^0 \\ \vartheta_x \\ \vartheta_y \end{pmatrix} = \mathbf{0} \tag{10.21}$$

where $\left(N^d, M_x^d, M_y^d\right)$ are prescribed normal force and moments on the beam, while $\left(N^{PS}, M_x^{PS}, M_y^{PS}\right)$ are obtained by using (10.19) with the plane strain stress state. In the mechanical calculation, equation (10.21) is solved at every iteration and the stress state in the section is corrected according to (10.20).

Mesh, Boundary Conditions and Input Parameters

Figure 10-23 shows the employed mesh in the model-based simulations. The only loading of the section is M_x^d. The boundary conditions are:

$$u_x(x = 0, y) = 0 \tag{10.22}$$

which is a symmetry condition.

The mechanical input parameters are based on data by Schneider & Chen and the microme-

Input Parameters	Mechanical Calculation		
	Intact	CH leached	Asymp. leached
δ [1]	1.55	1.39	1.00
c [MPa]	3.3	4.3	0.73
M [1]	1.84	1.72	1.39
p_t [MPa]	9.6	9.0	1.2
p_c [MPa]	51.6	47.9	3.1
λ [1]	0.01	0.01	0.01
κ [1]	0.05	0.05	0.05

Table 10.6: Mechanical input data for validation case 3.

chanical estimations. In the intact state, the uniaxial compressive strength is 55 MPa. From the bending moment of 88.53 Nm assuming a totally plastic section, we deduce a uniaxial tension strength of 2.9 MPa. These strength values lead to the friction coefficient and cohesion of the Drucker-Prager yield surface with (5.32). Table 10.6 reports the values. We assume that the frictional behavior in the compressive zone is changed by the slightly higher volume fraction of inclusions ($f_I \approx 0.6$) compared to the tested mortars in this study. With the micromechanical estimate (8.30), M can be calculated and from there p_t and p_c according to (9.61). In the intermediate leaching state, the micromechanical estimates (8.31) and (8.44) are applied. For the asymptotically leached state, we assume a compressive strength of 3.0 MPa and a tensile strength of 0.7 MPa. The compressive strength corresponds to values obtained in this study, while for the tensile strength equation (8.45) is applied which takes into account the inclusion volume fraction. In other words, the tensile strength, due to the higher inclusion volume fraction, is assumed to degrade slightly more than the one of the material tested in this study. The higher inclusion volume fraction is also taken into account in the compressive zone through (8.30). The Cam-Clay hardening parameters λ and κ remain as in the other validation cases.

Results

By means of model-based simulations, the maximum bending moment that can be supported for each of the leaching states is calculated. The comparisons of the experimental results by Schneider & Chen with the model-based simulations are shown in Figures 10-24 and 10-25. The figures show the bending strength ratio M/M_{28} in time, where M is the maximum bending moment the beam can sustain and M_{28} is the bending moment in the undegraded material state.

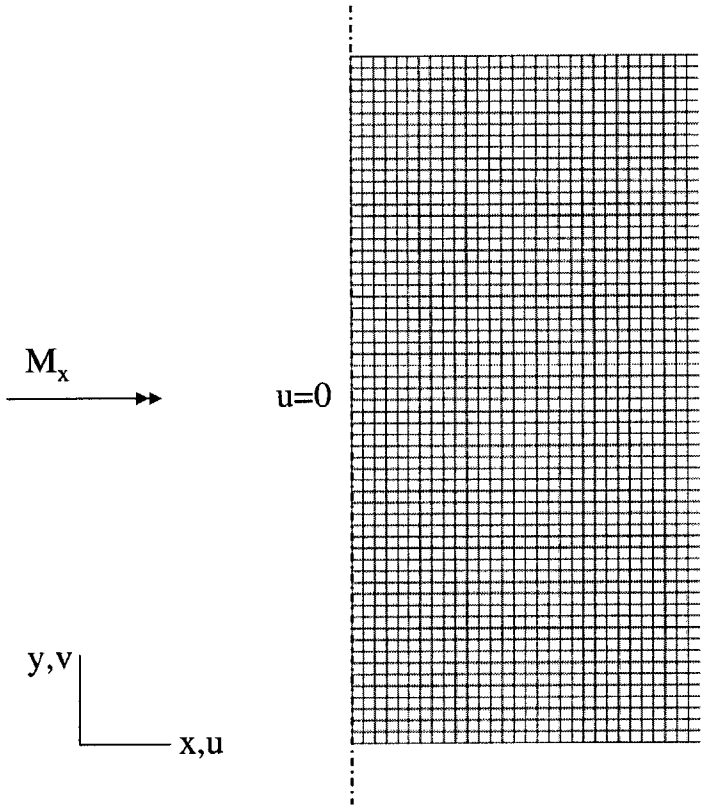

Figure 10-23: Mechanical loading conditions and boundary conditions.

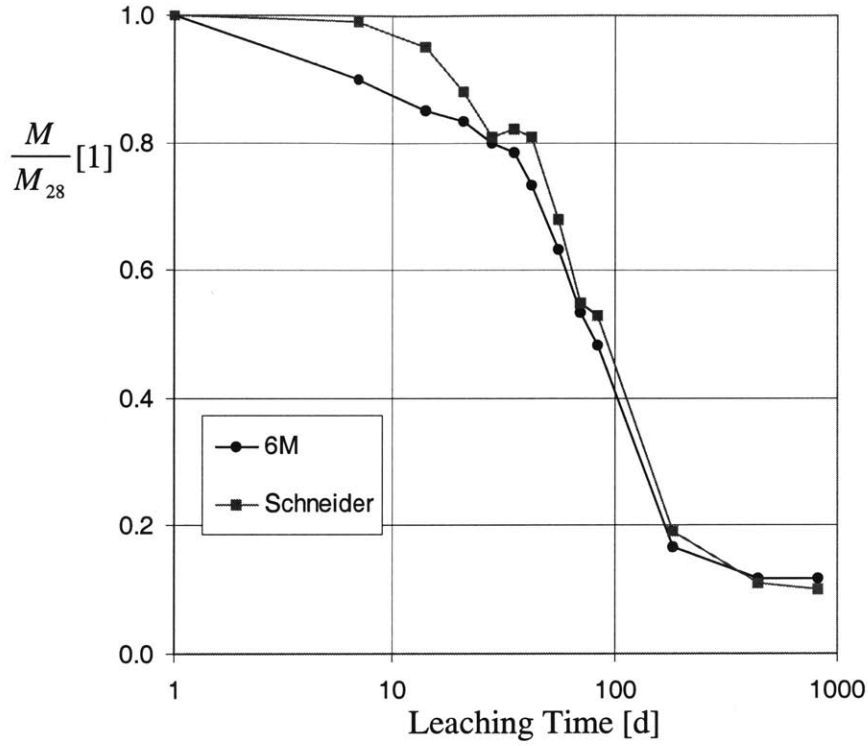

Figure 10-24: Comparison of the dimensionless bending strength between the experimental data by Schneider & Chen [129] and the model-based simulations.

For the 6M solution case (Figure 10-24), model-based predictions and experimental data are in rather good agreement. For very large leaching times, the experimental data show a slightly stronger reduction in bending strength than the model-based simulations. To investigate the time-scales involved in the evolution of the bending strength, Figure 10-25 shows the evolution of the bending strength for the 0.85M solution. If we compare the experimental results with the simulations of the 6M and 0.85M ammonium nitrate solution we note that all three curves for small leaching times (shorter than 100 days) almost coincide. For short leaching times, the differences in front propagation velocity is small. For large leaching times, the model-based prediction with the 6M solution and the experimental data closely match. In turn, the 0.85M solution predicts a much slower decay in bending strength. The good agreement of the 6M model-based simulation and the experimental data are surprising as Schneider & Chen report the use of a 0.85M solution. This surprising result suggests that the leaching conditions may well

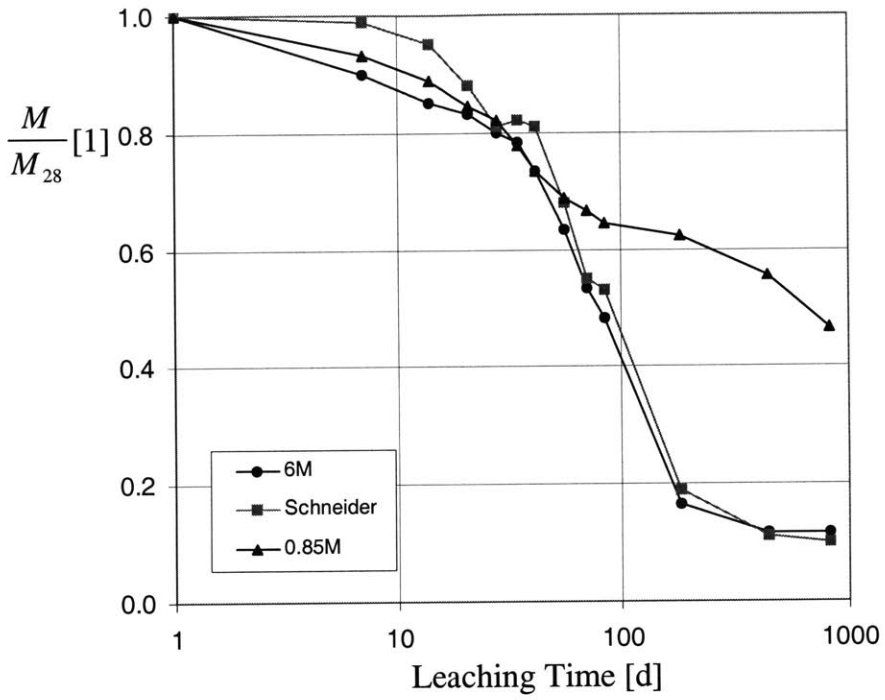

Figure 10-25: Model based simulations of the change in bending strength with two different leaching strengths in comparison with the experimental data by Schneider & Chen [129].

have varied, provided that the chemical equilibrium conditions used in this calculation (Table 10.5, from Section 3.2) are accurate. In contrast to the original Berner-curve which compiled many experimental results, the modified curve for ammonium nitrate based leaching relies on chemical equilibrium considerations. These have inherent uncertainties about the equilibrium constants etc. (see Chapter 3). However, numerical calculations accounting for the CH front and based on the equilibrium values compare well to experimental data[94].

Conclusion of the Validation Step

The comparison of the model-based simulations and the experimental results by Schneider & Chen lead to the following conclusions

- The time decay of the bending strength is correctly predicted by the model-based simu-

lations, which validates the strength description in the asymptotically leached state.

- The comparison of experimental data and model-based simulations at different leaching conditions shows that the experimental data and the model-based simulations coincide for the 6M solution. It is likely that the actual leaching conditions of Schneider & Chen's test do not correspond to a 0.85M solution.

10.6 Summary and Domain of Model Application

This chapter presented the validation of the multiscale model through comparison of experimental data and model-based simulations. Through a set of three different cases, the performance of the model elements was checked.

- In purely compressive stress states, the model-based simulations deliver an excellent result of the overall strength. The micromechanical strength modeling for the intermediate leaching state and the two front approach are validated here.

- On a notched beam in three-point bending, a good agreement of the force displacement curve is found until failure. The tensile strength modeling and the deformation behavior are validated. The increased ductility of leached parts of the structure makes the plasticity description particularly good in those zones. This is shown by the good prediction of the effect the notch has on the force-displacement curve. However, the fracture dominated final strength cannot be reproduced by the model. This is a limitation of the model as fracture mechanisms are not yet considered.

- The leaching progress is in good agreement with the experimental data. The location of the Portlandite is predicted with great accuracy for the notched beams. Differences between leaching prediction and Schneider & Chen's experimental leaching data seem rather to be due to changing experimental conditions.

- The bending strength reduction over time in an unnotched beam is well predicted by the model-based simulations, provided the leaching simulations coincide with the experimental data. This capacity of the model is of particular interest in durability design calculations

in which the load bearing capacity of structures in different degradation scenarios needs to be evaluated. Such a design case is presented in the next chapter.

Chapter 11

Case Study: Durability Mechanics Performance of Ultra High Performance Concretes in Leaching

In this chapter we present a first durability design application: The mechanical performance of Ultra High Performance Concretes (UHPC) when subjected to leaching. The goal is to show the capacity of the model-based simulation in durability design. This application focuses on the materials-to-structures approach and discuses the effects of replacing ordinary concrete by UHPC. After a brief presentation of UHPC, the four-point bending tests simulations that were introduced in the third validation case (Section 10.5) are developed for UHPC and compared to ordinary concrete. Particularly the effect of the diffusion coefficient and the higher strength and stiffness of UHPC are discussed. The chapter closes with some recommendations on the durability design of concrete materials and structures.

11.1 UHPC Characteristics

Ultra High Performance Concretes (UHPC) are a new generation of concrete materials with a uniaxial compressive strength above 200 MPa and a uniaxial tensile strength of some 12 – 15 MPa. UHPC were developed in the 1990s to improve traditional concrete mixes with respect to four criteria: Material homogeneity, compactness, microstructure and ductility [123, 122].

Component	Mass Ratio	Dosage
Cement	1	713 kg / m^3
Silica Fume	.325	232 kg / m^3
Ground Quartz ($d_{50} = 4\,\mu$m)	.3	214 kg / m^3
Fine Sand ($d_{50} = 310\,\mu$m)	1.43	1019 kg / m^3
Steel Fibers	.275	196 kg / m^3
Superplasticizer	.018	43 kg / m^3
Water	.2	143 kg / m^3

Table 11.1: Mix Design of Ductal from [33]

An example of a commercially available UHPC is DUCTAL®, produced by Lafarge. A typical DUCTAL® mix design is given in Table 11.1 [33]. The low water cement ratio (here 0.2) leads to an important presence of unhydrated clinker (about 13 vol-%) in the material which translates into a high stiffness (Young's modulus of about 50 GPa). Moreover, the silica fume consumes all the Portlandite in the Pozzolanic reaction. This leads to a very homogeneous material. It has been found that the interface between aggregates and paste has properties similar to the bulk paste and no ITZ exists. The compactness is optimized through the well graded distribution of aggregates, both ground quartz and sand, as well as the unhydrated clinker. The porosity of DUCTAL® is about 5% with respect to water. This low value makes UHPC a more durable material: The diffusion coefficient of UHPC is very low. A typical value is $10^{-14}\,\mathrm{m}^2\,/\,\mathrm{s}$ [33] which is roughly 100 times smaller than for an ordinary $w/c = 0.5$ concrete. The durability performance, measured for example for calcium leaching through the propagation of the first dissolution front, should be much higher: The front moves roughly three times less for a given time than for an ordinary concrete [115], [98]. UHPC have a similar leaching behavior as ordinary concrete and the sharp dissolution fronts and the diffusion dominated front propagation have been observed for UHPC [98]. Due to the large amount of unhydrated clinker and the absence of Portlandite in UHPC, some modifications in the leaching behavior are observed. First, there exists no Portlandite front. Second, when the aggressive water from the outside diffuses into the UHPC matrix, while some C-S-H decalcify, the unhydrated clinker phases hydrate with the available water in the pore space [116]. This has a retarding effect on the leaching front propagation. However, if the supply of aggressive solution from the outside continues, eventually the hydration products will undergo the same leaching transformation as

an ordinary concrete [98].

11.2 Model-Based Leaching Prediction for UHPC

11.2.1 Model Parameters

The 40 mm ×40 mm ×160 mm beams that were simulated in section 10.5 are studied for a UHPC-material. Again, a two-dimensional section of the beam is modeled instead of the three-dimensional problem, and the same mesh (Figure 10-18) is employed. The boundary conditions read:

$$\text{On } \Gamma_{\overline{Ca}} = \left\{ \begin{array}{c} 0 \leq x \leq 20, y = 0;\ x = 20, 0 \leq y \leq 40; \\ 0 < x \leq 20, y = 40 \end{array} \right\} : \left[Ca^{2+}\right]_s = 4.5\,\text{mol}/\text{l} \tag{11.1}$$

$$\text{on } \Gamma_{\overline{q}} = \{x = 0, 0 < y \leq 40\} : \overline{q} = 0 \tag{11.2}$$

and the initial conditions:

$$\left[Ca^{2+}\right]_s (x, y, t \leq 0) = 8.0\,\text{mol}/\text{l} \tag{11.3}$$

where we assume that the calcium concentration available for a leaching reaction is equal to the equilibrium concentration of Portlandite. A higher initial concentration would contradict the Berner-curve (Figure 2-11). On the other hand, the absence of Portlandite reduces the leaching simulation to a one-front problem of the C-S-H front at C/S=1. The equilibrium conditions are unchanged from the calculations for ordinary concretes, because they are considered intrinsic to the C-S-H. The simulations are performed with a 6M ammonium nitrate solution. The equilibrium concentration for the front is recalled in Table 11.2. For the diffusion coefficient, the same dependency on the porosity is assumed as for ordinary concretes (Table 11.2), however due to the lower initial porosity, the effective diffusion coefficient is considerably smaller. The porosity in the unleached state is 11% and in the leached state it estimated to be 20%. This estimate accounts for the increase in porosity through the decalcification of C-S-H that was measured for ordinary concretes [28]; it is considered to be intrinsic for C-S-H. The unhydrated clinker is assumed to hydrate as the leaching proceeds, leading primarily to more C-S-H.

Leaching Simulation Input Data for UHPC	6 M solution
Portlandite Front	not considered-
C-S-H Front	$\left[Ca^{2+}\right]_s = 4.5\,\mathrm{mol/l}$ | $\left[Ca^{2+}\right]_f = 0.5\,\mathrm{mol/l}$
Initial porosity	$\phi_0 = 0.11$
Diffusion Coefficient	$D(\phi) = a\exp(b\phi)$
	with $a = 2.35 \times 10^{-13}\,\mathrm{m^2/s}$ and $b = 9.95$

Table 11.2: Input data for the leaching simulation of UHPC

11.2.2 Results

Figure 11-1 shows the calcium concentration evolution over time along the A-B cut (see Figure 10-18). It takes about 1,000 days for the C-S-H front to reach the center of the beam. This is roughly 10 times more than it takes the Portlandite front in an ordinary concrete to reach the center. This is in good agreement with the leaching velocities reported for UHPC [98]. Moreover, it is more than twice the time for the C-S-H front in an ordinary concrete to reach the center. Figure 11-2 shows the front movement in the beam section for different leaching times. The front initially has the rectangular shape of the beam section. When it is far away from the boundaries, it takes a circular shape.

11.2.3 Discussion

The difference in leaching times can be explained with the dimensionless variables of the one-dimensional leaching model presented in Chapter 3. For the C-S-H front they read:

$$\overline{[Ca^{2+}]} = \frac{[Ca^{2+}]}{[Ca^{2+}]^{eq}_{C-S-H}}; \xi = \frac{x}{2\sqrt{Dt}}; \varepsilon_{C-S-H} = \frac{\phi[Ca^{2+}]^{eq}_{C-S-H}\mathcal{M}_{Ca^{2+}}}{\Delta m_s} \tag{11.4}$$

Considering these invariants, two essential factors for the better leaching performance of UHPC can be stated. First, the absence of Portlandite determines whether a one- or a two-front problem exists; and it changes the equilibrium concentration, and thus the macroscopic solubility parameter in ε_{C-S-H}. Second, the lower porosity is an important factor for the leaching time. It intervenes directly through the value of ε_{C-S-H}, but also through a lower diffusion coefficient, $D = D(\phi)$, which changes the ξ value.

- The presence of Portlandite in ordinary cement-based materials appears detrimental for

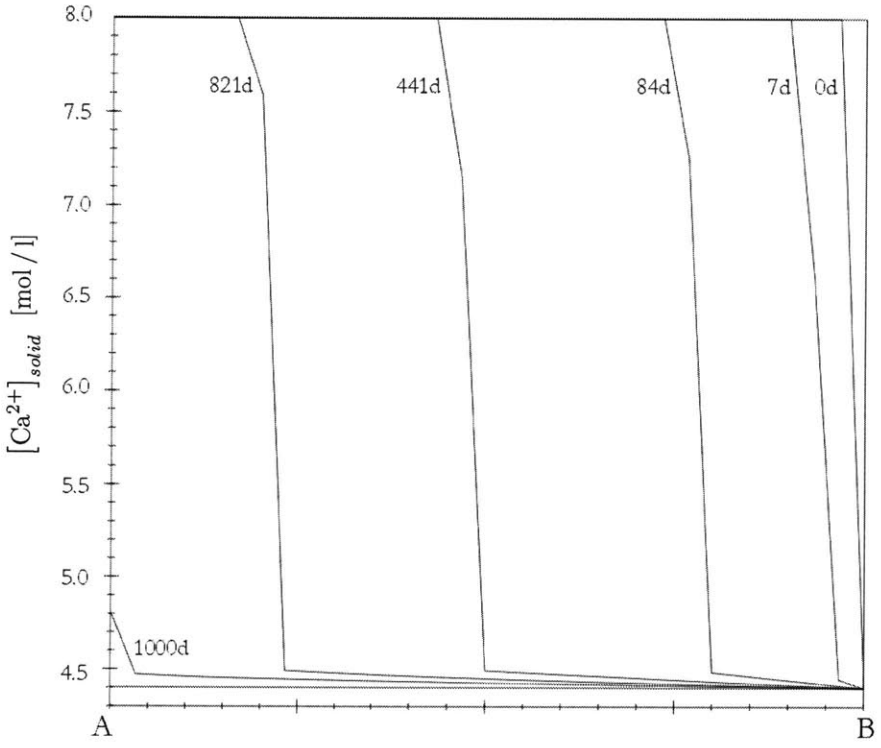

Figure 11-1: Calcium concentration at different times along the A-B section.

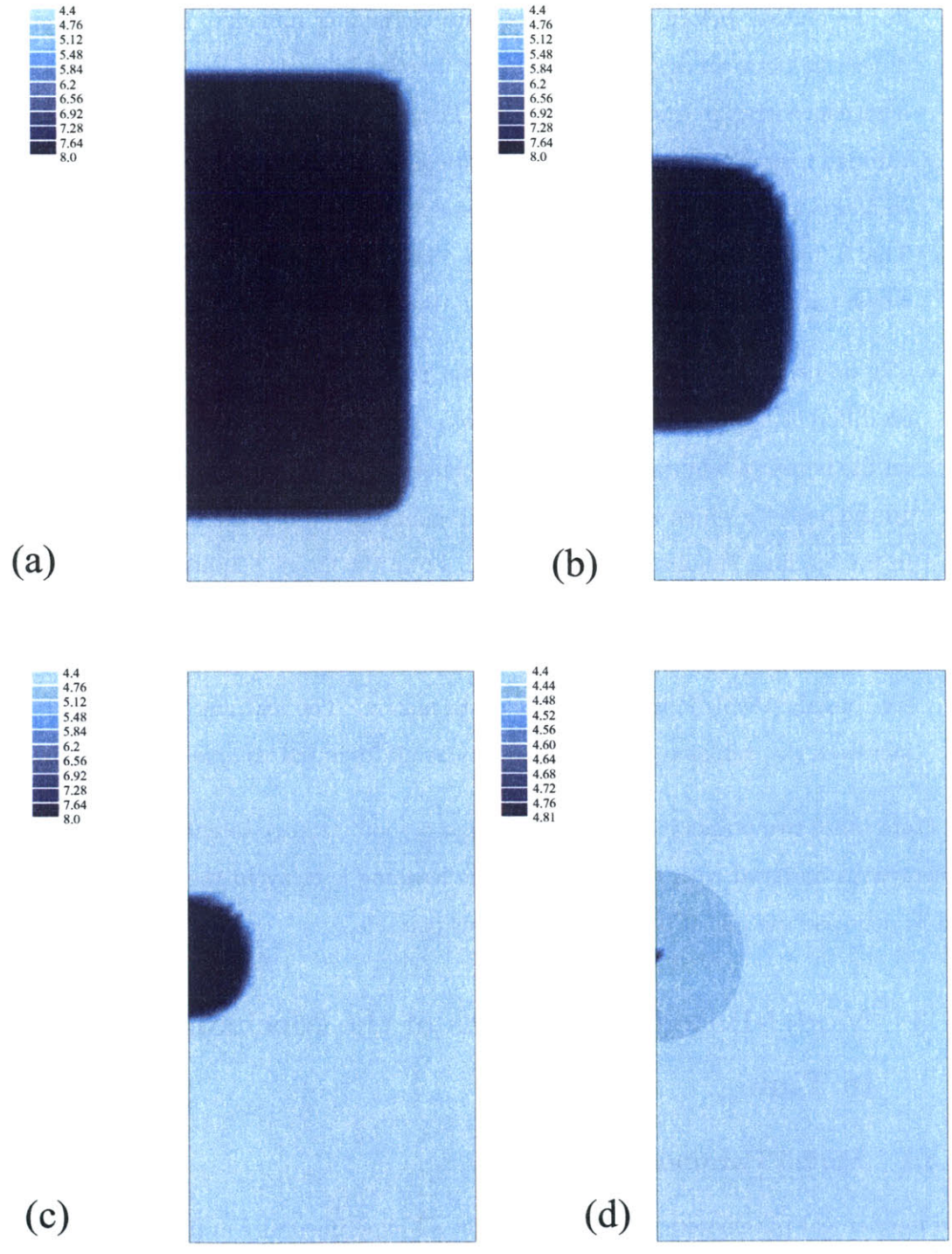

Figure 11-2: Solid calcium concentration in the UHPC leaching simulation. (a) 84 days, (b) 441 days, (c) 821 days and (d) 1000 days.

their leaching performance. The high equilibrium concentration of Portlandite leads to its dissolution before any other calcium containing mineral. The large concentration difference between aggressive water and Portlandite equilibrium concentration creates a high concentration gradient and a fast Portlandite dissolution front, expressed in (11.4) through a large ε_{CH} value. Portlandite therefore always leads to a fast first leaching front. In addition, the Portlandite crystals dissolve completely and create a large new porosity. This influences negatively the diffusion coefficient of the material. By contrast, UHPC, which have no Portlandite, overcome this drawback of traditional cement-based materials.

- The diffusion coefficient plays a dominant role in the total leaching time. Diffusion tests on different cementitious materials show a strong dependence of the diffusion coefficient on the porosity. Figure 11-3 shows the exponential dependency of the diffusion coefficient on the porosity which was proposed by Tognazzi [144]. It is the same function that is used in the leaching simulations (Eq. (9.75)). From the figure it appears that the value of the initial porosity as well as the increase through leaching can lead to vastly different diffusion coefficients. For example, the presence of Portlandite in an ordinary concrete accounts for roughly 15vol-% of the cement paste matrix. The leaching of Portlandite therefore increases the diffusion coefficient heavily as all its initial volume becomes porosity.

From these two points it becomes clear that a good strategy to enhance the durability of a cementitious material with respect to calcium leaching is to avoid the presence of Portlandite and to decrease the initial porosity as much as possible.

11.3 Model-Based Simulations of the Mechanical Performance in Time

11.3.1 Model Parameters

The mechanical parameters for UHPC are not all experimentally available. Some estimations based on the micromechanical modeling presented in Chapters 7 and 8 are necessary. These are presented in this subsection.

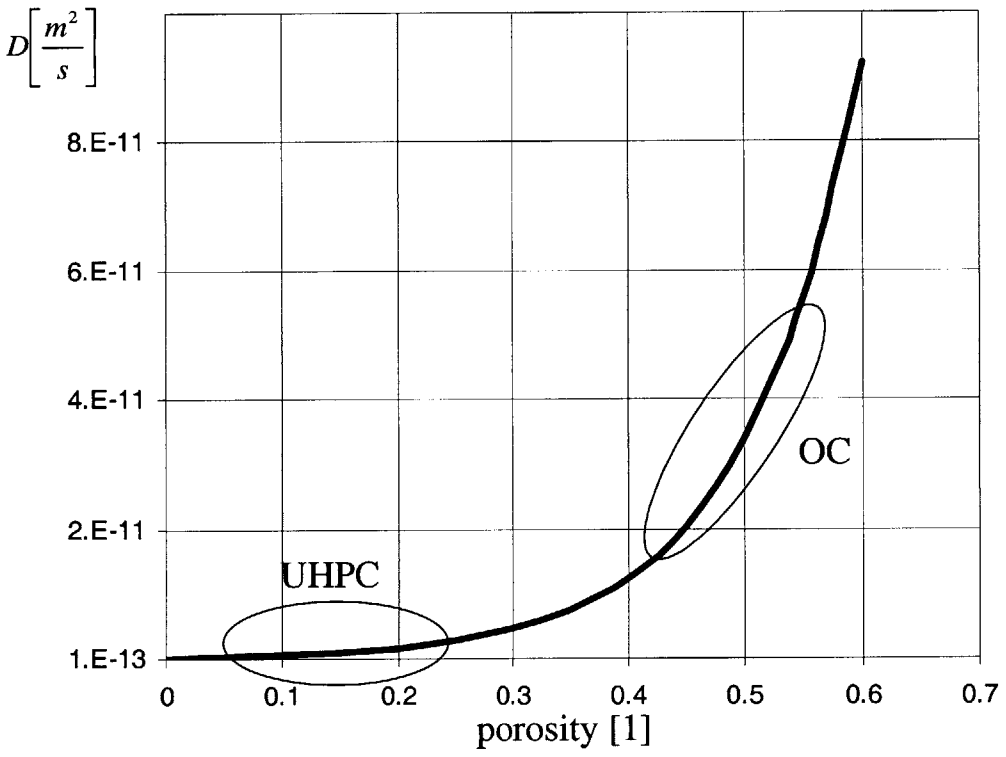

Figure 11-3: Exponential dependency of the diffusion coefficient on the porosity after tests from [3] and [144]. The ovals define the porosity domain in the matrix of Ultra-High-Performance Concretes (UHPC) and ordinary concretes (OC).

Undegraded	Input [GPa]	Output [GPa]
Level I	$E_\alpha = 21.7, E_\beta = 29.4$	$E^{est}_{\text{C-S-H}} = 23.0$
	$\nu_\alpha = \nu_\beta = 0.24$	$\nu^{est}_{\text{C-S-H}} = 0.24$
	$f_\alpha = 0.2, f_\beta = 0.8$	$k^{est}_{\text{C-S-H}} = 14.8$
		$\mu^{est}_{\text{C-S-H}} = 9.3$
Level II	$E_{\text{C-S-H}}, E_{\text{C}_3\text{S}} = 140, E_{\text{C}_2\text{S}} = 135, E_{\text{C}_3\text{A}} = 150,$	$E^{est}_{Paste} = 33.9$
	$E_{\text{C}_4\text{AF}} = 125, E_{\text{A}} = 23.8$	$\nu^{est}_{Paste} = 0.24$
	$\nu_{\text{C-S-H}}, \nu_{\text{C}_3\text{S}} = 0.3, \nu_{\text{C}_2\text{S}} = 0.3, \nu_{\text{C}_3\text{A}} = 0.3,$	$k^{est}_{Paste} = 21.8$
	$\nu_{\text{C}_4\text{AF}} = 0.3, \nu_{\text{A}} = 0.24$	$\mu^{est}_{Paste} = 13.6$
	$f_{\text{C-S-H}} = 0.52, f_{\text{C}_3\text{S}} = 0.15, f_{\text{C}_2\text{S}} = 0.13, f_{\text{C}_3\text{A}} = 0.05,$	
	$f_{\text{C}_4\text{AF}} = 0.01, f_{\text{A}} = 0.1, f_{voids} = 0.04$	
Level III	$E_{paste}, E_{agg.}, \nu_{paste}, \nu_{agg.}, f_{paste}, f_{agg.}$	$E^{est}_{UHPC} = 46.2$
		$\nu^{est}_{UHPC} = 0.22$

Table 11.3: Micromechanical modeling of the elastic properties for UHPC in the unleached state for Levels I and II

Elasticity

The elastic properties of UHPC are estimated using the three level homogenization scheme presented in Section 7.2. Based on hydration models [17], the C-S-H_α are estimated to form 80% of the C-S-H matrix. Roughly 13vol-% of the total volume are unhydrated clinker[2]. At Level III no ITZ is considered. The application of equations (7.10) through (7.17) and (7.24) through (7.26), respectively leads to a Young's modulus for the intact UHPC of $E_0 = 46.2\,\text{GPa}$, which is on the order of 50 GPa reported in the literature [2]. Table 11.3 gives the details of the parameter values for the undegraded homogenization procedure at Levels I through III.

As no Portlandite is present, there is no intermediate leaching state. For the asymptotic leaching state we assume that all the clinkers are hydrated to C-S-H and then leached. The C-S-H distribution is assumed unchanged. The porosity created through leaching is assumed to be 10% with respect to the total paste volume and localized on Level II of the microstructure. No ITZ is considered and a Young's modulus of $E_\infty = 9.3\,\text{GPa}$ is obtained for the overall asymptotic stiffness. The details are given in Tables 11.4. Accordingly, the reduction in stiffness is almost 80% which is somewhat more than for ordinary concrete. However, the absolute value in the asymptotic state is still considerably higher than for ordinary concrete. The absence of the ITZ and the smaller porosity, due to the absence of Portlandite, are beneficial for the stiffness.

Degraded	Input [GPa]	Output [GPa]
Level I	$E_\alpha = 3.0, E_\beta = 12.0$	$E^{est}_{\text{C-S-H}} = 3.8$
	$\nu_\alpha = \nu_\beta = 0.24$	$\nu^{est}_{\text{C-S-H}} = 0.24$
	$f_\alpha = 0.2, f_\beta = 0.8$	$k^{est}_{\text{C-S-H}} = 2.4$
		$\mu^{est}_{\text{C-S-H}} = 1.5$
Level II	$E_{\text{C-S-H}}$	$E^{est}_{Paste} = 2.9$
	$\nu_{\text{C-S-H}}$	$\nu^{est}_{Paste} = 0.23$
		$k^{est}_{Paste} = 1.8$
	$f_{\text{C-S-H}} = 0.87, f_{voids} = 0.13$	$\mu^{est}_{Paste} = 1.2$
Level III	$E_{paste}, E_{agg.}, \nu_{paste}, \nu_{agg.}, f_{paste}, f_{agg.}$	$E^{est}_{UHPC} = 9.3$
		$\nu^{est}_{UHPC} = 0.20$

Table 11.4: Micromechanical modeling of the elastic properties for UHPC in the leached state for Levels I and II

Strength Parameters

For the mechanical calculations, the following hypothesis are made[1]:

- $\mathcal{H}1$: The strength of UHPC can be described by the combination of the Drucker-Prager and Cam-Clay surfaces introduced in Section 6.7.2. More sophisticated strength descriptions of UHPC were developed by Chuang [35], but are not considered here.
- $\mathcal{H}2$: The micromechanical strength estimates can be applied to UHPC.

Based on these two hypothesis, we determine the parameters of the strength laws. From the uniaxial compressive strength of 200 MPa and the uniaxial tensile strength of 11.5MPa provided by Cheyrezy [33], we deduce from (5.32) the Drucker Prager model parameters $\delta_{DP} = 1.56$ and $c_{DP} = 12.6\,\text{MPa}$.

For the Cam-Clay surface, we determine the slope of the critical state line, M, with the help of the friction enhancement estimates in Section 8.2. Based on the experimental value of the Level II paste ($M_{II} = 1.42$) we estimate the friction coefficient of the C-S-H matrix with (8.31), which yields $M_I = 1.16$. Upscaling twice using (8.28), first taking the unhydrated clinker as grains (Level II) and then the aggregates (Level III) leads to $M_{UHPC} = 2.77$. The

[1]Note that for UHPC some effects of leaching on the mechanical properties have not been studied experimentally yet. While we use reasonable approximations, in the absence of experimental evidence it should be noted that this Chapter is rather a demonstration of the capacity of the model-based simulation for durability design than a final analysis of the durability performance of UHPC.

Material Parameters	Intact	Asymp. Leached
δ_{DP} [1]	1.56	0.78
c_{DP} [MPa]	12.6	1.0
M [1]	2.77	2.03
p_t [MPa]	6.2	1.7
p_c^0 [MPa]	149.7	2.0
λ [1]	0.01	0.01
κ [1]	0.05	0.05

Table 11.5: Mechanical Input Parameters for UHPC

analogous procedure in the asymptotically degraded state leads to $M = 2.03$. For the δ and c in the degraded state, equivalent calculations can be made with (8.31) and (8.28) for the friction coefficient, and with (8.44) and (8.47) for the cohesion. Table 11.5 summarizes the values for the intact and the asymptotically degraded state. Finally, p_t and p_c^0 are calculated from the previously determined values using (9.61). For the parameters λ and κ of the Cam-Clay hardening, we assume the same values as for concrete [32].

Boundary Conditions and Loading

The boundary conditions and loading for the beam section are identical to the third validation case (Section 10.5). The symmetry of the beam requires as boundary condition:

$$u_x(x = 0, y) = 0 \tag{11.5}$$

The employed mesh and loading are as in Figure 10-23. In the same way as for the third validation example, equations (10.18) through (10.21) are applied to calculate the bending problem in the two-dimensional section.

11.3.2 Results and Comparison with Ordinary Concrete

Figure 11-4 displays the decay of the bending strength for UHPC and ordinary concrete (OC). The data for ordinary concrete corresponds to the experimental results of Schneider & Chen. The bending strength decay is expressed as the ratio of the maximum bending moment that can be applied relative to the intact bending moment of the OC. The initial bending strength of the UHPC is more than three times the bending strength of OC. This is primarily due to

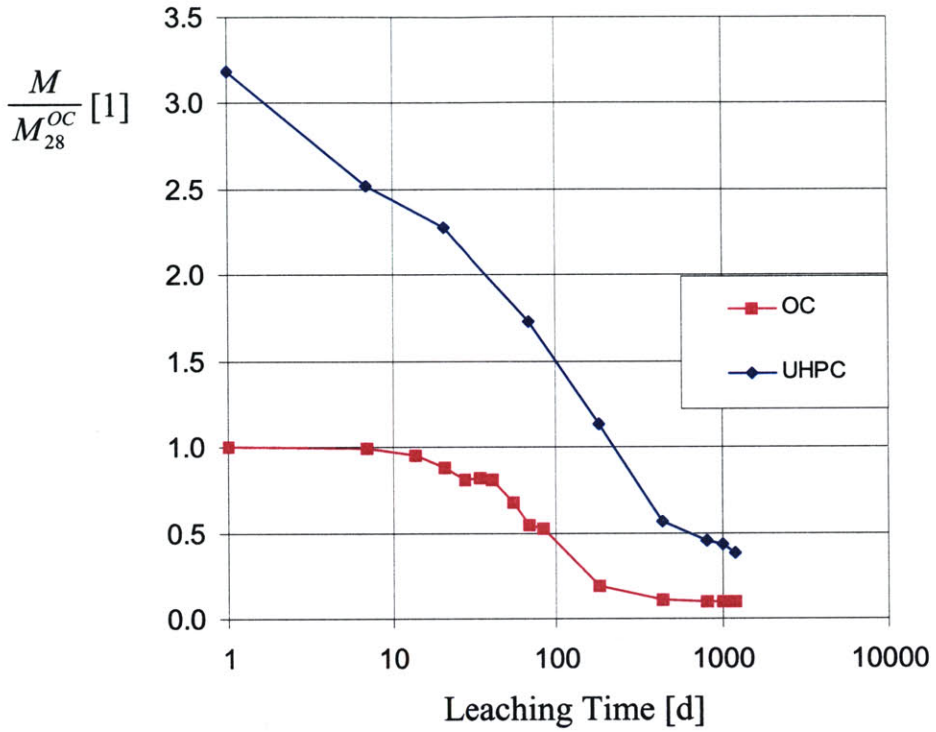

Figure 11-4: Comparison in bending capacity with leaching time of UHPC and ordinary concrete (OC).

the higher tensile strength of UHPC. The reduction in bending strength of the UHPC is very rapid with degradation time: After roughly 100 days, only 50% of the initial bending capacity is left. This shows that the strength reduction with leaching is very strong when the leaching front (Figure 11-1) has not progressed to more than 40% of the section. It is also interesting to note that the residual bending strength of the UHPC remains at around 35% of the OC initial bending strength or roughly three times higher than the residual OC bending strength.

Figure 11-5(a) shows the distribution of Σ_{zz}, the stress in the beam axis, at the maximum applied moment on the intact material. The maximum tensile and compression values show clearly that the tensile strength is the limiting factor in bending loading. For comparison, the Σ_{zz} distribution is plotted for the UHPC beam after 70 days of leaching in Figure 11-5(b). In the leached parts of the section, the tensile stress is limited to 1.4 MPa which leads to the steep reduction in overall bending strength observed in Figure 11-4. Finally for the asymptotically

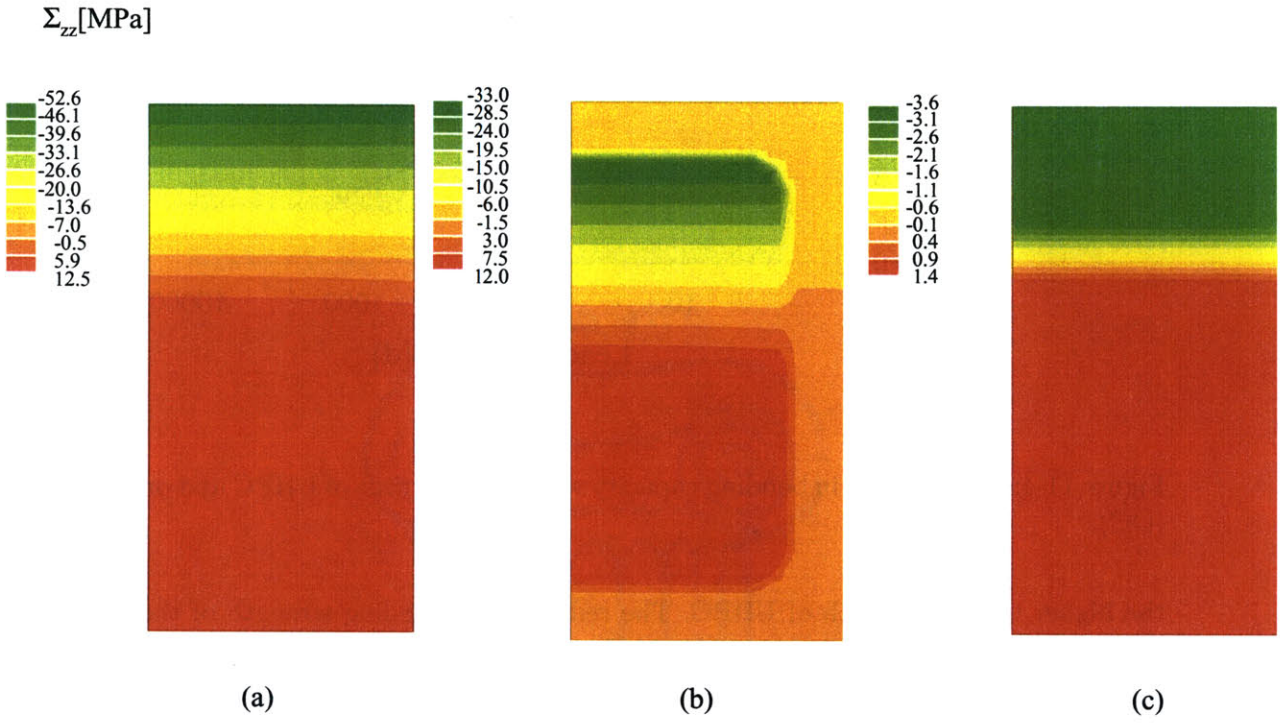

Figure 11-5: Σ_{zz} distribution at the maximum bending capacity for different leaching times. (a) intact, (b) 70 days of leaching, (c) 1200 days of leaching (asymptotically leached).

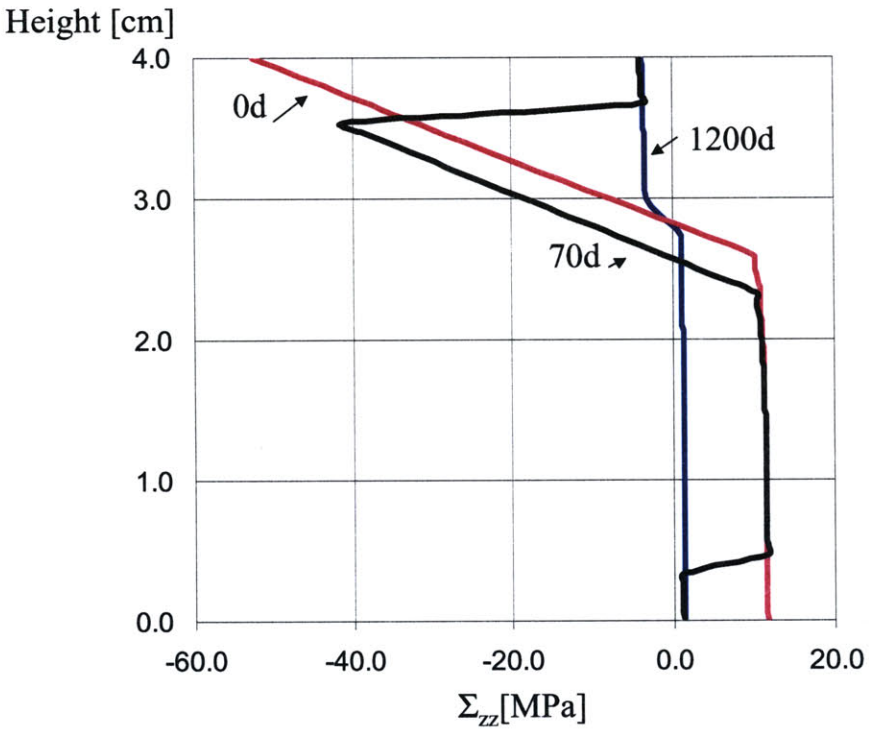

Figure 11-6: Σ_{zz} distribution at $x = 0$ for the maximum bending moment. Leaching times are 0 days (intact), 70 days and 1200 days (asymptotically leached).

leached section, the Σ_{zz} stresses are plotted in Figure 11-5(c). The large reduction of the strength by leaching both in the compression and tensile domain allows for only a small bending strength. Figure 11-6 displays the Σ_{zz} distribution along $x = 0$. The stress distribution changes very much with leaching and underscores the prior remarks.

The comparison of the OC and UHPC bending strength evolution shows that the relative decrease in time is similar for both materials. In both cases roughly 10% of the initial bending capacity remains, once the material is asymptotically leached. Besides the time-scale effects due to the leaching properties of UHPC, the important difference from a mechanical point of view is the increased strength of UHPC. From Figure 11-4, an inverse analysis for the time stability of a structure can be made. For a desired bending capacity, a residual life-time for OC and UHPC structures can be deduced. If for example a 50% bending moment capacity is desired then the life times are ~90days for OC and ~750 days for UHPC, respectively. This highlights how the employment of UHPC can lead to a substantial increase of the durability performance of concrete structures subjected to leaching.

11.4 Chapter Summary and Design Recommendations

In this chapter, the durability performance with respect to calcium leaching of UHPC has been analyzed by means of model-based simulations. This case study shows the capacity of the model-based simulations to make predictions about leaching times and strength evolution. The model-based simulations of leaching show that UHPC has a roughly ten times slower leaching rate. This is due to the absence of Portlandite and the lower initial porosity which is reflected also in the smaller diffusion coefficient. The invariants of the leaching model help to explain these origins of increased leaching resistance.

Estimates about the strength evolution of UHPC with leaching, involving the micromechanical approach developed in Chapters 7 and 8 are developed. Using these values in model-based simulations, the decay of the bending strength with time was estimated. This decay is rapid, due to the assumed large strength loss as leaching occurs. When compared with ordinary concretes, however, a service life time increase by a factor of about eight is obtained.

Based on the model-based simulations in this chapter, some recommendations for the design

of concretes that are subjected to leaching can be made:

- Increasing the leaching time. To achieve a slower leaching rate, the UHPC strategy should be followed. The absence of Portlandite reduces the concentration gradient that drives the diffusion Eq. (11.4). In addition, a lower increase in chemical porosity is obtained which reduces the increase in the diffusion coefficient. In addition, a compact microstructure with low initial porosity is obtained in the absence of Portlandite. The resulting low diffusion coefficient translates directly into longer leaching times.

- Increasing the asymptotic strength. Another strategy to enhance the durability performance can be to increase the strength of the asymptotically leached materials. Similarly to the leaching time, this quest is related to the minimization of the increase in chemical porosity. In addition, a more homogeneous material (i.e. without Portlandite) will perform better from a mechanical point of view.

This shows that, ultimately, both aspects a very much related: The more compact microstructure will perform better both from a diffusion and a mechanical point of view.

Part V

Conclusions & Perspectives

Chapter 12

Conclusions and Perspectives

This chapter presents a summary of this durability mechanics study of cement-based materials subjected to calcium leaching. In addition, conclusions are drawn underlining the main findings of the study. Based on the findings, some future research is proposed and perspectives on the durability mechanics of calcium leaching are given.

12.1 Summary and Conclusions

The durability mechanics study on cement-based materials revealed the following scientific findings about the leaching mechanisms and the mechanical performance, both at a material and a structural level:

- The microstructural analysis showed the characteristic multiscale structure of cement-based materials. A three-level division was proposed and used as a framework throughout the study.
- The effects of calcium leaching on the microstructure were analyzed through a combination of analytical techniques including chemical analysis, SEM and porosity measurements, as well as results available in the literature. It was found that the main aspects of calcium leaching from a chemical and a mechanical point of view can be traced by considering only the Portlandite and the C-S-H with a C/S ratio of one.
- As a consequence, for the leaching problem, a two-front modeling approach was developed.

A one-dimensional dissolution-diffusion model considering these two fronts was derived and used as a design tool for an accelerated leaching device, based on an ammonium nitrate solution. The developed accelerated leaching device is simple to operate and leads to an almost 300-fold acceleration of the leaching process. In addition, it can be used to compare the leaching performance of different cement-based materials.

- Asymptotically leached cement pastes and mortars were tested in multiaxial compression and uniaxial tension tests. From these tests the strength envelope for leached materials was obtained. In addition, the deformation behavior for asymptotically leached materials was studied. The experimental approach quantified the strength loss associated with calcium leaching. It showed that the change in strength is fundamentally different in high and low confinement. Moreover, the capacity of leached materials to undergo large plastic deformation was revealed along with the increase in ductility. Leached materials were shown to be sensitive to the fluid pressure in their pore space: Undrained loading situations can eliminate the frictional performance of leached pastes and mortars.

- The experimental inaccessibility of the intermediate leaching state in which only Portlandite is dissolved as well as the difference in strength of pastes and mortars was the motivation for the use of continuum micromechanics in the material analysis. Based on the three-level microstructure, the micromechanical tools for the homogenization of the elastic and poroelastic properties were introduced. It was shown through the estimation of the Biot coefficient, that for undegraded mortars and pastes no effect of the pore pressure has to be considered. On the other hand, asymptotically leached materials are influenced by the pore pressure, but the values of the Biot coefficient showed that the effective stress concept is not entirely valid for elasticity. This micromechanical result confirmed that the observed validity of the effective stress concept in the strength tests is related to the strength properties. The micromechanical estimation of the Biot modulus showed that the leaching process has a strong reducing influence, which makes leached materials sensitive to undrained loading situations. Furthermore, estimates for the frictional coefficient and the cohesive strength were developed. With these tools the strength relations between pastes and mortars could be clarified. In addition the role of the ITZ

on the mortar cohesion was quantified. Moreover, predictive formulas for the strength in the intermediate leaching state were developed. The micromechanical approach for the cohesion is a new contribution to the field of micromechanics.

- Based on the experimental and micromechanical approaches, a constitutive model for cement-based materials subjected to calcium leaching was developed. The model is a macroscopic poromechanical approach but based in its formulation on a microscopic analysis of the sources of dissipation. What is new is the identification of the chemical porosity as a state variable. The model combines the dissolution-diffusion and the mechanical aspects of calcium leaching durability mechanics and bridges between the leaching states. This includes the three-dimensional dissolution-diffusion model for two fronts and the chemoporoplastic constitutive law.

- The model is implemented in a commercial finite element code and validated through comparison with experimental data for three different cases. The validation shows the capacity of the material model to improve the understanding of experimental results at the scales of structures.

- In a case study of the durability performance of UHPC, the usefulness of the model-based simulations was shown. The sources of improved leaching resistance could be identified and quantified: The absence of Portlandite and the lower porosity. In addition, the performance in time under a mechanical loading can be compared for different materials and leaching conditions. This makes the model-based simulations a great durability mechanics design tool: Design decisions and maintenance plans on existing structures can be developed with the help of model-based simulations.

In this study several new elements have been developed. They include:

1. The experimental data on multiaxial strength and deformation behavior of leached cement pastes and mortars.

2. The micromechanical estimates for the Biot coefficient and modulus and the micromechanical strength estimate for the cohesion.

3. The constitutive model based on the chemical porosity as state variable.

But the most important contribution lies perhaps in the combination of analysis techniques that are employed in this durability mechanics study. They involve on the one hand application and/or use of results from sophisticated materials science analysis techniques such as SEM, XRD, XRF, SANS and NMR. On the other hand modeling techniques involving micromechanics and macro-poromechanics are used to enhance the understanding of experimental results and provide the basis for model-based simulations.

12.2 Industrial Benefits

The durability of concrete is a concern for all types of infrastructure elements. Particularly, applications with long lifetimes are vulnerable to calcium leaching. In this context, this study provides some industrial benefits:

- The experimental study on leached pastes and mortars showed that residual multiaxial strength can be taken into account in the design of structures. This can have a considerable economic impact, as presently the leached material is considered to have no strength.
- The micromechanical developments can be used for an optimized mix-design of cement-based materials subjected to calcium leaching.
- The finite element application is a powerful durability design tool. It can be used for the design of new structures and the lifetime analysis of existing structures.

12.3 Suggestions for Future Research

From the analysis of the material properties at the three levels of microstructure it emerged that the description of strength at Level I can be improved. The strength on Level I of the microstructure needs to be investigated experimentally. Recently, nanoindentation was successfully applied to the strength analysis of metals. The development of this method for cement-based materials has a great potential.

In the macroscopic strength description, fracture dominated failure can be introduced. At this time, clearly the non-consideration of fracture is a limiting factor for the application of the model. To address this challenge, a reliable fracture test for leached materials needs to be developed. In addition, an extension of the strength description needs to be developed which incorporates the fracture parameters.

In addition, the model could be extended to account for creep behavior of cement-based materials at different leaching states. Some first experimental results on asymptotically leached materials were provided by Bernard et al.[16].

The diffusion properties of cement-based materials are essential for the kinetics of leaching. The experimental data available in the open literature provide strongly varying results, which often limit the accuracy of the model-based prediction. A reliable diffusion property test needs to be developed.

12.4 Perspectives

The durability of concrete subject to calcium leaching is one of the important concerns for an increasingly old civil infrastructure. The results of this study can assist managing security of these structures and assessing the corresponding financial implications. From a materials science perspective, the increased knowledge about the degradation of cement-based materials is in itself also helpful for the design of new materials such as UHPC. Besides, a durable material will always also be a mechanically well performing material. Durability design and optimization of mechanical performance are not conflicting goals.

This study was motivated in part by the needs of nuclear waste storage projects. In nuclear waste storage, structural lifetimes beyond several hundred years are required. The tools developed in this study allow "looking into the future" at the expected material and structural performance over time. The degradation predictions are particularly useful during the lifetime of existing structures to estimate security risks and optimize intervention plans. A clear understanding of the potential problems arising from the durability of current containment solutions is important for the safe operation of future nuclear waste storage sites. Understanding these is prudent foresight, even though historical parallels might suggest the technologies available in

some hundred years may make today's approaches out of date.

Bibliography

[1] Britannica online. http://www.britannica.com.

[2] Acker, P. Micromechanical analysis of creep and shrinkage mechanisms. In: Ulm, F.-J., Bazant, Z., and Wittmann, F., Editors, *Proc. Creep, Shrinkage and Durability Mechanics of Concrete and other Quasi-Brittle Materials, CONCREEP-6@MIT*, pages 15–25, Cambridge, MA, 2001. Elsevier, Oxford UK.

[3] Adenot, F. *Durabilité du béton: Caractérisation et Modélisation des Processus Physiques et Chimiques de Dégradation du Ciment.* PhD thesis, University of Orleans, France, 1992. In French.

[4] Adenot, F. and Buil, M. Modeling of the corrosion of the cement by deionized water. *Cement and Concrete Research*, 22(4):451–457, 1992.

[5] Arulanandan, K. and Scott, R., Editors. *Proceedings of the International Conference on the Verification of Numerical Procedures for the Analysis of Soil Liquefaction Problems*, Davis, CA, 1994. A.A. Balkema, Rotterdam.

[6] ASTM. *C496-96, Standard Test Method for Splitting Tensile Strength of Cylindrical Concrete Specimens*, 1996.

[7] ASTM. *E290-97a Standard Test Method for Bend Testing of Material for ductility*, 1997.

[8] ASTM. *C39-01 Test Method for Compressive Strength of Cylindrical Concrete Specimens*, 2001.

[9] ASTM. *C78-02 Standard Test Method for Flexural Strength of Concrete (Using Simple Beam with Third-Point Loading)*, 2002.

[10] Barnes, B. D., Diamond, S., and Dolch, W. L. Micro-morphology of the interfacial zone around aggregates in portland-cement mortar. *Journal of the American Ceramic Society*, 62(1-2):21–24, 1979.

[11] Baroghel-Bouny, V. *Caractérisation des pâtes de ciment et des bétons. Méthodes, analyse, interprétations.* PhD thesis, ENPC, France, 1994. Published as LCPC Research Report ref. CARPAT, 1995. In French.

[12] Bassett, H. Notes on the system lime-water, and on the determination of calcium. *Journal od the Chemical Society*, 29:1999–2003, 1934.

[13] Bažant, Z. and Planas, J. *Fracture and Size Effect in Concrete and Other Quasibrittle Materials.* CRC Press, 1998.

[14] Beaudoin, J. Comparison of mechanical properties of compacted calcium hydroxide and portland cement paste systems. *Cement and Concrete Research*, 13:319–324, 1983.

[15] Beaudoin, J. and Feldman, R. Dependence of degree of silica polymerization and intrinsic mechanical properties of C-S-H on C/S. In: *8th International Congress on the Chemistry of Cement*, pages 1–6, Rio de Janeiro, 1986.

[16] Bernard, O., Ulm, F.-J., and Germaine, J. Volume and deviator basic creep of calcium-leached cement-based materials. *Cement and Concrete Research*, 2002. Submitted for publication.

[17] Bernard, O., Ulm, F.-J., and Lemarchand, E. A multiscale micromechanics-hydration model of early-age elastic properties of cement-based materials. *Cement and Concrete Research*, 2002. Submitted for publication.

[18] Berner, U. R. Modelling the incongruent dissolution of hydrated cement minerals. *Radiochimica Acta*, 44/45:387–393, 1988.

[19] Biot, M. General theory of three-dimensional consolidation. *Journal of Applied Physics*, (12):155–164, 1951.

[20] Bishop, A. The influence of an undrained change in stress on the pore pressure in porous media of low compressibility. *Geotechnique*, 23(3):435–442, 1973.

[21] Bishop, A. and Henkel, D. *The Measurement of Soil Properties in the Triaxial Test.* Edward Arnold, London, 2nd edition, 1962.

[22] Bishop, A. and Hight, D. The value of poisson's ratio in saturated soils and rocks stressed under undrained conditions. *Geotechnique*, 27(3):369–384, 1977.

[23] Bogue, R. *La chimie du ciment Portland.* Editions Eyrolles, Paris, 1952.

[24] Borja, R. and Lee, S. Cam-clay plasticity, part i: Implicit integration of elasto-plastic constitutive relations. *Computer Methods in Applied Mechanics and Engineering*, 78:49–72, 1990.

[25] Bourdette, B. *Durabilité du mortier: Prise en compte des auréoles de transition dans la caractérisation et la modélisation des processus physiques et chimiques d'altération.* PhD thesis, INSA Toulouse, France, 1994. In French.

[26] Brough, A., Dobson, C., Richardson, I., and Groves, G. Application of selective 29si isotopic enrichment to studies of the structure of calcium silicate hydrates (C-S-H). *Journal of the American Ceramic Society*, 77(2):593–596, 1994.

[27] de Buhan, P. and Dormieux, L. On the validity of the effective stress concept for assessing the strength of saturated porous materials: A homogenization approach. *Journal of the Mechanics and Physics of Solids*, 44(10):1649–1667, 1996.

[28] Carde, C. *Caractérisation et Modélisation de l'Alteration des Proprietés Mécaniques due à la Lixiviation des Matériaux Cimentaires.* PhD thesis, INSA Toulouse, 1996. In French.

[29] Carde, C. and Francois, R. Effect of the leaching of calcium hydroxide from cement paste on mechanical and physical properties. *Cement and Concrete Research*, 27(4):539–550, 1997.

[30] Carde, C. and Francois, R. Modelling the loss of strength and porosity increase due to the leaching of cement paste. *Cement and Concrete Composites*, (21):181–188, 1998.

[31] Carde, C., Francois, R., and Torrenti, J. Leaching of both calcium hydroxide and C-S-H from cement paste: Modeling the mechanical behavior. *Cement and Concrete Research*, 26(8):1257–1268, 1996.

[32] Chen, W. and Han, D. *Plasticity for structural engineers.* Springer Verlag, New York, 1988.

[33] Cheyrezy, M. Leaching of ultra high performance concrete ductal^{tm}. Powerpoint Presentation, MIT Workshop on Durablity of Cementitious Materials, 2000.

[34] Christensen, R. *Mechanics of Composite Materials.* John Wiley and Sons, New York, 1979.

[35] Chuang, E. *Ductility Enhancement of High Performance Cementitious Composites and Structures.* PhD thesis, MIT, 2002. Published as MIT-CEE Report 02-2.

[36] Consoli, N., Prietto, D., and Ulbrich, L. Influence of fiber and cement addition on behavior of sandy soil. *Journal of Geotechnical and Geoenvironmental Engineering*, 124(12):1211–1214, 1998.

[37] Constantinides, G. The elastic properties of calcium leached cement pastes and mortars: A multi-scale investigation. MSc thesis, MIT, 2002. Published as MIT-CEE Report 02-1.

[38] Constantinides, G. and Ulm, F.-J. The effect of two types of C-S-H on the elasticity of cementbased materials: results from nanoindentation and micromechanical modeling. *Cement and Concrete Research*, 2002. Submitted for publication.

[39] Cory, D., 2002. Personal Communication.

[40] Cotterell, B. and Mai, Y.-W. *Fracture Mechanics of Cementitious Materials.* Blackie Academic & Professional, Glasgow, 1996.

[41] Coussy, O. *Mechanics of porous continua.* Wiley, Chichester, 1995.

[42] Coussy, O. and Ulm, F.-J. Creep and plasticity due to chemo-mechanical couplings. *Archive of Applied Mechanics*, 66(8):523–535, 1996.

[43] Diamond, S. Aspects of concrete porosity revisited. *Cement and Concrete Research*, 29(8):1181–1188, 1999.

[44] Doerner, M. F. and Nix, W. D. A method for interpreting the data from depth sensing indentation instruments. *J. Mater. Res.*, 1:601–609, 1986.

[45] Dormieux, L. Apport des méthodes de changement d'échelle à la résolution de quelques problèmes de mécanique des milieux poreux. In: *Actes du Séminaire Descartes.* Presse des Ponts, 1999.

[46] Dormieux, L., Molinari, A., and Kondo, D. Micromechanical approach to the behavior of poroelastic materials. *Journal of the Mechanics and Physics of Solids*, (10):2203–2231, 2002.

[47] Eberhardsteiner, J., Meschke, G., and Mang, H. Triaxiales konstitutives modellieren von beton. Technical report, TU Wien Institut fuer Festigkeitslehre, 1987. In German.

[48] Eshelby, J. D. The determination of the elastic field of an ellipsoidal inclusion. *Proc. R. Soc. London A*, 241:376–392, 1957.

[49] Faucon, P. *Durabilité du béton: Physico-Chimie de l'Altération par l'Eau.* PhD thesis, University of Cergy-Pontoise, France, 1997. In French.

[50] Faucon, P., Adenot, F., Jacquinot, J., Petit, J., Cabrillac, R., and Jorda, M. Long-term behaviour of cement pastes used for nuclear waste disposal:review of physio-chemical mechanisms of water degradation. *Cement and Concrete Research*, 28(6):847–857, 1998.

[51] Faucon, P., Delagrave, A., Petit, J., Richet, C., Marchand, J., and Zanni, H. Aluminum incorporation in calcium silicate hydrate (c-s-h) depending on their ca/si ratio. *Journal of Physical Chemistry B*, 103:7796–7802, 1999.

[52] Feldman, R. F. and Sereda, P. J. A model for hydrated portland cement paste as deduced from sorption-length change and mechanical properties. *Materials and Structures*, 1(6):509–19, 1968.

[53] Fried, I. and Malkus, D. Finite element mass matrix lumping by numerical intergation with no convergence rate loss. *International Journal of Solids and Structures*, 11:461–466, 1975.

[54] Galle, C. Personal communication. 2002.

[55] Gassmann, F. Ueber die elastizitaet poroeser medien. *Vierteljahresschrift der Naturforschenden Gesellschaft in Zuerich*, (96):1–23, 1951. In German.

[56] Gérard, B. *Contribution des couplages mécanique-chimie-transfert dans la tenue à long terme des ouvrages de stockage des déchets radioactifs.* PhD thesis, ENS Cachan, France, 1996. In French.

[57] Giannakopoulos, A. E., Larsson, P. L., and Vestergaard, R. Analysis of vickers indentation. *International Journal of Solids and Structures*, 31(19):2679–2708, 1994.

[58] Green, S. and Swanson, S. Static constitutive relations for concrete. Technical Report AFWL-TR-72-244, Air Force Weapons Laboratory, Albuquerque, NM, 1973.

[59] Grenthe, I. *Chemical Thermodynamics of Uranium.* North-Holland, Amsterdam, 1992.

[60] de Groot, S. R. and Mazur, P. *Non-Equilibrium Thermodynamics.* Dover Publisher, New York, 1984.

[61] Hamid, S. A. The crystal-structure of the 11-A natural tobermorite $Ca_{2.25}[Si_3O_{7.5}(OH)_{1.5}].1H_2O$. *Zeitschrift Fur Kristallographie*, 154(3-4):189–198, 1981.

[62] Hashin, Z. and Monteiro, P. An inverse method to determine the elastic properties of the interphase between the aggregate and the cement paste. *Cement an Concrete Research*, 32:1291–1300, 2002.

[63] Heidug, W. Intergranular solid-fluid phase transformations under stress: The effect of surface forces. *Journal of Geophysical Research*, 100(B4):5931–5940, 1995.

[64] Hencky, H. Ueber die form des elastizitaetsgesetzes bei ideal elastischen stoffen. *Zeitschrift fuer Technische Physik*, 9(457):215–220, 1928.

[65] Hervé, E. and Zaoui, A. n-layered inclusion-based micromechanical modelling. *International Journal of Engineering Science*, 31(1):1–10, 1993.

[66] Hewlett, P., Editor. *Lea's Chemistry of Cement and Concrete.* Arnold, London, 4th edition, 1998.

[67] Hinton, E., Rock, T., and Zienkiewicz, O. A note on mass lumping and related processes in the finite element method. *Earthquake Engineering and Structural Dynamics*, 4:245–249, 1976.

[68] Hofstetter, G. and Taylor, R. Treatment of the corner region for drucker-prager type plasticity. *Zeitschrift fuer Angenwandte Mathematik und Mechanik*, 71(6):589–591, 1991.

[69] Hughes, T. *The Finite Element Method.* Prentice-Hall, Englewood Cliffs, NJ, 1987.

[70] Hugoniot, H. Sur la propoagation du mouvement dans les corps et spécialement les gaz parfaits. *Journal de l'Ecole Polytechnique*, (58):1–125, 1889.

[71] Humbert, P. Cesar-lcpc : un code général de calcul par éléments finis. *Bulletin de liaison des Laboratoires des Ponts et Chaussées*, (160):112–115, 1989.

[72] Ishai, O. and Bodner, R. Limits of linear viscoelasticity and yield of a filled and unfilled epoxy resin. *Transactions of the Soc. Rheology*, 14(2):253–273, 1970.

[73] Ismael, N. and Mollah, M. Leaching effects on properties of cemented sands in kuwait. *Journal of Geotechnical and Geoenvironmental Engineering*, 124(10):997–1004, 1998.

[74] Jennings, H. M. A model for the microstructure of calcium silicate hydrate in cement paste. *Cement and Concrete Research*, 30(1):101–116, 2000.

[75] Kendall, K., Howard, A., and Birchall, J. The relation between porosity, microstructure and strength, and the approach to cement-based materials. *Phil. Trans. R. Soc. London*, A310:139–153, 1983.

[76] Koiter, W. General theorem for elasto-plastic solids. In: Sneddon, I. and Hill, R., Editors, *Progress in Solid Mechanics*, volume I, pages 167–218. North-Holland Publishing Company, Amsterdam, 1960.

[77] Kreher, W. Residual stresses and stored elastic energy of composites and polycrystals. *Journal of the Mechanics and Physics of Solids*, 38:115–128, 1990.

[78] Kroener, E. *Statistical Continuum Mechanics.* Springer-Verlag, New York, 1971.

[79] LCPC Paris, Paris. *Manual of CESAR-LCPC 3.2*, 5ème edition, 1995. In French.

[80] Le Bellego, C. *Couplages chimie - mécanique dans les structures en béton attaquées par l'eau: étude expérimentale et analyse numérique.* PhD thesis, ENS Cachan, France, 2001. In French.

[81] Lea, F. The action of ammonium nitrate salts on concrete. *Magazine of Concrete Research*, 17(52):115–116, 1965.

[82] Lemarchand, E. Micro-chemomechanics. CEE Internal Note, 2002.

[83] Lemarchand, E., Ulm, F.-J., and Dormieux, L. The effect of inclusions on the friction coefficient of highly filled composite materials. *Journal of Engineering Mechanics ASCE*, 128(8), 2002.

[84] Lemarchand, E. *Contribution de la micromécanique à l'étude des phénomènes de transport et de couplage poromécanique dans les milieux poreux: Application aux phénomènes de gonflement des géomatériaux.* PhD thesis, Ecole Nationale des Ponts et Chaussées, 2001.

[85] Levin, V. Thermal expansion coefficients of heterogeneous materials. *Mechanics of Solids*, 2(1):58–61, 1967.

[86] Li, G. Q., Zhao, Y., and Pang, S. S. Four-phase sphere modeling of effective bulk modulus of concrete. *Cement and Concrete Research*, 29(6):839–845, 1999.

[87] Lutz, M. P., Monteiro, P. J. M., and Zimmerman, R. W. Inhomogeneous interfacial transition zone model for the bulk modulus of mortar. *Cement and Concrete Research*, 27(7):1113–1122, 1997.

[88] Lutz, M. P. and Zimmerman, R. W. Effect of the interphase zone on the bulk modulus of a particulate composite. *Journal of Applied Mechanics - Transactions of the ASME*, 63(4):855–861, 1996.

[89] Maggion, R. *Etude de l'Evolution Microtexturale de Pates de Silicate Tricalcique Hydrate.* PhD thesis, University of Orleans, 1992. In French.

[90] Mainguy, M. Diffusion and dissolution in a cylinder. Technical note, MIT, 1999.

[91] Mainguy, M. Implémentation et utilisation du module LIXI dans le code de calcul aux éléments finis CESAR-LCPC. Report to LCPC Paris, Cambridge, MA, 2000. In French.

[92] Mainguy, M. and Coussy, O. Propagation fronts during calcium leaching and chloride penetration. *Journal of Engineering Mechanics ASCE*, 126(3):250–257, 2000.

[93] Mainguy, M., Tognazzi, C., Torrenti, J.-M., and Adenot, F. Modelling of leaching in pure cement paste and mortar. *Cement and Concrete Research*, 30:83–90, 2000.

[94] Mainguy, M. and Ulm, F.-J. Coupled diffusion-dissolution around a fracture channel: the solute congestion phenomenon. *Transport in Porous Media*, 43(3):481–497, 2001.

[95] Mainguy, M., Ulm, F.-J., and Heukamp, F. Similarity properties of demineralization and degradation of cracked porous materials. *International Journal of Solids and Structures*, 38:7079–7100, 2001.

[96] Maso, J. C. Interfacial transition zone in concrete. Report 11, RILEM, 1996.

[97] MathWorks. *Matlab Program.* MathWorks Inc., Natick, MA, 2002.

[98] Matte, V. and Moranville, M. Durability of reactive powder composites: Influence of silica fume on the leaching properties of very low water/binder pastes. *Cement and Concrete Composites*, 21(1):1–9, 1999.

[99] McClintock, F. *Mechanical Behavior of Materials.* Addison-Wesley, Reading, MA, 1966.

[100] McKale, J. Analysis of type I portland cement. Technical report, Dragon Cements, Portland, ME, 1999.

[101] Megaw et al. *Nature*, 177:390, 1956.

[102] Mehta, P. K. and Monteiro, P. J. M. *Concrete: Structures, Properties and Materials.* Prentice Hall, 2nd edition, 1993.

[103] Mehta, P. and Monteiro, P. Effect of aggregate, cement, and mineral admixtures on the microstructure of the transition zone. In: Mindess, S. and Shah, S. P., Editors, *Proc. Symp. on Bonding in Cementitious Materials*, volume 114. Materials Research Society, 1988.

[104] van Mier, J. *Fracture processes of concrete: Assesment of material parameters for fracture models.* CRC Press, Boca Raton, FL, 1997.

[105] Mohr, A. Ueber die einwirkung von ammoniumsalzloesungen auf beton. *Der Bauingenieur*, 6(8):284–293, 1925. In German.

[106] Monteiro, P. J. M. and Chang, C. T. The elastic-moduli of calcium hydroxide. *Cement and Concrete Research*, 25(8):1605–1609, 1995.

[107] Monteiro, P. J. M. and Ostertag, C. P. Analysis of the aggregate cement paste interface using grazing-incidence X-ray scattering. *Cement and Concrete Research*, 19(6):987–988, 1989.

[108] Mori, T. and Tanaka, K. Average stress in matrix and average elastic energy of materials with misfitting inclusions. *Acta Metallurgica*, 21(5):571–574, 1973.

[109] Neville, A. M. *Properties of Concrete.* Longman group, Harlow, 4th edition, 1995.

[110] Office of Highway Policy Information. Highway funding bulletin 1998-2001. Technical report, Federal Highway Administration, Washington, D.C., 2001.

[111] Oliver, W. C. and Pharr, G. M. An improved technique for determining hardness and elastic-modulus using load and displacement sensing indentation experiments. *Journal of Materials Research*, 7(6):1564–1583, 1992.

[112] Parkhurst, D. and Appelo, C. User's guide to PHREEQC version 2. Water-Resources Investigations Report 99-4259, U.S. Geological Survey, Denver, CO, 1999.

[113] Pellenq, R.-M., Caillol, J., and Delville, A. Electrostatic attraction between two charged surfaces: A (n,v,t) monte carlo simulation. *Journal of Physical Chemistry B*, 101:8584–8594, 1997.

[114] Philippot, S., Korb, J., Petit, D., Counio, G., and Zanni, H. Analysis of microporosity of reactive powder concrete by proton nuclear relaxation. *Journal de Chimie Physique et de Physico-Chimie Biologique*, 95(2):332–336, 1998.

[115] Porteneuve, C. *Caractérisation des Bétons par Résonance Magnétique Nucléaire: Application à l'Etude de l'Altération par l'Eau.* PhD thesis, Université Paris VI, France, 2001. In French.

[116] Porteneuve, C., Korb, J., Petit, D., and Zanni, H. Structure-texture correlation in ultra-high-performance concrete - a nuclear magnetic resonance study. *Cement and Concrete Research*, 32(1):97–101, 2002.

[117] Porteneuve, C., Zanni, H., Vernet, C., Kjellsen, K., Korb, J.-P., and Petit, D. Nuclear magnetic resonance characterization of high- and ultrahigh-performance concrete: Application to the study of water leaching. *Cement and Concrete Research*, 31(12):1887–18894, 2001.

[118] Powers, T. and Brownyard, T. Studies of the physical properties of hardened portland cement paste. Bulletin 22, Portland Cement Association, Chicago, IL, 1948.

[119] Ramesh, G., Sotelino, E. D., and Chen, W. F. Effect of transition zone on elastic moduli of concrete materials. *Cement and Concrete Research*, 26(4):611–622, 1996.

[120] Rankine, W. On the thermodynamic theory of waves of finite longitudinal disturbances. *Transactions of the Royal Society of London*, 160:277–288, 1870.

[121] Re, G. D. *Physical Mechanisms Controlling the Pre-Failure Stress-Strain Behavior of Frozen Sand.* PhD thesis, MIT, 2000.

[122] Richard, P. and Cheyrezy, M. Composition of reacitve powder concrete. *Cement and Concrete Research*, 25(7):1501–1511, 1995.

[123] Richard, P. and Cheyrezy, M. Les bétons des poudres réactives (bpr) à ultra haute résistance (200 à 800 mpa). *Annales de l'Intitut Technique du Bâtiment et des Travaux Publics*, 532:8–16, 1995.

[124] Richardson, I. The nature of C-S-H in hardened cements. *Cement and Concrete Research*, 29:1131–1147, 1999.

[125] Roelfstra, P., Salet, A., and Kuiks, J. Defining and application of stress-analysis-based temperature difference limits to prevent early-age cracking in concrete structures. In: Springenschmid, R., Editor, *Proc. RILEM Int. Symposium: Thermal cracking in concrete at early age*, pages 273–280, Paris, 1994. RILEM.

[126] Roessler, C., 2002. Personal Communication.

[127] de Rooij, M. *Syneresis in cement paste systems.* PhD thesis, Technical University of Delft, 2000.

[128] Saito, H., Nakane, S., Ikari, S., and Fujiwara, A. Preliminary experimental study on the deterioration of cementitious materials by an acceleration method. *Nuclear Engineering and Design*, 138:151–155, 1992.

[129] Schneider, U. and Chen, S.-W. The chemomechanical effect and the mechanochemical effect on high-performance concrete subjected to stress corrosion. *Cement and Concrete Research*, 28(4):509–522, 1998.

[130] Schneider, U. and Chen, S.-W. Verhalten von hochfestem beton bei chemischer korrosion und spannungskorrosion. Technical report, Technische Universitaet Wien, 2002.

[131] Schofield, A. and Wroth, P. *Critical State Soil Mechanics.* McGraw-Hill, New York, 1968.

[132] Scrivener, K. and Gartner, E. Microstructural gradients in cement paste around aggregate particles. In: *Proc. of the Materials Research Society Symposium*, number 114, pages 77–85, 1988.

[133] Sheahan, T. and Germaine, J. Computer automation of conventional triaxial equipment. *ASTM Geotechnical Testing Journal*, 15(4):311–322, 1992.

[134] Simo, J. and Hughes, T. *Computational Inelasticity.* Springer, New York, 1998.

[135] Skempton, A. The pore-pressure coefficients A and B. *Geotechnique*, 4:143–147, 1954.

[136] Stark, J. and Wicht, B. *Zement und Kalk - Der Baustoff als Werkstoff.* Baupraxis. Birkhaeuser, 2000. In German.

[137] Stumm, W. and Morgan, J. *Aquatic Chemistry.* John Wiley and Sons, 1996.

[138] Stutzman, P. and Clifton, J. Specimen preparation for scanning electron microscopy. In: Jany, L. and Nisperos, A., Editors, *Proc. 21st Int. Conference on Cement Microscopy*, pages 10–22, Las Vegas, 1999.

[139] Suquet, P. Effective properties of nonlinear composites. In: Suquet, P., Editor, *Continuum Micromechanics*, number 377 in CISM Courses and Lectures, pages 197–264, New York, 1997. Springer.

[140] Suresh, S. and Mortensen, A. *Fundamentals of functionally graded materials: Processing and Thermomechanical Behaviour of Graded Metals and Metal-Ceramic Composites.* Cambridge University Press, Cambridge UK, 1998.

[141] Taylor, H. *Cement Chemistry.* Thomas Telford, London, 2nd edition, 1997.

[142] Tennis, P. D. and Jennings, H. M. A model for two types of calcium silicate hydrate in the microstructure of portland cement pastes. *Cement and Concrete Research*, 30(6):855–863, 2000.

[143] Terzaghi, K. *Theoretical Soil Mechanics.* John Wiley and Sons, 1943.

[144] Tognazzi, C. *Couplage Fissuration - Dégradation chimique dans les matériaux cimentaires: Caractérisation et modélisation.* PhD thesis, INSA Toulouse, France, 1998. In French.

[145] Tong, P., Pan, T., and Bucciarelli, L. Mode shapes and frequencies by finite element method using consistent and lumped masses. *Computers and Structures*, 1:623–638, 1971.

[146] Ubelhack, H. and Wittmann, F. Bonding characteristics of gel particles to structure of hardened cement paste. *American Ceramic Society Bulletin*, 55(4):405, 1976.

[147] Ulm, F.-J. Couplages thermochémomécaniques dans les bétons – un premier bilan. Research report oa31, Laboratoire des Ponts et Chaussées, Paris, 1999.

[148] Ulm, F.-J. and Coussy, O. *Mechanics and Durability of Solids*, volume I. Prentice Hall, 2002.

[149] Ulm, F.-J., Lemarchand, E., and Heukamp, F. Elements of chemomechanics of calcium leaching of cement-based materials at different scales. *Engineering Fracture Mechanics*, 2002. In Press.

[150] Ulm, F.-J., Torrenti, J.-M., and Adenot, F. Chemoporoplasticity of calcium leaching in concrete. *Journal of Engineering Mechanics ASCE*, 125(10):1200–1211, 1999.

[151] US Department of Energy. Yucca mountain project website. Online Document, 2002. http://www.ymp.gov.

[152] Velez, K., Maximilien, S., Damidot, D., Fantozzi, G., and Sorrentino, F. Determination by nanoindentation of elastic modulus and hardness of pure constituents of portland cement clinker. *Cement and Concrete Research*, 31(4):555–561, 2001.

[153] Venkatesh, T. A., van Vliet, K. J., Giannakopoulos, A. E., and Suresh, S. Determination of elasto-plastic properties by instrumented sharp indentation: Guidelines for property extraction. *Scripta Materialia*, 42(9):833–839, 2000.

[154] Watt, I. *The principles and practice of electron microscopy.* Cambridge University Press, Cambridge, UK, 2nd edition, 1997.

[155] Wittmann, F. H. Estimation of the modulus of elasticity of calcium hydroxide. *Cement and Concrete Research*, 16(6):971–972, 1986.

[156] Wittmann, F. Discussion of some factors influencing creep of concrete. Technical report, The State Institute for Technical Research Finland, 1971.

[157] Wittmann, F. Interaction of hardened cement paste and water. *Journal of the American Ceramic Society*, 56(8):409–415, 1973.

[158] Wittmann, F., Stockhausen, N., and Buhl, W. Disjoining pressure and its influence on mechanical-behavior of concrete. *American Ceramic Society Bulletin*, 55(4):405, 1976.

[159] Yuji, W. The effect of bond characteristics between steel slag fine aggregate and cement paste on mechanical properties of concrete and mortar. In: Mindess and Shah [103].

[160] Zaoui, A. *Matériaux Hétérogènes et Composites.* Ecole Polytechnique, Département de Mécanique, Paris, 1997. Lecture Notes. In French.

[161] Zaoui, A. Continuum micromechanics - a survey. *Journal of Engineering Mechanics ASCE*, 128(8):808–816, 2002.

[162] Zemansky, M. and Dittman, R. *Heat and Thermodynamics.* McGraw-Hill, Boston MA, 7th edition, 1997.

Part VI

Appendices

Appendix A

Publications Related to this Study

A.1 Refereed Journal Papers

Heukamp, F.H., Ulm, F.-J., Germaine, J.T., "Mechanical properties of calcium leached cement pastes: Triaxial stress states and the influence of the pore pressure", Cement and Concrete Research, Vol. 31, No. 5, pages 767-774, 2001.

Heukamp, F.H., Ulm, F.-J., Germaine, J.T., "Poroplastic Properties of Calcium leached Cement-based Materials", submitted to Cement and Concrete Research, 2001.

Mainguy, M., Ulm, F.-J., Heukamp, F.H., "Similarity properties of demineralization and degradation of cracked porous materials", Int. Journal of Solids and Structures, Vol. 38, pages 7079-7100, 2001.

Ulm, F,-J., Heukamp, F.H., Germaine, J.T., "Residual design strength of cement-based materials for nuclear waste storage systems", Nuclear Engineering and Design, No. 211, pages 51-60, 2002.

Heukamp, F.H., Lemarchand, E. Ulm, F.-J. "The Influence of the Interfacial Properties on the cohesion of highly filled Composite Materials", submitted to Int. Journal of Solids and Structures, 2002..

Ulm, F.-J., Lemarchand, E., Heukamp, F.H., "Elements of Chemomechanics of Calcium Leaching of Cement-based Materials at Different scales", Engineering Fracture Mechanics, in

press, 2002.

A.2 Conference Proceedings

Heukamp, F.H., Mainguy, M., Ulm, F.-J., "Beyond the Crack Size Criterion: The Effect of a Fracture on Calcium Depletion of Cementitious Materials", Proceedings FramCos-4, Int. Conf. On Fracture Mechanics, Paris, May-June 2001. Editors: R. de Borst, J. Mazars, G. Pijaudier-Cabot and J.G.M. van Mier. Balkema Publisher.

Ulm, F.-J., Heukamp, F.H., Germaine, J.T., "Durability mechanics of calcium leaching of concrete and beyond", Proceedings FramCos-4, Int. Conf. On Fracture Mechanics, Paris, May-June 2001. Editors: R. de Borst, J. Mazars, G. Pijaudier-Cabot and J.G.M. van Mier, Balkema Publisher.

Heukamp, F.H., Ulm, F.-J., Germaine, J.T.,"The consequences of calcium leaching on structural integrity of concrete containment structures: New experimental evidence from triaxial tests on mortars and cement pastes", Proceedings SMiRT-16, 16th Int. Conf. on Structural Mechanics in Reactor Technology, Washington August 2001.

Mainguy, M., Ulm, F.-J., Heukamp, F.H., "Model-Based Simulation of Demineralization Processes in Cracked Porous Media", Proceedings 1st MIT Conference on Computational Mechanics of Fluid & Solids, June, 2001. Editor: K.-J. Bathe, Elsevier Science Ltd.

Heukamp, F.H., Ulm, F.-J., "Multiscale Model-Based Simulation of the Load Bearing Capacity of Calcium Leached Concrete Structures", EURO-C 2003 conference, in preparation.

A.3 Additional Publications Related to DOE Project

Mainguy, M., Ulm, F.-J., "Coupled diffusion-dissolution around a fracture channel: the solute congestion phenomenon", Transport in porous media, Vol. 45, No. 3, pages 481-497, 2001.

Lemarchand, E., Ulm, F.-J., Dormieux, L., "The Effect of Inclusions on the Friction Coefficient of Highly Filled Composite Materials", ASCE Journal of Engineering Mechanics, Vol. 128,

No. 8, pages 876-884, 2002.

Constantinides, G., Ulm, F.-J., "The Effect of two Types of C-S-H on the Elasticity of Cement-Based Materials: Results from Nanoindentation and Micromechanical Modeling", Cement and Concrete Research, submitted, 2002.

Bernard, O., Ulm, F.-J., Lemarchand, E. , "A Multiscale Micromechanics-Hydration Model of Early-Age Elastic Properties of Cement-Based Materials", Cement and Concrete Research, submitted, 2002.

Bernard, O., Ulm, F.-J., Germaine, J.T., "Volume and Deviator Basic Creep of Calcium-Leached Cement-Based Materials", Cement and Concrete Research, submitted, 2002.

Appendix B

Triaxial Test Evaluation

The following formulae are used for the evaluation of the triaxial compression tests. The logarithmic volumetric strains are calculated through:

$$\delta E_v^{\ln} = \ln\left(\frac{V_t}{V_{ref}}\right) = 2\ln\frac{R_{t,0}}{R_{ref}} + \ln\frac{L_t}{L_{ref}} + \ln\left[\frac{8}{15}\left(\frac{R_{t,\max}}{R_{t,0}}\right)^2 + \frac{4}{15}\frac{R_{t,\max}}{R_{t,0}} + \frac{1}{5}\right] \tag{B.1}$$

where the maximum radius (in the specimen center) can be calculated assuming a parabolic specimen shape:

$$\frac{R_{t,\max}}{R_{t,0}} = \frac{1}{4}\left(\sqrt{30\frac{V_t}{V_{ref}} \times \frac{L_{ref}}{L_t} \times \left(\frac{R_{ref}}{R_{t,0}}\right)^2 - 5} - 1\right) \tag{B.2}$$

$R_{t,0}$ is the radius at the end of the hydrostatic loading part and determined from (5.12). For the experimental determination of $R_{t,\max}$, we choose:

$$\frac{R_{ref}}{R_{t,0}} = 1;\ \frac{V_t}{V_{ref}} \simeq 1 + \frac{\phi - \phi_{ref}}{1 + \phi_{ref} - \phi_0} \tag{B.3}$$

The maximum radius leads to the minimum magnitude of the vertical Cauchy Stress in the specimen center that is calculated from the additional vertical load $\delta F_z = \pi R_{t,\max}^2 (\Sigma_{zz,\min} - \Sigma_{zz,ref})$, with $\Sigma_{zz,ref} = \Sigma_{rr} = \Sigma_{\theta\theta}$ the mean stress at the end of the hydrostatic loading ($\Sigma_{rr} = \Sigma_{\theta\theta}$ are held constant during deviatoric loading). This stress is retained in all the results as the relevant stress, leading to failure.

The external work increment can be written in the following way ($\mathbf{D}$ = strain rate in

deformed configuration)

$$\frac{dW_{ext}}{dt} = \int_{V_t} \boldsymbol{\Sigma} : \mathbf{D} dV + p\frac{dV_f}{dt} = 2\Sigma_{rr}\frac{dE_{rr}^{\ln}}{dt} + \Sigma_{zz}\frac{dE_{zz}^{\ln}}{dt} + p\frac{dV}{dt}_f = \Sigma_{rr}\frac{dE_v^{\ln}}{dt} + \tag{B.4}$$
$$(\Sigma_{zz} - \Sigma_{rr})\frac{dE_{zz}^{\ln}}{dt} + pdV_f \simeq \Sigma'_M\frac{d\phi}{dt}V_0 + (\Sigma_{zz} - \Sigma_{rr})\frac{(dE_{zz}^{\ln} - dE_v^{\ln}/3)}{dt}V_t$$

which suggests that the results be presented in $\Sigma'_M \times d\phi$ and $(\Sigma_{zz} - \Sigma_{rr}) \times (dE_{zz}^{\ln} - dE_v^{\ln}/3)$ halfplanes.

Appendix C

Commented Maple® Input File for the Cohesion Homogenization

The following commands are used in a typical calculation with Maple®. The comments are in *Italics.*

> restart:

> with(linalg):

> file1:=fopen("res100.txt",WRITE):

>

>

> for eta from 0.1 by 0.1 to 1.0 do *Loop over different values of* η starts

> nph:=3: *Number of phases that are considered*

> c1:=0.5: *The* c_i *are the volume fractions*

> c2:=0.25:

> R(1):=1:c3:=1-c1-c2:R(3):=R(1)/c1^(1/3):R(2):=R(3)*(c1+c2)^(1/3): *Definition of the radii. (1) is the inclusion, (2) the ITZ and (3) the matrix*

> mu(1):=100000:mu(3):=0.001:mu(2):=eta*mu(3): *Input of the shear moduli. Note that the inclusion shear modulus is much bigger than the shear modulus of the other phases. The modulus in the ITZ is controlled by* η *times the modulus in the matrix.*

> ck(1):=100000:ck(3):=1:ck(2):=eta*ck(3): *Analogous for the bulk modulus*

```
> nu(1):=(3*ck(1)-2*mu(1))/2/(mu(1)+3*ck(1)):      Calculation of the Poisson's ratio
> nu(2):=(3*ck(2)-2*mu(2))/2/(mu(2)+3*ck(2)):
> nu(3):=(3*ck(3)-2*mu(3))/2/(mu(3)+3*ck(3)):
> for k from 1 to (nph-1) do a(k):=mu(k)/mu(k+1)*(7.+5*nu(k))*(7.-10*nu(k+1))-(7-
10*nu(k))*(7+5*nu(k+1)) od:      Calculation of the coefficients a(k) through alpha(k) for
Hervé-Zaoui's model (see above)
> for k from 1 to (nph-1) do b(k):=4*(7-10*nu(k))+(mu(k)/mu(k+1)*(7+5*nu(k))) od:
>
> for k from 1 to (nph-1) do c(k):=(7-5*nu(k+1))+2*mu(k)/mu(k+1)*(4-5*nu(k+1)) od:
> for k from 1 to (nph-1) do d(k):=(7+5*nu(k+1))+4*mu(k)/mu(k+1)*(7-10*nu(k+1)) od:
>
> for k from 1 to (nph-1) do e(k):=2*(4-5*nu(k))+mu(k)/mu(k+1)*(7-5*nu(k)) od:
> for k from 1 to (nph-1) do f(k):=(4-5*nu(k))*(7-5*nu(k+1))-mu(k)/mu(k+1)*(4-5*nu(k+1))
*(7-5*nu(k)) od:
> for k from 1 to (nph-1) do alpha(k):=mu(k)/mu(k+1)-1 od:
>
> for k from 1 to (nph-1) do coef(k):=1/5/(1-nu(k+1)) od:
> for k from 1 to (nph-1) do M(1,1,k):=limit(coef(k)*(c(k)/3),ck1=infinity) od:      Com-
ponents of the M matrices
> for k from 1 to (nph-1) do M(1,2,k):=coef(k)*(R(k)^2*(3*b(k)-7*c(k))/5/(1-2*nu(k)))
od:
> for k from 1 to (nph-1) do M(1,3,k):=coef(k)*(-12*alpha(k)/R(k)^5) od:
>
> for k from 1 to (nph-1) do M(1,4,k):=coef(k)*(4*(f(k)-27*alpha(k))/15/(1-2*nu(k))/R(k)^3)
od:
>
> for k from 1 to (nph-1) do M(2,1,k):=0 od:
> for k from 1 to (nph-1) do M(2,2,k):=coef(k)*((1-2*nu(k+1))*b(k)/7/(1-2*nu(k))) od:
>
> for k from 1 to (nph-1) do M(2,2,k):=coef(k)*((1-2*nu(k+1))*b(k)/7/(1-2*nu(k))) od:
```

```
>
> for k from 1 to (nph-1) do M(2,3,k):=coef(k)*(-20*(1-2*nu(k+1))*alpha(k)/7/R(k)^7)
od:
> for k from 1 to (nph-1) do M(2,4,k):=coef(k)*(-12*(1-2*nu(k+1))*alpha(k)/7/
(1-2*nu(k))/R(k)^5) od:
> for k from 1 to (nph-1) do M(3,1,k):=coef(k)*(R(k)^5*alpha(k)/2) od:
> for k from 1 to (nph-1) do M(3,2,k):=coef(k)*(-R(k)^7*(2*a(k)+147*alpha(k))/70/(1-
2*nu(k))) od:
> for k from 1 to (nph-1) do M(3,3,k):=coef(k)*(d(k)/7) od:
>
> for k from 1 to (nph-1) do M(3,4,k):=coef(k)*(R(k)^2*(105*(1-nu(k+1))+12*alpha(k)*(7-
10*nu(k+1))-7*e(k))/35/(1-2*nu(k))) od:
> for k from 1 to (nph-1) do M(4,1,k):=coef(k)*(-5/6*(1-2*nu(k+1))*alpha(k)*R(k)^3) od:
> for k from 1 to (nph-1) do M(4,2,k):=coef(k)*(7*(1-2*nu(k+1))*alpha(k)*R(k)^5/2/(1-
2*nu(k))) od:
> for k from 1 to (nph-1) do M(4,3,k):=0 od:
>
> for k from 1 to (nph-1) do M(4,4,k):=coef(k)*(e(k)*(1-2*nu(k+1))/3/(1-2*nu(k))) od:
> P1:=matrix(4,4):M1:=matrix(4,4):M2:=matrix(4,4):
> for i from 1 to 4 do M1[i,1]:=M(i,1,1) od:      Assembling of the M matrices from the
different elements
> for i from 1 to 4 do M1[i,2]:=M(i,2,1) od:
> for i from 1 to 4 do M1[i,3]:=M(i,3,1) od:
> for i from 1 to 4 do M1[i,4]:=M(i,4,1) od:
> for i from 1 to 4 do M2[i,1]:=M(i,1,2) od:
> for i from 1 to 4 do M2[i,2]:=M(i,2,2) od:
> for i from 1 to 4 do M2[i,3]:=M(i,3,2) od:
> for i from 1 to 4 do M2[i,4]:=M(i,4,2) od:
> P1:=M1:
> P2:=multiply(M2,M1):      Calculating P as the product of the M matrices
```

> for i from 1 to 4 do Z[i,1]:=P2[i,1]*P2[1,2]-P2[1,1]*P2[i,2] od:

> for i from 1 to 4 do Z[i,2]:=P2[i,1]*P2[2,2]-P2[2,1]*P2[i,2] od:

> for i from 1 to 4 do Z[i,3]:=P2[i,1]*P2[3,2]-P2[3,1]*P2[i,2] od:

> for i from 1 to 4 do Z[i,4]:=P2[i,1]*P2[4,2]-P2[4,1]*P2[i,2] od:

> A1:=4*R(nph)^10*(1-2*nu(nph))*(7-10*nu(nph))*Z[1,2]+20*R(nph)^7*(7-12*nu(nph)+8*nu(nph)**2)*Z[4,2]+12*R(nph)^5*(1-2*nu(nph))*(Z[1,4]-7*Z[2,3])+20*R(nph)^3*(1-2*nu(nph))^2*Z[1,3]+16*(4-5*nu(nph))*(1-2*nu(nph))*Z[4,3]: *Setting up the quadratic equation* $A1\left(\frac{\mu_{\text{hom}}}{\mu_{matrix}}\right)^2$+B1*$\left(\frac{\mu_{\text{hom}}}{\mu_{matrix}}\right) + C1 = 0$

> B1:=3*R(nph)^10*(1-2*nu(nph))*(15*nu(nph)-7)*Z[1,2]+60*R(nph)^7*(nu(nph)-3)*nu(nph)*Z[4,2]-24*R(nph)^5*(1-2*nu(nph))*(Z[1,4]-7*Z[2,3])-40*R(nph)^3*(1-2*nu(nph))^2*Z[1,3]-8*(1-5*nu(nph))*(1-2*nu(nph))*Z[4,3]:

> C1:=-R(nph)^10*(1-2*nu(nph))*(7+5*nu(nph))*Z[1,2]+10*R(nph)^7*(7-nu(nph)^2)*Z[4,2]+12*R(nph)^5*(1-2*nu(nph))*(Z[1,4]-7*Z[2,3])+20*R(nph)^3*(1-2*nu(nph))^2*Z[1,3]-8*(7-5*nu(nph))*(1-2*nu(nph))*Z[4,3]:

> DDelta:=B1^2-4*A1*C1:racdelta:=DDelta^0.5:

> sol1:=(-B1+racdelta)/2/A1*mu(nph): *Solution 1 for* μ_{hom}

> sol2:=(-B1-racdelta)/A1/2*mu(nph): *Solution 2 for* μ_{hom} (< 0)

> mu(4):=sol1: *Solution 1 retained*

> for k from 1 to (nph-1) do coefficient(k):=1/(3*ck(k+1)+4*mu(k+1)) od: *Coefficient for the 4th phase - the homogenized phase*

> for k from 1 to (nph-1) do N(1,1,k):=coefficient(k)*(3*ck(k)+4*mu(k+1)) od: *Calculation of the elements of the N-matrices for the bulk modulus determination.*

> for k from 1 to (nph-1) do N(1,2,k):=coefficient(k)*4/R(k)^3*(mu(k+1)-mu(k)) od:

> for k from 1 to (nph-1) do N(2,1,k):=coefficient(k)*3*R(k)^3*(ck(k+1)-ck(k)) od:

> for k from 1 to (nph-1) do N(2,2,k):=coefficient(k)*(3*ck(k+1)+4*mu(k)) od:

> Q1:=matrix(2,2):N1:=matrix(2,2):N2:=matrix(2,2):

> for i from 1 to 2 do N1[i,1]:=N(i,1,1) od:

> for i from 1 to 2 do N1[i,2]:=N(i,2,1) od:

> for i from 1 to 2 do N2[i,1]:=N(i,1,2) od:

> for i from 1 to 2 do N2[i,2]:=N(i,2,2) od:

> Q1:=N1:

> Q2:=multiply(N2,N1):

> ck(4):=(3*ck(3)*R(3)^3*Q2[1,1]-4*mu(3)*Q2[2,1])/3/(R(3)^3*Q2[1,1]+Q2[2,1]): *Solution for the bulk modulus* k_{hom}

> nu(4):=(3*ck(4)-2*mu(4))/2/(mu(4)+3*ck(4)): *Corresponding Poisson's ratio.*

> for k from nph to (nph) do a(k):=mu(k)/mu(k+1)*(7.+5*nu(k))*(7.-10*nu(k+1))-(7-10*nu(k))*(7+5*nu(k+1)) od: *Determination of the additional elements of the M-matrices relating to the homogenized phase (=4)*

> for k from nph to (nph) do b(k):=4*(7-10*nu(k))+(mu(k)/mu(k+1)*(7+5*nu(k))) od:

>

> for k from nph to (nph) do c(k):=(7-5*nu(k+1))+2*mu(k)/mu(k+1)*(4-5*nu(k+1)) od:

> for k from nph to (nph) do d(k):=(7+5*nu(k+1))+4*mu(k)/mu(k+1)*(7-10*nu(k+1)) od:

> for k from nph to (nph) do d(k):=(7+5*nu(k+1))+4*mu(k)/mu(k+1)*(7-10*nu(k+1)) od:

> for k from nph to (nph) do e(k):=2*(4-5*nu(k))+mu(k)/mu(k+1)*(7-5*nu(k)) od:

> for k from nph to (nph) do f(k):=(4-5*nu(k))*(7-5*nu(k+1))-mu(k)/mu(k+1)*(4-5*nu(k+1))*(7-5*nu(k)) od:

> for k from nph to (nph) do alpha(k):=mu(k)/mu(k+1)-1 od:

>

> for k from nph to (nph) do coef(k):=1/5/(1-nu(k+1)) od:

> for k from nph to (nph) do M(1,1,k):=coef(k)*(c(k)/3) od:

> for k from nph to (nph) do M(1,2,k):=coef(k)*(R(k)^2*(3*b(k)-7*c(k))/5/(1-2*nu(k))) od:

> for k from nph to (nph) do M(1,3,k):=coef(k)*(-12*alpha(k)/R(k)^5) od:

>

> for k from nph to (nph) do M(1,4,k):=coef(k)*(4*(f(k)-27*alpha(k))/15/(1-2*nu(k))/R(k)^3) od:

> for k from nph to (nph) do M(2,1,k):=0 od:

> for k from nph to (nph) do M(2,2,k):=coef(k)*((1-2*nu(k+1))*b(k)/7/(1-2*nu(k))) od:

```
>
> for k from nph to (nph) do M(2,3,k):=coef(k)*(-20*(1-2*nu(k+1))*alpha(k)/7/R(k)^7)
od:
> for k from nph to (nph) do M(2,4,k):=coef(k)*(-12*(1-2*nu(k+1))*alpha(k)/7/(1-2*nu(k))/R(k)^5)
od:
> for k from nph to (nph) do M(3,1,k):=coef(k)*(R(k)^5*alpha(k)/2) od:
> for k from nph to (nph) do M(3,2,k):=coef(k)*(-R(k)^7*(2*a(k)+147*alpha(k))/70/(1-
2*nu(k))) od:
> for k from nph to (nph) do M(3,3,k):=coef(k)*(d(k)/7) od:
>
> for k from nph to (nph) do M(3,4,k):=coef(k)*(R(k)^2*(105*(1-nu(k+1))+12*alpha(k)*(7-
10*nu(k+1))-
7*e(k))/35/(1-2*nu(k))) od:
> for k from nph to (nph) do M(4,1,k):=coef(k)*(-5/6*(1-2*nu(k+1))*alpha(k)*R(k)^3)
od:
> for k from nph to (nph) do M(4,2,k):=coef(k)*(7*(1-2*nu(k+1))*alpha(k)*R(k)^5/2/(1-
2*nu(k))) od:
> for k from nph to (nph) do M(4,3,k):=0 od:
>
> for k from nph to (nph) do M(4,4,k):=coef(k)*(e(k)*(1-2*nu(k+1))/3/(1-2*nu(k))) od:
> M3:=matrix(4,4):
> for i from 1 to 4 do M3[i,1]:=M(i,1,3) od:
> for i from 1 to 4 do M3[i,2]:=M(i,2,3) od:
> for i from 1 to 4 do M3[i,3]:=M(i,3,3) od:
> for i from 1 to 4 do M3[i,4]:=M(i,4,3) od:
> P3:=multiply(M3,P2):
> w1:=vector(4):w2:=vector(4):w3:=vector(4):w4:=vector(4):      Introducing the w-vectors
> w4[1]:=gamma0:      E_d is equal to γ_0
> con:=w4[1]/(P3[2,2]*P3[1,1]-P3[1,2]*P3[2,1]):
> w1[1]:=P3[2,2]*con:      Evaluation of the w_1 vector components
```

```
> w1[2]:=-P3[2,1]*con:
> w1[3]:=0:
> w1[4]:=0:
> Phelp:=vector([P3[2,2],-P3[2,1],0,0]):
> w2:=multiply(P1,Phelp):      Evaluation of the w2 vector components
> w2:=matadd(w2,Phelp,con,0):
> w3:=multiply(M2,w2):      Evaluation of the w3 vector components
> w4:=multiply(M3,w3):      Evaluation of the w4 vector components
> A:=w3[1]:      Extraction of the elements of w3
> B:=w3[2]:
> C:=w3[3]:
> DD:=w3[4]:
> nu3:=nu(3):
> T3:=1/w4[1]*(A-21/5*(R(3)^5-R(2)^5)/(1-2*nu3)/(R(3)^3-R(2)^3)*B):      Evaluation
of A_3^d
> T2:=1/w4[1]*(w2[1]-21/5*(R(2)^5-R(1)^5)/(1-2*nu(2))/(R(2)^3-R(1)^3)*w2[2]):      Eval-
uation of A_2^d
> chi:=eta*T2/T3;      Evaluation of χ
> result1:=mu(4)/mu(3)/T3; Evaluation of c_hom/c_m
> fprintf(file1,"%g,%g, %g\n",eta,result1,chi):      Save results to file
> end do;      End of do-loop
> fclose(file1):
```

Appendix D

Numerical Implementation into CESAR-LCPC

D.1 CESAR-LCPC

D.1.1 Program Overview

CESAR-LCPC is an all-round finite-element based engineering analysis program, distributed by the Laboratoire Central des Ponts et Chaussées (LCPC), Paris, France [71]. Its development started in the early 1980's. CESAR-LCPC consists of three programs:

- MAX is the preprocessor. It is being used for the data set generation, that is the mesh and the input parameters for the calculation. MAX2D and MAX3D denote the two and three-dimensional versions of this program, respectively.
- CESAR is the core of the program. It executes the input data files and performs the actual calculations. Result files are produced as output. Commercial users of the CESAR-LCPC program have a fixed version of CESAR. Users with a developer's licence can create their own versions of CESAR. Through the development platform, the modified source files are combined with the unmodified standard files to a new CESAR program. The source files are all written in FORTRAN77
- PEGGY is the postprocessor program. It is used to visualize the output files produced

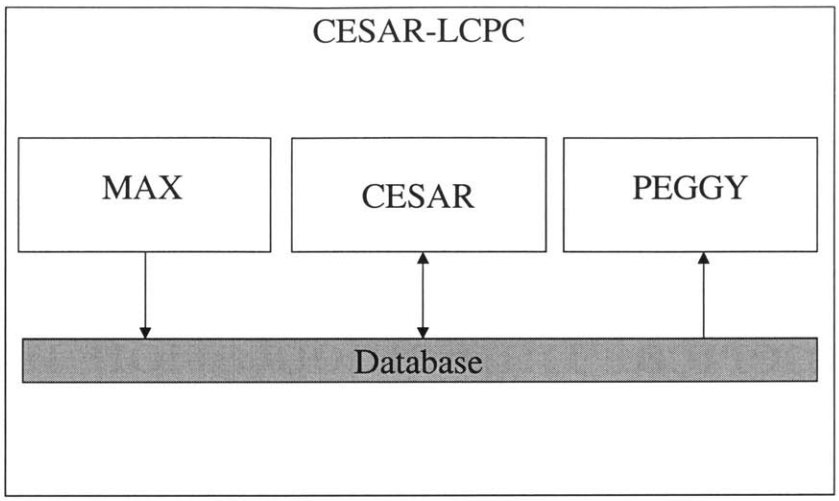

Figure D-1: Overview of the CESAR-LCPC program structure.

by CESAR. PEGGY2D and PEGGY3D denote the two and three-dimensional versions of this program, respectively.

Figure D-1 gives an overview of the program structure. CESAR-LCPC contains the standard capacities of solid and structural mechanics problems. More uncommon are the program modules for linear and nonlinear poromechanical problems (MPLI, MPNL), which allow a finite element calculation with algorithms based on the Biot-Coussy [41] theory of porous media.

D.1.2 Organization of CESAR

CESAR is divided in its organization into different entities. Figure D-2 gives a schematic overview to facilitate the understanding of the architecture. The principal program is the backbone of the code which treats the general configuration of the calculation and the dialogue with the user. The input treatment modules are program parts that are general to the code in which the physical representation (coordinates, elements etc.) are treated. The calculation modules, like MPNL or LIXI which are used in this study treat specific mechanical problems and contain the specific algorithm for the solution of the modeled problem. The finite elements are classified in families which each have a number. They are to be used in connection with

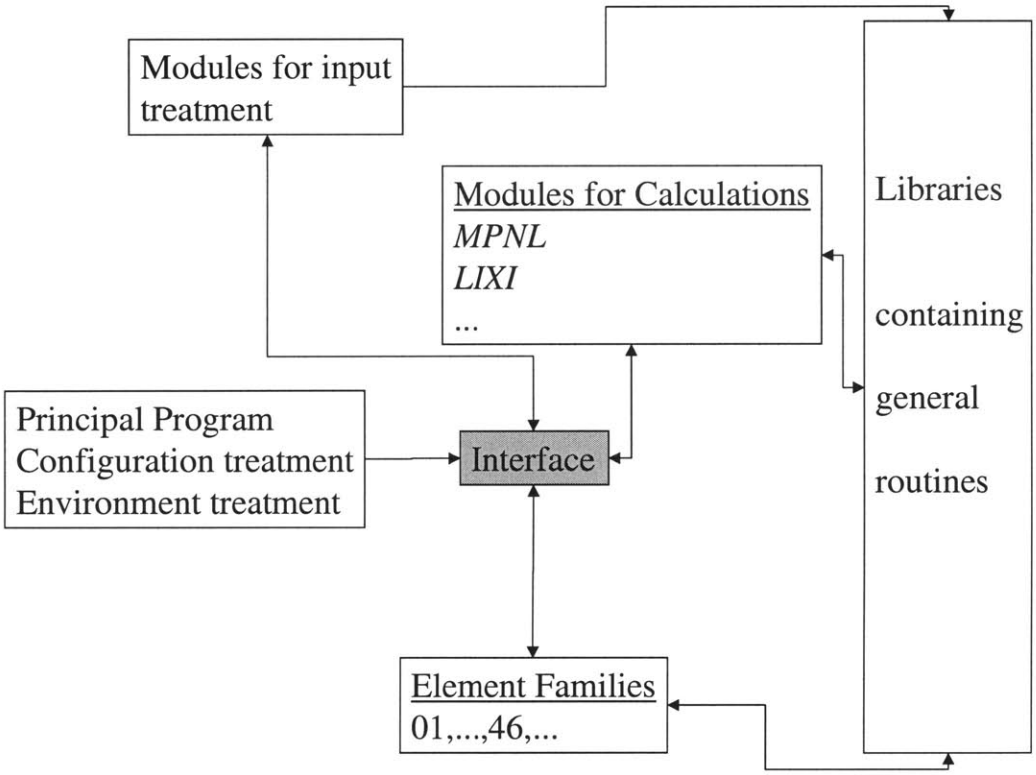

Figure D-2: Schematic representation of the CESAR architecture.

a calculation module. For example, if MPNL is the calculation module, the finite element family must be adapted to porous media problems, which is the case of families 45 and 46. In addition, a library with general routines exists. They are mostly not specific to an element family or module and can be called at any time. The switch between the different parts of the program is organized by an interface. This program part depends on the initial set of problem properties (calculation module, element family, sequence in overall calculation) direct the computing flow to the right place.

D.1.3 Intervention Levels

The program architecture of CESAR allows intervention at different levels:

- The integration point level: Programing at the integration point level means that an existing element family and calculation module is being used. Additions and changes are made within a preexisting algorithm once it is in a loop over the integration points. An example for this are return mapping algorithms in plasticity which are treated in CESAR at the integration point level.

- The element level: Intervention at the element level refers to changes that concern a whole element. An example is the introduction of new degrees of freedom in an element, which requires the creation of a new element family.

- The calculation module level: At the calculation module level, an intervention can be the change of the problem algorithm, that adds a new feature. An example for this is the switch from a Newton-Raphson to a Fixed-Point solution technique of the global stiffness matrix.

- The principal program level: At the principal program level, an intervention can take place as well. This could be for example the creation of a new calculation module.

Included in the mentioned intervention levels are changes or additions in the library routines that are associated to changes in the calculation modules, element families or input treatment modules.

D.2 FE Formulation of the Dissolution-Transport Part

This section deals with the finite element formulation of the dissolution-transport part of the constitutive model that was presented in Chapter 9. In CESAR, it is contained in a new calculation module, LIXI, which was created by Mainguy [91] at MIT. It will be included in the standard CESAR-LCPC body. Some changes to LIXI are necessary for the specific two-front model that we consider.

D.2.1 Model Considered in LIXI

The calculation module LIXI is capable of solving a general non-linear dissolution-diffusion problem in a porous medium. The general equation that is being solved is

$$F_1(u)\frac{\partial u}{\partial t} + \frac{\partial F_2(u)}{\partial t} - \nabla \cdot (F_3(u)\nabla F_4(u)) + \nabla \cdot (F_4(u)\mathbf{V}) = 0 \tag{D.1}$$

where u is the unknown. The functions F_i are piecewise linear functions of u. $\mathbf{V}$ is a fluid velocity in the case, advection is being considered. Depending on the choice of u and F_i, very different diffusion problems can be solved. For a complete overview see [91]. For the solution of the two-front leaching approach, the following specifications are made: $u = \left[Ca^{2+}\right]_s$, the calcium concentration in the solid. The following functions F_i are chosen:

$$F_1(u) = 1;\ F_2(u) = \phi\left[Ca^{2+}\right]_{sol};\ F_3(u) = \phi D(\phi);\ F_4(u) = \left[Ca^{2+}\right]_{sol} \tag{D.2}$$

The equilibrium conditions for the two leaching fronts (Eqs. (9.78) and (9.79))are considered through a relation between the calcium concentration in the solid and in the fluid phase:

$$\left[Ca^{2+}\right]_{sol} = F\left(\left[Ca^{2+}\right]_s\right) \tag{D.3}$$

Figure D-3 shows a formal representation of this relation in which the equilibrium concentrations for the two fronts explicitly intervene. In addition, boundary conditions and initial conditions need to be specified. The initial condition reads:

$$u(t=0) = u_0 = \left[Ca^{2+}\right]_s^0 \tag{D.4}$$

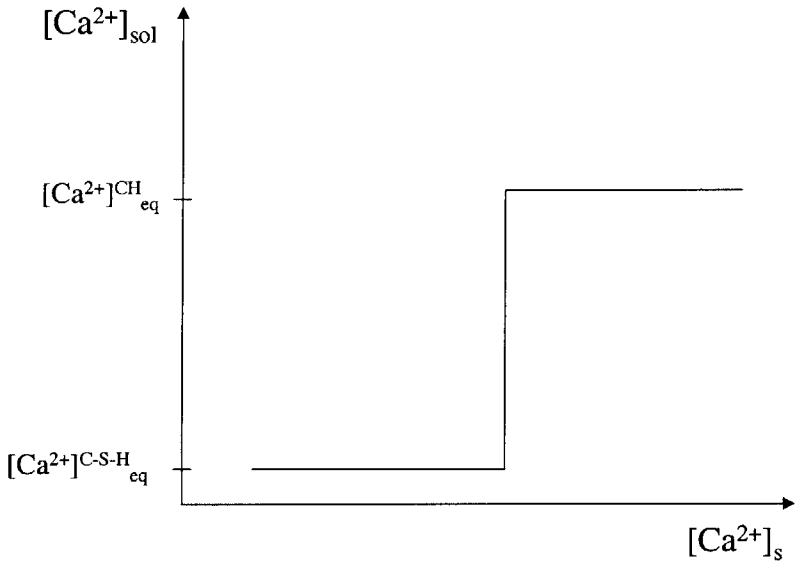

Figure D-3: Representation of the equilibrium relation between solid and solute calcium concentration which replaces the two individual sets of equilibrium conditions.

in which the initial calcium concentration in the solid is being fixed. Boundary conditions on the contour Γ of the considered geometry Ω are either directly related to the unknown or the flux and read:

$$\begin{cases} \text{Parameter imposed on } \Gamma_u : & u = \overline{u} \\ \text{Entering Flux imposed on } \Gamma_q : & F_3(u)\,\nabla F_4(u)\cdot\mathbf{n} - F_4(u)\,\mathbf{V}\cdot\mathbf{n} = \overline{q} \end{cases} \tag{D.5}$$

where Γ_u and Γ_q are the two complementary parts of the contour of Ω.

D.2.2 Solution in CESAR-LCPC@MIT

The leaching problem given by Equations (D.1), (D.4) and (D.5) is solved in CESAR in the calculation module LIXI. The solution is based on the variational formulation which reads [91]: Find $u \in \mathcal{D}_{\overline{u}}$ such that for all $v \in \mathcal{D}_0$ we have:

$$\int_\Omega F_3(u)\,\nabla F_4(u)\cdot\nabla v d\Omega + \int_\Omega F_1(u)\frac{\partial u}{\partial t} v d\Omega + \int_\Omega \frac{\partial F_2(u)}{\partial t} v d\Omega = \int_{\Gamma_q} \overline{q} v d\Gamma \tag{D.6}$$

where $\mathcal{D}_{\overline{u}}$ and $\mathcal{D}_0$ are vector spaces defined on Ω that are sufficiently regular and that satisfy $u = \overline{u}$ on Γ_u. The variational problem is discretized by the finite element method. The time derivatives in Equation (D.6) are approximated with an implicit Euler scheme:

$$\frac{\partial u}{\partial t} \simeq \frac{u^{t+\Delta t} - u^t}{\Delta t} \tag{D.7}$$

which guarantees unconditional stability of the solution scheme. The unknown u and v are discretized with interpolation functions:

$$u_n = \sum_{j=1}^{n_t} u_j \mathrm{N}_j;\ v_n = \sum_{i=1}^{n_t} v_i N_i \tag{D.8}$$

where n is the node number and n_t is the total number nodes. A similar discretization is assumed for the functions F_i. The variational formulation leads to n equations for the n unknowns $u_j^{t+\Delta t}$.

The i-th equation reads:

$$
\begin{aligned}
&\sum_{j=1}^{n}\int_{\Omega} F_3\Big(\sum_{k=1}^{n_t} u_k^{t+\Delta t}N_k\Big)\boldsymbol{\nabla}N_j.\boldsymbol{\nabla}N_i\,d\Omega\;F_4(u_j^{t+\Delta t})\\
&+\sum_{j=1}^{n}\int_{\Omega}\frac{1}{\Delta t}F_1\Big(\sum_{k=1}^{n_t} u_k^{t+\Delta t}N_k\Big)N_jN_i\,d\Omega\;(u_j^{t+\Delta t}-u_j^t)\\
+\;&\sum_{j=1}^{n}\int_{\Omega}\frac{1}{\Delta t}N_jN_i\,d\Omega\;\big(F_2(u_j^{t+\Delta t})-F_2(u_j^t)\big)=\int_{\Gamma_q}\bar{q}v\,d\Gamma\\
&-\sum_{j=n+1}^{n_t}\int_{\Omega} F_3\Big(\sum_{k=1}^{n_t} u_k^{t+\Delta t}N_k\Big)\boldsymbol{\nabla}N_j.\boldsymbol{\nabla}N_i\,d\Omega\;F_4(\bar{u}_j^{t+\Delta t})\\
&-\sum_{j=n+1}^{n_t}\int_{\Omega}\frac{1}{\Delta t}F_1\Big(\sum_{k=1}^{n_t} u_k^{t+\Delta t}N_k\Big)N_jN_i\,d\Omega\;(\bar{u}_j^{t+\Delta t}-\bar{u}_j^t)\\
&-\sum_{j=n+1}^{n_t}\int_{\Omega}\frac{1}{\Delta t}N_jN_i\,d\Omega\;\big(F_2(\bar{u}_j^{t+\Delta t})-F_2(\bar{u}_j^t)\big)
\end{aligned}
\tag{D.9}
$$

This non linear problem is linearized. The matrices for the linear system are composed of contributions from the different elements. For each individual element Ω_e we note the following terms:

$$
g_i^{34}=\sum_{p=1}^{n}\int_{\Omega_e} F_3\Big(\sum_{k=1}^{n_t} u_k^{t+\Delta t}N_k\Big)\boldsymbol{\nabla}N_p\,.\,\boldsymbol{\nabla}N_i\,d\Omega_e\;F_4(u_p^{t+\Delta t}) \tag{D.10}
$$

$$
g_i^{1}=\sum_{p=1}^{n}\int_{\Omega_e}\frac{1}{\Delta t}F_1\Big(\sum_{k=1}^{n_t} u_k^{t+\Delta t}N_k\Big)N_pN_i\,d\Omega_e\;(u_p^{t+\Delta t}-u_p^t) \tag{D.11}
$$

$$
g_i^{2}=\sum_{p=1}^{n}\int_{\Omega}\frac{1}{\Delta t}N_pN_i\,d\Omega\;\big(F_2(u_p^{t+\Delta t})-F_2(u_p^t)\big) \tag{D.12}
$$

The non linear system is solved with the Newton-Raphson technique. The vector $\mathbf{U}^\alpha$ with the u_i^α as components is defined. Its initial value is given by

$$
\mathbf{U}^1=\mathbf{U}^t \tag{D.13}
$$

and then for the next steps:

$$
\mathbf{U}^{\alpha+1}=\mathbf{U}^\alpha+\boldsymbol{\Delta}_\alpha \tag{D.14}
$$

where $\mathbf{\Delta}_\alpha$ is the solution of the linear system in which the i-th component of the right hand side contains partly the terms g_i^{34}, g_i^1 and g_i^2. In addition, the $i-j$ term of the matrix contains the partial derivatives of g_i^{34}, g_i^1 and g_i^2 with respect to the component $u_j^{t+\Delta t}$ of $\mathbf{U}^{t+\Delta t}$. The term g_i^{34} leads to an elementary conduction matrix that reads:

$$\int_{\Omega_e} F_3\Big(\sum_{k=1}^{n_t} u_k^{t+\Delta t} N_k\Big) \boldsymbol{\nabla} N_j . \boldsymbol{\nabla} N_i \, d\Omega_e \; F_4'(u_j^{t+\Delta t}) \tag{D.15}$$

and to a tangent conduction matrix:

$$\int_{\Omega_e} F_3'\Big(\sum_{k=1}^{n_t} u_k^{t+\Delta t} N_k\Big) \Big[\sum_{p=1}^{n} F_4(u_p^{t+\Delta t}) \boldsymbol{\nabla} N_p\Big] . \boldsymbol{\nabla} N_i N_j \, d\Omega_e \tag{D.16}$$

Moreover, the term g_i^1 leads to the storage matrix:

$$\int_{\Omega_e} \frac{1}{\Delta t} F_1\Big(\sum_{k=1}^{n_t} u_k^{t+\Delta t} N_k\Big) \, N_j N_i \, d\Omega_e \tag{D.17}$$

and to the tangent storage matrix:

$$\int_{\Omega_e} \frac{1}{\Delta t} F_1'\Big(\sum_{k=1}^{n_t} u_k^{t+\Delta t} N_k\Big) \Big[\sum_{p=1}^{n} N_p (u_p^{t+\Delta t} - u_p^t)\Big] \, N_i N_j \, d\Omega_e \tag{D.18}$$

Finally, g_i^2 leads to an elementary matrix associated to the source term:

$$\int_{\Omega_e} \frac{1}{\Delta t} N_j N_i \, d\Omega_e \; F_2'(u_j^{t+\Delta t}) \tag{D.19}$$

These matrices lead to a non symmetric elementary matrix. In addition, a mass lumping option exists, which diagonalizes the elementary matrices corresponding to (D.11) and (D.12). This technique which has received quite some attention in the finite element literature (see for example [69] for an overview and [67, 145, 53]), minimizes the oscillation of the solution around sharp dissolution fronts. It is used in a way that the total mass is conserved in which case convergence is guaranteed [69]. This leads to an equivalence with the finite volume method [92], if linear interpolation elements are employed.

D.2.3 Typical Input Data Format and Output Results

The calculations of the leaching problem are performed with the module LIXI. The module uses the steering variable IMOD with a value of 90 for an ordinary leaching problem and 96 in the presence of advection. Table D.1 shows the input data format that is required in conjunction with the key word ELEM. ELEM is part of the input treatment routines that assign the material properties to the calculation. The input data for the calculation module LIXI are given in Table D.2. They determine the method of numerical solution of the equation system and the time steps. The result of the leaching calculation is a calcium concentration field in the solid phase (or more generally a distribution of the unknown u) in Ω. This distribution can be visualized in the post processor Peggy. At the end of the leaching calculation, a result file is written by LIXI which contains the calcium concentration for the final time step at every node plus the node coordinates. LIXI uses elements of the family 21 which limits its applications to two-dimensional problems.

D.3 FE-Formulation of the Mechanical Part

D.3.1 Introduction

Following the staggered scheme (see Sections 9.5 and 10.2), the mechanical model part is implemented in a different module than the leaching part. In CESAR-LCPC, the module MPNL solves poroplasticity problems of saturated porous media. This module is chosen as the backbone for the implementation of our model into CESAR. In the following, the discretized equations of the mechanical model are presented and the developed return mapping algorithm [134] for multisurface poroplasticity are detailed.

D.3.2 Degradation State

The degradation state is determined through the local values of the chemical porosity. LIXI provides the data for the field variable calcium concentration. The chemical porosity calculated according to Eq. (9.55) at the integration points. Although LIXI provides only a two-dimensional data field, in MPNL a two-dimensional or three-dimensional calculation can be performed with the families 45 (2D) or 46(3D). In the case of the three-dimensional calculation,

TITLE	
IMOD, INAT	
NC	Number of values that define the piecewise linear F_i
D_x, D_y, D_{xy}	Reference values for the diffusion tensor ass. with F_3
C_1, C_4, C_2	Reference values for the functions F_1, F_4, F_2
I_3, I_1, I_2	Indicators constant/variable for the functions F_3, F_3, F_2
	$I_i = 0 \rightarrow F_i$ constant
	$I_i = 1 \rightarrow F_i$ piecewise linear
	$I_3 = 2 \rightarrow F_3$ is an exponential function of the porosity
IF $I_3 = 2 : D_1, D_2$	Coefficients of the exponential diffusion law $D(\phi) = \exp(D_1\phi - D_2)$
$F_1(I), I = 1$,NC	Discrete values of F_1 in increasing order
IF $I_3 = 1 : F_3(I), I = 1$,NC	Discrete values of F_3
IF $I_3 = 2 :$ PORO$(I), I = 1$,NC	Discrete values of the total porosity
$F_4(I), I = 1$,NC	Discrete values of F_4
IF $I_2 = 1 : F_2(I), I = 1$,NC	Discrete values of F_2

Table D.1: Input format for the key word ELEM in a leaching input file of CESAR-LCPC, used with LIXI

LIXI	
M	Printing variable
METHOD	Numerical solution method
	METHOD=N → Newton Raphson
	METHOD=P → Fixed Point
	METHOD=M → First Fixed Point and Newton Raphson when the variation of the unknown is smaller that 0.01
NITER, TOL	Number of iterations (NITER) and tolerance (TOL) on unknown
IND_CM	Mass lumping indicator:
	IND_CM=0: No mass lumping
	IND_CM=1: Mass lumping activated
Δ_{obj}	Variable for the time step variation. Used to compare with the relative variation of the unknown between two time steps. Increasing Δ_{obj} decreases the total calculation time
NENL	Number of groups with non linear exchange elements
NPAS1	Number of time steps (=NPAS+1)
T_0 ($\Delta T(I)$, I=1, NPAS)	Time origin (T_0) and the time step values

Table D.2: Input format for the key word LIXI in a leaching input file of CESAR-LCPC

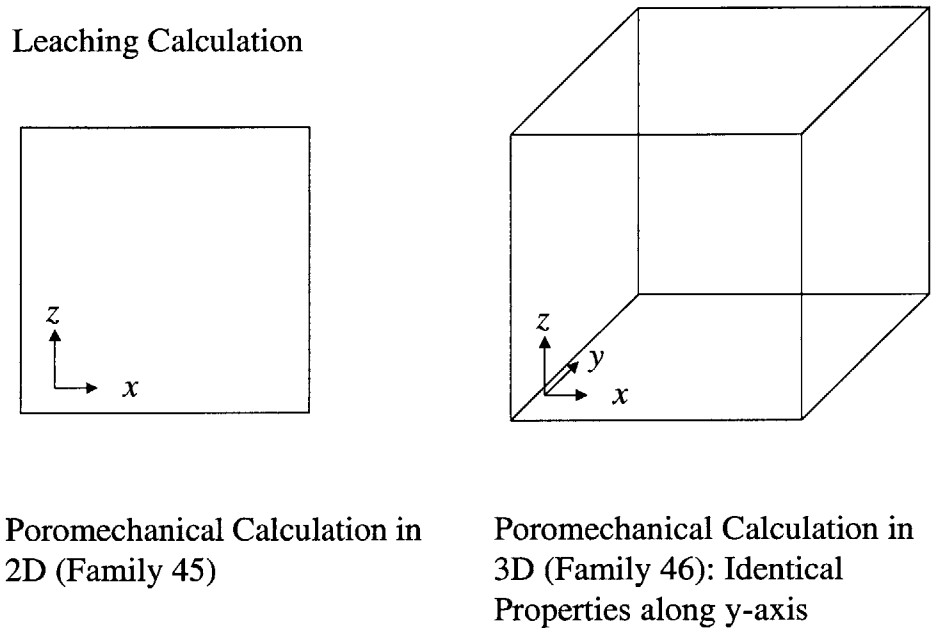

Figure D-4: Schematical presentation of the three-dimensional operating mode, using family 46: From the two-dimensional leaching calculation chemical porosities in three dimensions are assigned by a translation along the y-axis.

the results from the leaching calculation are assigned to the 3D mechanical calculation assuming that no variation with respect to one axis takes place. Figure D-4 illustrates this procedure.

D.3.3 Field Equations

The poroplastic problem needs to be discretized in time. We consider the problem between times t_n and t_{n+1} so that $t_{n+1} = t_n + \Delta t$. The time derivative of a function reads:

$$\frac{df}{dt} = \frac{f_{n+1} - f_n}{t_{n+1} - t_n} = \frac{\Delta f}{\Delta t} \tag{D.20}$$

In addition, the function f is discretized with an implicit scheme:

$$f(t_n + \Delta t) = f(t_{n+1}) \tag{D.21}$$

which assures unconditional stability[1]. The three field equations that need to be satisfied in the considered domain Ω are the static equilibrium:

$$\text{In } \Omega : \boldsymbol{\nabla} \cdot \boldsymbol{\Sigma} + \rho \mathbf{f} = \mathbf{0} \tag{D.22}$$

the fluid mass conservation:

$$\text{In } \Omega : \boldsymbol{\nabla} \cdot \mathbf{w} + \frac{\partial m_f}{\partial t} = 0 \tag{D.23}$$

and the heat equation:

$$\text{In } \Omega : \boldsymbol{\nabla} \cdot \mathbf{q} + T_0 \left[\frac{\partial S}{\partial t} - s_m^0 \frac{\partial m_f}{\partial t} \right] = 0 \tag{D.24}$$

these three field equations are discretized, using the introduced discretization scheme and denoting $\boldsymbol{\Sigma}_{n+1} = \boldsymbol{\Sigma}_n + \Delta\boldsymbol{\Sigma}$ etc.:

$$\boldsymbol{\nabla} \cdot (\Delta\boldsymbol{\Sigma}) + \rho_0 \Delta \mathbf{f} = \mathbf{0} \tag{D.25}$$

$$\boldsymbol{\nabla} \cdot (\mathbf{w}_n + \Delta\mathbf{w}) + \frac{\Delta m_f}{\Delta t} = 0 \tag{D.26}$$

$$\boldsymbol{\nabla} \cdot (\mathbf{q}_n + \Delta\mathbf{q}) + T_0 \frac{\Delta \left(S - s_m^0 m_f \right)}{\Delta t} = 0 \tag{D.27}$$

[1]This means that the time step Δt can be chosen without restrictions and still guaranteeing convergence. This is of interest in porous media problems where the asymptotical regime is usually calculated using very large time steps.

The field equations(D.25) through (D.27) are complemented with boundary conditions which read in a discretized form:

$$\Delta\boldsymbol{\Sigma}\cdot\mathbf{n} = \Delta\mathbf{T}^d \text{ on } \Gamma_{\mathbf{T}} \tag{D.28}$$

$$\Delta\mathbf{u} = \Delta\mathbf{u}^d \text{ on } \Gamma_{\mathbf{u}} \tag{D.29}$$

$$\Delta p = \Delta p^d \text{ on } \Gamma_p \tag{D.30}$$

$$\Delta\mathbf{w}_f\cdot\mathbf{n} = \Delta w_f^d \text{ on } \Gamma_w \tag{D.31}$$

$$\Delta T = \Delta T^d \text{ on } \Gamma_{T^d} \tag{D.32}$$

$$\Delta\mathbf{q}\cdot\mathbf{n} = \Delta q^d \text{ on } \Gamma_{q^d} \tag{D.33}$$

where Γ is the boundary of Ω. In addition, the mass flux and heat flux read as a function of the pressure and temperature gradients, respectively:

$$\frac{\Delta\mathbf{w}}{\rho_o^f} = -k\mathbf{1}\cdot\left(\boldsymbol{\nabla}\left(\Delta p\right) - \rho_o^f\Delta\mathbf{f}\right) \tag{D.34}$$

$$\frac{\Delta\mathbf{q}}{T_o} = -\frac{\mathbf{K}}{T_0}\cdot\boldsymbol{\nabla}\left(\Delta T\right) \tag{D.35}$$

where $\mathbf{K}$ is the heat conductivity matrix.

D.3.4 Variational Formulation

In the following, the implemented variational formulation in MPNL is described. The thermo-poroelastic state equations (see Chapter 9) read in a discretized form:

$$\begin{pmatrix} \Delta\Sigma \\ -\frac{\Delta m_f}{\rho_o^f} \\ -\Delta\left(S - s_m^0 m_f\right) \end{pmatrix} = \begin{pmatrix} \mathbb{C}_0 & -\mathbf{B} & -\mathbf{A}_0 \\ -\mathbf{B} & -\frac{1}{M} & 3\alpha_m \\ -\mathbf{A}_0 & 3\alpha_m & -\frac{C_\varepsilon^0}{T_0} \end{pmatrix} \begin{pmatrix} \Delta\mathbf{E} \\ \Delta p \\ \Delta T \end{pmatrix} \tag{D.36}$$

in which the elastic poroelastic properties depend on the degradation state, expressed through the chemical porosity. Note that in the existing implementation not the change in porosity but the change in the fluid mass is chosen as a state variable. The variational formulation of the

field equations can be written as:

$$\begin{aligned}
&\int_\Omega \begin{pmatrix} \Delta\mathbf{E} \\ \Delta p \\ \Delta T \end{pmatrix}^T \begin{pmatrix} \mathbb{C}_0 & -\mathbf{B} & -\mathbf{A}_0 \\ -\mathbf{B} & -\frac{1}{M} & 3\alpha_m \\ -\mathbf{A}_0 & 3\alpha_m & -\frac{C_\varepsilon^0}{T_0} \end{pmatrix} \begin{pmatrix} \Delta\mathbf{E}' \\ \Delta p' \\ \Delta T' \end{pmatrix} d\Omega \\
&-\Delta t \int_\Omega \begin{pmatrix} \boldsymbol{\nabla}(\Delta p) \\ \boldsymbol{\nabla}(\Delta T) \end{pmatrix}^T \begin{pmatrix} K & 0 \\ 0 & \frac{K}{T_0} \end{pmatrix} \begin{pmatrix} \boldsymbol{\nabla}\left(\Delta p'\right) \\ \boldsymbol{\nabla}\left(\Delta T'\right) \end{pmatrix} d\Omega \qquad \text{(D.37)} \\
-\ & F\left(\Delta\mathbf{u}', \Delta p', \Delta T'\right) = 0
\end{aligned}$$

where the test fields $\Delta\mathbf{u}'$, $\Delta p'$ and $\Delta T'$ are admissible but otherwise arbitrary fields. The linear form $F\left(\Delta\mathbf{u}', \Delta p', \Delta T'\right)$ is given by:

$$\begin{aligned}
F\left(\Delta\mathbf{u}', \Delta p', \Delta T'\right) \ = \ & \Delta t \int_\Omega \begin{pmatrix} \boldsymbol{\nabla}(p_n) \\ \boldsymbol{\nabla}(T_n) \end{pmatrix}^T \begin{pmatrix} K & 0 \\ 0 & \frac{K}{T_0} \end{pmatrix} \begin{pmatrix} \boldsymbol{\nabla}\left(\Delta p'\right) \\ \boldsymbol{\nabla}\left(\Delta T'\right) \end{pmatrix} d\Omega \\
& + \int_\Omega \rho_0 \Delta\mathbf{f}\cdot\Delta\mathbf{u}' d\Omega + \int_{\Gamma_{\mathbf{T}^d}} \Delta\mathbf{T}^d \cdot \Delta\boldsymbol{\xi}' + \Delta t \int_{\Gamma_{q^q}} \Delta T' \frac{q^d}{T_0} dA \qquad \text{(D.38)} \\
& + \Delta t \int_\Omega \boldsymbol{\nabla}\left(\Delta p'\right) \cdot \mathbf{K}\rho_0 \Delta\mathbf{f} d\Omega + \int_{\Gamma_{w^d}} \Delta p' \frac{w^d}{\rho_0^f} dA
\end{aligned}$$

This variational formulation is then discretized spatially with finite elements of family 45 or 46.

D.3.5 Solution in the Case of Plasticity

When plastic evolutions are considered, the state equations include the plastic porosity and plastic strains (Chapter 9) and read in a discretized form:

$$\begin{pmatrix} \Delta\Sigma \\ -\frac{\Delta m_f}{\rho_o^f} + \Delta\phi^p + \Delta\phi^c \\ -\Delta\left(S - s_m^0 m_f\right) \end{pmatrix} = \begin{pmatrix} \mathbb{C}_0 & -\mathbf{B} & -\mathbf{A}_0 \\ -\mathbf{B} & -\frac{1}{M} & 3\alpha_m \\ -\mathbf{A}_0 & 3\alpha_m & -\frac{C_\varepsilon^0}{T_0} \end{pmatrix} \begin{pmatrix} \Delta\mathbf{E} - \Delta\mathbf{E}^p \\ \Delta p \\ \Delta T \end{pmatrix} \qquad \text{(D.39)}$$

In the following developments, we assume that the increment in chemical porosity, $\Delta\phi^c$, is always zero, consistent with our calculation scheme that assumes that the dissolution occurs prior to any mechanical loading. In addition to the changed state equations, we need to consider

the evolution laws of plasticity. For the developed two surface plasticity model, following the works by Koiter [76], the flow rules read as the sum of the individual contributions:

$$\begin{cases} \Delta \mathbf{E}^p = \sum \Delta\lambda_i \frac{\partial f_i}{\partial \boldsymbol{\Sigma}} \\ \Delta \phi^p = \sum \Delta\lambda_i \frac{\partial f_i}{\partial p} \end{cases} \tag{D.40}$$

where

$$\begin{cases} \Delta\lambda_i \geq 0 \text{ if } f_i = 0 \\ \Delta\lambda_i = 0 \text{ if } f_i \leq 0 \end{cases} \tag{D.41}$$

Within a time step, the poroplastic problem needs to be solved by an iterative procedure, owing to the non-linearity of the problem. We assume that the variables are known at iteration k, that is $\Delta\mathbf{u}_k$, Δp_k, etc. For $k = 0$, all variables are zero. To determine the solution for a given time step, a particular solution algorithm needs to be applied. We choose a return mapping algorithm.

D.3.6 Return Mapping Algorithm

The Return Mapping Algorithm is a numerical solution technique that transforms a plasticity problem in an optimization problem for which standard solution techniques exist. Particularly Simo and Hughes [134] can be credited for the development of algorithms in this field. For the poroplastic problem at hand, the following return mapping algorithm is proposed.

Initial Linear Problem

We assume that at the end of the k-th iteration step, the state of the poroplastic system is known, and given by the variable set:

$$\{\Delta\mathbf{E}, \Delta\mathbf{E}^p, \Delta\phi^p, \Delta p, \Delta T\}_k = \{\Delta\mathbf{E}_k, \Delta\mathbf{E}^p_k, \Delta\phi^p_k, \Delta p_k, \Delta T_k\} \tag{D.42}$$

The displacement increment in the next time step, $\Delta\mathbf{u}_{k+1}$ leads to an increment in total strains:

$$\Delta\mathbf{E}_{k+1} = \boldsymbol{\nabla}^s (\Delta\mathbf{u}_{k+1}) \tag{D.43}$$

The same holds for the increments in pressure Δp_{k+1} and temperature ΔT_{k+1} which are determined from the loading conditions at the beginning of the time step. In a first step the elastic solution is determined, using the variational formulation presented before and the following state equations:

$$\begin{pmatrix} \Delta\boldsymbol{\Sigma}_{k+1} \\ -\frac{\Delta m_f^{k+1}}{\rho_o^f} + \Delta\phi_k^p \\ -\Delta\left(S_{k+1} - s_m^0 m_f^{k+1}\right) \end{pmatrix} = \begin{pmatrix} \mathbb{C}_0 & -\mathbf{B} & -\mathbf{A}_0 \\ -\mathbf{B} & -\frac{1}{M} & 3\alpha_m \\ -\mathbf{A}_0 & 3\alpha_m & -\frac{C_\epsilon^0}{T_0} \end{pmatrix} \begin{pmatrix} \Delta\mathbf{E}_{k+1} - \boldsymbol{\Delta}\mathbf{E}_k^p \\ \Delta p_{k+1} \\ \Delta T_{k+1} \end{pmatrix} \tag{D.44}$$

where it should be noted that the plastic deformation and porosity belong to the prior iteration step. They are "frozen" in the beginning of the new iteration.

Non Linear Problem

Once the linear changes in pressure, temperature and displacement are obtained, additional increments need to be determined that lead to a plastically admissible solution. More precisely, the following set of equations needs to be solved:

$$\begin{pmatrix} \Delta\boldsymbol{\Sigma}_{k+1}^* \\ -\frac{\Delta m_{k+1}^*}{\rho_o^f} + \Delta\phi_{k+1}^p \\ -\Delta\left(S_{k+1}^* - s_m^0 m_{k+1}^*\right) \end{pmatrix} = \begin{pmatrix} \mathbb{C}_0 & -\mathbf{B} & -\mathbf{A}_0 \\ -\mathbf{B} & -\frac{1}{M} & 3\alpha_m \\ -\mathbf{A}_0 & 3\alpha_m & -\frac{C_\epsilon^0}{T_0} \end{pmatrix} \begin{pmatrix} \Delta\mathbf{E}_{k+1} - \Delta\mathbf{E}_{k+1}^p \\ \Delta p_{k+1} \\ \Delta T_{k+1} \end{pmatrix} \tag{D.45}$$

$$\begin{cases} \Delta\mathbf{E}_{k+1}^p = \sum \Delta\lambda_i \frac{\partial f_i\left(\Sigma_n + \Delta\Sigma_{k+1}^*, p_n + \Delta p_{k+1}\right)}{\partial\boldsymbol{\Sigma}} \\ \Delta\phi_{k+1}^p = \sum \Delta\lambda_i \frac{\partial f_i\left(\Sigma_n + \Delta\Sigma_{k+1}^*, p_n + \Delta p_{k+1}\right)}{\partial p} \end{cases} \tag{D.46}$$

$$\begin{cases} \Delta\lambda_i \geq 0 \text{ if } f_i\left(\Sigma_n + \Delta\Sigma_{k+1}^*, p_n + \Delta p_{k+1}\right) = 0 \\ \Delta\lambda_i = 0 \text{ if } f_i\left(\Sigma_n + \Delta\Sigma_{k+1}^*, p_n + \Delta p_{k+1}\right) \leq 0 \end{cases} \tag{D.47}$$

This system of equations can be solved by introducing the following trial stress state:

$$\boldsymbol{\Sigma}_{n+1}^{trial} = \boldsymbol{\Sigma}_n + \mathbb{C}_0 : \Delta\mathbf{E}_{k+1} - \mathbf{B}\Delta p_{k+1} - \mathbf{A}_0\Delta T_{k+1} \tag{D.48}$$

With the trial stress state calculated, the loading function is checked to determine whether plastic flow occurs. If only one loading surface exists, this reads:

$$f\left(\boldsymbol{\Sigma}_{n+1}^{trial}\right) > 0 \rightarrow \Delta\lambda_{n+1} > 0 \tag{D.49}$$

$$f\left(\boldsymbol{\Sigma}_{n+1}^{trial}\right) < 0 \rightarrow \Delta\lambda_{n+1} = 0 \tag{D.50}$$

However, in the case of multisurface plasticity, the format is [134]:

$$f_i\left(\boldsymbol{\Sigma}_{n+1}^{trial}\right) > 0 \rightarrow \Delta\lambda_{i,n+1} > 0 \vee \Delta\lambda_{i,n+1} = 0 \tag{D.51}$$

$$f_i\left(\boldsymbol{\Sigma}_{n+1}^{trial}\right) < 0 \rightarrow \Delta\lambda_{i,n+1} = 0 \tag{D.52}$$

In other words, in contrast to single surface plasticity, the fact that the loading function has a positive value for the trial state is not sufficient to determine whether the loading surface is actually active. Strategies to determine the active loading surfaces were presented by Simo and Hughes [134]. Once the active loading surfaces are known, the plastic multipliers and plastic variables are obtained through a correction of the trial stress so that the loading surfaces become inactive. This reads:

$$\begin{cases} f_\alpha\left(\Sigma_n + \Delta\Sigma_{k+1}^*, p_n + \Delta p_{k+1}\right) = 0 \\ \text{with } \Sigma_n + \Delta\Sigma_{k+1}^* = \boldsymbol{\Sigma}_{n+1}^{trial} - \mathbb{C}_0 : \sum_{\alpha \in J_{act}} \Delta\lambda_{\alpha,n+1} \frac{\partial f_\alpha}{\partial \boldsymbol{\Sigma}} \end{cases} \tag{D.53}$$

where J_{act} denotes the set of active yield surfaces:

$$J_{act} = \left\{\alpha \in 1, 2, ..., N \mid f_\alpha\left(\boldsymbol{\Sigma}_{n+1}^{trial}\right) = 0\right\} \tag{D.54}$$

Equation (D.53) serves to obtain the plastic strains and porosity. Geometrically, equating the plastic deformations in a way that the stress state meets the loading conditions corresponds to an orthogonal projection of the trial stress state on the plastically admissible stress surface [134, 79]. The updated stress $\Sigma_n + \Delta\Sigma_{k+1}^*$ fulfills the loading functions. However, it is not certain that the updated stress fields are statically admissible or that the fluid and heat flux etc., still meet the conservation field equations. The complete procedure therefore needs to be repeated until both the field equations and the plastic equations are satisfied.

D.3.7 Return Mapping Algorithm for the chosen Loading Surfaces

The two loading surfaces considered are the Drucker-Prager surface and the Cam-Clay surface introduced in Chapter 9. The trial values of the two surfaces read:

$$f_{DP,n+1}^{trial} = \sqrt{J_{2,n+1}^{trial}} + \delta\left(\Sigma_{M,n+1}^{trial} + p_n + \Delta p_{k+1}\right) - c \tag{D.55}$$

$$f_{CC,n+1}^{trial} = \frac{3J_{2,n+1}^{trial}}{M^2} + \left[\Sigma_{M,n+1}^{trial} + p_n + \Delta p_{k+1} + (p_c - p_t)\right]^2 - (p_c + p_t)^2 \tag{D.56}$$

To facilitate the further treatment of the Cam-Clay criterion, we introduce the notations $d = \sqrt{3}J_2$ and $I = \Sigma_M' = \Sigma_M + p$. We can then rewrite the Cam Clay criterion as:

$$f_{cc} = \frac{d^2}{M^2} + (I - 2p_t)(I + 2p_c) \leq 0 \tag{D.57}$$

With the trial values of the loading surfaces at hand, the active loading surfaces are tested. Different scenarios need to be distinguished:

1. No active yield surface: $f_{DP,n+1}^{trial} \leq 0$ and $f_{CC,n+1}^{trial} \leq 0$. In this case then the loading step is elastic. No further corrections need to be made.

$$\boldsymbol{\Sigma}_{n+1} = \boldsymbol{\Sigma}_{n+1}^{trial} \tag{D.58}$$

2. One active yield surface: $f_{DP,n+1}^{trial} \geq 0$ or $f_{CC,n+1}^{trial} \geq 0$. The plastic strains and porosity calculated for the active surface according to (D.46). The updated stress state is determined through (D.53).

3. Two active yield surfaces: $f_{DP,n+1}^{trial} > 0$ and $f_{CC,n+1}^{trial} > 0$. Either one or both surfaces are active.

   (a) Assumption that only one surface is active. With (D.46) the plastic strains and porosity are determined for the first surface. An updated trial stress state is computed from:

$$\boldsymbol{\Sigma}_{n+1}^{trial*} = \boldsymbol{\Sigma}_{n+1}^{trial} - \mathbb{C}_0 : \Delta\lambda_{1,n+1}\frac{\partial f_1}{\partial \boldsymbol{\Sigma}} \tag{D.59}$$

With the updated trial stress both loading surfaces are tested. If $f^{trial*}_{DP,n+1} \leq 0$ and $f^{trial*}_{CC,n+1} \leq 0$, the modified trial state becomes the new stress state:

$$\boldsymbol{\Sigma}_{n+1} = \boldsymbol{\Sigma}^{trial*}_{n+1} \tag{D.60}$$

If this loading surfaces are active, the trial stress state is reinitialized to $\boldsymbol{\Sigma}^{trial}_{n+1}$. The updated trial stress is recomputed according to:

$$\boldsymbol{\Sigma}^{trial*}_{n+1} = \boldsymbol{\Sigma}^{trial}_{n+1} - \mathbb{C}_0 : \Delta\lambda_{2,n+1}\frac{\partial f_2}{\partial \boldsymbol{\Sigma}} \tag{D.61}$$

With the updated trial stress state both loading surfaces are tested. If $f^{trial*}_{DP,n+1} \leq 0$ and $f^{trial*}_{CC,n+1} \leq 0$, the modified trial state becomes the new stress state:

$$\boldsymbol{\Sigma}_{n+1} = \boldsymbol{\Sigma}^{trial*}_{n+1} \tag{D.62}$$

If this is not the case, both surfaces are active at the same time.

(b) Both surfaces are active at the same time. The plastic strains and porosity are determined according to (D.46). The updated stress state is given through (D.53).

Drucker-Prager Projection Algorithm

The Drucker-Prager projection algorithm is a standard algorithm in most commercially available finite element codes. The discretized flow rules read:

$$\Delta\mathbf{E}^p_{n+1} = \Delta\lambda_{DP,n+1}\left(\frac{\delta}{3}\mathbf{1}+\frac{\mathbf{S}_{n+1}}{2\sqrt{J_{2,n+1}}}\right) = \Delta\lambda_{DP,n+1}\left(\frac{\delta}{3}\mathbf{1}+\mathbf{n}_{n+1}\right) \tag{D.63}$$

$$\Delta\phi^p_{n+1} = \Delta\lambda_{DP,n+1}\delta \tag{D.64}$$

with $\mathbf{n}_{n+1} = \frac{\mathbf{S}_{n+1}}{2\sqrt{J_{2,n+1}}}$. The stress reads in the discretized form:

$$\begin{aligned}\boldsymbol{\Sigma}_{n+1} &= \boldsymbol{\Sigma}_n + \Delta\boldsymbol{\Sigma}^*_{k+1} = \boldsymbol{\Sigma}^{trial}_{n+1} - \mathbb{C}_0 : \Delta\lambda_{DP,n+1}\frac{\partial f_{DP}}{\partial \boldsymbol{\Sigma}} \\ &= \boldsymbol{\Sigma}^{trial}_{n+1} - \Delta\lambda_{DP,n+1}\left[k_0\delta\mathbf{1}+2\mu\mathbf{n}_{n+1}\right]\end{aligned} \tag{D.65}$$

where we made use of the relation $\mathbb{C}_0 = 3k_0\mathbb{K} + 2\mu\mathbb{J}$ [160]. With (D.65), the stress deviator can be written as:

$$\mathbf{S}_{n+1} = \boldsymbol{\Sigma}_{n+1} : \mathbb{J} = \mathbf{S}_{n+1}^{trial} - \Delta\lambda_{DP,n+1} 2\mu \frac{\mathbf{S}_{n+1}}{2\sqrt{J_{2,n+1}}} \tag{D.66}$$

which leads to the trial deviator stress:

$$\mathbf{S}_{n+1}^{trial} = \mathbf{S}_{n+1} \left(1 - 2\mu \frac{\Delta\lambda_{DP,n+1}}{2\sqrt{J_{2,n+1}}} \right) \tag{D.67}$$

In the Drucker-Prager model, the direction of the plastic flow is the same as the direction of the trial deviator stress [134]. Therefore, the plastic multiplier can be obtained from the solution of one algebraic equation:

$$f_{DP}\left(\boldsymbol{\Sigma}_{n+1}\right) = 0 \tag{D.68}$$

which leads to:

$$\Delta\lambda_{DP,n+1} = \frac{c - \delta\left(\Sigma_{M,n+1}^{trial} + p_n + \Delta p_{k+1}\right) - \sqrt{J_{2,n+1}^{trial}}}{k_0\delta^2 + 2\mu} \tag{D.69}$$

from where the plastic strains and the plastic porosity can be calculated. A special situation can occur in a Drucker-Prager yield surface when a stress state is in the corner region of the yield surface. This region is given by [68]:

$$\Sigma_{M,n+1}^{trial} + p_n + \Delta p_{k+1} < \frac{k_0\delta\sqrt{J_{2,n+1}^{trial}}}{2\mu} + \frac{3c}{\delta} \tag{D.70}$$

In this zone, the projection is made to the corner point for which $\sqrt{J_{2,n+1}} = 0$.

Cam-Clay Projection Algorithm

The Cam-Clay projection algorithm follows the developments by Borja and Lee [24] who proposed an implicit formulation for the complete projection algorithm. The discretized form of the flow rule, including the notations employed in (D.57):

$$\begin{aligned} \Delta\mathbf{E}_{n+1}^{p} &= \Delta\lambda_{CC,n+1} \left(\frac{2}{3}\left(I_{n+1} + p_c - p_t\right)\mathbf{1} + \frac{6d_{n+1}}{M^2} \frac{\mathbf{S}_{n+1}}{2\sqrt{J_{2,n+1}}} \right) \\ &= \Delta\lambda_{CC,n+1} \left(\frac{2}{3}\left(I_{n+1} + p_c - p_t\right)\mathbf{1} + \frac{6d_{n+1}}{M^2}\mathbf{n}_{n+1} \right) \end{aligned} \tag{D.71}$$

and the hardening rule reads:

$$p_{c,n+1} = p_{c,n} \exp\left[2\frac{1+e}{\lambda-\kappa}\Delta\lambda_{CC,n+1}\left(I + p_c - p_t\right)\right] \tag{D.72}$$

With the definition of the trial stress state, two scalar equations are obtained for the stress invariants:

$$I_{n+1} = I_{n+1}^{trial} - k_0\Delta\lambda_{CC,n+1}2\left(I_{n+1} + p_c - p_t\right) \tag{D.73}$$

$$d_{n+1} = d_{n+1}^{trial}/\left(1 + \frac{6\mu\Delta\lambda_{CC,n+1}}{M^2}\right) \tag{D.74}$$

Introducing these scalar stress invariants facilitates the calculation of the plastic multiplier which reduces to the solution of a nonlinear scalar equation. To find the plastic multiplier, we solve:

$$f_{cc}\left(\boldsymbol{\Sigma}_{n+1}, p_{c,n+1}\right) = \frac{d_{n+1}^2}{M^2} + \left(I_{n+1} - 2p_t\right)\left(I_{n+1} + 2p_{c,n+1}\right) = 0 \tag{D.75}$$

This is a nonlinear equation for $\Delta\lambda_{CC,n+1}$ and which also includes a coupling between I_{n+1} and p_c via (D.73). It is solved with a two-level Newton iteration as proposed by Borja and Lee [24].

Corner Zone Algorithm

A corner zone algorithm needs to be used when both yield surfaces are active. To economize the calculation time, an explicit treatment of the routine was chosen, while plastic hardening is frozen during the iteration. The discretized form of the flow rule reads:

$$\Delta\mathbf{E}_{n+1}^p = \Delta\lambda_{DP,n+1}\left(\frac{\delta}{3}\mathbf{1} + \mathbf{n}_{n+1}\right) + \Delta\lambda_{CC,n+1}\left(\frac{2}{3}\left(I_{n+1} + p_{c,n} - p_t\right)\mathbf{1} + \frac{6d_{n+1}}{M^2}\mathbf{n}_{n+1}\right) \tag{D.76}$$

where $p_{c,n}$ is the consolidation pressure of the prior iteration. The sought stress state then reads:

$$\boldsymbol{\Sigma}_{n+1} = \boldsymbol{\Sigma}_{n+1}^{trial} - \Delta\lambda_{DP,n+1}\left[k_0\delta\mathbf{1} + 2\mu\mathbf{n}_{n+1}\right] \tag{D.77}$$

$$- \Delta\lambda_{CC,n+1}\left[2\left(I_{n+1} + p_c - p_t\right)\mathbf{1} + \frac{12\mu d_{n+1}}{M^2}\mathbf{n}_{n+1}\right] \tag{D.78}$$

It turns out that the direction of $\mathbf{S}_{n+1}$ and $\mathbf{S}_{n+1}^{trial}$ are the same and the invariants d_{n+1} and $I_{n+1}$are determined from:

$$d_{n+1} = \sqrt{3J_{2,n+1}} = \frac{d_{n+1}^{trial} - \sqrt{6}\mu\Delta\lambda_{DP,n+1}}{1 + \frac{6\mu\Delta\lambda_{CC,n+1}}{M^2}} \tag{D.79}$$

$$I_{n+1} = \frac{I_{n+1}^{trial} - \Delta\lambda_{DP,n+1}k_0 - \Delta\lambda_{CC,n+1}k_0\left(p_{c,n} - p_t\right)}{1 - 2k_0\Delta\lambda_{CC,n+1}} \tag{D.80}$$

Finally, the two plastic multipliers are solutions of the following two-equation system:

$$\begin{cases} f_{DP}\left(\boldsymbol{\Sigma}_{n+1}, p_{c,n+1}\right) = \frac{1}{\sqrt{3}}d_{n+1} + \delta I_{n+1} - c = 0 \\ f_{cc}\left(\boldsymbol{\Sigma}_{n+1}, p_{c,n+1}\right) = \frac{d_{n+1}^2}{M^2} + \left(I_{n+1} - 2p_t\right)\left(I_{n+1} + 2p_{c,n}\right) = 0 \end{cases} \tag{D.81}$$

Last, the consolidation pressure is updated from the hardening rule. Taking into account the expression for the plastic strains it reads:

$$p_{c,n+1} = p_{c,n}\exp\left[\frac{1+e}{\lambda-\kappa}\left(\Delta\lambda_{DP,n+1}\delta + 2\Delta\lambda_{CC,n+1}\left(I_{n+1} + p_{c,n} - p_t\right)\right)\right] \tag{D.82}$$

D.3.8 Numerical Treatment and Convergence

The presented plasticity routines were implemented into the existing calculation module MPNL. The general solution algorithm of this model is preserved. It uses a modified Newton-Raphson method to solve the equation system. During the calculation, the stiffness matrix is not updated. This is a standard strategy in CESAR-LCPC as it is assumed that the time to reassemble the stiffness matrix is more important than the increased number of local iterations. The convergence is checked after every iteration based on the three norms of variations between two iterations:

$$\|\Delta F\| = \sqrt{\left(\Delta F_1\right)^2 + \left(\Delta F_1\right)^2 + ... + \left(\Delta F_n\right)^2} \tag{D.83}$$

$$\|\Delta \mathcal{U}\| = \sqrt{\left(\Delta \mathcal{U}_1\right)^2 + \left(\Delta \mathcal{U}_1\right)^2 + ... + \left(\Delta \mathcal{U}_n\right)^2} \tag{D.84}$$

$$\|\Delta \mathcal{W}\| = \sqrt{\left(\Delta \mathcal{W}_1\right)^2 + \left(\Delta \mathcal{W}_1\right)^2 + ... + \left(\Delta \mathcal{W}_n\right)^2} \tag{D.85}$$

which are the norms on the change in the right hand side member of the global equation system (D.83), the change in unknowns $\Delta\mathcal{U}$ (D.84) and the change in work $\Delta\mathcal{W}$ (D.85). n is the number of equations.

D.3.9 Verification

The described return mapping algorithm was verified through a two step process. First the individual algorithms for the two yield surfaces were compared individually with the existing algorithms in CESAR of the same type. In a second step, the corner zone algorithm was tested by comparing the output of the FE calculation with a manual calculation. Both verification steps were performed for a homogeneous material.

D.3.10 Input Parameters

Table D.3 gives the set of input parameters for an MPNL calculation with IMOD=39. The input data for the MPNL key word are identical to the standard CESAR version except for an additional key word "LIX" which indicates if stated that an input file from a LIXI calculation is being read.

* TITLE	
* IMOD, (INAT),	Control variables for the calculation. INAT only for family 45
* ρ_{sat},E_0, ν_0	Density of saturated porous medium, drained Young's modulus and Poisson's. ratio
* $\rho_{fl}, \phi_0, 1/\mathrm{M}$	Fluid phase density, initial porosity and inverse of the Biot Modulus
* $k_{xx}, k_{yy}, (k_{zz}), k_{xy}, (k_{yz}, k_{xz})$	Permeability coefficients, in parenthesis only for family 46
* $b, (b_2)$	Biot coefficient(s)
* $\frac{C_\epsilon}{T_0}, \lambda_{xx}/T_0, \lambda_{yy}/T_0, (\lambda_{zz}/T_0)$,	Volumetric heat capacity at constant drained deformation
$\lambda_{xy}/T0, (\lambda_{yz}/T_0, \lambda_{xz}/T_0)$	normalized by the reference temperature. Therm. conductivities normalized by the ref. Temp.
* $\mathrm{a}_0, (a_{02}), 3\alpha_m$	Thermoelastic compressibility coefficient(s) at zero drained volume deformation Dilation coefficient at zero volumetric deformation in drained conditions
Material law Parameters	
* $\lambda, \kappa, M_0, e_0, p_c^0, p_t^0$	Cam -Clay parameters for the undegraded state
* c_0, δ_0, ψ_0	Drucker-Prager parameters for the undegraded state
* $M_{\rightarrow \mathrm{CH}}, p_c^{\rightarrow \mathrm{CH}}, p_t^{\rightarrow \mathrm{CH}}$	Cam -Clay parameters for the intermediate state
* $c_{\rightarrow \mathrm{CH}}, \delta_{\rightarrow \mathrm{CH}}$	Drucker-Prager parameters for the intermediate state
* $M_\infty, p_c^\infty, p_t^\infty$	Cam -Clay parameters for the degraded state
* c_∞, δ_∞	Drucker-Prager parameters for the degraded state
* MAT	=1 for a paste and 2 for a mortar/concrete. Control variable for the elasticity
* β	Coussy coefficient

Table D.3: Input parameters for a calculation with IMOD=39, leached cementitious materials.